QUANTUM PROPERTIES OF FEW-LAYER GRAPHENE AND VAN DER WAALS HETEROSTRUCTURES

A THESIS SUBMITTED TO THE UNIVERSITY OF MANCHESTER
FOR THE DEGREE OF DOCTOR OF PHILOSOPHY
IN THE FACULTY OF SCIENCE AND ENGINEERING

2023

Christian L. Moulsdale

School of Natural Sciences

Contents

Word Count: 26118

List of Tables

List of Figures

Abstract

In this thesis, we study the quantum properties of semimetallic few-layer graphene, and its van der Waals (vdW) heterostructures with insulating hexagonal boron nitride (hBN) and the ferromagnetic semiconducting chromium trihalides (CrX_3, X=Cl,Br,I). Monolayer graphene is an atomically thin two-dimensional (2D) material, which was first isolated from bulk graphite at the University of Manchester 2004. It is famed for its physical properties, including its large tensile strength and electrical and thermal conductivities. Constructing van der Waals (vdW) heterostructures of graphene and different materials allows for novel two-dimensional materials synergising their properties, and the interference of the incommensurate lattices of each layer gives a long-range moiré superlattice (mSL). This reduces the density scale of effects such as the umklapp scattering of electrons off a periodic lattice potential.

We start with a study into engineering the topological properties of bilayer graphene using strain and a vertical bias, predicting that the topological magnetic moment is enhanced by two orders of magnitude with modest variation of the parameters. We also show how this manifests in the Landau level spectrum and the anomalous contribution to the Hall conductivity. Then, we consider a highly-aligned hBN/graphene/hBN heterostructure, which features a Kagomé network of chiral channels between regions of different topology. We derive the Aharonov-Bohm oscillations in the electrical conductivity of coherent electron wave packets propagating through this network, which is a signature of structural inversion symmetry breaking. We continue with an experimental study into the opening of a bandgap in bilayer graphene resulting from the charge transfer to a CrX_3 substrate. We demonstrate excellent agreement with our theoretical predictions, and show that electrons in the conduction band of the CrX_3 layer are strongly correlated. After this, we discuss the electrical properties of a 3D material composed of alternating stacks of commensurate graphene and hBN. This exhibits semimetallic and semiconducting behaviour, depending on the coupling between the graphene layers and the relative stacking of the hBN layers. We conclude with a study into the contribution of umklapp electron-electron scattering to the p-doped resistivity of a bilayer graphene/hBN heterostructure. This has distinct features from the corresponding monolayer graphene/hBN heterostructure, with the resistivity rapidly growing with hole density above a threshold before reaching a peak value, both of which are determined by the size of the mSL.

Declaration

Parts of material included in Chapter 5 have been submitted by Giulia Tenasini in support of an application to the Université de Genève for the degree of Doctor of Philosophy. This relates to the shared authorship of G. Tenasini, D. Soler-Delgado, Z. Wang, F. Yao, D. Dumcenco, E. Giannini, K. Watanabe, T. Taniguchi, C. Moulsdale, A. Garcia-Ruiz, V. I. Fal'ko, I. Gutiérrez-Lezama and A. F. Morpurgo, "Band Gap Opening in Bilayer Graphene-$CrCl_3$/$CrBr_3$/CrI_3 van der Waals Interfaces", Nano Lett., **22** (16), 6760-6766 (2022).

Parts of material included in Chapter 6 have been submitted by Xi Chen in support of an application to the University of Manchester for the degree of Master of Science. This relates to the shared authorship of X. Chen, C. Moulsdale, V. I. Fal'ko and A. Knothe, "Semimetallic and semiconducting graphene-hBN multilayers with parallel or reverse stacking", arXiv:2210.16393 (2022). [**Submitted to Physical Review B**]

Otherwise, no portion of the work referred to in this thesis has been submitted in support of an application for another degree or qualification of this or any other university or other institute of learning.

Copyright

i. The author of this thesis (including any appendices and/or schedules to this thesis) owns certain copyright or related rights in it (the “Copyright”) and they have given The University of Manchester certain rights to use such Copyright, including for administrative purposes.

ii. Copies of this thesis, either in full or in extracts and whether in hard or electronic copy, may be made **only** in accordance with the Copyright, Designs and Patents Act 1988 (as amended) and regulations issued under it or, where appropriate, in accordance with licensing agreements which the University has from time to time. This page must form part of any such copies made.

iii. The ownership of certain Copyright, patents, designs, trademarks and other intellectual property (the “Intellectual Property”) and any reproductions of copyright works in the thesis, for example graphs and tables (“Reproductions”), which may be described in this thesis, may not be owned by the author and may be owned by third parties. Such Intellectual Property and Reproductions cannot and must not be made available for use without the prior written permission of the owner(s) of the relevant Intellectual Property and/or Reproductions.

iv. Further information on the conditions under which disclosure, publication and commercialisation of this thesis, the Copyright and any Intellectual Property and/or Reproductions described in it may take place is available in the University IP Policy (see `http://documents.manchester.ac.uk/DocuInfo.aspx?DocID=24420`), in any relevant Thesis restriction declarations deposited in the University Library, The University Library’s regulations (see `http://www.library.manchester.ac.uk/about/regulations/`) and in The University’s policy on presentation of Theses

Acknowledgements

Foremost, I must thank my supervisor, Vladimir Fal'ko, alongside my co-supervisor, Neil Drummond, and Angelika Knothe, whose assistance I consider to be comparable to a co-supervisor. I acknowledge funding from the Graphene NOWNANO CDT, which is funded by the University of Manchester and the Engineering and Physical Sciences Research Council (EPSRC). I am grateful to my family for their support throughout my studies, in particular Caroline Moulsdale, Sheila Seymour and Peter Toner. I have had many useful discussions, especially with my academic adviser, Thomas Waigh, alongside Sergey Slizovskiy, Vladimir Enaldiev and Aitor García-Ruiz.

Chapter 1

Introduction

1.1 Graphene

Graphene is the quintessential two-dimensional (2D) material, first isolated from its bulk three-dimensional (3D) form, graphite, at the University of Manchester in 2004 [1, 2, 3]. Graphene features an atomically thin honeycomb lattice of carbon atoms, whose robust structural bonds give its contrasting flexibility and famously high tensile strength [4]. It is a semimetal with large electrical and thermal conductivities from diffuse bonds which are reminiscent of the cloud of delocalised electrons in a metal [5]. The low-energy excitations are massless chiral Dirac fermions, making graphene a low-energy analogue to quantum electrodynamics, featuring a half-integer quantum Hall effect [6, 7] alongside suppressed backscattering and the resulting Klein paradox of perfect transmittance through a square barrier [8, 9, 10]. The large mean free paths of electrically neutral spin currents in graphene [11, 12] make it an ideal candidate for spintronic devices, manipulating the spin degree of freedom for information storage and logic devices [13, 14]. Graphene is also an ideal material for valleytronics [15, 16]: manipulating a pseudo-spin degree of freedom whose up and down projections are the wavefunction components in the two valleys at the band edges in its dispersion, with an approximate symmetry under rotations of this pseudo-spin vector due to the weak inter-valley scattering [17, 18, 19].

This has inspired an exploration into other multivalley 2D materials such as few-layer graphene, whose electronic properties depend strongly upon the number of layers [20]. In particular, we consider semimetallic Bernal-stacked bilayer graphene, whose low-energy excitations are massive chiral Dirac fermions [21, 22]. The distinct chirality from the monolayer allows backscattering and gives the alternative Klein paradox of perfect reflectance from a sufficiently wide square barrier [9]. Unlike the monolayer, a tunable bandgap may be opened by biasing each layer with electrostatic gating [23, 24, 25, 26], allowing for tunable confinement into quantum dots [27, 28, 29]. Another bulk material which can be decomposed into atomically thin honeycomb layers is hexagonal boron nitride (hBN), an insulator with a large intrinsic bandgap resulting from the inequivalent boron and nitrogen atoms [30, 31, 32, 33]. Finally, we consider the chromium trihalides (CrX_3, X=Cl,Br,I), a family of ferromagnetic semiconductors whose layers feature a honeycomb lattice of Cr atoms [34].

In turn, this has inspired the stacking of different 2D materials into van der Waals heterostructures (vdW), with the aim of synergising their properties [35, 36, 37]. A recurring theme in vdW heterostructures is the formation of a long-range moiré superlattice (mSL), due to the interference of the incommensurate lattices at the interface between different layers. The large mSL period gives a reduced density scale for effects such as umklapp scattering off [38, 39, 40, 41] and Landau level broadening by a periodic lattice potential [42, 43, 44, 45]. Twisted bilayer graphene is not a vdW heterostructure, but its mSL induces zero Fermi velocity and strong correlation at several magic twist angles [46, 47], the first of which famously exhibits unconventional superconductivity [48]. An atomically smooth hBN substrate suppresses ripples in graphene and enhances its mobility [49], enhances the on-off ratio of a graphene field-effect transistor [50], and makes it an ideal choice for a gate dielectric [49, 51, 52].

This thesis contains a collection of works studying the quantum properties of few-layer graphene and vdW heterostructures combining few-layer graphene, hBN and CrX_3. In Chapter 3, we study the enhancement of topological effects in bilayer graphene using strain and a vertical bias. In Chapter 4, we derive the form of a chiral Kagomé network between regions of distinct topology in a highly-aligned hBN/-graphene/hBN heterostructure. In Chapter 5, we present an experimental study into the opening of a bandgap in bilayer graphene by a CrX_3 substrate. In Chapter 6, we explore the electronic properties of 3D stacks of alternating graphene and hBN layers with matching lattices. In Chapter 7, we investigate the contribution of umklapp electron-electron scattering to the resistivity of a bilayer graphene/hBN heterostructure.

A common theme throughout this thesis, and Physics in general, is the study of the symmetries of systems and their consequences. By Noether's theorem, each continuous symmetry of a system implies a corresponding conserved quantity [53, 54]. For example, continuous symmetries with respect to time translations, (space) translations and rotations result in the well-known conservation laws for energy, momentum and angular momentum, respectively. There are also discrete symmetries, which constrain the form of the electron bands [55, 56, 57, 58]. For example, specific allotropes of few-layer graphene featuring both time reversal and (spatial) inversion symmetry[1] have a corresponding gapless spectrum at low energies. A more esoteric example is the chiral symmetry [59], protecting the chirality, and the combination of time reversal and chiral symmetries in monolayer graphene gives a particle-hole (eh) symmetry, with respect to exchange of electrons in the conduction (particle) and valence (hole) bands.

A lattice breaks the continuous translational and rotational symmetries, although a periodic lattice features corresponding discrete symmetries, including translation with respect to its lattice vectors. The momentum is conserved up to a (Bragg) lattice vector in the reciprocal space, which leads to umklapp electron-electron scattering, considered in Chapter 7, where two interacting electrons receive a momentum kick Bragg scattering off the lattice [38, 60, 61, 62, 63]. The mSL further breaks the translational symmetry, with the mSL-reconstructed minibands of monolayer and bilayer graphene featuring in Chapters 4 and 7, respectively [46, 64, 65, 66]. Monolayer graphene features a six-fold discrete rotational symmetry, which is broken to three-fold by the interface with hBN in Chapters 4 and 6, while the three-fold symmetry of bilayer graphene is totally broken by strain in Chapter 3.

The neighbouring hBN layers induce a sublattice bias in monolayer graphene in Chapters 4 and 6, breaking inversion symmetry and opening a bandgap. In bilayer graphene in Chapters 3, 5 and 7, this is achieved by a vertical bias, which is induced by external gating [23, 25, 26] or charge transfer to a magnetic substrate [67, 68, 69, 70], as discussed in Chapter 5. Breaking time reversal symmetry with an external magnetic field gives the dispersionless Landau levels seen in Chapters 3 and 5, corresponding to quantised cyclotron orbits [71, 72, 73]. The intrinsic eh symmetry breaking of bilayer graphene can be seen in Chapters 3, 5 and 7 [22], while hBN-induced eh symmetry breaking can be seen in Chapters 4, 6 and 7 [64, 66, 65].

Finally, we consider the topology of the electron states. This coincides with the

---

[1] E.g., monolayer graphene in Section 2.1 and Bernal-stacked bilayer graphene in Section 2.6.

chirality in the gapless case, which is protected by the chiral symmetry and quantified by the non-kinematic Berry phase incurred on trajectories enclosing each of the Dirac points [74]. The distinct chiralities of monolayer and bilayer graphene [9] is reflected in their Berry phases, π [7, 75] and 2π [76], respectively. The Berry phase of a trajectory is expressed as the flux of the Berry curvature through the surface enclosed by the trajectory in Chapters 3 and 4 and 6 [77, 78]. The Berry curvature induces an anomalous velocity in an external electric field [43, 77, 79] responsible for the anomalous quantum Hall effect in the absence of a magnetic field [80, 81, 78], and an anomalous contribution to the classical effect at small fields [81, 82] in Chapter 3. The flux of the Berry curvature through the unit cell of the reciprocal lattice gives the Chern number, a topological invariant protected in the absence of gap closures. In Chapters 4 and 6, we consider the flux through a large region surrounding each valley, giving the corresponding valley Chern number which is protected by the weak inter-valley scattering in graphene [17, 18, 19]. By the bulk-boundary correspondence [83, 84], we derive the network of valley-polarised chiral channels along the zero-gap lines between regions of different topology (valley Chern number) in Chapter 4.

1.2 Thesis structure

In light of Christian Moulsdale's publications[2], this thesis is presented in the journal format of the University of Manchester. Chapter 2 serves as an armamentarium, introducing the various systems and analytical techniques used in this thesis. Chapters 3-7 represent manuscripts presented in chronological order of their publication, or submission to journals where they are being peer-reviewed at the time of submission of this thesis. Each chapter starts with a preface, where we discuss the context of the corresponding manuscript, including its authors, how electronic copies of the manuscript and any supplementary material may be accessed, and the contributions of Christian Moulsdale. The rest of the chapter represents the main text of the manuscript, corresponding to its most recent preprint on an open-access repository, arxiv, at the time of submission of this thesis. Any changes to this are strictly to match the format of this thesis or minor corrections in response to examiner comments, and any supplementary material is

---

[2] See Section 1.3

included as appendices to the chapter. Chapter 8 provides a short conclusion of the findings of each paper and their wider context, including more recent publications, before we conclude the thesis. Abstracts summarising the findings of each chapter are given in the following paragraphs.

Chapter 3: Engineering of the topological magnetic moment of electrons in bilayer graphene using strain and electrical bias. We study the tunability of the topological properties of bilayer graphene with moderate uniaxial strain and interlayer offset, which equivalently break the rotational symmetry, and interlayer bias, which breaks inversion symmetry and opens a bandgap. The topological magnetic moment of the electron states, a consequence of their finite Berry curvature, is enhanced at the band edge up to two orders of magnitude compared to the intrinsic value, with an anisotropic dependence on the strain direction. This gives a valley splitting in an external magnetic field, which is seen in the Landau level dispersion and the anomalous contribution to the Hall conductivity. The strain causes a Lifshitz transition as the Dirac cones in each valley coalesce, enhancing the density of states at the van Hove singularity.

Chapter 4: Kagomé network of miniband-edge states in double-aligned graphene-hexagonal boron nitride structures. We study a Kagomé network of channels appearing between regions of different local stacking configurations in an hBN/graphene/hBN heterostructure. The broken inversion symmetry is represented by an oscillating electron mass for electrons near the secondary Dirac point, whose different signs in the alternating triangular and hexagonal regions of the Kagomé structure gives distinct topology, represented by the valley Chern number. We predict chiral states propagating along these channels by the bulk-boundary correspondence, which are separated from the bulk states in either region by the minigap. We derive the form of Aharonov-Bohm oscillations in the electrical conductivity of the states with respect to an external magnetic field, with a period less than 1 Tesla as a result of the large super cell. These oscillations are the signature of the inversion symmetry breaking from parallel hBN layers, not appearing when one of the layers is inverted.

Chapter 5: Band Gap Opening in Bilayer Graphene-$CrCl_3$/$CrBr_3$/CrI_3 van der Waals Interfaces. We present an experimental study into how the charge transfer from bilayer graphene to a CrX_3 substrate induces the vertical bias discussed in Chapter 3, opening a bandgap. The zero-magnetic field bandgap is determined from the activation energy of the electrical conductivity, with magnitudes up to 170 meV, for $CrCl_3$. The magnitude of the bandgap decreases with increasing magnetic field, determined from the dependence of the low-temperature conductivity on the gate voltages. Using a modified Hartree approach for the screening of the bandgap, accounting for the out-of-plane polarisation of the π and σ bands of bilayer graphene, we find excellent agreement with the ab initio and experimental results. We demonstrate that the CrX_3 layer features flat bands consistent with strong correlation, as electrons transferred to its conduction band are virtually localised to the Cr atoms.

Chapter 6: Semimetallic and semiconducting graphene-hBN multilayers with parallel or reverse stacking. We discuss how the electronic properties of a commensurate three-dimensional stack of alternating graphene and hBN layers depends upon the stacking configuration. Recent ab initio calculations have predicted that such a system is possible, as the graphene and hBN layers expand and contract, respectively, to match their lattice periods. As in Chapter 4, there are two distinct configurations, featuring inversion symmetry if neighbouring hBN layers are parallel, which is broken in the antiparallel configuration where every other hBN layer is rotated by 180°. Depending on the couplings between the graphene layers, the system features semimetallic phases, both trivial and Weyl in nature. We produce a phase diagram for the parallel configuration, which also includes semiconducting gapped phases.

Chapter 7: Umklapp electron-electron scattering in bilayer graphene moiré superlattice. We study the contribution of umklapp electron-electron (Uee) scattering to the electrical resistivity of a p-doped heterostructure of bilayer graphene and hBN, which features a T^2 dependent on the temperature. Uee scattering is distinguished from normal Coulomb electron-electron scattering by one of the electrons Bragg scattering off the superlattice, imparting a momentum “kick” which violates the conservation of momentum. The Uee resistivity grows rapidly with hole density above a threshold, before reaching a peak value, both of whose values depend upon the size of the superlattice. The strong eh symmetry breaking results in a negligible Uee contribution to the e-doped resistivity. The vertical bias splits the hole dispersion into minivalleys at low densities, with electrons undergoing Uee scattering between the minivalleys, enhancing the Uee contribution to the resistivity in both bands.

1.3 Publications

- C. Moulsdale, P. A. Pantaleón, R. Carrillo-Bastos and Y. Xian, “Unconventional Thermal Magnon Hall Effect in a Ferromagnetic Topological Insulator”, Phys. Rev. B **99**, 214424 (2019) [3].

- C. Moulsdale, A. Knothe and V. Fal’ko, “Engineering of the topological magnetic moment of electrons in bilayer graphene using strain and electrical bias”, Phys. Rev. B **101**, 085118 (2020).

- C. Moulsdale, A. Knothe and V. Fal’ko, “Kagomé network of chiral miniband-edge states in double-aligned graphene-hexagonal boron nitride structures”, Phys. Rev. B **105**, L201112 (2022).

- G. Tenasini, D. Soler-Delgado, Z. Wang, F. Yao, D. Dumcenco, E. Giannini, K. Watanabe, T. Taniguchi, C. Moulsdale, A. Garcia-Ruiz, V. I. Fal’ko, I. Gutiérrez-Lezama and A. F. Morpurgo, “Band Gap Opening in Bilayer Graphene-$CrCl_3$/$CrBr_3$/CrI_3 van der Waals Interfaces”, Nano Lett., **22** (16), 6760-6766 (2022).

- X. Chen, C. Moulsdale, V. I. Fal’ko and A. Knothe, “Semimetallic and semiconducting graphene-hBN multilayers with parallel or reverse stacking”, arXiv:2210.16393 (2022). [**Submitted to Physical Review B**]

- C. Moulsdale and V. Fal’ko, “Umklapp electron-electron scattering in bilayer graphene moiré superlattice”, arXiv:2211.01005 (2022). [**Submitted to Physical Review Letters**]

Bibliography

[1] R. Saito, M. S. Dresselhaus, and G. Dresselhaus, *Physical Properties of Carbon Nanotubes*. Imperial College Press, 1998.

---

[3] This publication was the result of work began during my masters project with my then supervisor, Yang Xian, and submitted during my PhD. Its contents are outside of the scope of this thesis, and are not included.

[2] K. S. Novoselov, A. K. Geim, S. V. Morozov, D. Jiang, Y. Zhang, S. V. Dubonos, I. V. Grigorieva, and A. A. Firsov, Electric Field Effect in Atomically Thin Carbon Films *Science*, vol. 306, no. 5696, pp. 666–669, 2004.

[3] A. H. Castro Neto, F. Guinea, N. M. R. Peres, K. S. Novoselov, and A. K. Geim, The electronic properties of graphene *Rev. Mod. Phys.*, vol. 81, pp. 109–162, Jan 2009.

[4] D. G. Papageorgiou, I. A. Kinloch, and R. J. Young, Mechanical properties of graphene and graphene-based nanocomposites *Progress in Materials Science*, vol. 90, pp. 75–127, 2017.

[5] A. A. Balandin, S. Ghosh, W. Bao, I. Calizo, D. Teweldebrhan, F. Miao, and C. N. Lau, Superior Thermal Conductivity of Single-Layer Graphene *Nano Letters*, vol. 8, no. 3, pp. 902–907, 2008. PMID: 18284217.

[6] K. S. Novoselov, A. K. Geim, S. V. Morozov, D. Jiang, M. I. Katsnelson, I. V. Grigorieva, S. V. Dubonos, and A. A. Firsov, Two-dimensional gas of massless Dirac fermions in graphene *Nature*, vol. 438, pp. 197–200, Nov 2005.

[7] Y. Zhang, Y.-W. Tan, H. L. Stormer, and P. Kim, Experimental observation of the quantum Hall effect and Berry's phase in graphene *Nature*, vol. 438, pp. 201–204, Nov 2005.

[8] A. C. Neto, F. Guinea, and N. M. Peres, Drawing conclusions from graphene *Physics World*, vol. 19, p. 33, nov 2006.

[9] M. I. Katsnelson, K. S. Novoselov, and A. K. Geim, Chiral tunnelling and the Klein paradox in graphene *Nature Physics*, vol. 2, pp. 620–625, Sep 2006.

[10] M. Katsnelson and K. Novoselov, Graphene: New bridge between condensed matter physics and quantum electrodynamics *Solid State Communications*, vol. 143, no. 1, pp. 3–13, 2007. Exploring graphene.

[11] N. Tombros, C. Jozsa, M. Popinciuc, H. T. Jonkman, and B. J. van Wees, Electronic spin transport and spin precession in single graphene layers at room temperature *Nature*, vol. 448, pp. 571–574, Aug 2007.

[12] W. Han, K. Pi, K. M. McCreary, Y. Li, J. J. I. Wong, A. G. Swartz, and R. K. Kawakami, Tunneling Spin Injection into Single Layer Graphene *Phys. Rev. Lett.*, vol. 105, p. 167202, Oct 2010.

[13] I. Žutić, J. Fabian, and S. Das Sarma, Spintronics: Fundamentals and applications *Rev. Mod. Phys.*, vol. 76, pp. 323–410, Apr 2004.

[14] W. Han, R. K. Kawakami, M. Gmitra, and J. Fabian, Graphene spintronics *Nature Nanotechnology*, vol. 9, pp. 794–807, Oct 2014.

[15] J. R. Schaibley, H. Yu, G. Clark, P. Rivera, J. S. Ross, K. L. Seyler, W. Yao, and X. Xu, Valleytronics in 2D materials *Nature Reviews Materials*, vol. 1, p. 16055, Aug 2016.

[16] M. S. Mrudul, Álvaro Jiménez-Galán, M. Ivanov, and G. Dixit, Light-induced valleytronics in pristine graphene *Optica*, vol. 8, pp. 422–427, Mar 2021.

[17] S. V. Morozov, K. S. Novoselov, M. I. Katsnelson, F. Schedin, L. A. Ponomarenko, D. Jiang, and A. K. Geim, Strong Suppression of Weak Localization in Graphene *Phys. Rev. Lett.*, vol. 97, p. 016801, Jul 2006.

[18] A. F. Morpurgo and F. Guinea, Intervalley Scattering, Long-Range Disorder, and Effective Time-Reversal Symmetry Breaking in Graphene *Phys. Rev. Lett.*, vol. 97, p. 196804, Nov 2006.

[19] R. V. Gorbachev, F. V. Tikhonenko, A. S. Mayorov, D. W. Horsell, and A. K. Savchenko, Weak Localization in Bilayer Graphene *Phys. Rev. Lett.*, vol. 98, p. 176805, Apr 2007.

[20] R. M. Torres-Rojas, D. A. Contreras-Solorio, L. Hernández, and A. Enciso, Band gap variation in bi, tri and few-layered 2D graphene/hBN heterostructures *Solid State Communications*, vol. 341, p. 114553, 2022.

[21] E. McCann and V. I. Fal'ko, Landau-Level Degeneracy and Quantum Hall Effect in a Graphite Bilayer *Phys. Rev. Lett.*, vol. 96, p. 086805, Mar 2006.

[22] E. McCann and M. Koshino, The electronic properties of bilayer graphene *Reports on Progress in Physics*, vol. 76, p. 056503, apr 2013.

[23] E. McCann, Asymmetry gap in the electronic band structure of bilayer graphene *Phys. Rev. B*, vol. 74, p. 161403, Oct 2006.

[24] K. F. Mak, C. H. Lui, J. Shan, and T. F. Heinz, Observation of an Electric-Field-Induced Band Gap in Bilayer Graphene by Infrared Spectroscopy *Phys. Rev. Lett.*, vol. 102, p. 256405, Jun 2009.

[25] Y. Zhang, T.-T. Tang, C. Girit, Z. Hao, M. C. Martin, A. Zettl, M. F. Crommie, Y. R. Shen, and F. Wang, Direct observation of a widely tunable bandgap in bilayer graphene *Nature*, vol. 459, pp. 820–823, Jun 2009.

[26] A. Ramasubramaniam, D. Naveh, and E. Towe, Tunable Band Gaps in Bilayer Graphene-BN Heterostructures *Nano Letters*, vol. 11, no. 3, pp. 1070–1075, 2011. PMID: 21275424.

[27] S. Dröscher, C. Barraud, K. Watanabe, T. Taniguchi, T. Ihn, and K. Ensslin, Electron flow in split-gated bilayer graphene *New Journal of Physics*, vol. 14, p. 103007, oct 2012.

[28] M. Eich, F. c. v. Herman, R. Pisoni, H. Overweg, A. Kurzmann, Y. Lee, P. Rickhaus, K. Watanabe, T. Taniguchi, M. Sigrist, T. Ihn, and K. Ensslin, Spin and Valley States in Gate-Defined Bilayer Graphene Quantum Dots *Phys. Rev. X*, vol. 8, p. 031023, Jul 2018.

[29] R. Garreis, A. Knothe, C. Tong, M. Eich, C. Gold, K. Watanabe, T. Taniguchi, V. Fal'ko, T. Ihn, K. Ensslin, and A. Kurzmann, Shell Filling and Trigonal Warping in Graphene Quantum Dots *Phys. Rev. Lett.*, vol. 126, p. 147703, Apr 2021.

[30] Y. Shi, C. Hamsen, X. Jia, K. K. Kim, A. Reina, M. Hofmann, A. L. Hsu, K. Zhang, H. Li, Z.-Y. Juang, M. S. Dresselhaus, L.-J. Li, and J. Kong, Synthesis of Few-Layer Hexagonal Boron Nitride Thin Film by Chemical Vapor Deposition *Nano Letters*, vol. 10, no. 10, pp. 4134–4139, 2010. PMID: 20812716.

[31] S. K. Jang, J. Youn, Y. J. Song, and S. Lee, Synthesis and Characterization of Hexagonal Boron Nitride as a Gate Dielectric *Scientific Reports*, vol. 6, p. 30449, Jul 2016.

[32] D. Wickramaratne, L. Weston, and C. G. Van de Walle, Monolayer to Bulk Properties of Hexagonal Boron Nitride *The Journal of Physical Chemistry C*, vol. 122, no. 44, pp. 25524–25529, 2018.

[33] M. J. Molaei, M. Younas, and M. Rezakazemi, A Comprehensive Review on Recent Advances in Two-Dimensional (2D) Hexagonal Boron Nitride *ACS Applied Electronic Materials*, vol. 3, no. 12, pp. 5165–5187, 2021.

[34] W.-B. Zhang, Q. Qu, P. Zhu, and C.-H. Lam, Robust intrinsic ferromagnetism and half semiconductivity in stable two-dimensional single-layer chromium trihalides *J. Mater. Chem. C*, vol. 3, pp. 12457–12468, 2015.

[35] A. K. Geim and I. V. Grigorieva, Van der Waals heterostructures *Nature*, vol. 499, pp. 419–425, Jul 2013.

[36] Y. Liu, N. O. Weiss, X. Duan, H.-C. Cheng, Y. Huang, and X. Duan, Van der Waals heterostructures and devices *Nature Reviews Materials*, vol. 1, p. 16042, Jul 2016.

[37] K. S. Novoselov, A. Mishchenko, A. Carvalho, and A. H. C. Neto, 2D materials and van der Waals heterostructures *Science*, vol. 353, no. 6298, p. aac9439, 2016.

[38] A. H. MacDonald, R. Taylor, and D. J. W. Geldart, Umklapp electron-electron scattering and the low-temperature electrical resistivity of the alkali metals *Phys. Rev. B*, vol. 23, pp. 2718–2730, Mar 1981.

[39] S. Y. Ren and J. D. Dow, Thermal conductivity of superlattices *Phys. Rev. B*, vol. 25, pp. 3750–3755, Mar 1982.

[40] J. R. Wallbank, R. Krishna Kumar, M. Holwill, Z. Wang, G. H. Auton, J. Birkbeck, A. Mishchenko, L. A. Ponomarenko, K. Watanabe, T. Taniguchi, K. S. Novoselov, I. L. Aleiner, A. K. Geim, and V. I. Fal'ko, Excess resistivity in graphene superlattices caused by umklapp electron–electron scattering *Nature Physics*, vol. 15, pp. 32–36, Jan 2019.

[41] H. Ishizuka and L. Levitov, Wide-range T2 resistivity and umklapp scattering in moiré graphene *New Journal of Physics*, vol. 24, p. 052001, may 2022.

[42] D. R. Hofstadter, Energy levels and wave functions of Bloch electrons in rational and irrational magnetic fields *Phys. Rev. B*, vol. 14, pp. 2239–2249, Sep 1976.

[43] M.-C. Chang and Q. Niu, Berry Phase, Hyperorbits, and the Hofstadter Spectrum *Phys. Rev. Lett.*, vol. 75, pp. 1348–1351, Aug 1995.

[44] K. Hejazi, C. Liu, and L. Balents, Landau levels in twisted bilayer graphene and semiclassical orbits *Phys. Rev. B*, vol. 100, p. 035115, Jul 2019.

[45] X. Chen, J. R. Wallbank, A. A. Patel, M. Mucha-Kruczyński, E. McCann, and V. I. Fal'ko, Dirac edges of fractal magnetic minibands in graphene with hexagonal moiré superlattices *Phys. Rev. B*, vol. 89, p. 075401, Feb 2014.

[46] R. Bistritzer and A. H. MacDonald, Moiré bands in twisted double-layer graphene *Proceedings of the National Academy of Sciences*, vol. 108, no. 30, pp. 12233–12237, 2011.

[47] Y. Cao, V. Fatemi, A. Demir, S. Fang, S. L. Tomarken, J. Y. Luo, J. D. Sanchez-Yamagishi, K. Watanabe, T. Taniguchi, E. Kaxiras, R. C. Ashoori, and P. Jarillo-Herrero, Correlated insulator behaviour at half-filling in magic-angle graphene superlattices *Nature*, vol. 556, pp. 80–84, Apr 2018.

[48] Y. Cao, V. Fatemi, S. Fang, K. Watanabe, T. Taniguchi, E. Kaxiras, and P. Jarillo-Herrero, Unconventional superconductivity in magic-angle graphene superlattices *Nature*, vol. 556, pp. 43–50, Apr 2018.

[49] C. R. Dean, A. F. Young, I. Meric, C. Lee, L. Wang, S. Sorgenfrei, K. Watanabe, T. Taniguchi, P. Kim, K. L. Shepard, and J. Hone, Boron nitride substrates for high-quality graphene electronics *Nature Nanotechnology*, vol. 5, pp. 722–726, Oct 2010.

[50] K. H. Lee, H.-J. Shin, J. Lee, I.-y. Lee, G.-H. Kim, J.-Y. Choi, and S.-W. Kim, Large-Scale Synthesis of High-Quality Hexagonal Boron Nitride Nanosheets for Large-Area Graphene Electronics *Nano Letters*, vol. 12, no. 2, pp. 714–718, 2012. PMID: 22220633.

[51] Y. Ji, C. Pan, M. Zhang, S. Long, X. Lian, F. Miao, F. Hui, Y. Shi, L. Larcher, E. Wu, and M. Lanza, Boron nitride as two dimensional dielectric: Reliability and dielectric breakdown *Applied Physics Letters*, vol. 108, no. 1, p. 012905, 2016.

[52] T. Knobloch, Y. Y. Illarionov, F. Ducry, C. Schleich, S. Wachter, K. Watanabe, T. Taniguchi, T. Mueller, M. Waltl, M. Lanza, M. I. Vexler, M. Luisier, and T. Grasser, The performance limits of hexagonal boron nitride as an insulator for scaled CMOS devices based on two-dimensional materials *Nature Electronics*, vol. 4, pp. 98–108, Feb 2021.

[53] E. Noether, Invariante Variationsprobleme *Nachrichten von der Gesellschaft der Wissenschaften zu Göttingen, Mathematisch-Physikalische Klasse*, vol. 1918, pp. 235–257, 1918.

[54] J. V. José and E. J. Saletan, *Classical Dynamics: A Contemporary Approach*. Cambridge University Press, 1998.

[55] M. König, H. Buhmann, L. W. Molenkamp, T. Hughes, C.-X. Liu, X.-L. Qi, and S.-C. Zhang, The Quantum Spin Hall Effect: Theory and Experiment *Journal of the Physical Society of Japan*, vol. 77, no. 3, p. 031007, 2008.

[56] M. Z. Hasan and C. L. Kane, Colloquium: Topological insulators *Rev. Mod. Phys.*, vol. 82, pp. 3045–3067, Nov 2010.

[57] X.-L. Qi and S.-C. Zhang, Topological insulators and superconductors *Rev. Mod. Phys.*, vol. 83, pp. 1057–1110, Oct 2011.

[58] C. D. Beule, V. T. Phong, and E. J. Mele, Network model for periodically strained graphene arXiv:2209.02554, 2022.

[59] Y. Hatsugai, T. Morimoto, T. Kawarabayashi, Y. Hamamoto, and H. Aoki, Chiral symmetry and its manifestation in optical responses in graphene: interaction and multilayers *New Journal of Physics*, vol. 15, p. 035023, mar 2013.

[60] J. Bass, W. P. Pratt, and P. A. Schroeder, The temperature-dependent electrical resistivities of the alkali metals *Rev. Mod. Phys.*, vol. 62, pp. 645–744, Jul 1990.

[61] V. Gasparov and R. Huguenin, Electron-phonon, electron-electron and electron-surface scattering in metals from ballistic effects *Advances in Physics*, vol. 42, no. 4, pp. 393–521, 1993.

[62] I. L. Aleiner and O. Agam, Saturation of strong electron-electron umklapp scattering at high temperature *Annals of Physics*, vol. 385, pp. 716–728, 2017.

[63] T. M. Rice, N. J. Robinson, and A. M. Tsvelik, Umklapp scattering as the origin of T-linear resistivity in the normal state of high-T_c cuprate superconductors *Phys. Rev. B*, vol. 96, p. 220502, Dec 2017.

[64] J. R. Wallbank, A. A. Patel, M. Mucha-Kruczyński, A. K. Geim, and V. I. Fal'ko, Generic miniband structure of graphene on a hexagonal substrate *Phys. Rev. B*, vol. 87, p. 245408, Jun 2013.

[65] P. Moon and M. Koshino, Electronic properties of graphene/hexagonal-boron-nitride moiré superlattice *Phys. Rev. B*, vol. 90, p. 155406, Oct 2014.

[66] X. Chen, J. R. Wallbank, M. Mucha-Kruczyński, E. McCann, and V. I. Fal'ko, Zero-energy modes and valley asymmetry in the Hofstadter spectrum of bilayer graphene van der Waals heterostructures with hBN *Phys. Rev. B*, vol. 94, p. 045442, Jul 2016.

[67] M. M. Ugeda, A. J. Bradley, S. F. Shi, F. H. D. Jornada, Y. Zhang, D. Y. Qiu, W. Ruan, S. K. Mo, Z. Hussain, Z. X. Shen, F. Wang, S. G. Louie, and M. F. Crommie, Giant bandgap renormalization and excitonic effects in a monolayer transition metal dichalcogenide semiconductor *Nature Materials*, vol. 13, pp. 1091–1095, 8 2014.

[68] C. Gong and X. Zhang, Two-dimensional magnetic crystals and emergent heterostructure devices *Science*, vol. 363, p. eaav4450, Feb. 2019.

[69] Q. Tong, M. Chen, and W. Yao, Magnetic Proximity Effect in a van der Waals Moiré Superlattice *Physical Review Applied*, vol. 12, p. 024031, Aug 2019.

[70] B. Zhou, J. Balgley, P. Lampen-Kelley, J. Q. Yan, D. G. Mandrus, and E. A. Henriksen, Evidence for charge transfer and proximate magnetism in graphene–$\alpha-$RuCl$_3$ heterostructures *Physical Review B*, vol. 100, p. 165426, 10 2019.

[71] K. v. Klitzing, G. Dorda, and M. Pepper, New Method for High-Accuracy Determination of the Fine-Structure Constant Based on Quantized Hall Resistance *Phys. Rev. Lett.*, vol. 45, pp. 494–497, Aug 1980.

[72] A. H. MacDonald, ed., *Quantum Hall Effect: A Perspective*. Springer Netherlands, 1989.

[73] R. E. Prange and S. M. Girvin, eds., *The Quantum Hall Effect*. Springer New York, 1990.

[74] Quantal phase factors accompanying adiabatic changes *Proceedings of the Royal Society of London. A. Mathematical and Physical Sciences*, vol. 392, pp. 45–57, Mar. 1984.

[75] T. Ando, T. Nakanishi, and R. Saito, Berry's Phase and Absence of Back Scattering in Carbon Nanotubes *Journal of the Physical Society of Japan*, vol. 67, no. 8, pp. 2857–2862, 1998.

[76] K. S. Novoselov, E. McCann, S. V. Morozov, V. I. Fal'ko, M. I. Katsnelson, U. Zeitler, D. Jiang, F. Schedin, and A. K. Geim, Unconventional quantum Hall effect and Berry's phase of 2π in bilayer graphene *Nature Physics*, vol. 2, pp. 177–180, Mar 2006.

[77] M.-C. Chang and Q. Niu, Berry phase, hyperorbits, and the Hofstadter spectrum: Semiclassical dynamics in magnetic Bloch bands *Phys. Rev. B*, vol. 53, pp. 7010–7023, Mar 1996.

[78] D. Xiao, M.-C. Chang, and Q. Niu, Berry phase effects on electronic properties *Rev. Mod. Phys.*, vol. 82, pp. 1959–2007, Jul 2010.

[79] G. Sundaram and Q. Niu, Wave-packet dynamics in slowly perturbed crystals: Gradient corrections and Berry-phase effects *Phys. Rev. B*, vol. 59, pp. 14915–14925, Jun 1999.

[80] F. D. M. Haldane, Model for a Quantum Hall Effect without Landau Levels: Condensed-Matter Realization of the "Parity Anomaly" *Phys. Rev. Lett.*, vol. 61, pp. 2015–2018, Oct 1988.

[81] N. Nagaosa, J. Sinova, S. Onoda, A. H. MacDonald, and N. P. Ong, Anomalous Hall effect *Rev. Mod. Phys.*, vol. 82, pp. 1539–1592, May 2010.

[82] S. Slizovskiy, E. McCann, M. Koshino, and V. I. Fal'ko. arXiv:1905.13094, 2019.

[83] Y. Hatsugai, Edge states in the integer quantum Hall effect and the Riemann surface of the Bloch function *Phys. Rev. B*, vol. 48, pp. 11851–11862, Oct 1993.

[84] Y. Hatsugai, Chern number and edge states in the integer quantum Hall effect *Phys. Rev. Lett.*, vol. 71, pp. 3697–3700, Nov 1993.

Chapter 2

Theory armamentarium

2.1 Monolayer graphene

A monolayer of graphene features a honeycomb lattice of carbon atoms, shown in Fig. 2.1 a), composed of two inequivalent triangular sublattices, A and B [1, 2]. This structure results from the sp^2 hybridisation of the $2s$, $2p^x$ and $2p^y$ orbitals in the outer shell of neighbouring carbon atoms into three robust σ bonds per atom, giving graphene its flexibility and large tensile strength [3]. The remaining orbital in the outer shell of each atom, the out-of-plane $2p^z$ orbital, forms two diffuse π bonds that dominate the electronic transport and give the large electrical and thermal conductivities [4].

The space symmetry group of the lattice is P6/mmm [5], featuring a translational symmetry with respect to the lattice vectors, which are an integer linear combination of the primitive lattice vectors shown in Fig. 2.1 a),

$$\boldsymbol{a}_1 = a\left(\frac{1}{2}, \frac{\sqrt{3}}{2}\right), \quad \boldsymbol{a}_2 = a\left(-\frac{1}{2}, \frac{\sqrt{3}}{2}\right), \tag{2.1}$$

where the lattice constant is $a = 0.246\,\text{nm}$. Each hexagonal (primitive) unit cell contains one atom from each sublattice, with the B atoms offset by $\boldsymbol{\tau}_B = r_{AB}(0,1)$ ($r_{AB} = a/\sqrt{3}$). Each atom in sublattice A has three nearest neighbours in sublattice B, translated by

$$\boldsymbol{\sigma}_0 = r_{AB}(0,1), \quad \boldsymbol{\sigma}_1 = r_{AB}\left(-\frac{\sqrt{3}}{2}, -\frac{1}{2}\right), \quad \boldsymbol{\sigma}_2 = r_{AB}\left(\frac{\sqrt{3}}{2}, -\frac{1}{2}\right), \tag{2.2}$$

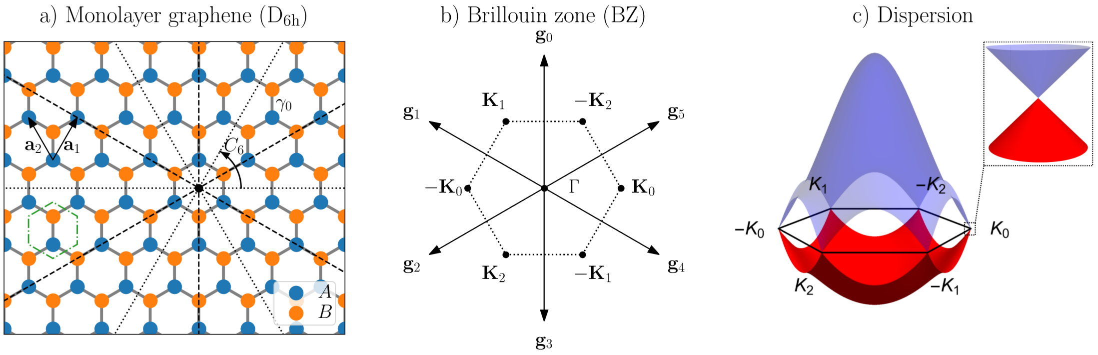

Figure 2.1: a) The honeycomb lattice structure of graphene, composed of two inequivalent triangular sublattices, A and B, related by spatial inversion. Each hexagonal unit cell contains one atom from each sublattice, and the dotted and dashed lines show three of the high-symmetry zigzag and armchair axes, respectively. b) The hexagonal Brillouin zone (BZ) of the reciprocal lattice, whose centre is the Γ point and whose corners are the $\boldsymbol{K}^{\pm}$ points at the centre of the corresponding valleys. c) The dispersion of the conduction and valence bands of graphene in the BZ. The inset shows the Dirac cones at low energy, with the two bands touching at the Dirac point at each $\boldsymbol{K}^{\pm}$ point at zero energy.

respectively. In the reciprocal space, the primitive lattice (Bragg) vectors, $\boldsymbol{g}_1$ and $\boldsymbol{g}_2$, are orthogonal to their real space counterparts, $\boldsymbol{g}_1 \cdot \boldsymbol{a}_1 \equiv 0$ and $\boldsymbol{g}_2 \cdot \boldsymbol{a}_2 \equiv 0$, and are part of the first star of Bragg vectors,

$$\boldsymbol{g}_m = \frac{4\pi}{\sqrt{3}a}\left(-\sin\frac{m\pi}{3}, \cos\frac{m\pi}{3}\right). \quad (m = 0, 1, \cdots, 5) \tag{2.3}$$

These define the hexagonal primitive cell in b), called the Brillouin zone (BZ), whose centre is the Γ point and whose corners are the $\boldsymbol{K}^{\pm}$ points (valleys), appearing at

$$\pm\boldsymbol{K}_j = \pm K\left(\cos\frac{j2\pi}{3}, \sin\frac{j2\pi}{3}\right), \quad (j = 0, 1, 2) \tag{2.4}$$

respectively, where $K = 4\pi/(3a)$.

The lattice features a six-fold rotational symmetry about the centre of each hexagon, represented by a point symmetry group, $\mathrm{D}_{6\mathrm{h}}$ [6], whose elements are:

- E: Identity.

- $2C_6, 2C_3, C_2$: ±60°, ±120° and 180° counter-clockwise rotations about the z-axis, respectively.
- $3C_2', 3C_2''$: 180° counter-clockwise rotations about each of the three (dotted) zigzag and three (dashed) armchair axes, respectively
- i: (Spatial) inversion.
- $2S_3, 2S_6$: ±120° and ±60° counter-clockwise improper rotations about the z-axis, respectively.
- σ_h: Reflection in the horizontal plane.
- $3\sigma_d, 3\sigma_v$: Reflections in the three vertical planes bisecting and three intersecting the C_2' axes, respectively.

This reduces to one of its subgroups, $C_{6v} = \{E, 2C_6, 2C_3, C_2, 3\sigma_d, 3\sigma_v\}$, in a strictly two-dimensional sense.

2.2 The tight-binding model

We derive the electronic properties of monolayer graphene in the tight-binding approximation for the π bands [7, 1], with the dispersion of the conduction and valence bands in the BZ shown in Fig. 2.1 c)[1]. In this approximation, the π electron wave function at a position, $(\boldsymbol{r}, z)$, is a superposition of the $2p^z$ electronic wavefunction, $\Phi_\lambda(\boldsymbol{r} - \boldsymbol{R} - \boldsymbol{\tau}_\lambda, z)$, of each atom, at $(\boldsymbol{R} + \boldsymbol{\tau}_\lambda, 0)$ in sublattice $\lambda = A, B$. This gives a Hamiltonian in the basis of atoms (sites), $\hat{\mathcal{H}}_G$, whose dimensionality is proportional to the number of unit cells, N. Its diagonal elements are the on-site potentials, ε_λ ($\varepsilon_A = \varepsilon_B$ by inversion symmetry), of each sublattice, λ, which we set to zero energy for simplicity, and its off-diagonal elements quantify the amplitude of electrons hopping between atoms.

We consider a basis of Bloch states,

$$\Psi_\lambda(\boldsymbol{k}; \boldsymbol{r}, z) = \frac{1}{\sqrt{N}} \sum_{\boldsymbol{R}} e^{i\boldsymbol{k}\cdot(\boldsymbol{R}+\boldsymbol{\tau}_\lambda)} \Phi_\lambda(\boldsymbol{r} - \boldsymbol{R} - \boldsymbol{\tau}_\lambda, z), \tag{2.5}$$

---

[1] There will be higher energy bands, including the σ bands, although these are largely irrelevant to electronic transport.

in each sublattice, λ, corresponding to a plane wave state which satisfies the translational symmetry. Bloch states of each wavevector, $\boldsymbol{k}$, are decoupled from those with different wavevector, and are described by a 2×2 Hamiltonian, $[H_\mathrm{G}(\boldsymbol{k})]_{\lambda\lambda'} = \langle \Psi_\lambda(\boldsymbol{k}) | \hat{\mathcal{H}}_\mathrm{G} | \Psi_{\lambda'}(\boldsymbol{k}) \rangle$. The electron dispersion results from electrons hopping between atoms and the non-orthogonality of the atomic wavefunctions, described by the overlap matrix, $[S_\mathrm{G}(\boldsymbol{k})]_{\lambda\lambda'} = \langle \Psi_\lambda(\boldsymbol{k}) | \Psi_{\lambda'}(\boldsymbol{k}) \rangle$ ($[S_\mathrm{G}]_{\lambda\lambda} \approx 1$). We neglect coupling between spins, and treat each spin projection, up and down, separately. The crystal momentum, $\boldsymbol{p} = \hbar \boldsymbol{k}$, is only conserved up to a Bragg vector.

The dispersion of the conduction ($s = +$) and valence ($-$) bands,

$$\varepsilon_\pm(\boldsymbol{k}) = \frac{\pm\gamma_0 |g(\boldsymbol{k})|}{1 \mp s_0 |g(\boldsymbol{k})|}, \quad g(\boldsymbol{k}) = \sum_{j=0}^{2} e^{i\boldsymbol{k}\cdot\boldsymbol{\sigma}_j}, \tag{2.6}$$

is shown in Fig. 2.1 c), with the identical low-energy linear dispersion in each valley highlighted in the inset, corresponding to a pseudo-relativistic Dirac cone[2]. These bands are obtained with a minimal model, where we consider only nearest neighbours with respective hopping amplitude and overlap,

$$\begin{aligned} -\gamma_0 &= \langle \Phi_B(\boldsymbol{r} - \boldsymbol{R} - \boldsymbol{\sigma}_j, z) | \hat{\mathcal{H}}_\mathrm{G} | \Phi_A(\boldsymbol{r} - \boldsymbol{R}_n, z) \rangle \approx -3\,\mathrm{eV}, \\ s_0 &= \langle \Phi_B(\boldsymbol{r} - \boldsymbol{R} - \boldsymbol{\sigma}_j, z) | \Phi_A(\boldsymbol{r} - \boldsymbol{R}_n, z) \rangle \approx 0.13, \end{aligned} \quad (j = 0, 1, 2) \tag{2.7}$$

valid for $|\varepsilon| < \gamma_0$ [1]. They have corresponding anti-bonding and bonding wavefunctions,

$$|\psi_\pm(\boldsymbol{k})\rangle = \frac{1}{\sqrt{2}} e^{i\boldsymbol{k}\cdot\boldsymbol{r}} \begin{pmatrix} 1 \\ \mp g(\boldsymbol{k})^* / |g(\boldsymbol{k})| \end{pmatrix}, \tag{2.8}$$

respectively, and are the solutions to the generalised time-independent Schrödinger equation (TISE),

$$H_\mathrm{G}(\boldsymbol{k}) \, |\psi(\boldsymbol{k})\rangle = \varepsilon(\boldsymbol{k}) S_\mathrm{G}(\boldsymbol{k}) \, |\psi(\boldsymbol{k})\rangle, \tag{2.9}$$

where

$$H_\mathrm{G}(\boldsymbol{k}) = -\gamma_0 \begin{pmatrix} 0 & g(\boldsymbol{k}) \\ g(\boldsymbol{k})^* & 0 \end{pmatrix}, \quad S_\mathrm{G}(\boldsymbol{k}) = I + s_0 \begin{pmatrix} 0 & g(\boldsymbol{k}) \\ g(\boldsymbol{k})^* & 0 \end{pmatrix}, \tag{2.10}$$

---

[2] See Section 2.4.

in terms of the identity matrix, I. In fact, the effects of the non-orthogonality are minimal in this energy range and are accounted for by an additional term in the graphene Hamiltonian, $s_0\gamma_0|g(\boldsymbol{k})|^2 I$ to first order in s_0[3], which then satisfies the (simplified) TISE, $H_{\mathrm{G}}(\boldsymbol{k})\,|\psi(\boldsymbol{k})\rangle = \varepsilon(\boldsymbol{k})\,|\psi(\boldsymbol{k})\rangle$[4].

2.3 Discrete symmetries of monolayer graphene

The symmetry of the dispersion of monolayer graphene about the Γ point reflects the rotational symmetry of its lattice, $\mathrm{C_{6v}}$ in 2D, and is further constrained by the discrete symmetries of the Hamiltonian, $H_{\mathrm{G}}(\boldsymbol{k})$ in Eq. (2.10) [8, 9, 10, 11]. The first is inversion (i) symmetry,

$$H_{\mathrm{G}}(\boldsymbol{k}) = \sigma_x H_{\mathrm{G}}(-\boldsymbol{k})\sigma_x, \tag{2.11}$$

where σ_i ($i = x, y, z$) is a Pauli matrix, which is broken with a sublattice potential asymmetry (bias), $\Delta_{AB}\sigma_z/2$ ($\Delta_{AB} = \varepsilon_A - \varepsilon_B$), reducing the rotational symmetry of the lattice to three-fold, $\mathrm{D_{3h}} = \{\mathrm{E}, 2\mathrm{C}_3, 3\mathrm{C}_2', \sigma_\mathrm{h}, 2\mathrm{S}_3, 3\sigma_\mathrm{v}\}$[5] ($\mathrm{C_{3v}} = \{\mathrm{E}, 2\mathrm{C}_3, 3\sigma_\mathrm{v}\}$ in 2D). Another is (spinless) time reversal symmetry,

$$H_{\mathrm{G}}(\boldsymbol{k}) = H^*_{\mathrm{G}}(-\boldsymbol{k}), \tag{2.12}$$

in the absence of spin-orbit coupling [12][6] or an external magnetic field. Either symmetry ensures a valley degeneracy in the dispersion, $\varepsilon_\pm(\boldsymbol{K}_j + \boldsymbol{k}) = \varepsilon_\pm(-\boldsymbol{K}_j - \boldsymbol{k})$ ($j = 0, 1, 2$), and their combination ensures that the dispersion is gapless.

The Hamiltonian features a (sublattice) chiral symmetry [13],

$$H_{\mathrm{G}}(\boldsymbol{k}) = -\sigma_z H_{\mathrm{G}}(\boldsymbol{k})\sigma_z, \tag{2.13}$$

which protects the chirality discussed in the next section, and ensures the dispersion is reflected by zero energy, $\varepsilon_+(\boldsymbol{k}) = -\varepsilon_-(\boldsymbol{k})$. Chiral symmetry is broken by on-site

---

[3] An equivalent term, $(3 - |g(\boldsymbol{k})|^2)\gamma_n I$, is found if we consider next-nearest neighbours, whose hopping amplitude is $\gamma_n \ll \gamma_0$.

[4] See Section 7.A

[5] The C_2' axes now correspond to the armchair axes.

[6] Strict time reversal symmetry is not broken by the spin-orbit coupling as reversing time exchanges the spin projections.

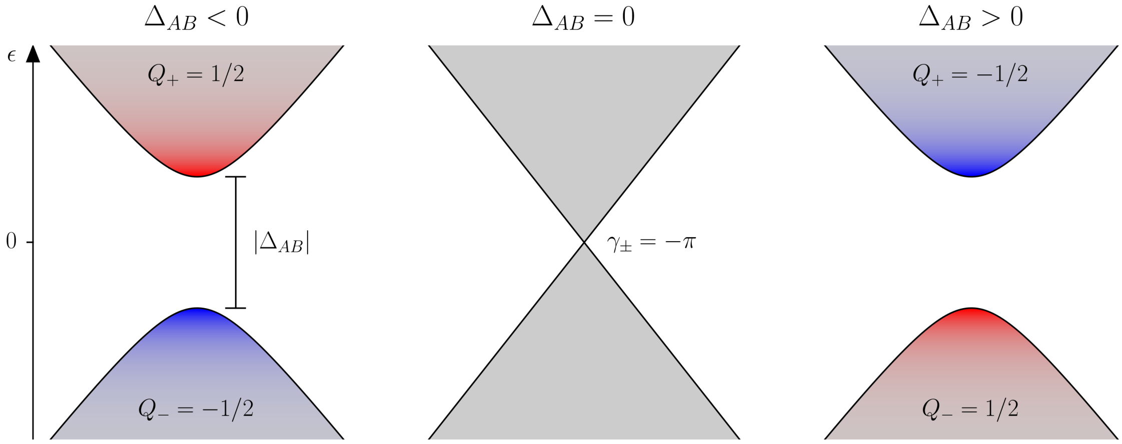

Figure 2.2: The inversion of the Dirac cone in the $\boldsymbol{K}^+$ valley as the sublattice potential asymmetry, Δ_{AB}, changes sign. This asymmetry breaks inversion symmetry and opens a bandgap, $|\Delta_{AB}|$, at the Dirac point, giving a non-zero Berry curvature, $\Omega_\pm \propto \mp\Delta_{AB}$, in each band, $\pm$, with red shading corresponding to positive Berry curvature and blue to negative. The net transfer of a unit of valley Chern number, $Q_\pm$, between each band as Δ_{AB} changes sign is associated with the Berry phase of the gapless Dirac cone, $\gamma_\pm = -\pi$, as inversion symmetry is restored at $\Delta_{AB} = 0$.

potentials which cannot be offset to zero, e.g. the dispersive energy shift from the non-orthogonality of atomic wavefunctions and next-nearest-neighbour couplings, or the sublattice potential asymmetry, Δ_{AB}. Combining the chiral and time reversal symmetries gives the particle-hole symmetry,

$$H_{\mathrm{G}}(\boldsymbol{k}) = -\sigma_z H^*_{\mathrm{G}}(-\boldsymbol{k})\sigma_z, \tag{2.14}$$

ensuring an equivalence of the conduction (particle) and valence (hole) bands, $\varepsilon_+(\boldsymbol{k}) = -\varepsilon_-(-\boldsymbol{k})$.

2.4 Dirac fermions in monolayer graphene

The low-energy ($|\varepsilon| < 1\,\mathrm{eV}$) excitations of monolayer graphene shown in Fig. 2.2 are massless chiral Dirac fermions, whose (Fermi) velocity, $v_0 = \sqrt{3}a\gamma_0/(2\hbar)$, is two orders of magnitude smaller than the speed of light in a vacuum. They are described by the continuum (Dirac) Hamiltonian for an isotropic Dirac cone,[7]

$$\hat{H}_{\mathrm{G}} = v_0 \begin{pmatrix} 0 & \hat{\pi}^\dagger \\ \hat{\pi} & 0 \end{pmatrix}, \quad \hat{\pi} = \hbar(-i\xi\partial_x + \partial_y), \tag{2.15}$$

in each valley, $\boldsymbol{K}^\xi$ ($\xi = \pm$) [14]. This is derived from Eq. (2.10) by expanding the momentum, $\boldsymbol{p} = \hbar(\xi\boldsymbol{K}_j + \boldsymbol{k})$, to first order in the wavevector, $\boldsymbol{k}$, then upgrading to an operator, $\hbar\boldsymbol{k} \to \hat{\boldsymbol{p}} \equiv -i\hbar\nabla$, whose components mutually commute, $[\hat{p}_x, \hat{p}_y] \equiv \hat{p}_x\hat{p}_y - \hat{p}_y\hat{p}_x = 0$[8]. The chirality gives vanishing intraband and perfect interband backscattering,

$$\langle\psi_s(-\boldsymbol{k})|e^{-i2\boldsymbol{k}\cdot\boldsymbol{r}}|\psi_{s'}(\boldsymbol{k})\rangle = 1 - \delta_{ss'}, \quad (s, s' = \pm) \tag{2.16}$$

of the conduction and valence bands,

$$\begin{gathered} \varepsilon_\pm(\boldsymbol{k}) = \pm\hbar v_0 k, \quad |\psi_\pm(\boldsymbol{k})\rangle = \frac{1}{\sqrt{2}} e^{i\boldsymbol{k}\cdot\boldsymbol{r}} \begin{pmatrix} 1 \\ \pm\xi e^{i\xi\theta_{\boldsymbol{k}}} \end{pmatrix}, \\ k = |\boldsymbol{k}|, \quad \theta_{\boldsymbol{k}} = \arctan(k_y/k_x), \end{gathered} \tag{2.17}$$

respectively. This is reflected in the large electrical and thermal conductivities [2, 4] and the Klein paradox, where electrons tunnel through a square barrier with perfect transmittance, in contrast to a non-chiral semiconductor where the transmittance oscillates with the barrier width [16].

The chirality is quantified by the Berry phase, $-\xi\pi$, of the Dirac point in each valley, $\boldsymbol{K}^\xi$ ($\xi = \pm$), which is generic to Dirac cones in a multiband system [17, 18, 19, 20]. This is a non-kinematic phase incurred as an electron undergoes an adiabatic evolution along a trajectory in the reciprocal space, $\mathcal{C}$, winding counterclockwise around this Dirac point once, and only this Dirac point[9]. The Berry phase of each band, n, is given by the gauge invariant expression,

$$\gamma_s = \int_C d\boldsymbol{k} \cdot \mathcal{A}_s(\boldsymbol{k}), \quad \mathcal{A}_s(\boldsymbol{k}) = i\,\langle\psi_s(\boldsymbol{k})|\nabla_{\boldsymbol{k}}|\psi_s(\boldsymbol{k})\rangle\,, \tag{2.18}$$

---

[7] A general expression, featuring anisotropy and tilting, is given in Eq. (4.3).

[8] This can also be derived using $\boldsymbol{k}\cdot\boldsymbol{p}$ theory, where the basis is the sublattice components of a slowly varying envelope function for a Bloch state at each $\boldsymbol{K}^\pm$ point [14], and a recent study which combines $\boldsymbol{k}\cdot\boldsymbol{p}$ theory with the tight-binding model [15].

[9] Otherwise, the details of this trajectory do not matter.

where the Berry connection, $\mathcal{A}_s(\boldsymbol{k})$, is an irrotational vortex centred on the Dirac point in graphene, $\mathcal{A}_s^k = 0$ and $\mathcal{A}_s^{\theta_{\boldsymbol{k}}} = -\xi/(2k)$. Stoke's theorem gives

$$\gamma_s = \int_{\mathcal{S}} d\mathcal{S} \cdot \boldsymbol{\Omega}_s(\boldsymbol{k}), \quad \boldsymbol{\Omega}_s(\boldsymbol{k}) = \nabla_{\boldsymbol{k}} \times \mathcal{A}_s(\boldsymbol{k}), \tag{2.19}$$

and the Berry phase is the flux of the Berry curvature, $\boldsymbol{\Omega}_s(\boldsymbol{k})$, through a surface, $\mathcal{S}$, bounded by $\mathcal{C}$ [21, 18]. The Berry curvature is a momentum space analogue to the magnetic field, giving an anomalous velocity in an external electric field [22, 21, 23] responsible for the anomalous quantum Hall effect [24, 25, 18]. In a 2D material such as graphene, its in-plane components are vanishing due to the lack of out-of-plane dispersion, $\Omega_s^x = \Omega_s^y = 0$, while its out-of-plane component, Ω_s^z, is singular at the Dirac point unless a gap is opened[10].

We show the gapped Dirac cones of monolayer graphene with a sublattice potential asymmetry, Δ_{AB}, in Fig. 2.2. The magnitude of each band's Berry curvature, $\Omega_\pm^z = \mp\xi\hbar^2 v_0^2 \Delta_{AB}/\varepsilon^3$, falls off with increasing bandgap, $|\Delta_{AB}|$, in the dispersion, $\varepsilon_\pm = \pm\varepsilon = \pm\sqrt{(\Delta_{AB}/2)^2 + (\hbar v_0 k)^2}$. The chiral symmetry is broken, and the Berry phase depends upon the surface, $\mathcal{S}$. The flux of the Berry curvature through the BZ gives the Chern number,

$$C_s = \frac{1}{2\pi} \int_{\mathrm{BZ}} d\mathcal{S} \cdot \boldsymbol{\Omega}_s(\boldsymbol{k}), \tag{2.20}$$

an integer-valued topological invariant whose value is protected in the absence of gap closures [26, 27], and associated with the winding number of topologically protected edge states propagating around the finite system [28, 29]. This minimal model is topologically trivial, with vanishing Chern number, $C_\pm = 0$. However, there are non-trivial edge states in each valley for $\Delta_{AB} \neq 0$, as indicated by non-zero values of the valley Chern number,

$$Q_s = \frac{1}{2\pi} \int_{\xi} d\mathcal{S} \cdot \boldsymbol{\Omega}_s(\boldsymbol{k}), \tag{2.21}$$

which is the flux through a large surface surrounding each valley[11], $\xi = \pm$, with half-integer $Q_\pm \approx \mp\xi\Delta_{AB}/(2|\Delta_{AB}|)$ in monolayer graphene [30]. This is weakly topologically protected by the absence of significant inter-valley scattering [31, 32, 33]. The

---

[10] An alternative expression is given in Eq. (4.9), which avoids derivatives of the wavefunctions and is more appropriate for numerical diagonalisation.

[11] We neglect the other valley, considering the continuum Hamiltonian in each valley, $\xi = \pm$, for all $\boldsymbol{k}$.

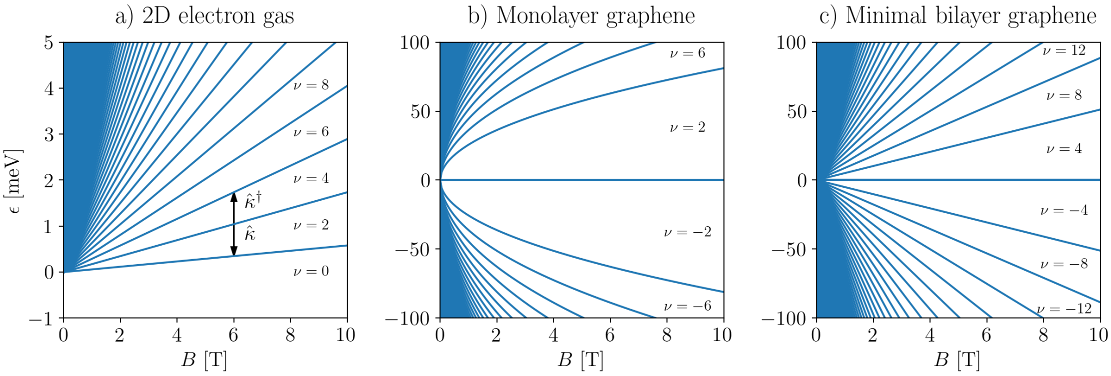

Figure 2.3: The fan diagram of the energies, ε, of the quantised cyclotron orbits (Landau levels) of electrons against magnetic field, B, in a) a two-dimensional electron gas, b) monolayer graphene and c) a minimal model for bilayer graphene. The filling factor, ν, is shown for various gaps, and the corresponding quantum Hall conductivity is $\sigma_{xy} = \nu e^2/h$. The complex momentum operator, $\hat{\kappa}$, and its Hermitian conjugate, $\hat{\kappa}^\dagger$, act as a lowering and raising operator, respectively, in the ladder of states of the 2D electron gas.

Dirac cones invert as Δ_{AB} changes sign, with the π Berry phase of the Dirac cone at $\Delta_{AB} = 0$ transferring a unit of valley Chern number between the bands. Hence, we find a one-dimensional state[12] propagating with opposite directions in each valley along the zero-gap boundary between regions with opposite signs of Δ_{AB} [34, 35][13]. Summing over both valleys gives the total Chern number, which is always an integer and vanishing in systems with time reversal symmetry.

2.5 Landau quantisation of cyclotron orbits

In a 2D electron gas with a transverse magnetic field, $\boldsymbol{B} = (0, 0, -B)$, electrons move in cyclotron orbits, which are quantified into the Landau levels for sufficiently strong fields [36, 37, 38], whose fan diagram is shown in Fig. 2.3 a). There are an infinite number of these levels, $n = 0, 1, \cdots$, forming a ladder of energies, $\varepsilon_n = \hbar\omega_B(n + 1/2) > 0$ ($n \geq 0$), evenly separated by $\hbar\omega_B$, where the cyclotron frequency, $\omega_B = |eB|/m_e$, is inversely proportional to the electron mass, m_e. Each level has an approximate radius, $\sqrt{n}\lambda_B$, proportional to the magnetic length, $\lambda_B = \sqrt{\hbar/|eB|}$ ($e < 0$ is the electron charge),

---

[12] This features a two-fold spin multiplicity.

[13] See Chapter 4.

and contributes a quantum, $1/(2\pi\lambda_B^2)$, to the electron density when filled. The Landau levels appear when the magnetic length is smaller than the electron mean free path, giving the minimum field condition. The integer quantum Hall effect is observed at much higher fields, with the Landau levels distinguishable as plateaus in the transverse electrical conductivity, $\sigma_{xy} = \nu e^2/h$, corresponding to the total number of filled levels (filling factor), ν.

These Landau levels are the solutions to the 2D electron gas Hamiltonian, $\hat{\boldsymbol{p}}^2/(2m_*)$, with the (minimal coupling) Peierls substitution in the momentum operator, $\hat{\boldsymbol{p}} \to \hat{\boldsymbol{p}} - e\boldsymbol{A}$, where the magnetic vector potential, $\boldsymbol{A}$, satisfies $\boldsymbol{B} = \nabla \times \boldsymbol{A}$[14]. This breaks time reversal symmetry, and the components of the momentum operator no longer commute, $[\hat{p}_x, \hat{p}_y] = i\hbar^2/\lambda_B^2$. We choose the Landau gauge, $\boldsymbol{A} = (0, -Bx, 0)$, and the Hamiltonian corresponds to a quantum harmonic oscillator with cyclotron frequency, ω_B, along the x-axis with broken translational symmetry[15]. The corresponding wavefunctions,

$$\phi_{n,k_y}(x,y) = A_n e^{ik_y y} e^{-z^2/2} H_n(z), \quad z = \frac{x}{\lambda_B} - k_y\lambda_B, \quad A_n = \frac{1}{\sqrt{n!2^n\sqrt{\pi}\lambda_B}}, \quad (n = 0, 1, \cdots) \tag{2.22}$$

are decomposed into a plane-wave state along the y-axis, of wavevector k_y, and an oscillator state along the x-axis, where $H_n(z)$ is the Hermite polynomial of the corresponding order, n. On the ladder of states, the complex momentum operator, $\hat{\kappa} = \hbar(-i\partial_x + \partial_y) \to (-i\hbar/\lambda_B)(\partial_z + z)$, is a lowering operator,

$$\hat{\kappa}\phi_{n,k_y} = \begin{cases} 0, & n = 0, \\ -i\sqrt{2n}\frac{\hbar}{\lambda_B}\phi_{n-1,k_y}, & n \geq 1, \end{cases} \tag{2.23}$$

while its Hermitian conjugate, $\hat{\kappa}^\dagger = \hbar(-i\partial_x - \partial_y) \to (-i\hbar/\lambda_B)(\partial_z - z)$, is a raising operator,

$$\hat{\kappa}^\dagger\phi_{n,k_y} = i\sqrt{2(n+1)}\frac{\hbar}{\lambda_B}\phi_{n+1,k_y}, \tag{2.24}$$

with $\hat{\boldsymbol{p}}^2/(2m_*) = (\hat{\kappa}^\dagger\hat{\kappa} + \hat{\kappa}\hat{\kappa}^\dagger)/(4m_*)$ and $[\hat{\kappa}, \hat{\kappa}^\dagger] = 2\hbar^2/\lambda_B^2$.

---

[14] This is the continuum limit of the Peierls substitution for a lattice, which gives an additional field-dependent phase factor, $(ie/\hbar)\int_{\boldsymbol{R}}^{\boldsymbol{R}+\boldsymbol{d}} d\boldsymbol{r} \cdot \boldsymbol{A}(\boldsymbol{r})$, in the hopping amplitude between atoms at $\boldsymbol{R}$ and $\boldsymbol{R}+\boldsymbol{d}$. Such a substitution is appropriate since there is little variation of this phase factor over atomic distances, $\lambda_B \gg a$, at reasonable fields, $B \ll 10000\,\mathrm{T}$.

[15] This is a consequence of our specific gauge choice.

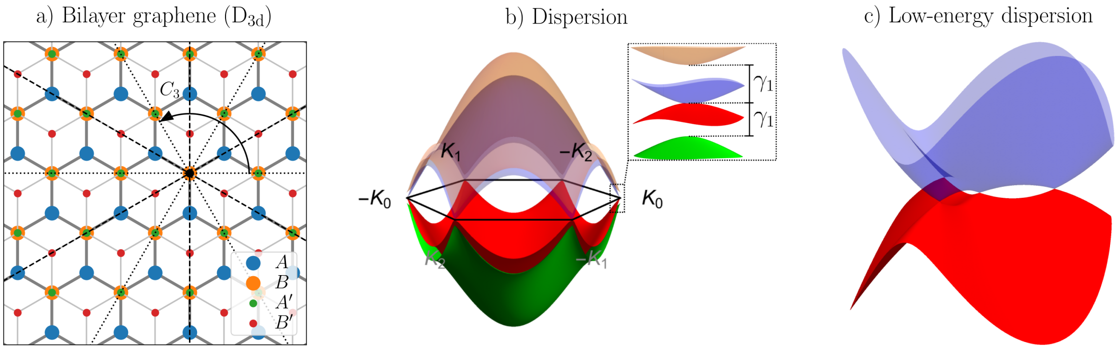

Figure 2.4: a) The lattice structure of Bernal (AB) bilayer graphene, composed of two stacked graphene layers, with the top layer offset in-plane by $\boldsymbol{\tau}_B = (a/\sqrt{3}, 0)$. b) The dispersion of each of the four bands in the hexagonal Brillouin zone, with the inset highlighting the separation, $\tilde{\gamma}_1$, of the two high-energy bands from the two low-energy bands at each $\boldsymbol{K}^\pm$ point. c) The low-energy dispersion in the $\boldsymbol{K}^+$ valley, with the two bands touching at each of the four Dirac points.

We now discuss monolayer graphene, considering a basis of Landau level states, $\phi_{\lambda,n}$[16], in each sublattice, $\lambda = A, B$, which gives the fan diagram shown in Fig. 2.3 b) [39, 40, 41, 42]. The below-diagonal operator, $\hat{\pi}$, acts as a lowering operator in the $\boldsymbol{K}^+$ valley ($\hat{\pi} = \hat{\kappa}$), coupling $\phi_{A,n}$ to $\phi_{B,n-1}$ ($n > 0$), and conversely raising in the $\boldsymbol{K}^-$ valley ($\hat{\pi} = -\hat{\kappa}^\dagger$). The π Berry phase gives a chiral symmetry protected zero-energy level in each valley, $\varepsilon_0 = 0$, corresponding to a sublattice-polarised wavefunction in the $\boldsymbol{K}^+$ valley, $\psi_0 = (\phi_0, 0)^T$, which is inverted in the $\boldsymbol{K}^-$ valley, $(0, \phi_0)^T$. There are also an infinite number of levels, $n = 1, 2, \cdots$, of increasing energy, $\varepsilon_n^\pm = \pm\hbar v_0\sqrt{n}/\ell_B$, on the particle $(+)$ and hole $(-)$ sides, whose wavefunctions are $\psi_n^\pm = \frac{1}{\sqrt{2}}(\phi_n, \mp i\phi_{n-1})^T$ and $\pm\sigma_x\psi_n^\pm$ in the $\boldsymbol{K}^+$ and $\boldsymbol{K}^-$ valleys, respectively. Each level features a four-fold spin/valley degeneracy, and the filling factor is a half-integer multiple of four, increasing directly from $\nu = -2$ to $\nu = 2$ as the zero-energy level is crossed, where $\nu = 0$ corresponds to charge neutrality [43, 19].

2.6 Bilayer graphene

We show the lattice structure of Bernal (AB) bilayer graphene in Fig. 2.4 a), which is composed of two parallel layers of graphene, with the top layer ($'$) offset out-of-plane

---

[16] We suppress the momentum index, k_y.

by $c_0 \approx 0.33\,\mathrm{nm}$ [44] and in-plane by $\boldsymbol{\tau}_0 = \boldsymbol{\tau}_B$ [45]. There are vertical dimers of A' atoms above B atoms, with a reduced three-fold rotational symmetry (including inversion) about their centres, $\mathrm{D_{3d}} = \{\mathrm{E}, 2\mathrm{C}_3, 3\mathrm{C}_2', \mathrm{i}, 2\mathrm{S}_6, 3\sigma_\mathrm{d}\}$. Another configuration is AA stacking, $\boldsymbol{\tau}_0 = 0$, which features the full six-fold rotational symmetry of the monolayer, $\mathrm{D_{6h}}$, and is not considered in this thesis.

We construct a tight-binding Hamiltonian for Bernal bilayer graphene, $\hat{\mathcal{H}}_{\mathrm{GG}}$, in the format of the Slonczewski-Weiss-McClure model (SWM) for bulk graphite [46, 47, 48, 49][17], with parameters determined by infrared spectroscopy [50]. This features intralayer hopping amplitudes analogous to monolayer graphene, $\gamma_0 = 3.16\,\mathrm{eV}$, alongside three distinct interlayer couplings:

- A vertical coupling between dimer sites:

$$\gamma_1 = \langle \Phi_B(\boldsymbol{r}-\boldsymbol{R}, z-c_0)|\hat{\mathcal{H}}_{\mathrm{GG}}|\Phi_{A'}(\boldsymbol{r}-\boldsymbol{R}, z)\rangle = 0.381\,\mathrm{eV}. \qquad (2.25)$$

- A skew coupling between non-dimer sites:

$$-\gamma_3 = \langle \Phi_{B'}(\boldsymbol{r}-\boldsymbol{R}+\boldsymbol{\sigma}_j, z-c_0)|\hat{\mathcal{H}}_{\mathrm{GG}}|\Phi_A(\boldsymbol{r}-\boldsymbol{R}, z)\rangle = -0.38\,\mathrm{eV}^{18}. \quad (j = 0,1,2) \qquad (2.26)$$

- A second skew coupling between sites in the same monolayer sublattice:

$$\gamma_4 = \langle \Phi_{\lambda'}(\boldsymbol{r}-\boldsymbol{R}-\boldsymbol{\sigma}_j, z-c_0)|\hat{\mathcal{H}}_{\mathrm{GG}}|\Phi_\lambda(\boldsymbol{r}-\boldsymbol{R}, z)\rangle = 0.14\,\mathrm{eV}. \quad \begin{pmatrix} \lambda = A, B \\ j = 0,1,2 \end{pmatrix} \qquad (2.27)$$

The different environments of the dimer atoms increases their on-site potential by the dimer asymmetry, $\Delta' = 0.022\,\mathrm{eV}$. We introduce an interlayer potential asymmetry (vertical bias), Δ, via electrostatic gating or by the intrinsic properties of a substrate, which

---

[17] This also includes vertical couplings between next-nearest-neighbouring layers, γ_2 and γ_5, discussed in Chapter 6.

[18] There is an ongoing discussion as to the sign of γ_3 [51, 52, 53, 54, 45, 55, 56], although the choice bears little effect on the low-energy electronic properties, by itself. In this thesis, we follow the positive sign convention of the SWM model, $\gamma_3 > 0$ [46, 47, 48, 49]. However, recent investigations into the trigonal warping at low energies, including a theoretical study from density functional theory [55] and an experimental study using angle-resolved photoemission spectroscopy (ARPES) [56], suggest a negative sign, $\gamma_3 < 0$.

breaks inversion symmetry and reduces the point symmetry group to $\mathrm{C_{3v}}$[19].

We derive the dispersion of the four bands shown in Fig. 2.4 b) by considering Bloch states, of wavevector $\boldsymbol{k}$, in the sublattice basis, (A, B, A', B'), whose Hamiltonian is

$$H_{\mathrm{GG}}(\boldsymbol{k}) = \begin{pmatrix} -\Delta/2 & -\gamma_0 g(\boldsymbol{k}) & \gamma_4 g(\boldsymbol{k}) & -\gamma_3 g(\boldsymbol{k})^* \\ -\gamma_0 g(\boldsymbol{k})^* & -\Delta/2+\Delta' & \gamma_1 & \gamma_4 g(\boldsymbol{k}) \\ \gamma_4 g(\boldsymbol{k})^* & \gamma_1 & \Delta/2+\Delta' & -\gamma_0 g(\boldsymbol{k}) \\ -\gamma_3 g(\boldsymbol{k}) & \gamma_4 g(\boldsymbol{k})^* & -\gamma_0 g(\boldsymbol{k})^* & \Delta/2 \end{pmatrix}. \tag{2.28}$$

These bands are the solutions to the TISE from Eq. (2.9), and we neglect the non-orthogonality ($S_{\mathrm{GG}} \approx I$) since its effects are small at low energies, $|\varepsilon| < \gamma_1$ [45]. There are a low-energy conduction and valence band, $\varepsilon^1_\pm$, respectively, which are predominantly located on the non-dimer atoms, A and B'. There are also two high-energy bands, $\varepsilon^2_\pm$, predominantly located on the dimer atoms, A' and B, and separated from the low-energy bands at each $\boldsymbol{K}^\pm$ point by an energy gap, $\sim \gamma_1$. Expanding about each point gives the continuum Hamiltonian,[8]

$$\hat{H}_{\mathrm{GG}} = \begin{pmatrix} -\Delta/2 & v_0\hat{\pi}^\dagger & -v_4\hat{\pi}^\dagger & v_3\hat{\pi} \\ v_0\hat{\pi} & -\Delta/2+\Delta' & \gamma_1 & -v_4\hat{\pi}^\dagger \\ -v_4\hat{\pi} & \gamma_1 & \Delta/2+\Delta' & v_0\hat{\pi}^\dagger \\ v_3\hat{\pi}^\dagger & -v_4\hat{\pi} & v_0\hat{\pi} & \Delta/2 \end{pmatrix}, \tag{2.29}$$

where $v_j = \sqrt{3}a\gamma_j/(2\hbar)$ $(j = 0,1,3)$. There is no general analytical solution to either Hamiltonian, requiring numerical diagonalisation which is of particularly high computational complexity for the Landau levels[20].

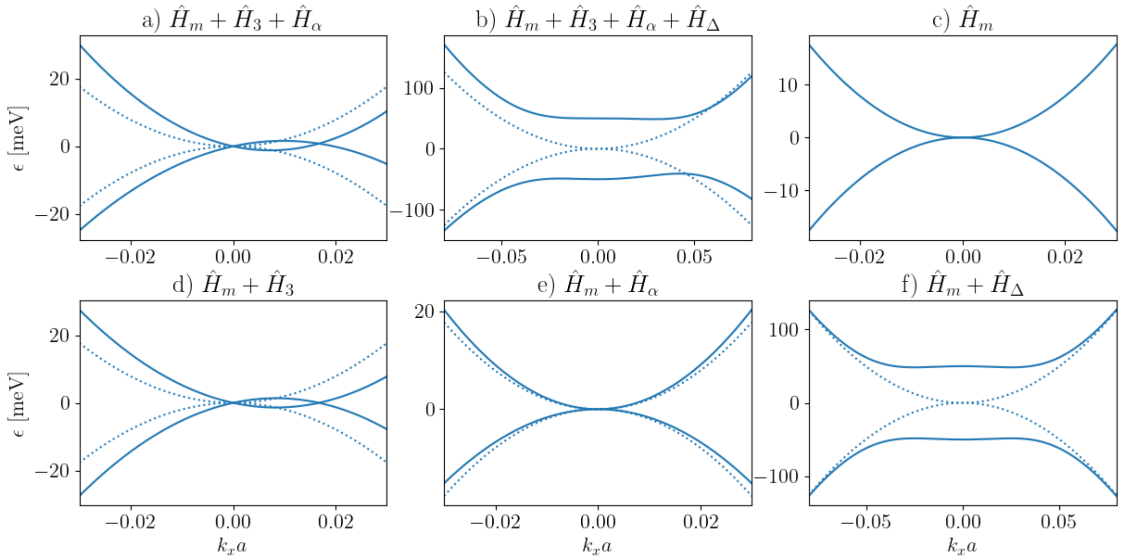

Figure 2.5: The low-energy dispersion of bilayer graphene along a wavevector slice, $(k_x, 0)$, in the $\boldsymbol{K}^+$ valley for various combinations of the terms in its two-band effective Hamiltonian in Eq. (2.30). We consider a large interlayer potential asymmetry, $\Delta = 100\,\text{meV}$, in b) and f). The dotted line in each case is the dispersion of the minimal effective model, $\hat{H}_m$ only.

2.7 Effective model for bilayer graphene

Fortunately, we can describe the low-energy states of bilayer graphene near each $\boldsymbol{K}^{\pm}$ point, whose dispersion is shown in Fig. 2.4 c), by a 2×2 effective continuum Hamiltonian, [45]

$$\begin{gathered}
\hat{H}^{(2)}_{\mathrm{GG}} = \hat{H}_m + \hat{H}_3 + \hat{H}_\alpha + \hat{H}_\Delta, \\
\hat{H}_m = \frac{-1}{2m_*}\begin{pmatrix} 0 & \hat{\pi}^{\dagger 2} \\ \hat{\pi}^2 & 0 \end{pmatrix}, \quad \hat{H}_3 = v_3\begin{pmatrix} 0 & \hat{\pi} \\ \hat{\pi}^\dagger & 0 \end{pmatrix}, \quad \hat{H}_\alpha = \frac{\alpha}{2m_*}\begin{pmatrix} \hat{\pi}^\dagger\hat{\pi} & 0 \\ 0 & \hat{\pi}\hat{\pi}^\dagger \end{pmatrix}, \\
\hat{H}_\Delta = -\frac{\Delta}{2}\left[\begin{pmatrix} 1 & 0 \\ 0 & -1 \end{pmatrix} - \frac{1}{m_*\gamma_1}\begin{pmatrix} \hat{\pi}^\dagger\hat{\pi} & 0 \\ 0 & -\hat{\pi}\hat{\pi}^\dagger \end{pmatrix}\right], \\
m_* = \frac{\gamma_1}{2v_0^2} \approx 0.032 m_e, \quad \alpha = \frac{2v_4}{v_0} + \frac{\Delta'}{\gamma_1} \approx 0.15,
\end{gathered} \tag{2.30}$$

valid for energies away from the high-energy bands, $|\varepsilon| \ll \gamma_1$. This is obtained by Löwdin partitioning,

$$\begin{gathered}
\hat{H}^{(2)}_{\mathrm{GG}} \approx \hat{H}_1 + \hat{T}^\dagger(-\hat{H}_2)^{-1}\hat{T}, \\
\hat{H}_1 = \begin{pmatrix} -\Delta/2 & v_3\hat{\pi} \\ v_3\hat{\pi}^\dagger & \Delta/2 \end{pmatrix}, \quad \hat{H}_2 = \begin{pmatrix} -\Delta/2+\Delta' & \gamma_1 \\ \gamma_1 & \Delta/2+\Delta' \end{pmatrix}, \quad \hat{T} = \begin{pmatrix} -v_4\hat{\pi} & v_0\hat{\pi}^\dagger \\ v_0\hat{\pi} & -v_4\hat{\pi}^\dagger \end{pmatrix},
\end{gathered} \tag{2.31}$$

which projects the high-energy components on the dimer sublattices, A' and B, onto the low-energy non-dimer sublattices, A and B', before expanding to first order in γ_1^{-1} [57, 58, 59, 51, 60, 45].

The first term, $\hat{H}_m$, represents a minimal effective model for massive chiral Dirac fermions in bilayer graphene, whose dispersion, $\varepsilon_\pm(\boldsymbol{k}) = \pm\hbar^2k^2/(2m_*)$, is shown in Fig. 2.5. The effective electron mass, m_*, is much smaller than the free electron mass, m_e, and the bands touch at the $\boldsymbol{K}^\xi$ points. This Hamiltonian satisfies all the discrete

---

[19] A theory background to electrostatic gap opening is given in Section 2.9. An experimental study into gap opening by a magnetic substrate is presented in Chapter 5.

[20] We consider a finite cut-off, N_λ, for the Landau levels in each sublattice, λ, which is chosen to limit erroneous annihilation as the raising operator, $\hat{\kappa}^\dagger$, increases the order above the cut-off. For bilayer graphene, we prevent such errors in the most relevant couplings, γ_0 and γ_1, with cut-offs $(N, N-1, N-1, N-2)$ and $(N-2, N-1, N-1, N)$, for some $N > 2$ (we use $N > 100$), in the sublattice basis, (A, B, A', B'), and each valley, $\boldsymbol{K}^\pm$, respectively.

symmetries from Section 2.3, including the chiral symmetry, and the 2π Berry phase of the corresponding wavefunctions,

$$|\psi_{\pm}(\boldsymbol{k})\rangle = \frac{1}{\sqrt{2}} e^{i\boldsymbol{k}\cdot\boldsymbol{r}} \begin{pmatrix} 1 \\ \mp e^{i\xi 2\theta_{\boldsymbol{k}}} \end{pmatrix}, \tag{2.32}$$

gives a distinct chirality from the monolayer. Correspondingly, bilayer graphene features near-perfect intraband and near-vanishing interband backscattering[21],

$$\langle\psi_s(-\boldsymbol{k})|e^{-i2\boldsymbol{k}\cdot\boldsymbol{r}}|\psi_{s'}(\boldsymbol{k})\rangle \approx \delta_{ss'}, \quad (s,s'=\pm) \tag{2.33}$$

and there is an alternative Klein paradox, where electrons have perfect reflectance from a sufficiently wide square barrier [16].

This chirality is reflected in its Landau level spectrum, shown in Fig. 2.3 c), which features an eight-fold degenerate zero-energy level, $\varepsilon_n = 0$, where each spin/valley features two levels, $n = 0,1$, with a sublattice-polarised wavefunction, $\psi_n = (\phi_n, 0)^T$ and $(0, \phi_n)^T$ in the $\boldsymbol{K}^{\pm}$ valley, respectively. Then, there are an infinite number of four-fold degenerate levels, $n = 2,3,\cdots$, of increasing energy, $\varepsilon_n^{\pm} = \pm\hbar\omega_B^*\sqrt{n(n-1)}$, on the particle and hole sides, with increased cyclotron frequency, $\omega_B^* = |e|B/m_*$. The corresponding wavefunctions are $\psi_n^{\pm} = \frac{1}{\sqrt{2}}(\phi_n, \pm\phi_{n-2})^T$ and $\pm\sigma_x\psi_n^{\pm}$ in the $\boldsymbol{K}^+$ and $\boldsymbol{K}^-$ valleys, respectively. Otherwise, the fan diagram is qualitatively similar to the free electron gas.

We now discuss the effects of each remaining term in Eq. (2.30) on the minimal effective model[22]. The skew interlayer coupling, γ_3, gives the second term, $\hat{H}_3$, inducing trigonal warping of the dispersion, which is most relevant at small densities, $|n| < \pi(2mv_3/\hbar)^2$ [51]. The ultra-low-energy dispersion, below a Lifshitz transition at $|\varepsilon| \approx \gamma_1 v_3^2/(4v_0^2) \approx 1\,\mathrm{meV}$ [61], comprises three Dirac cones of Berry phase π, surrounding a central Dirac cone of Berry phase $-\pi$, and the 2π total Berry phase is conserved [62]. The second skew interlayer coupling, γ_4, and the dimer potential asymmetry, Δ', give the third term, $\hat{H}_\alpha$, which induces a parabolic energy shift, $\alpha k^2/(2m_*)$, in each band[23]. This breaks the particle-hole symmetry in Eq. (2.14), and is relevant at

---

[21] Not strictly perfect due to the trigonal warping term in Eq. (2.30), $\hat{H}_3$.

[22] See Chapter 7 for a discussion of the synergy between terms.

[23] This is an order of magnitude larger than the contribution from the non-orthogonality of atomic

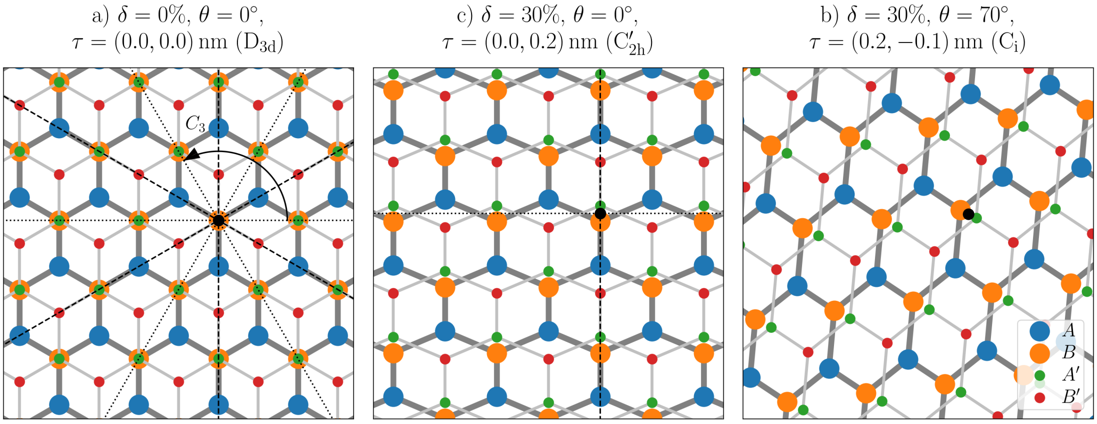

Figure 2.6: The lattice structure of Bernal (*AB*) bilayer graphene under small uniaxial strain, of magnitude δ and along a principal axis at an angle, θ, to the x-axis, and interlayer offsets, $\boldsymbol{\tau}$. a) Neither strain nor offset, with a three-fold rotational symmetry, D_{3d}. Either breaks the rotational symmetry, which preserves one of the zigzag axes if the offset and one of the strain axes are along it, C'_{2h} for $\delta = 30\%$, $\theta = 0^\circ$ and $\boldsymbol{\tau} = (0, 0.2)$ nm in b), and not otherwise, C_i for $\delta = 30\%$, $\theta = 70^\circ$ and $\boldsymbol{\tau} = (0.2, -0.1)$ nm in c).

all densities. The interlayer asymmetry, Δ, gives the final term, $\hat{H}_\Delta$, inducing a Mexican hat-shaped dispersion, whose band edge appears as a circle of non-zero k, with a bandgap whose magnitude is reduced from $|\Delta|$ [63]. This is most relevant in the density range $|n| < 2\pi m_* |\Delta| / \hbar^2$.

2.8 Strain in few-layer graphene

The lattice structure of bilayer graphene is substantially altered by the rotational symmetry breaking effects of the in-plane strain and interlayer offset shown in Fig. 2.6 [64, 65, 66][24]. The strain field, $\boldsymbol{u}(\boldsymbol{r})$, modifies the atomic positions, $\boldsymbol{R} \to \boldsymbol{R} + \boldsymbol{u}(\boldsymbol{R})$, and we consider the continuum approximation, $\boldsymbol{R} \to (I + \mathcal{U}(\boldsymbol{R}))\boldsymbol{R}$, to first order in the strain tensor, $\mathcal{U}_{ij} = (\partial_i u_j + \partial_j u_i)/2$ ($|\mathcal{U}_{ij}| \ll 1$) [67, 68, 69]. We consider uniaxial strain, [70]

$$\mathcal{U} = \begin{pmatrix} \delta \cos^2\theta + \delta' \sin^2\theta & (\delta - \delta')\cos\theta \sin\theta \\ (\delta - \delta')\cos\theta\sin\theta & \delta \sin^2\theta + \delta' \cos^2\theta \end{pmatrix}. \tag{2.34}$$

---

wavefunctions and the next-nearest-neighbour couplings, see Section 7.A.

[24] See Chapter 3

with an expansion, $\delta \ll 1$, along a principal axis, $\boldsymbol{e}_\delta = (\cos\theta, \sin\theta)$, and perpendicular contraction by the Poisson effect, $-\delta' = -\rho\delta$ ($\rho = -0.165$) along $\boldsymbol{e}_z \times \boldsymbol{e}_\delta$ [71]. The latter corresponds to a small constant offset, $\boldsymbol{\tau}$ ($|\boldsymbol{\tau}| \ll r_{AB}$), relative to Bernal stacking, $\boldsymbol{\tau}_0 = \boldsymbol{\tau}_B + \boldsymbol{\tau}$. The point symmetry group is $\mathrm{C}'_{2\mathrm{h}} = \{\mathrm{E}, \mathrm{C}'_2, \mathrm{i}, \sigma'_h\}$[25] if the offset and one of the strain axes are parallel to and hence preserve one of the C'_2 zigzag axes, otherwise it is $\mathrm{C}_\mathrm{i} = \{\mathrm{E}, \mathrm{i}\}$. Breaking inversion symmetry (i) with an interlayer potential asymmetry, Δ, reduces the symmetry to $\mathrm{C}'_\mathrm{s} = \{\mathrm{E}, \sigma'_h\}$ or (trivial) $\mathrm{C}_1 = \{\mathrm{E}\}$, respectively.

The low-energy Physics of monolayer graphene is unchanged by small, homogeneous strain, where it simply induces a shift in the Dirac point [68, 70]. To first order in the strain tensor, the anisotropic amplitude of the intralayer coupling, γ_0, for each vector, $\boldsymbol{\sigma}_n$, is

$$\gamma_0^{(n)} \approx \left(1 + \frac{3\eta_0}{a^2} \boldsymbol{\sigma}_n^T \mathcal{U} \boldsymbol{\sigma}_n\right)\gamma_0, \quad (n = 0, 1, 2), \tag{2.35}$$

respectively, quantified by the Grüneisen parameter, $\eta_0 = \partial \ln\gamma_0 / \partial \ln r_{AB}$ ($-3 \leq \eta_0 \leq -2$) [72, 73]. This corresponds to a substitution in Hamiltonian (2.10),

$$v_0\hat{\pi} \to v_0\hat{\pi} + \mathcal{A}_0, \quad \mathcal{A}_0 = -\frac{3}{4}\eta_0\gamma_0(\mathcal{U}_{yy} - \mathcal{U}_{xx} + i\xi 2\mathcal{U}_{xy}), \tag{2.36}$$

where the gauge field, $\mathcal{A}_0$, corresponds to a pseudo-magnetic field,

$$\mathcal{B} = -\frac{1}{ev_0}(\partial_x \mathrm{Im}\,\mathcal{A}_0 - \xi\partial_y \mathrm{Re}\,\mathcal{A}_0). \tag{2.37}$$

This is only non-zero for inhomogeneous strain, where it can easily reach the tens of Teslas regime [69], and does not break time reversal symmetry as it has opposite signs in each valley, $\boldsymbol{K}^\xi$ ($\xi = \pm$). The shifts in the Dirac points are $\xi\frac{\sqrt{3}}{2}\eta_0(\mathcal{U}_{yy} - \mathcal{U}_{xx}, 2\mathcal{U}_{xy})$, which are removed by a gauge transformation,

$$\hat{H}_G \to e^{-i\xi\phi}\hat{H}_G e^{i\xi\phi}, \quad \phi(x,y) = \frac{\sqrt{3}}{2}\frac{\eta_0}{a}[(\mathcal{U}_{yy} - \mathcal{U}_{xx})x + 2\mathcal{U}_{xy}y]. \tag{2.38}$$

Strain and interlayer offset strongly affect the low-energy Physics of bilayer graphene, where their effects on the skew interlayer couplings, γ_3 and γ_4, cannot be gauged away [64, 65, 66]. There are shifts in the four Dirac points in each valley,

---

[25] The "vertical" axis is oriented along the C'_2 axis.

with Berry phase-conserving collisions reducing the number of Dirac cones to two, which become increasingly broad and deep. Sufficiently large strain/offset effectively decouples each layer at low energy, with each Dirac cone exhibiting a monolayer-style Klein paradox with perfect transmittance through a square barrier [74]. The anisotropic couplings for each vector, $(-1)^j\boldsymbol{\sigma}_n$, are

$$\gamma_j^{(n)} \approx \left[1+\frac{3\eta_j}{a^2}\left(\boldsymbol{\sigma}_n^T\,\mathcal{U}\boldsymbol{\sigma}_n+(-1)^j\boldsymbol{\tau}\cdot\boldsymbol{\sigma}_n\right)\right]\gamma_j, \qquad \begin{pmatrix} j=3,4 \\ n=0,1,2 \end{pmatrix} \tag{2.39}$$

and we use a geometric estimate[26], $\eta_{3/4}\sim-1$, for their unknown Grüneisen parameters [75]. The substitutions in Hamiltonian (2.28) are Eq. (2.36) and [27]

$$\begin{gathered} v_j\hat{\pi}\to v_j\hat{\pi}+\mathcal{A}_j, \\ \mathcal{A}_j=-\tfrac{3}{4}\eta_j\gamma_j\left[\mathcal{U}_{yy}-\mathcal{U}_{xx}+i\xi 2\,\mathcal{U}_{xy}-(-1)^j 2\sqrt{3}(-\tau_y+i\xi\tau_x)/a\right]. \end{gathered} \qquad (j=3,4) \tag{2.40}$$

2.9 Screened bandgap in bilayer graphene

A tunable bandgap, Δ_g, is opened with a vertical displacement field, D [63, 76, 77, 2, 45], with an approximately linear relationship ($\Delta_g\ll\gamma_1$) shown in the first panel of Fig. 2.7 for an electrically neutral bilayer. The displacement field can also be induced by charge transfer to a magnetic substrate [78, 79, 80, 81][28]. The field induces an interlayer potential asymmetry, Δ ($\Delta_g<|\Delta|$), whose theoretical maximum value, $\Delta_0=eDc_0/(\varepsilon_z\varepsilon_0)$, depends on the out-of-plane dielectric susceptibility, $\varepsilon_z\approx2.6$ [77]. This asymmetry induces an out-of-plane dipole, n_t-n_b, in the electron density of the bottom/top electron layer, $n_{b/t}$, as the electron wave functions are biased towards the layer at higher electrostatic potential ($n_t>n_b$ for $D>0$). This dipole in turn induces a (screening) field opposing the external field, and so on, leading to a self-consistent value of the asymmetry, Δ, and gap, Δ_g [63, 77, 45]. Charging the bilayer, $n=n_b+n_t\neq0$,

---

[26] We assume an isotropic form of the carbon-coupling hopping amplitude, $\gamma(d)\approx\gamma_0 e^{\eta_0 d/r_{AB}}$, which depends only on their separation, d. For the skew interlayer couplings, $\gamma_{3/4}$, this gives $\eta_{3/4}=\partial\ln\gamma_{3/4}/\partial\ln r_{AB}\sim\partial\gamma(\sqrt{r_{AB}^2+c_0^2})/\partial r_{AB}\approx\eta_0 r_{AB}/\sqrt{r_{AB}^2+c_0^2}$ with respect to in-plane displacements (changes in r_{AB}).

[27] Removing the interlayer gauge field, $\mathcal{A}_0$, with the gauge transformation from Eq. (2.38), then we have $\mathcal{A}_j\to w_j=\mathcal{A}_j-\gamma_j\mathcal{A}_0/\gamma_0$ ($j=3,4$). Inserting the expression for uniaxial strain in Eq. (2.34) gives the modified gauge fields, w_3 and w_4, in Eq. (3.1.a) and used throughout Chapter 3.

[28] See Chapter 5.

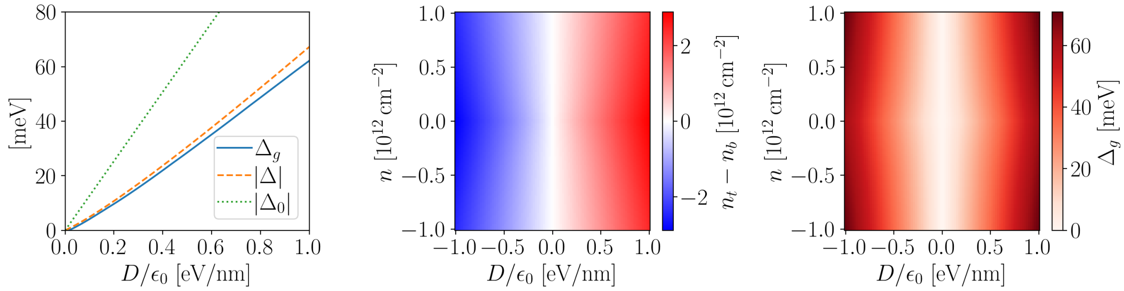

Figure 2.7: Dielectric screening of the bandgap in bilayer graphene. *Left.* The bandgap, Δ_g, and magnitude of the interlayer potential asymmetry, Δ, and its theoretical maximum, Δ_0, against the vertical displacement field, D, they are induced by. *Centre and right.* The difference, $n_t - n_b$, between the electron densities, $n_{b/t}$, in the bottom and top layers, respectively, and the bandgap, Δ_g, against the displacement field, D, and total electron density, $n = n_b + n_t$.

has little effect beyond slightly suppressing the screening, which we attribute to the reduced dependence of the higher energy wavefunctions on the asymmetry. The bandgap decreases with the formation of Landau levels in a transverse magnetic field [82][28].

The interlayer asymmetry, Δ, is calculated self-consistently via an expression, [77]

$$\Delta = \frac{eDc_0}{\varepsilon_z \varepsilon_0} + \frac{e^2(n_t - n_b)c_0}{4\bar{\varepsilon}_z \varepsilon_0}, \tag{2.41}$$

with the Δ-dependence of the right-hand-side contained in the electron densities of each layer. The first term is the theoretical maximum, Δ_0, which is screened by the second term, representing a semiclassical calculation of the electric field induced by the charge density of each layer, $en_{b/t}$[29]. The screening term features an effective susceptibility, $\bar{\varepsilon}_z = (1 + 1/\varepsilon_z)^{-1} \sim 1$, since the charge induced on each layer produces no net polarisation of that layer due to the even and odd parity of the σ- and π-bonds with respect to reflections in the horizontal plane (σ_h).

Including the four-fold spin/valley multiplicity at zero magnetic field, the layer densities are given by

$$n_L = 4 \sum_n \int \frac{d^2\boldsymbol{k}}{(2\pi)^2} f_0(\varepsilon_n(\boldsymbol{k})) \left(|\psi_{n,L}(\boldsymbol{k})|^2 - \frac{1}{4} \right), \quad (L = b, t) \tag{2.42}$$

---

[29] This is frequently referred to as a Hartree approach in the literature [63, 83, 84, 45, 77, 85], although it is not strictly a local approach.

where $\psi_{n,L}$ is the wavefunction of each of the four bands, n, projected onto the corresponding layer, L. The dependence on the temperature, T, is contained in the Fermi-Dirac distribution function, $f_0(\varepsilon) = 1/(e^{(\varepsilon-\varepsilon_F)/(k_B T)} + 1)$, where the Fermi energy, ε_F, is determined by the total density, $n = n_b + n_t$ [86, 87]. We simplify by considering low temperatures, $T \to 0$, in which case the distribution is a step function, $f_0(\varepsilon) \approx \theta(\varepsilon_F - \varepsilon)$, and electron states below and above the Fermi energy are occupied and vacant, respectively[30]. For non-zero magnetic field, we determine the layer densities by the components of each non-dispersive Landau level, each of which contributes a density quantum when filled[28,31].

2.10 van der Waals heterostructures of graphene and hexagonal boron nitride (hBN)

Hexagonal boron nitride (hBN) features layers with a similar honeycomb lattice to graphene, albeit with a longer lattice period, $(1+\delta)a$ ($\delta = 0.018$) [88, 89, 90, 91], and the interference of the incommensurate lattices at a graphene/hBN interface results in a long-range moiré superlattice (mSL) [92, 93, 94, 95]. The inequivalent boron and nitrogen atoms in the hBN layer break inversion symmetry, reducing the rotational symmetry to three-fold, $\mathrm{C}_{3\mathrm{v}}$. Including a counter-clockwise twist, θ, of the hBN layer removes the high symmetry planes, $\mathrm{C}_3 = \{\mathrm{E}, 2\mathrm{C}_3\}$, and reduces the mSL period, $\lambda \approx a/\sqrt{\delta^2+\theta^2}$, where we assume that the mSL is much larger than either lattice, $\lambda \gg a$ ($\delta, \theta \ll 1$). The first star mSL Bragg vectors,

$$\boldsymbol{G}_m \equiv \boldsymbol{g}_m - \boldsymbol{g}'_m \approx \delta \cdot \boldsymbol{g}_m - \theta \boldsymbol{e}_z \times \boldsymbol{g}_m, \quad (m = 0, 1, \cdots, 5) \tag{2.43}$$

are the difference between the corresponding vectors for graphene, $\boldsymbol{g}_m$ from Eq. (2.3), and hBN, $\boldsymbol{g}'_m = (1+\delta)^{-1} \left(\begin{smallmatrix} \cos\theta & -\sin\theta \\ \sin\theta & \cos\theta \end{smallmatrix}\right) \boldsymbol{g}_m$. In the continuum approximation [96, 97], appropriate for $\lambda \gg a$, we relate the electronic properties in the vicinity of a point, $\boldsymbol{r}$, to an equivalent commensurate graphene/hBN bilayer, $\delta = \theta = 0$, with an interlayer offset

---

[30] See Section 7.C.

[31] See Section 2.5.

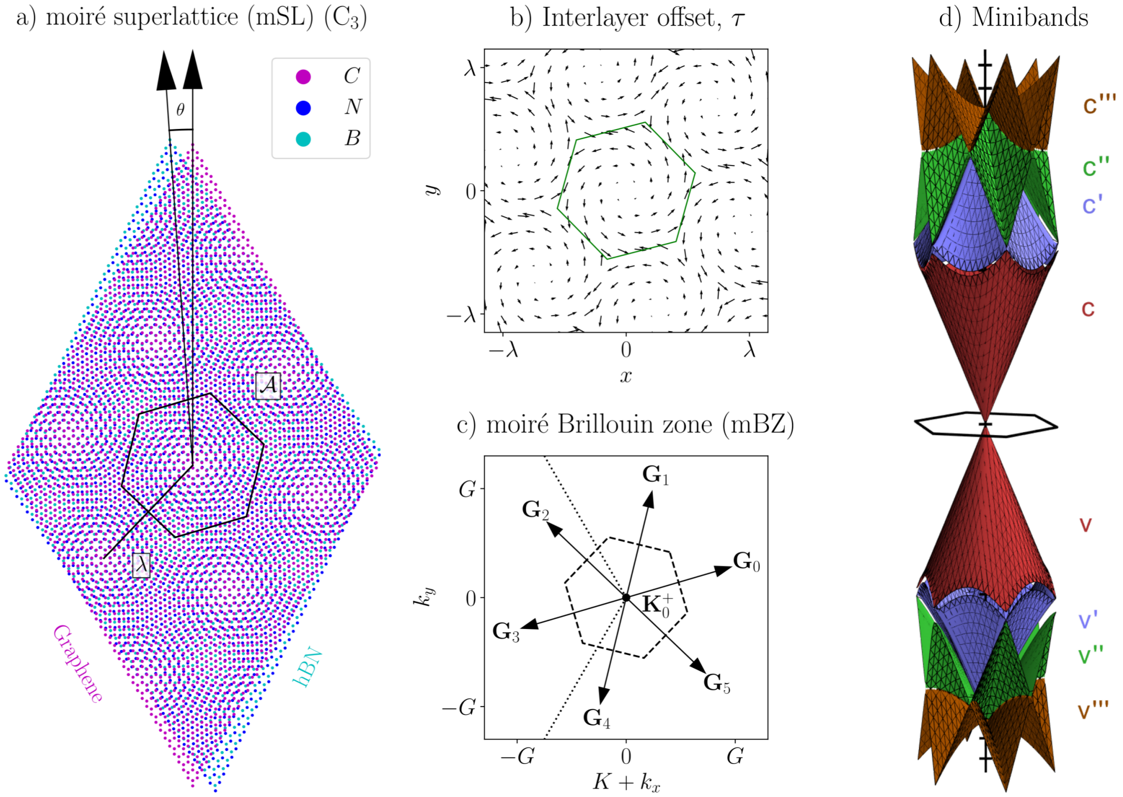

Figure 2.8: a) The moiré superlattice (mSL) at the interface between a graphene and an hBN layer, resulting from the longer lattice period, of mismatch $\delta = 0.018$, and counterclockwise twist, θ, of the latter. The mSL period is $\lambda \approx a/\sqrt{\delta^2+\theta^2}$, and its hexagonal unit cell has area $\mathcal{A} = \sqrt{3}\lambda^2/2$. b) The interlayer offset, $\boldsymbol{\tau}$, between the centre of the unit cells in each layer, given by Eq. (2.44) (we choose the shortest value of $\boldsymbol{\tau}$). c) The moiré Brillouin zone (mBZ) of the mSL centred on the $\boldsymbol{K}^+$ valley, with the first star mSL Bragg vectors, $\boldsymbol{G}_m$ ($m = 0, 1, \cdots, 5$), given by Eq. (2.43). d) The mSL-reconstructed minibands of monolayer graphene in this mBZ in the $\boldsymbol{K}^+$ valley.

shown in b),

$$\boldsymbol{\tau}(\boldsymbol{r}) = \boldsymbol{\tau}_0 + \delta \cdot \boldsymbol{r} + \theta \boldsymbol{e}_z \times \boldsymbol{r}, \tag{2.44}$$

which varies slowly over each graphene unit cell, with $\boldsymbol{\tau}(0) = \boldsymbol{\tau}_0$.

The effective Hamiltonian of this bilayer in each valley, $\boldsymbol{K}^{\xi}$ ($\xi = \pm$), is[32]

$$\begin{gathered}
\hat{H} = \begin{pmatrix} \hat{H}_{\mathrm{G}} & \hat{T}^{\dagger} \\ \hat{T} & \hat{H}_{\mathrm{hBN}} \end{pmatrix}, \\
\hat{H}_{\mathrm{hBN}} \approx \begin{pmatrix} V_N & 0 \\ 0 & V_B \end{pmatrix}, \quad \hat{T} = \frac{1}{3} \sum_{j=0}^{2} e^{i\xi(\boldsymbol{K}_j - \boldsymbol{K}_0)\cdot\boldsymbol{\tau}} \begin{pmatrix} \gamma_N & \gamma_N e^{-i\xi 2\pi j/3} \\ \gamma_B e^{i\xi 2\pi j/3} & \gamma_B \end{pmatrix}.
\end{gathered} \tag{2.45}$$

This is a block Hamiltonian, whose upper diagonal block, $\hat{H}_{\mathrm{G}}$ from Eq. (2.15), corresponds to the graphene layer, while the lower block, $\hat{H}_{\mathrm{hBN}}$, is hBN. The nitrogen and boron atoms appear at sublattices A and B of the hBN layer with on-site potentials[33], $V_N \approx -1.4\,\mathrm{eV}$ and $V_B \approx 3.3\,\mathrm{eV}$, respectively, which gives a large bandgap, $|\Delta_{AB}| \sim 5\,\mathrm{eV}$ [98]. The interlayer block, $\hat{T}$, is derived using $\boldsymbol{k}\cdot\boldsymbol{p}$ theory [99, 97], and includes couplings, γ_N and γ_B, to each of the nitrogen and boron atoms, respectively, analogous to γ_1 in Eq. (2.25). Then, we perform a Schrieffer-Wolff transformation, see Eq. (2.31), giving a perturbation in the graphene Hamiltonian, $\hat{M} = \hat{T}^{\dagger}(-\hat{H}_{\mathrm{hBN}})^{-1}\hat{T}$, which we expand to first order in V_N^{-1} and V_B^{-1}[34].

The hBN layer induces a mSL-periodic local energy shift, $\mathcal{E}$, sublattice potential asymmetry, $\mathcal{M}$, and pseudo-magnetic field, $\mathcal{B}$, in the graphene layer [92], which we show in Fig. 2.9. These are derived from the local mSL perturbation,

$$\begin{aligned}
\hat{M} &\equiv \begin{pmatrix} \mathcal{E} + \mathcal{M}/2 & \mathcal{A}_0^* \\ \mathcal{A}_0 & \mathcal{E} - \mathcal{M}/2 \end{pmatrix} = \sum_{\mathcal{P}=\pm} \sum_{m=0}^{5} \hat{M}_{\boldsymbol{G}_m}^{\mathcal{P}}, \\
\hat{M}_{\boldsymbol{G}_m}^{+} &= \begin{pmatrix} u_0^+ + i(-1)^m u_3^+ & e^{-i\xi m 2\pi/3}(-1)^m u_1^+ \\ e^{i\xi m 2\pi/3}(-1)^m u_1^+ & u_0^+ - i(-1)^m u_3^+ \end{pmatrix} e^{i\boldsymbol{g}_m\cdot\boldsymbol{\tau}_0} e^{i\boldsymbol{G}_m\cdot\boldsymbol{r}}, \\
\hat{M}_{\boldsymbol{G}_m}^{-} &= \begin{pmatrix} i(-1)^m u_0^- + u_3^- & -ie^{-i\xi m 2\pi/3} u_1^- \\ -ie^{i\xi m 2\pi/3} u_1^- & i(-1)^m u_0^- - u_3^- \end{pmatrix} e^{i\boldsymbol{g}_m\cdot\boldsymbol{\tau}_0} e^{i\boldsymbol{G}_m\cdot\boldsymbol{r}},
\end{aligned} \tag{2.46}$$

---

[32] We neglect an intralayer coupling in the hBN layer, analogous to γ_0, alongside skew interlayer couplings, analogous to γ_3 and γ_4, since their effects on the low-energy bands in the graphene layer are minimal.

[33] Relative to graphene.

[34] See Chapter 6.

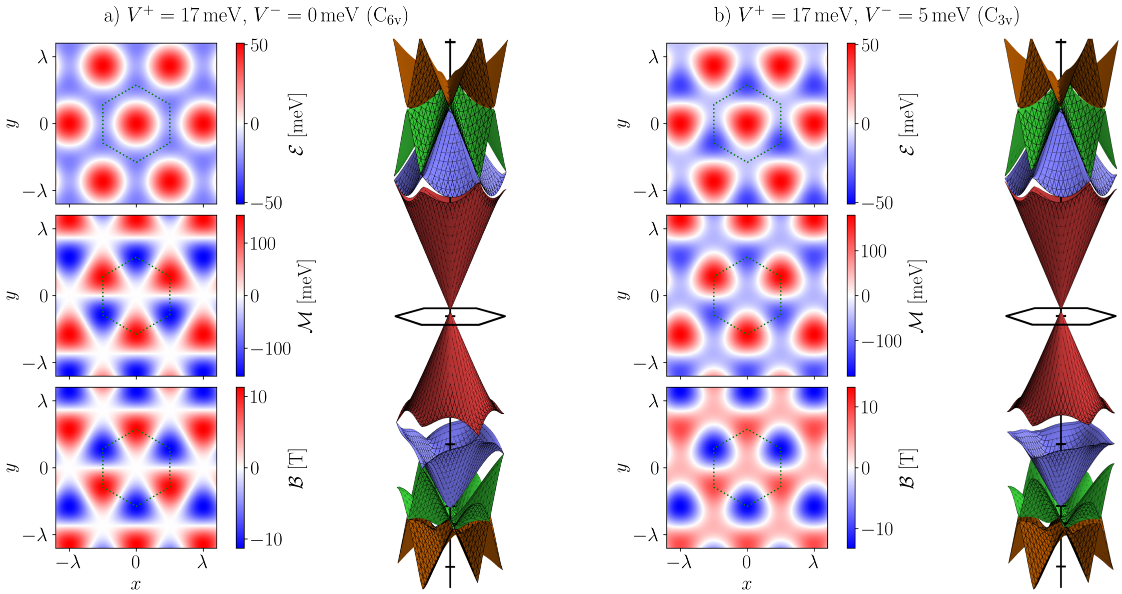

Figure 2.9: The local energy shift, $\mathcal{E}$, sublattice potential asymmetry, $\mathcal{M}$, and pseudomagnetic gauge field, $\mathcal{B}$, induced by the moiré superlattice (mSL) perturbation, alongside the dispersion of the reconstructed minibands in the mSL Brillouin zone in the $\boldsymbol{K}^+$ valley of an aligned graphene/hBN heterostructure. The even parity potential is $V^+ = 17\,\mathrm{meV}$. a) Preserving inversion symmetry with a vanishing odd parity potential, $V^- = 0\,\mathrm{meV}$, gives a $\mathrm{C_{6v}}$ symmetric perturbation and a gapless dispersion. b) Breaking inversion symmetry with $V^- = 5\,\mathrm{meV}$ gives a perturbation of reduced $\mathrm{C_{3v}}$ symmetry and a dispersion featuring minigaps.

obtained by inserting the offset, $\boldsymbol{\tau}(\boldsymbol{r})$ in Eq. (2.44), into the commensurate perturbation from the previous paragraph[8], with the pseudo-magnetic field given by Eq. (2.37). This perturbation features twelve harmonics, $\hat{M}^{\mathcal{P}}_{\boldsymbol{G}_m}$, for each of the first star Bragg vectors, $\boldsymbol{G}_m$ ($m = 0, 1, \cdots, 5$), and of even ($\mathcal{P} = +$) and odd ($\mathcal{P} = -$) parity under inversion, the latter of which break inversion symmetry. The six parameters,

$$\begin{gathered}(u_0^{\pm}, u_1^{\pm}, u_3^{\pm}) = \left(\pm\frac{1}{2}, -1, -\frac{\sqrt{3}}{2}\right)V^{\pm}, \\ V^{+} = \frac{1}{18}\left(\frac{\gamma_N^2}{V_N} + \frac{\gamma_B^2}{V_B}\right), \quad V^{-} = \frac{\sqrt{3}}{18}\left(\frac{\gamma_N^2}{V_N} - \frac{\gamma_B^2}{V_B}\right),\end{gathered} \tag{2.47}$$

are related to two potentials, $V^{\mathcal{P}}$, of corresponding parity, $\mathcal{P} = \pm$, and magnetic focusing measurements reveal weak inversion symmetry breaking, $V^{+} = 17\,\text{meV}$ and $|V^{-}| < 5\,\text{meV}$ [100][35]. The plots in Fig. 2.9 correspond to an aligned heterostructure ($\theta = 0$), featuring the expected $\mathrm{C_{6v}}$ symmetry for preserved in-plane inversion symmetry in a) ($V^{-} = 0\,\text{meV}$), and $\mathrm{C_{3v}}$ when it is broken in b) ($V^{-} = 5\,\text{meV}$).

This perturbation reconstructs the Dirac cones of monolayer graphene into a collection of minibands, shown in Fig. 2.8 d) and 2.9, in the two smaller mSL Brillouin zones (mBZ) whose centres are the the $\boldsymbol{K}^{\pm}$ points [102, 92, 94], with the $\boldsymbol{K}^{+}$ mBZ shown in Fig. 2.8 c). The first conduction and valence minibands, c ($s = +$) and v ($s = -$), respectively, are largely unchanged from their isolated counterparts, except for significant reconstruction near the mBZ sides, and there are also minibands of increasing energy above ($c', c'', \cdots$) and below ($v', v'', \cdots$) these minibands. Each harmonic, $\hat{M}_{\boldsymbol{G}_m}$, couples graphene states whose wavevectors, $\boldsymbol{k}$ and $\boldsymbol{k}'$, are separated by the corresponding mSL Bragg vector, $\boldsymbol{G}_m$:

$$\langle \psi_s(\boldsymbol{k})|\hat{M}|\psi_{s'}(\boldsymbol{k}')\rangle = \sum_{m=0}^{5} \langle \psi_s(\boldsymbol{k})|\hat{M}_{\boldsymbol{G}_m}|\psi_{s'}(\boldsymbol{k}-\boldsymbol{G}_m)\rangle\, \delta_{\boldsymbol{k},\boldsymbol{k}'+\boldsymbol{G}_m}, \tag{2.48}$$

Hence, we consider a basis of graphene states[36], $|\psi_s(\boldsymbol{k}+\boldsymbol{G})\rangle$ from Eq. (2.17), for each

---

[35] This includes other contributions, such as the electrostatic interaction between the π electrons in each layer [92, 101].

[36] Alternatively, if analytical expressions for the isolated wavefunctions, $|\psi_s(\boldsymbol{k})\rangle$, are unknown or otherwise unsuitable, we consider a basis of plane wave states in each sublattice, λ.

band, s, and mSL Bragg vector, $\boldsymbol{G}$[37], whose wavevectors, $\boldsymbol{k}+\boldsymbol{G}$, are folded into a single wavevector in the mBZ, $\boldsymbol{k}$, with translation by $-\boldsymbol{G}$ [92, 94]. The diagonal elements of the reconstructed Hamiltonian are approximately the eigenvalues of graphene, $[H(\boldsymbol{k})]_{s\boldsymbol{G},s\boldsymbol{G}} \approx \varepsilon_s(\boldsymbol{k}+\boldsymbol{G})$, while each off-diagonal element, $[H(\boldsymbol{k})]_{s\boldsymbol{G},s'\boldsymbol{G}'}$, gives the amplitude of a momentum-violating "kick", $\hbar(\boldsymbol{G}-\boldsymbol{G}')$, from the mSL perturbation[38]. Breaking inversion symmetry ($V^- \neq 0$) opens minigaps between the minibands, as seen in Fig. 2.9 b) for $V^- = 5\,\mathrm{meV}$, and each miniband has a well-defined valley Chern number[39].

2.11 Umklapp electron-electron scattering in graphene/hBN superlattices heterostructures

Umklapp electron-electron (Uee) scattering substantially limits the electrical conductivity of monolayer graphene/hBN van der Waals heterostructures and hence their utility in nanoscale electronics [103, 104], especially those formed by epitaxial growth with a typically close alignment [105, 106, 107]. During normal electron-electron scattering via the Coulomb interaction, shown in Fig. 2.10 a, the total (crystal) momentum is preserved and there is a negligible contribution to the resistivity, ρ_{xx}. However, the scattering of electrons with thermally-excited holes for densities close to the miniband edges provides a substantial resistivity contribution in Fig. 2.10 b. By comparison, during Uee scattering from a periodic lattice, the total momentum is only conserved up to one of its Bragg vectors, $\boldsymbol{g}$:

$$\boldsymbol{k}_3+\boldsymbol{k}_4=\boldsymbol{k}_1+\boldsymbol{k}_2+\boldsymbol{g}, \tag{2.49}$$

where $\boldsymbol{k}_{1,2}$ and $\boldsymbol{k}_{3,4}$ are the wavevectors of the incoming and outgoing electrons, respectively. Unlike a typical metal whose long Bragg vectors, $|\boldsymbol{g}| \sim 10\,\mathrm{nm}^{-1}$, only allow experimental Uee observation for ultraclean samples at low temperatures [108, 109, 110, 111, 112], the arbitrarily large mSL Bragg vectors allow Uee scattering to dominate the resistivity, ρ_{xx} of a graphene/hBN heterostructure across a large parameter space and at

---

[37] We consider mSL Bragg vectors which are the sum of at most two of the first star vectors, $\boldsymbol{G}_m$, guaranteeing milli-electronvolt convergence of the first valence and conduction minibands. Otherwise, we sum up to three first star mSL Bragg vectors.

[38] See Chapter 7.

[39] See Chapter 4.

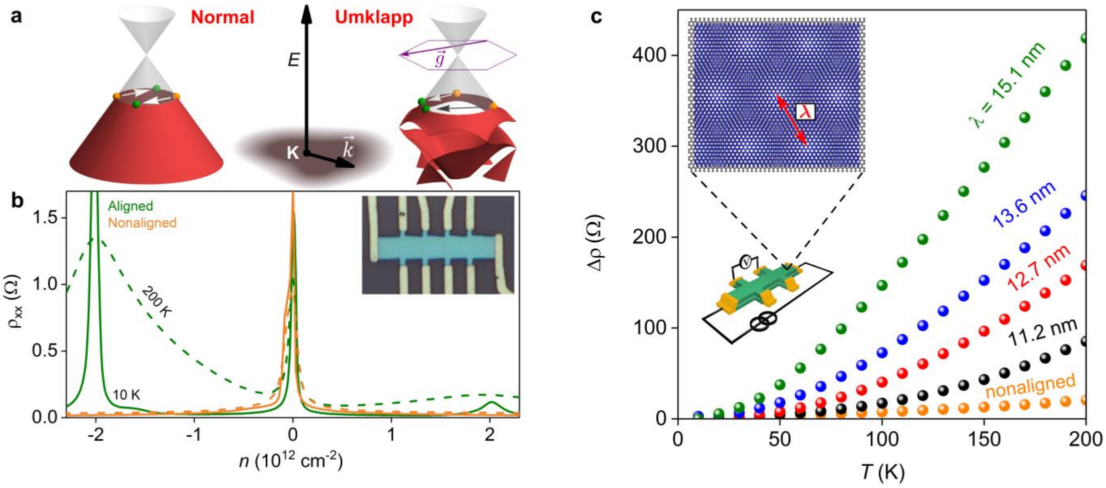

Figure 2.10: **Umklapp scattering and excess resistivity in graphene superlattices.** a, Normal e-e scattering for, e.g., holes in graphene does not lead to resistivity (left), in contrast to the umklapp scattering for holes in a graphene superlattice (right). Here we also illustrate the mSL Brillouin zone (purple hexagon) and mSL minibands in the valence band of graphene. b, Longitudinal resistivity, ρ_{xx}, for nonaligned (orange) and aligned (green) graphene/hBN devices. Solid curves: low temperature, $T = 10$ K. Dashed: 200 K. Inset: Optical image of the mSL device (from [103]) in b. c, T-dependent resistivity, $\Delta\rho(T) = \rho_{xx}(T) - \rho_{xx}(10\,\mathrm{K})$, at a fixed $n = -1 \times 10^{12}\,\mathrm{cm}^{-2}$ for four mSL devices and the nonaligned device (orange symbols). Error bars are smaller than the data points. Inset: Device schematic and measurement scheme. The top illustration is a moiré pattern arising from 1.8 % lattice mismatch in aligned graphene (blue) and hBN (grey) crystals. **Figure and caption adapted from [103].**

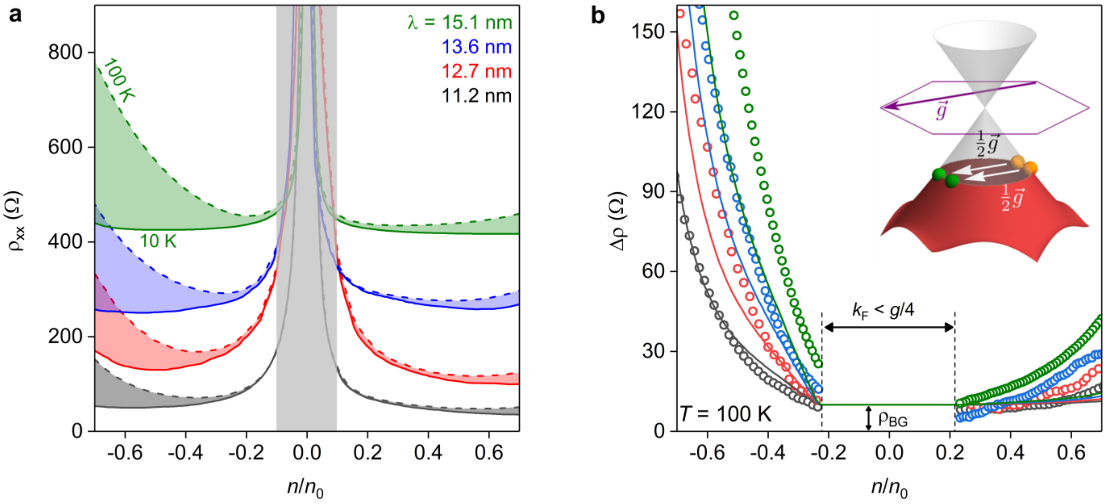

Figure 2.11: **Electron-electron scattering and its electron-hole asymmetry in graphene superlattices.** a, Resistivity for different mSL periods, λ (color coded), as a function of n. Their n_0 were between 2 and $3.7\times10^{12}\,\mathrm{cm}^{-2}$. Solid curves: 10 K. Dashed: 100 K. The curves for $\lambda = 13.6$ and 15.1 nm are offset for clarity by 200 and $400\,\Omega$, respectively. The color shaded areas emphasize the T-dependent parts of ρ_{xx} for different λ. b, Open circles show experimental $\Delta\rho(T)$ (same color coding as in a). The error bars are smaller than the symbols. Solid curves: calculated Uee contribution (no fitting parameters). Note that a small density-independent offset, $\rho_{\mathrm{BG}} = 10\,\Omega$, has been added to the theoretical curves. The inset depicts an umklapp process for the threshold density, n_*, such that $|\boldsymbol{k}_{1,2,3,4}| = g/4$, where the momentum transferred to the mSL corresponds to the exact backscattering of a pair of electrons (orange and green balls). **Figure and caption adapted from [103].**

large temperatures in Fig. 2.10 c.

Theoretical predictions of the excess resistivity due to Uee scattering versus the experimental observations are shown in Fig. 2.11. The Uee contribution, ρ_{Uee}, is estimated using semiclassical linear transport theory [113, 114, 103][40] in the density range, $0.2n_0 \le |n| \le 0.7n_0$ ($n_0 = 8/(\sqrt{3}\lambda^2)$ gives four electrons per supercell), where the reconstruction of the dispersion can be neglected and the mSL interaction is treated perturbatively. The most significant Uee processes involve one of the incoming or outgoing electrons Bragg scattering off the mSL[41], giving the conservation-violating momentum kick in Eq. (2.49). The Uee contribution is suppressed below a threshold density,

---

[40] See Section 7.E.

[41] See Eq. (7.4)

$n_* = n_0\pi/(8\sqrt{3}) \approx 0.23n_0$, at which point Eq. (2.49) is first satisfied by electrons on the Fermi line, subsequently increasing monotonically with density, n, and temperature, T, according to $\rho_{\mathrm{Uee}} \propto |n - n_*|^{3/2}T^2$. This gradual rise with respect to density is a consequence of the chirality-suppressed backscattering of monolayer graphene in Eq. (2.16)[42]. The Uee contribution features substantial particle-hole symmetry breaking from Eq. (2.46), being two orders of magnitude larger for holes then electrons, and dominates over other contributions, including electron-phonon scattering.

Bibliography

[1] R. Saito, M. S. Dresselhaus, and G. Dresselhaus, *Physical Properties of Carbon Nanotubes*. Imperial College Press, 1998.

[2] A. H. Castro Neto, F. Guinea, N. M. R. Peres, K. S. Novoselov, and A. K. Geim, The electronic properties of graphene *Rev. Mod. Phys.*, vol. 81, pp. 109–162, Jan 2009.

[3] D. G. Papageorgiou, I. A. Kinloch, and R. J. Young, Mechanical properties of graphene and graphene-based nanocomposites *Progress in Materials Science*, vol. 90, pp. 75–127, 2017.

[4] A. A. Balandin, S. Ghosh, W. Bao, I. Calizo, D. Teweldebrhan, F. Miao, and C. N. Lau, Superior Thermal Conductivity of Single-Layer Graphene *Nano Letters*, vol. 8, no. 3, pp. 902–907, 2008. PMID: 18284217.

[5] M. Hulman, 7 - Raman spectroscopy of graphene in *Graphene* (V. Skákalová and A. B. Kaiser, eds.), pp. 156–183, Woodhead Publishing, 2014.

[6] D. J. Willock, *Molecular Symmetry*. Wiley, Feb. 2009.

[7] J. C. Slater and G. F. Koster, Simplified LCAO Method for the Periodic Potential Problem *Phys. Rev.*, vol. 94, pp. 1498–1524, Jun 1954.

---

[42] In Chapter 7, we discuss the analogous bilayer graphene/hBN heterostructure, whose different chirality gives a strong, non-monotonic dependence of the Uee resistivity contribution on the density.

[8] M. König, H. Buhmann, L. W. Molenkamp, T. Hughes, C.-X. Liu, X.-L. Qi, and S.-C. Zhang, The Quantum Spin Hall Effect: Theory and Experiment *Journal of the Physical Society of Japan*, vol. 77, no. 3, p. 031007, 2008.

[9] M. Z. Hasan and C. L. Kane, Colloquium: Topological insulators *Rev. Mod. Phys.*, vol. 82, pp. 3045–3067, Nov 2010.

[10] X.-L. Qi and S.-C. Zhang, Topological insulators and superconductors *Rev. Mod. Phys.*, vol. 83, pp. 1057–1110, Oct 2011.

[11] C. D. Beule, V. T. Phong, and E. J. Mele, Network model for periodically strained graphene arXiv:2209.02554, 2022.

[12] C. L. Kane and E. J. Mele, Quantum Spin Hall Effect in Graphene *Phys. Rev. Lett.*, vol. 95, p. 226801, Nov 2005.

[13] Y. Hatsugai, T. Morimoto, T. Kawarabayashi, Y. Hamamoto, and H. Aoki, Chiral symmetry and its manifestation in optical responses in graphene: interaction and multilayers *New Journal of Physics*, vol. 15, p. 035023, mar 2013.

[14] G. W. Semenoff, Condensed-Matter Simulation of a Three-Dimensional Anomaly *Phys. Rev. Lett.*, vol. 53, pp. 2449–2452, Dec 1984.

[15] A. Garcia-Ruiz, H.-Y. Deng, V. V. Enaldiev, and V. I. Fal'ko, Full Slonczewski-Weiss-McClure parametrization of few-layer twistronic graphene *Phys. Rev. B*, vol. 104, p. 085402, Aug 2021.

[16] M. I. Katsnelson, K. S. Novoselov, and A. K. Geim, Chiral tunnelling and the Klein paradox in graphene *Nature Physics*, vol. 2, pp. 620–625, Sep 2006.

[17] Quantal phase factors accompanying adiabatic changes *Proceedings of the Royal Society of London. A. Mathematical and Physical Sciences*, vol. 392, pp. 45–57, Mar. 1984.

[18] D. Xiao, M.-C. Chang, and Q. Niu, Berry phase effects on electronic properties *Rev. Mod. Phys.*, vol. 82, pp. 1959–2007, Jul 2010.

[19] Y. Zhang, Y.-W. Tan, H. L. Stormer, and P. Kim, Experimental observation of the quantum Hall effect and Berry's phase in graphene *Nature*, vol. 438, pp. 201–204, Nov 2005.

[20] T. Ando, T. Nakanishi, and R. Saito, Berry's Phase and Absence of Back Scattering in Carbon Nanotubes *Journal of the Physical Society of Japan*, vol. 67, no. 8, pp. 2857–2862, 1998.

[21] M.-C. Chang and Q. Niu, Berry phase, hyperorbits, and the Hofstadter spectrum: Semiclassical dynamics in magnetic Bloch bands *Phys. Rev. B*, vol. 53, pp. 7010–7023, Mar 1996.

[22] M.-C. Chang and Q. Niu, Berry Phase, Hyperorbits, and the Hofstadter Spectrum *Phys. Rev. Lett.*, vol. 75, pp. 1348–1351, Aug 1995.

[23] G. Sundaram and Q. Niu, Wave-packet dynamics in slowly perturbed crystals: Gradient corrections and Berry-phase effects *Phys. Rev. B*, vol. 59, pp. 14915–14925, Jun 1999.

[24] F. D. M. Haldane, Model for a Quantum Hall Effect without Landau Levels: Condensed-Matter Realization of the "Parity Anomaly" *Phys. Rev. Lett.*, vol. 61, pp. 2015–2018, Oct 1988.

[25] N. Nagaosa, J. Sinova, S. Onoda, A. H. MacDonald, and N. P. Ong, Anomalous Hall effect *Rev. Mod. Phys.*, vol. 82, pp. 1539–1592, May 2010.

[26] T. Fukui, Y. Hatsugai, and H. Suzuki, Chern Numbers in Discretized Brillouin Zone: Efficient Method of Computing (Spin) Hall Conductances *Journal of the Physical Society of Japan*, vol. 74, no. 6, pp. 1674–1677, 2005.

[27] Y. Ren, Z. Qiao, and Q. Niu, Topological phases in two-dimensional materials: a review vol. 79, p. 066501, may 2016.

[28] Y. Hatsugai, Edge states in the integer quantum Hall effect and the Riemann surface of the Bloch function *Phys. Rev. B*, vol. 48, pp. 11851–11862, Oct 1993.

[29] Y. Hatsugai, Chern number and edge states in the integer quantum Hall effect *Phys. Rev. Lett.*, vol. 71, pp. 3697–3700, Nov 1993.

[30] H. Watanabe, Y. Hatsugai, and H. Aoki, Half-integer contributions to the quantum Hall conductivity from single Dirac cones *Phys. Rev. B*, vol. 82, p. 241403, Dec 2010.

[31] S. V. Morozov, K. S. Novoselov, M. I. Katsnelson, F. Schedin, L. A. Ponomarenko, D. Jiang, and A. K. Geim, Strong Suppression of Weak Localization in Graphene *Phys. Rev. Lett.*, vol. 97, p. 016801, Jul 2006.

[32] A. F. Morpurgo and F. Guinea, Intervalley Scattering, Long-Range Disorder, and Effective Time-Reversal Symmetry Breaking in Graphene *Phys. Rev. Lett.*, vol. 97, p. 196804, Nov 2006.

[33] R. V. Gorbachev, F. V. Tikhonenko, A. S. Mayorov, D. W. Horsell, and A. K. Savchenko, Weak Localization in Bilayer Graphene *Phys. Rev. Lett.*, vol. 98, p. 176805, Apr 2007.

[34] R. Jackiw and C. Rebbi, Solitons with fermion number ½ *Phys. Rev. D*, vol. 13, pp. 3398–3409, Jun 1976.

[35] J. T. Chalker and P. D. Coddington, Percolation, quantum tunnelling and the integer Hall effect *Journal of Physics C: Solid State Physics*, vol. 21, p. 2665, may 1988.

[36] K. v. Klitzing, G. Dorda, and M. Pepper, New Method for High-Accuracy Determination of the Fine-Structure Constant Based on Quantized Hall Resistance *Phys. Rev. Lett.*, vol. 45, pp. 494–497, Aug 1980.

[37] A. H. MacDonald, ed., *Quantum Hall Effect: A Perspective*. Springer Netherlands, 1989.

[38] R. E. Prange and S. M. Girvin, eds., *The Quantum Hall Effect*. Springer New York, 1990.

[39] J. W. McClure, Diamagnetism of Graphite *Phys. Rev.*, vol. 104, pp. 666–671, Nov 1956.

[40] Y. Zheng and T. Ando, Hall conductivity of a two-dimensional graphite system *Phys. Rev. B*, vol. 65, p. 245420, Jun 2002.

[41] V. P. Gusynin and S. G. Sharapov, Unconventional Integer Quantum Hall Effect in Graphene *Phys. Rev. Lett.*, vol. 95, p. 146801, Sep 2005.

[42] I. F. Herbut, Theory of integer quantum Hall effect in graphene *Phys. Rev. B*, vol. 75, p. 165411, Apr 2007.

[43] K. S. Novoselov, A. K. Geim, S. V. Morozov, D. Jiang, M. I. Katsnelson, I. V. Grigorieva, S. V. Dubonos, and A. A. Firsov, Two-dimensional gas of massless Dirac fermions in graphene *Nature*, vol. 438, pp. 197–200, Nov 2005.

[44] Y. Fukaya, Y. Zhao, H.-W. Kim, J. R. Ahn, H. Fukidome, and I. Matsuda, Atomic arrangements of quasicrystal bilayer graphene: Interlayer distance expansion *Phys. Rev. B*, vol. 104, p. L180202, Nov 2021.

[45] E. McCann and M. Koshino, The electronic properties of bilayer graphene *Reports on Progress in Physics*, vol. 76, p. 056503, apr 2013.

[46] J. C. Slonczewski and P. R. Weiss, Band Structure of Graphite *Phys. Rev.*, vol. 109, pp. 272–279, Jan 1958.

[47] J. W. McClure, Band Structure of Graphite and de Haas-van Alphen Effect *Phys. Rev.*, vol. 108, pp. 612–618, Nov 1957.

[48] J. W. McClure, Theory of Diamagnetism of Graphite *Phys. Rev.*, vol. 119, pp. 606–613, Jul 1960.

[49] M. S. Dresselhaus and G. Dresselhaus, Intercalation compounds of graphite *Advances in Physics*, vol. 51, no. 1, pp. 1–186, 2002.

[50] A. B. Kuzmenko, I. Crassee, D. van der Marel, P. Blake, and K. S. Novoselov, Determination of the gate-tunable band gap and tight-binding parameters in bilayer graphene using infrared spectroscopy *Phys. Rev. B*, vol. 80, p. 165406, Oct 2009.

[51] E. McCann and V. I. Fal'ko, Landau-Level Degeneracy and Quantum Hall Effect in a Graphite Bilayer *Phys. Rev. Lett.*, vol. 96, p. 086805, Mar 2006.

[52] B. Partoens and F. M. Peeters, From graphene to graphite: Electronic structure around the K point *Phys. Rev. B*, vol. 74, p. 075404, Aug 2006.

[53] J. Nilsson, A. H. Castro Neto, F. Guinea, and N. M. R. Peres, Electronic properties of bilayer and multilayer graphene *Phys. Rev. B*, vol. 78, p. 045405, Jul 2008.

[54] J. Jung, F. Zhang, and A. H. MacDonald, Lattice theory of pseudospin ferromagnetism in bilayer graphene: Competing interaction-induced quantum Hall states *Phys. Rev. B*, vol. 83, p. 115408, Mar 2011.

[55] J. Jung and A. H. MacDonald, Accurate tight-binding models for the π bands of bilayer graphene *Phys. Rev. B*, vol. 89, p. 035405, Jan 2014.

[56] F. Joucken, Z. Ge, E. A. Quezada-López, J. L. Davenport, K. Watanabe, T. Taniguchi, and J. Velasco, Determination of the trigonal warping orientation in Bernal-stacked bilayer graphene via scanning tunneling microscopy *Phys. Rev. B*, vol. 101, p. 161103, Apr 2020.

[57] J. H. Van Vleck, On σ-Type Doubling and Electron Spin in the Spectra of Diatomic Molecules *Phys. Rev.*, vol. 33, pp. 467–506, Apr 1929.

[58] P.-O. Löwdin, Partitioning technique, perturbation theory, and rational approximations *International Journal of Quantum Chemistry*, vol. 21, no. 1, pp. 69–92, 1982.

[59] C. Cohen-Tannoudji, J. Dupont-Roc, and G. Grynberg, *Atom—Photon Interactions*. Wiley, Apr 1998.

[60] L. M. Zhang, M. M. Fogler, and D. P. Arovas, Magnetoelectric coupling, Berry phase, and Landau level dispersion in a biased bilayer graphene *Phys. Rev. B*, vol. 84, p. 075451, Aug 2011.

[61] J. L. Mañes, F. Guinea, and M. A. H. Vozmediano, Existence and topological stability of Fermi points in multilayered graphene *Phys. Rev. B*, vol. 75, p. 155424, Apr 2007.

[62] G. P. Mikitik and Y. V. Sharlai, Electron energy spectrum and the Berry phase in a graphite bilayer *Phys. Rev. B*, vol. 77, p. 113407, Mar 2008.

[63] E. McCann, Asymmetry gap in the electronic band structure of bilayer graphene *Phys. Rev. B*, vol. 74, p. 161403, Oct 2006.

[64] M. Mucha-Kruczyński, I. L. Aleiner, and V. I. Fal'ko, Strained bilayer graphene: Band structure topology and Landau level spectrum *Phys. Rev. B*, vol. 84, p. 041404(R), Jul 2011.

[65] Y.-W. Son, S.-M. Choi, Y. P. Hong, S. Woo, and S.-H. Jhi, Electronic topological transition in sliding bilayer graphene *Phys. Rev. B*, vol. 84, p. 155410, Oct 2011.

[66] M. Mucha-Kruczyński, I. L. Aleiner, and V. I. Fal'ko, Landau levels in deformed bilayer graphene at low magnetic fields *Solid State Communications*, vol. 151, no. 16, pp. 1088 – 1093, 2011.

[67] H. Suzuura and T. Ando, Phonons and electron-phonon scattering in carbon nanotubes *Phys. Rev. B*, vol. 65, p. 235412, May 2002.

[68] J. L. Mañes, Symmetry-based approach to electron-phonon interactions in graphene *Phys. Rev. B*, vol. 76, p. 045430, Jul 2007.

[69] F. Guinea, M. I. Katsnelson, and A. K. Geim, Energy gaps and a zero-field quantum Hall effect in graphene by strain engineering *Nature Physics*, vol. 6, no. 1, pp. 30–33, 2010.

[70] V. M. Pereira, A. H. Castro Neto, and N. M. R. Peres, Tight-binding approach to uniaxial strain in graphene *Phys. Rev. B*, vol. 80, p. 045401, Jul 2009.

[71] A. R. Botello-Méndez, J. C. Obeso-Jureidini, and G. G. Naumis, Toward an Accurate Tight-Binding Model of Graphene's Electronic Properties under Strain *The Journal of Physical Chemistry C*, vol. 122, no. 27, pp. 15753–15760, 2018.

[72] T. M. G. Mohiuddin, A. Lombardo, R. R. Nair, A. Bonetti, G. Savini, R. Jalil, N. Bonini, D. M. Basko, C. Galiotis, N. Marzari, K. S. Novoselov, A. K. Geim, and A. C. Ferrari, Uniaxial strain in graphene by Raman spectroscopy: *G* peak

splitting, Grüneisen parameters, and sample orientation *Phys. Rev. B*, vol. 79, p. 205433, May 2009.

[73] F. Ding, H. Ji, Y. Chen, A. Herklotz, K. Dörr, Y. Mei, A. Rastelli, and O. G. Schmidt, Stretchable Graphene: A Close Look at Fundamental Parameters through Biaxial Straining *Nano Letters*, vol. 10, no. 9, pp. 3453–3458, 2010.

[74] D. A. Gradinar, H. Schomerus, and V. I. Fal'ko, Conductance anomaly near the Lifshitz transition in strained bilayer graphene *Phys. Rev. B*, vol. 85, p. 165429, Apr 2012.

[75] B. Verberck, B. Partoens, F. M. Peeters, and B. Trauzettel, Strain-induced band gaps in bilayer graphene *Phys. Rev. B*, vol. 85, p. 125403, Mar 2012.

[76] Y. Zhang, T.-T. Tang, C. Girit, Z. Hao, M. C. Martin, A. Zettl, M. F. Crommie, Y. R. Shen, and F. Wang, Direct observation of a widely tunable bandgap in bilayer graphene *Nature*, vol. 459, pp. 820–823, Jun 2009.

[77] S. Slizovskiy, A. Garcia-Ruiz, A. I. Berdyugin, N. Xin, T. Taniguchi, K. Watanabe, A. K. Geim, N. D. Drummond, and V. I. Fal'ko, Out-of-Plane Dielectric Susceptibility of Graphene in Twistronic and Bernal Bilayers *Nano Letters*, vol. 21, no. 15, pp. 6678–6683, 2021. PMID: 34296602.

[78] M. M. Ugeda, A. J. Bradley, S. F. Shi, F. H. D. Jornada, Y. Zhang, D. Y. Qiu, W. Ruan, S. K. Mo, Z. Hussain, Z. X. Shen, F. Wang, S. G. Louie, and M. F. Crommie, Giant bandgap renormalization and excitonic effects in a monolayer transition metal dichalcogenide semiconductor *Nature Materials*, vol. 13, pp. 1091–1095, 8 2014.

[79] C. Gong and X. Zhang, Two-dimensional magnetic crystals and emergent heterostructure devices *Science*, vol. 363, p. eaav4450, Feb. 2019.

[80] Q. Tong, M. Chen, and W. Yao, Magnetic Proximity Effect in a van der Waals Moiré Superlattice *Physical Review Applied*, vol. 12, p. 024031, Aug 2019.

[81] B. Zhou, J. Balgley, P. Lampen-Kelley, J. Q. Yan, D. G. Mandrus, and E. A. Henriksen, Evidence for charge transfer and proximate magnetism in graphene–$\alpha-\mathrm{RuCl}_3$ heterostructures *Physical Review B*, vol. 100, p. 165426, 10 2019.

[82] A. Varlet, D. Bischoff, P. Simonet, K. Watanabe, T. Taniguchi, T. Ihn, K. Ensslin, M. Mucha-Kruczyński, and V. I. Fal'ko, Anomalous Sequence of Quantum Hall Liquids Revealing a Tunable Lifshitz Transition in Bilayer Graphene *Phys. Rev. Lett.*, vol. 113, p. 116602, Sep 2014.

[83] H. Min, B. Sahu, S. K. Banerjee, and A. H. MacDonald, Ab initio theory of gate induced gaps in graphene bilayers *Phys. Rev. B*, vol. 75, p. 155115, Apr 2007.

[84] E. V. Castro, K. S. Novoselov, S. V. Morozov, N. M. R. Peres, J. M. B. L. dos Santos, J. Nilsson, F. Guinea, A. K. Geim, and A. H. C. Neto, Biased Bilayer Graphene: Semiconductor with a Gap Tunable by the Electric Field Effect *Physical Review Letter*, vol. 99, p. 216802, Nov 2007.

[85] E. Icking, L. Banszerus, F. Wörtche, F. Volmer, P. Schmidt, C. Steiner, S. Engels, J. Hesselmann, M. Goldsche, K. Watanabe, T. Taniguchi, C. Volk, B. Beschoten, and C. Stampfer, Transport Spectroscopy of Ultraclean Tunable Band Gaps in Bilayer Graphene *Advanced Electronic Materials*, vol. 8, no. 11, p. 2200510, 2022.

[86] E. Fermi, Sulla quantizzazione del gas perfetto monoatomico. (Italian) [On the Quantization of the Ideal Monatomic Gas] vol. 3, no. 6, pp. 145–149, 1926.

[87] P. A. M. Dirac, On the theory of quantum mechanics *Proceedings of the Royal Society of London. Series A, Containing Papers of a Mathematical and Physical Character*, vol. 112, pp. 661–677, Oct. 1926.

[88] Y. Shi, C. Hamsen, X. Jia, K. K. Kim, A. Reina, M. Hofmann, A. L. Hsu, K. Zhang, H. Li, Z.-Y. Juang, M. S. Dresselhaus, L.-J. Li, and J. Kong, Synthesis of Few-Layer Hexagonal Boron Nitride Thin Film by Chemical Vapor Deposition *Nano Letters*, vol. 10, no. 10, pp. 4134–4139, 2010. PMID: 20812716.

[89] S. K. Jang, J. Youn, Y. J. Song, and S. Lee, Synthesis and Characterization of Hexagonal Boron Nitride as a Gate Dielectric *Scientific Reports*, vol. 6, p. 30449, Jul 2016.

[90] D. Wickramaratne, L. Weston, and C. G. Van de Walle, Monolayer to Bulk Properties of Hexagonal Boron Nitride *The Journal of Physical Chemistry C*, vol. 122, no. 44, pp. 25524–25529, 2018.

[91] M. J. Molaei, M. Younas, and M. Rezakazemi, A Comprehensive Review on Recent Advances in Two-Dimensional (2D) Hexagonal Boron Nitride *ACS Applied Electronic Materials*, vol. 3, no. 12, pp. 5165–5187, 2021.

[92] J. R. Wallbank, A. A. Patel, M. Mucha-Kruczyński, A. K. Geim, and V. I. Fal'ko, Generic miniband structure of graphene on a hexagonal substrate *Phys. Rev. B*, vol. 87, p. 245408, Jun 2013.

[93] B. Hunt, J. D. Sanchez-Yamagishi, A. F. Young, M. Yankowitz, B. J. LeRoy, K. Watanabe, T. Taniguchi, P. Moon, M. Koshino, P. Jarillo-Herrero, and R. C. Ashoori, Massive Dirac Fermions and Hofstadter Butterfly in a van der Waals Heterostructure *Science*, vol. 340, no. 6139, pp. 1427–1430, 2013.

[94] X. Chen, J. R. Wallbank, M. Mucha-Kruczyński, E. McCann, and V. I. Fal'ko, Zero-energy modes and valley asymmetry in the Hofstadter spectrum of bilayer graphene van der Waals heterostructures with hBN *Phys. Rev. B*, vol. 94, p. 045442, Jul 2016.

[95] M. Yankowitz, S. Chen, H. Polshyn, Y. Zhang, K. Watanabe, T. Taniguchi, D. Graf, A. F. Young, and C. R. Dean, Tuning superconductivity in twisted bilayer graphene *Science*, vol. 363, pp. 1059–1064, 2019.

[96] P. Moon and M. Koshino, Optical absorption in twisted bilayer graphene *Phys. Rev. B*, vol. 87, p. 205404, May 2013.

[97] P. Moon and M. Koshino, Electronic properties of graphene/hexagonal-boron-nitride moiré superlattice *Phys. Rev. B*, vol. 90, p. 155406, Oct 2014.

[98] J. Sławińska, I. Zasada, and Z. Klusek, Energy gap tuning in graphene on hexagonal boron nitride bilayer system *Phys. Rev. B*, vol. 81, p. 155433, Apr 2010.

[99] P. San-Jose, A. Gutiérrez-Rubio, M. Sturla, and F. Guinea, Electronic structure of spontaneously strained graphene on hexagonal boron nitride *Phys. Rev. B*, vol. 90, p. 115152, Sep 2014.

[100] M. Lee, J. R. Wallbank, P. Gallagher, K. Watanabe, T. Taniguchi, V. I. Fal'ko, and D. Goldhaber-Gordon, Ballistic miniband conduction in a graphene superlattice *Science*, vol. 353, no. 6307, pp. 1526–1529, 2016.

[101] J. Wallbank, M. Mucha-Kruczynski, X. Chen, and V. Fal'ko, Moiré superlattice effects in graphene/boron-nitride van der Waals heterostructures *Annalen der Physik*, vol. 527, pp. 359 – 376, June 2015.

[102] R. Bistritzer and A. H. MacDonald, Moiré bands in twisted double-layer graphene *Proceedings of the National Academy of Sciences*, vol. 108, no. 30, pp. 12233–12237, 2011.

[103] J. R. Wallbank, R. Krishna Kumar, M. Holwill, Z. Wang, G. H. Auton, J. Birkbeck, A. Mishchenko, L. A. Ponomarenko, K. Watanabe, T. Taniguchi, K. S. Novoselov, I. L. Aleiner, A. K. Geim, and V. I. Fal'ko, Excess resistivity in graphene superlattices caused by umklapp electron–electron scattering *Nature Physics*, vol. 15, pp. 32–36, Jan 2019.

[104] M. Kim, S. G. Xu, A. I. Berdyugin, A. Principi, S. Slizovskiy, N. Xin, P. Kumaravadivel, W. Kuang, M. Hamer, R. Krishna Kumar, R. V. Gorbachev, K. Watanabe, T. Taniguchi, I. V. Grigorieva, V. I. Fal'ko, M. Polini, and A. K. Geim, Control of electron-electron interaction in graphene by proximity screening *Nature Communications*, vol. 11, p. 2339, May 2020.

[105] W. Yang, G. Chen, Z. Shi, C.-C. Liu, L. Zhang, G. Xie, M. Cheng, D. Wang, R. Yang, D. Shi, K. Watanabe, T. Taniguchi, Y. Yao, Y. Zhang, and G. Zhang, Epitaxial growth of single-domain graphene on hexagonal boron nitride *Nature Materials*, vol. 12, pp. 792–797, Sep 2013.

[106] A. Summerfield, A. Davies, T. S. Cheng, V. V. Korolkov, Y. Cho, C. J. Mellor, C. T. Foxon, A. N. Khlobystov, K. Watanabe, T. Taniguchi, L. Eaves, S. V. Novikov, and P. H. Beton, Strain-Engineered Graphene Grown on Hexagonal Boron Nitride by Molecular Beam Epitaxy *Scientific Reports*, vol. 6, p. 22440, Mar 2016.

[107] J. Thomas, J. Bradford, T. S. Cheng, A. Summerfield, J. Wrigley, C. J. Mellor, A. N. Khlobystov, C. T. Foxon, L. Eaves, S. V. Novikov, and P. H. Beton, Step-flow growth of graphene-boron nitride lateral heterostructures by molecular beam epitaxy *2D Materials*, vol. 7, p. 035014, may 2020.

[108] A. H. MacDonald, R. Taylor, and D. J. W. Geldart, Umklapp electron-electron scattering and the low-temperature electrical resistivity of the alkali metals *Phys. Rev. B*, vol. 23, pp. 2718–2730, Mar 1981.

[109] J. Bass, W. P. Pratt, and P. A. Schroeder, The temperature-dependent electrical resistivities of the alkali metals *Rev. Mod. Phys.*, vol. 62, pp. 645–744, Jul 1990.

[110] V. Gasparov and R. Huguenin, Electron-phonon, electron-electron and electron-surface scattering in metals from ballistic effects *Advances in Physics*, vol. 42, no. 4, pp. 393–521, 1993.

[111] I. L. Aleiner and O. Agam, Saturation of strong electron-electron umklapp scattering at high temperature *Annals of Physics*, vol. 385, pp. 716–728, 2017.

[112] T. M. Rice, N. J. Robinson, and A. M. Tsvelik, Umklapp scattering as the origin of T-linear resistivity in the normal state of high-T_c cuprate superconductors *Phys. Rev. B*, vol. 96, p. 220502, Dec 2017.

[113] J. M. Ziman, ch. 9.14. Oxford Univ. Press, 1960.

[114] L. D. Landau and E. M. Lifshitz, vol. 10, ch. 79. Pergamon Press Ltd., 1981.

Chapter 3

Engineering of the topological magnetic moment of electrons in bilayer graphene using strain and electrical bias

Preface

The contents of this chapter represent the main body of a manuscript previously published in Physical Review B [1]. The manuscript was authored by Christian Moulsdale[1,2], Angelika Knothe[2] and Vladimir Fal'ko[1,2,3].

Christian Moulsdale performed all the analytical and numerical calculations and produced the figures for the manuscript, under the guidance and supervision of Angelika Knothe and Vladimir Fal'ko. The writing of the manuscript was primarily done by Christian Moulsdale, with assistance from Angelika Knothe and Vladimir Fal'ko.

---

[1] School of Physics and Astronomy, University of Manchester, Manchester M13 9PL, UK

[2] National Graphene Institute, University of Manchester, Manchester M13 9PL, UK

[3] Henry Royce Institute, Institute for Advanced Materials, Manchester M13 9PL, UK

Abstract

Topological properties of electronic states in multivalley two-dimensional materials, such as mono- and bilayer graphene, or thin films of rhombohedral graphite, give rise to various unusual magneto-transport regimes. Here, we investigate the tunability of the topological magnetic moment (related to the Berry curvature) of electronic states in bilayer graphene using strain and vertical bias. We show how one can controllably vary the valley g-factor of the band-edge electrons, g_v^*, across the range $10 < |g_v^*| < 200$, and we discuss the manifestations of the topological magnetic moment in the anomalous contribution towards the Hall conductivity and in the Landau level spectrum.

Strain in bilayer graphene (BLG), sketched in Fig. 3.1, affects its low-energy electronic properties far greater than in its monolayer allotrope [7, 8, 9, 10, 11], generating qualitative changes in its low-energy spectrum close to the neutrality point. The earlier-discussed effects [7, 8, 9] of unilateral strain and shear deformations in Bernal $(A'B)$ stacked bilayers include the Lifshitz transition [12] for weakly n-doped and p-doped structures, accompanied by a redistribution (even a coalescence) of the Berry phase $\pm\pi$ singularities in the bilayer's electronic bands [5, 7]. These changes are caused by the interplay between the intralayer and skew (AB') interlayer hopping parameters of electrons, modified by the deformations.

A transverse displacement field, induced by electrostatic gating of bilayers, is another factor that qualitatively changes their electronic properties. The displacement field generates an asymmetry between the layers, opening up a gap in the energy spectrum [5, 13] and smearing the Berry phase singularities into "hot spots" of Berry curvature, $\mathbf{\Omega}_\pm(\boldsymbol{p})$, located near the valley centers $\boldsymbol{K}^\pm$ (sign-inverted distributions are found in opposite valleys, $\mathbf{\Omega}_+(\boldsymbol{p}) = \mathbf{\Omega}_-(-\boldsymbol{p})$). According to the fundamental properties of Bloch-Wannier functions [14, 15], a finite Berry curvature of the electronic bands is associated with a finite intrinsic angular momentum, therefore, a resulting magnetic moment of the plane-wave states of the electrons in the corresponding parts of the Brillouin zone (BZ) of the material [14, 15, 16]. The experimental signatures of such topological magnetic moments (TMM), with anomalously large effective g-factors

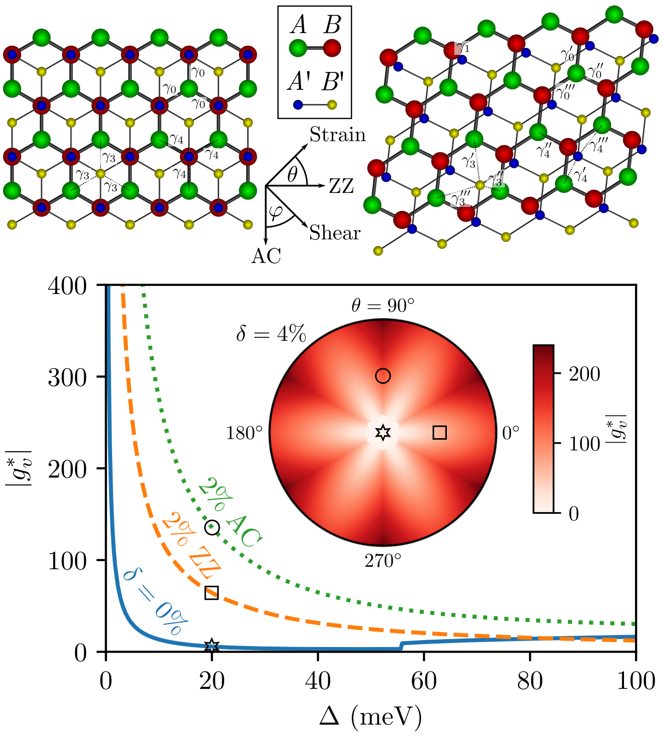

Figure 3.1: *Top.* Unstrained (*left*) and strained (*right*) bilayer graphene (BLG) with the intra- and interlayer couplings $\gamma_{0,3,4}$ (modified by the strain) marked along the relevant hopping directions. *Bottom.* The magnitude of the valley g-factor at the conduction band edge of BLG, $|g_v^*|$, as a function of the interlayer asymmetry gap, Δ, for uniaxial strains of magnitude $\delta = 0\%$ and 2% applied along the zigzag (ZZ) and armchair (AC) directions. A jump in $|g_v^*|$ at $\Delta \sim 55\,\text{meV}$ for $\delta = 0\%$ is due to the disappearance of a central minivalley in the unstrained BLG spectrum upon the increase of the gap [5]. *Inset* shows $|g_v^*|$ against uniaxial strain (up to $\delta = 4\%$) for various orientations of the strain tensor axes and $\Delta = 20\,\text{meV}$ (strain values used in the plot are marked by shapes). These images can also be used to characterize the effect of shear deformations described by Eq. (3.2) later in the text.

($g_v \sim 10 - 100$), have recently been predicted [16] and, consequently, observed experimentally [17, 18, 19, 20] in the studies of magnetotransport characteristics of electrostatically controlled wires in bilayer graphene. The Berry curvature and related intrinsic angular momentum are also associated with a “Hall-like” drift of electrons in a direction perpendicular to an external electric field, which causes topological valley currents [21] at $B = 0$ and an anomalous contribution toward the Hall conductivity of a 2D material subjected to an external magnetic field [22].

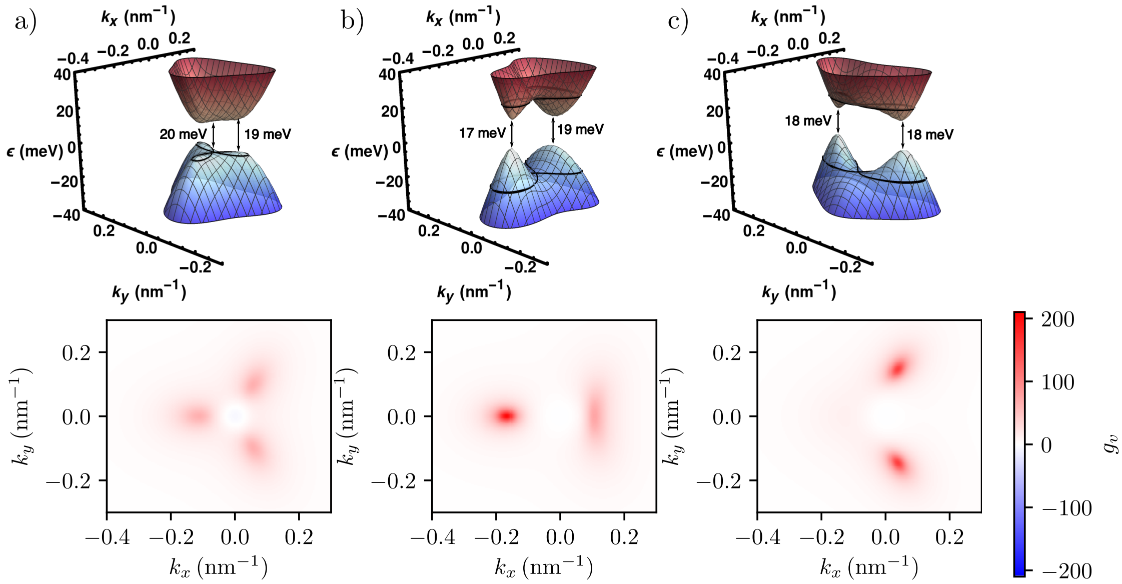

Figure 3.2: *Top row*. The dispersion $\varepsilon(\boldsymbol{k})$ of bilayer graphene in the $\boldsymbol{K}^-$ valley for $\Delta = 20\,\text{meV}$ and a) unstrained; b) 2% uniaxial strain along the zigzag axis and c) 2% uniaxial strain along the armchair axis (shear with parameters set by the relation in Eq. (3.2)). Black lines indicate an energy cut at the van Hove singularity. *Bottom row*. Contour plots of the corresponding valley g-factor g_v.

In this paper, we study the interplay between strain and the interlayer asymmetry gap [5] in BLG in determining topological properties of electronic states, such as the Berry curvature, recently analyzed in [23], and the topological magnetic moment, and their manifestations in the magnetotransport characteristics and Landau level spectra of bilayers. The outcome of this analysis is summarized in Fig. 3.1, where we show how strain and shear increase the size of the effective valley g-factor for electrons and holes near the respective band edges of the gapped BLG, g_v^*, giving rise to its tunability by two orders of magnitude.

To describe electrons in the $\boldsymbol{K}^\xi$ ($\xi = \pm$) valley of bilayers, we use the low-energy

Hamiltonian written in the (A,B',A',B) sublattice basis (marked in Fig. 3.1),

$$H_\xi = \begin{pmatrix} -\frac{1}{2}\Delta & v_3\pi + w_3 & -v_4\pi^\dagger - w_4^* & v_0\pi^\dagger \\ v_3\pi^\dagger + w_3^* & \frac{1}{2}\Delta & v_0\pi & -v_4\pi - w_4 \\ -v_4\pi - w_4 & v_0\pi^\dagger & \frac{1}{2}\Delta + \delta\varepsilon & \gamma_1 \\ v_0\pi & -v_4\pi^\dagger - w_4^* & \gamma_1 & -\frac{1}{2}\Delta + \delta\varepsilon \end{pmatrix}; \qquad (3.1.a)$$

$$w_{j=3,4} = \frac{3}{4}[e^{-i2\xi\theta}(\delta - \delta')(\eta_j - \eta_0) + 2\sqrt{3}(-1)^j e^{i\xi\varphi}\rho\eta_j]\gamma_j. \qquad (3.1.b)$$

Here, $\pi = \xi p_x + ip_y$ and $v_{0,3,4} = \sqrt{3}a\gamma_{0,3,4}/2\hbar$ are determined by the intra- (γ_0) and interlayer $(\gamma_{1,3,4})$ Slonczewski-Weiss hopping parameters [24], marked on the bilayer lattice in Fig. 3.1, and a is the lattice constant. For completeness, we take into account the dimer asymmetry $\delta\varepsilon$ which, together with γ_4, breaks the particle-hole symmetry of the spectrum. The interlayer asymmetry, $\Delta = -eE_zd$, is induced by a transverse electric field E_z, where d is the interlayer distance and $e < 0$ is the electron charge. The effect of strain is incorporated in Eq. (3.1.a) in the form of gauge fields, $w_{3,4}$ in Eq. (3.1.b), with the magnitude of w_3 partly enhanced by the Coulomb interaction [7, 9]. These come from the directional dependence of the $\gamma_{0,3,4}$ couplings [7, 8, 25], generated by strain and shear (relative shift of the layers). Note that the vertical γ_1 coupling is unaffected to first order in the strain amplitude. Here, θ is the angle between the zigzag crystallographic direction in graphene and the principal axis of the the strain tensor with components δ and $\delta' = -0.165\delta$ [26]; shear deformations are described by $\rho = \delta r/a$, the interlayer lattice shift normalized by the lattice constant, where φ is the angle between the shear direction and the armchair axis. Their effect is quantified using the Grüneisen parameters $\eta_j = \frac{r_{AB}}{\gamma_j}\frac{\partial\gamma_j}{\partial r_{AB}}$, with the values $\eta_0 \sim -3$ [27, 28] and $\eta_{3,4} \sim -1$ taken from the literature [29]. Note that an uniaxial strain of magnitude δ at an angle θ is approximately equivalent to the shear deformation of magnitude ρ and direction φ,

$$\rho = 0.336\delta\frac{\eta_0 - \eta_3}{\eta_0}; \quad \varphi = 180^\circ - 2\theta, \qquad (3.2)$$

with an equal value of the more relevant gauge field, w_3, while the different value of w_4 has negligible effect since $|w_4| < |w_3| \ll \gamma_1$.

Without any strain and for $\Delta = 0$, the BLG spectrum in the $\boldsymbol{K}^\pm$ valley [30] features a central Dirac cone with a Berry phase $\mp\pi$, surrounded by three Dirac points with Berry phase $\pm\pi$ (giving a total topological charge of $\pm 2\pi$). Strain causes the displacement in the momentum plane and a coalescence of $\pm\pi$ singularities, whereas opening up a gap spreads them into hot spots of Berry curvature [15, 31, 23],

$$\Omega_n^z = -2\hbar^2 \,\mathrm{Im} \sum_{m\neq n} \frac{\langle n|\partial_{p_x} H|m\rangle \langle m|\partial_{p_y} H|n\rangle}{(\varepsilon_n - \varepsilon_m)^2}. \tag{3.3}$$

In Fig. 3.2, we illustrate the cumulative effect of the strain ($\delta = 2\%$, corresponding to $|w_3| = 19\,\mathrm{meV}$ and $|w_4| = 5\,\mathrm{meV}$) and a gap ($\Delta = 20\,\mathrm{meV}$) on the BLG spectrum in the $\boldsymbol{K}^-$ valley, where the role of strain is to deform the three minivalleys at the BLG band edge [5, 32] into two [7, 8, 31]. Moreover, the particle-hole symmetry breaking caused by the hopping γ_4 and energy shift $\delta\varepsilon$ of the dimer orbitals makes the bilayer band gap indirect for strain applied along the zigzag direction, as marked on Fig. 3.2b). For strain applied along the armchair axis, the band edges remain degenerate in Fig. 3.2c). In the bottom panels of Fig. 3.2, we show the variation of the topological magnetic moment of the plane wave states of electrons across the Brillouin zone, computed using the relation derived in Ref. [15],

$$\mu_n^z = -e\hbar \,\mathrm{Im} \sum_{m\neq n} \frac{\langle n|\partial_{p_x} H|m\rangle \langle m|\partial_{p_y} H|n\rangle}{\varepsilon_n - \varepsilon_m} \equiv \xi \mu_B g_v, \tag{3.4}$$

where, for a band n, we sum across all three other bands $m \neq n$. This parameter reflects the valley splitting induced by simultaneous inversion (by E_z) and time-inversion (by B) symmetry breaking. We express μ^z in units of the Bohr magneton μ_B, hence, present its values in terms of the valley g-factor, g_v. The dependence of g_v at the conduction band edge, g_v^*, on the gap size, for BLG with 2% strain applied along the zigzag and armchair axis of graphene is shown in Fig. 3.1, together with a map describing the variation of g_v^* with the change of the strain magnitude and orientation of its axes. Using a 2-band model [33, 7], which can be solved analytically, we estimate [34] that for $|w_3| \gtrsim \Delta$, $g_v^* \sim -10^2 \xi |w_3|/\Delta$, in a good agreement with the numerical result.

We also use the Hamiltonian in Eq. (3.1.a) to compute [35] the Landau level (LL) spectra in a simultaneously strained and vertically biased bilayer, in particular in the case of $\Delta \sim |w_3|$. In Fig. 3.3, we show the LL spectra for a bilayer with $\Delta = 20\,\mathrm{meV}$ and, due to 2% uniaxial strain applied along the zigzag (ZZ) and armchair (AC) directions (or a $\rho = 0.4\%$ shear anti-parallel and parallel to the AC axis according to Eq. (3.2)), $|w_3| = 19\,\text{meV}$ and $|w_4| = 5\,\text{meV}$. Alongside this, we show the density of states (DoS) of the spectra at $B = 0$, marking van Hove singularities, and we extrapolate the LL spectra to the zero-field limit using semiclassical quantization [6] in the two minivalleys shown in Fig. 3.2b) and c). While for an arbitrary orientation of the strain tensor axes these minivalleys are not degenerate, for strain applied along an armchair direction, the mirror symmetry of the crystal, retained despite the deformations, provides the degeneracy of the minivalleys. This also results in a double degeneracy of LLs at low energies which is lifted by magnetic breakdown that takes place at the saddle points in the spectra shown in Fig. 3.2c). For the larger gap $\Delta = 100\,\text{meV} \gg |w_3|$, the effects of lattice deformations are diminished, so that the LL spectra in Fig. 3.4 roughly coincide with what has been found earlier in gapped bilayers [32].

The formation of the topological magnetic moment may also manifest itself in the anomalous contribution towards the classical Hall effect in the bilayer. The latter is the result of a drift experienced by electrons in the bands with a finite $\boldsymbol{\Omega}$, in the direction perpendicular to the external electric field. Due to time-inversion symmetry, the resulting drift currents have the opposite signs in the opposite valleys ($\boldsymbol{K}^{\pm}$), compensating each other at $B = 0$. However, a topological magnetic moment $\pm\mu^z$ leads to the splitting of BLG band edges between the $\boldsymbol{K}^{\pm}$ valleys, $\pm g_v \mu_B B_z$, and a valley contribution to the imbalance in the filling of the band edge state, leading to a finite anomalous Hall conductivity [21, 22],

$$\sigma_{xy}^{A} = -\frac{e^2 B}{\pi^2 \hbar^3} \sum_n \oint_{\varepsilon_n(\boldsymbol{p})=\varepsilon_F} \frac{\Omega_n^z \mu_n^z}{|\boldsymbol{\nabla}_{\boldsymbol{p}} \varepsilon_n|} dp. \tag{3.5}$$

The former should be added to the classical Hall contribution [22],

$$\sigma_{xy}^{H} = -\frac{e^3 \tau^2}{\pi^2 \hbar^2} \sum_{n,\gamma} \oint_{\varepsilon_n(\boldsymbol{p})=\varepsilon_F} \frac{\partial_{p_x} \varepsilon_n}{|\boldsymbol{\nabla}_{\boldsymbol{p}} \varepsilon_n|} (\boldsymbol{\nabla}_{\boldsymbol{p}} \varepsilon_n \times \boldsymbol{B})_\gamma \frac{dp}{m_{n,\gamma y}}, \tag{3.6}$$

where $m_{n,\alpha\beta}^{-1} = \partial^2 \varepsilon_n / \partial_{p_\alpha} \partial_{p_\beta}$ and τ is the elastic scattering rate. The anomalous Hall conductivity originates from the TMM and is not suppressed by scattering, so its effect should be most pronounced in disordered bilayers. In Fig. 3.5, we show both σ_{xy}^{A} and the total Hall conductivity $\sigma_{xy} = \sigma_{xy}^{H} + \sigma_{xy}^{A}$ against carrier density, n_e, for a strained and unstrained BLG with $\tau \sim 10^{-13}\,\mathrm{s}$ [36], and $\Delta = 20\,\mathrm{meV}$ or $100\,\mathrm{meV}$.

Overall, the results presented above demonstrate that the topological characteristics of electron states in gapped bilayer graphene can be substantially enhanced by strain. This results in an anomalously large topological magnetic moment, leading to a valley splitting of band-edge states by magnetic field in a bias-gapped bilayer that leads to an anomalous correction to the Hall conductivity. The enhancement of topological effects may also be detected by measuring photocurrents induced by optically pumping bilayers using circularly polarized light similarly to that studied earlier in unstrained topological materials [22, 37].

Bibliography

[1] C. Moulsdale, A. Knothe, and V. Fal'ko, Engineering of the topological magnetic moment of electrons in bilayer graphene using strain and electrical bias *Phys. Rev. B*, vol. 101, p. 085118, Feb 2020.

[2] J. N. Fuchs, F. Piéchon, M. O. Goerbig, and G. Montambaux, Topological Berry phase and semiclassical quantization of cyclotron orbits for two dimensional electrons in coupled band models *The European Physical Journal B*, vol. 77, pp. 351–362, Oct 2010.

[3] A. B. Kuzmenko, I. Crassee, D. van der Marel, P. Blake, and K. S. Novoselov, Determination of the gate-tunable band gap and tight-binding parameters in bilayer graphene using infrared spectroscopy *Phys. Rev. B*, vol. 80, p. 165406, Oct 2009.

[4] E. McCann and M. Koshino, The electronic properties of bilayer graphene *Reports on Progress in Physics*, vol. 76, p. 056503, Apr. 2013.

[5] E. McCann and V. I. Fal'ko, Landau-Level Degeneracy and Quantum Hall Effect in a Graphite Bilayer *Phys. Rev. Lett.*, vol. 96, p. 086805, Mar 2006.

[6] The semiclassical quantization of a cyclotron orbit (isoenergy line of the eigenvalues of Eq. (3.1.a)) of energy ε is $S(\varepsilon)\ell_B^2 = \pi(n+1) - \Gamma(\varepsilon)$, where $S(\varepsilon)$ is its area

in $\boldsymbol{k}$-space, $\ell_B = \sqrt{\hbar/|e|B}$ is the magnetic length, $\Gamma(\varepsilon)$ is the Berry phase accumulated along the contour (0 for $\Delta > 0$) and n is the index. For an explanation of this expression, see appendix A of [2].

[7] M. Mucha-Kruczyński, I. L. Aleiner, and V. I. Fal'ko, Strained bilayer graphene: Band structure topology and Landau level spectrum *Phys. Rev. B*, vol. 84, p. 041404(R), Jul 2011.

[8] Y.-W. Son, S.-M. Choi, Y. P. Hong, S. Woo, and S.-H. Jhi, Electronic topological transition in sliding bilayer graphene *Phys. Rev. B*, vol. 84, p. 155410, Oct 2011.

[9] M. Mucha-Kruczyński, I. L. Aleiner, and V. I. Fal'ko, Landau levels in deformed bilayer graphene at low magnetic fields *Solid State Communications*, vol. 151, no. 16, pp. 1088 – 1093, 2011.

[10] L. Wang, S. Zihlmann, A. Baumgartner, J. Overbeck, K. Watanabe, T. Taniguchi, P. Makk, and C. Schönenberger, In Situ Strain Tuning in hBN-Encapsulated Graphene Electronic Devices *Nano Letters*, vol. 19, pp. 4097–4102, Jun 2019.

[11] L. Wang, P. Makk, S. Zihlmann, A. Baumgartner, D. I. Indolese, K. Watanabe, T. Taniguchi, and C. Schönenberger. arXiv:1909.13484, 2019.

[12] I. Lifshitz *et al.*, Anomalies of electron characteristics of a metal in the high pressure region *Sov. Phys. JETP*, vol. 11, no. 5, pp. 1130–1135, 1960.

[13] E. McCann, Asymmetry gap in the electronic band structure of bilayer graphene *Phys. Rev. B*, vol. 74, p. 161403(R), Oct 2006.

[14] M.-C. Chang and Q. Niu, Berry phase, hyperorbits, and the Hofstadter spectrum: Semiclassical dynamics in magnetic Bloch bands *Phys. Rev. B*, vol. 53, pp. 7010–7023, Mar 1996.

[15] D. Xiao, M.-C. Chang, and Q. Niu, Berry phase effects on electronic properties *Rev. Mod. Phys.*, vol. 82, pp. 1959–2007, Jul 2010.

[16] A. Knothe and V. Fal'ko, Influence of minivalleys and Berry curvature on electrostatically induced quantum wires in gapped bilayer graphene *Phys. Rev. B*, vol. 98, p. 155435, Oct 2018.

[17] H. Overweg, A. Knothe, T. Fabian, L. Linhart, P. Rickhaus, L. Wernli, K. Watanabe, T. Taniguchi, D. Sánchez, J. Burgdörfer, F. Libisch, V. I. Fal'ko, K. Ensslin, and T. Ihn, Topologically Nontrivial Valley States in Bilayer Graphene Quantum Point Contacts *Phys. Rev. Lett.*, vol. 121, p. 257702, Dec 2018.

[18] R. Kraft, I. V. Krainov, V. Gall, A. P. Dmitriev, R. Krupke, I. V. Gornyi, and R. Danneau, Valley Subband Splitting in Bilayer Graphene Quantum Point Contacts *Phys. Rev. Lett.*, vol. 121, p. 257703, Dec 2018.

[19] M. Eich, F. Herman, R. Pisoni, H. Overweg, A. Kurzmann, Y. Lee, P. Rickhaus, K. Watanabe, T. Taniguchi, M. Sigrist, T. Ihn, and K. Ensslin, Spin and Valley States in Gate-Defined Bilayer Graphene Quantum Dots *Phys. Rev. X*, vol. 8, p. 031023, Jul 2018.

[20] Y. Lee, A. Knothe, P. Rickhaus, H. Overweg, M. Eich, A. Kurzmann, T. Taniguchi, K. Wantanabe, V. Fal'ko, T. Ihn, and K. Ensslin. arXiv:1911.05968, 2019.

[21] N. Nagaosa, J. Sinova, S. Onoda, A. H. MacDonald, and N. P. Ong, Anomalous Hall effect *Rev. Mod. Phys.*, vol. 82, pp. 1539–1592, May 2010.

[22] S. Slizovskiy, E. McCann, M. Koshino, and V. I. Fal'ko. arXiv:1905.13094, 2019.

[23] J. Son, K.-H. Kim, Y. H. Ahn, H.-W. Lee, and J. Lee, Strain Engineering of the Berry Curvature Dipole and Valley Magnetization in Monolayer MoS_2 *Phys. Rev. Lett.*, vol. 123, p. 036806, Jul 2019.

[24] $\gamma_0 = \langle A|\mathcal{H}|B\rangle = \langle A'|\mathcal{H}|B'\rangle = 3.161\,\mathrm{eV}$, $\gamma_1 = \langle A'|\mathcal{H}|B\rangle = 0.381\,\mathrm{eV}$, $\gamma_3 = \langle A|\mathcal{H}|B'\rangle = 0.38\,\mathrm{eV}$, $\gamma_4 = \langle A|\mathcal{H}|A'\rangle = \langle B|\mathcal{H}|B'\rangle = 0.14\,\mathrm{eV}$ and $\delta\varepsilon = \langle B|\mathcal{H}|B\rangle - \langle A|\mathcal{H}|A\rangle = \langle A'|\mathcal{H}|A'\rangle - \langle B'|\mathcal{H}|B'\rangle = 0.022\,\mathrm{eV}$. Here we use parameters proposed in Ref. [3].

[25] T. Ando, Anomaly of Optical Phonon in Monolayer Graphene *Journal of the Physical Society of Japan*, vol. 75, no. 12, p. 124701, 2006.

[26] A. R. Botello-Méndez, J. C. Obeso-Jureidini, and G. G. Naumis, Toward an Accurate Tight-Binding Model of Graphene's Electronic Properties under Strain *The Journal of Physical Chemistry C*, vol. 122, no. 27, pp. 15753–15760, 2018.

[27] T. M. G. Mohiuddin, A. Lombardo, R. R. Nair, A. Bonetti, G. Savini, R. Jalil, N. Bonini, D. M. Basko, C. Galiotis, N. Marzari, K. S. Novoselov, A. K. Geim, and A. C. Ferrari, Uniaxial strain in graphene by Raman spectroscopy: *G* peak splitting, Grüneisen parameters, and sample orientation *Phys. Rev. B*, vol. 79, p. 205433, May 2009.

[28] F. Ding, H. Ji, Y. Chen, A. Herklotz, K. Dörr, Y. Mei, A. Rastelli, and O. G. Schmidt, Stretchable Graphene: A Close Look at Fundamental Parameters through Biaxial Straining *Nano Letters*, vol. 10, no. 9, pp. 3453–3458, 2010.

[29] B. Verberck, B. Partoens, F. M. Peeters, and B. Trauzettel, Strain-induced band gaps in bilayer graphene *Phys. Rev. B*, vol. 85, p. 125403, Mar 2012.

[30] G. P. Mikitik and Y. V. Sharlai, Electron energy spectrum and the Berry phase in a graphite bilayer *Phys. Rev. B*, vol. 77, p. 113407, Mar 2008.

[31] R. Battilomo, N. Scopigno, and C. Ortix, Berry Curvature Dipole in Strained Graphene: A Fermi Surface Warping Effect *Phys. Rev. Lett.*, vol. 123, p. 196403, Nov 2019.

[32] A. Varlet, D. Bischoff, P. Simonet, K. Watanabe, T. Taniguchi, T. Ihn, K. Ensslin, M. Mucha-Kruczyński, and V. I. Fal'ko, Anomalous Sequence of Quantum Hall Liquids Revealing a Tunable Lifshitz Transition in Bilayer Graphene *Phys. Rev. Lett.*, vol. 113, p. 116602, Sep 2014.

[33] K. S. Novoselov, E. McCann, S. V. Morozov, V. I. Fal'ko, M. I. Katsnelson, U. Zeitler, D. Jiang, F. Schedin, and A. K. Geim, Unconventional quantum Hall effect and Berry's phase of 2p in bilayer graphene *Nature Physics*, vol. 2, no. 3, pp. 177–180, 2006.

[34] The two-band model for strained bilayer is given by $H = \begin{pmatrix} -\frac{1}{2}\Delta & -(\pi^\dagger)^2/2m + w_3 \\ -\pi^2/2m + w_3^* & \frac{1}{2}\Delta \end{pmatrix}$, where $m = \gamma_1/2v_0^2$ and $w_3 = |w_3|e^{i\phi}$. In this case, we find band edges at $\boldsymbol{p} = \pm\sqrt{2m|w_3|}(\xi\cos(\frac{\phi}{2}), -\sin(\frac{\phi}{2}))$ and $\varepsilon = \pm\frac{1}{2}\Delta$. At the band edge, the magnetic moment is given by $\mu^{z,*} = \xi 2e\hbar\frac{|w_3|}{m\Delta}$, leading to the estimation $g_v^* \sim -100\xi\frac{|w_3|}{\Delta}$.

[35] Here we use the basis of LL orbitals $|n\rangle$ $(n = 0, 1, \cdots)$, such that $\pi|n\rangle = -i\sqrt{2n\hbar eB}\,|n-1\rangle$ and $\pi^\dagger|n\rangle = i\sqrt{2(n+1)\hbar eB}\,|n+1\rangle$ in the $\boldsymbol{K}^+$ valley [4]. In the $\boldsymbol{K}^-$ valley, the roles are reversed: $\pi|n\rangle = -i\sqrt{2(n+1)\hbar eB}\,|n+1\rangle$ and $\pi^\dagger|n\rangle = i\sqrt{2n\hbar|e|B}\,|n-1\rangle$. We then expand Eq. (4.2) into a $4N\times 4N$ basis, where each of the sublattices (A, B', A', B) has a total of $(N+1, N, N, N-1)$ LLs considered in the $\boldsymbol{K}^+$ valley ($(N-1, N, N, N+1)$ in the $\boldsymbol{K}^-$ valley). In Fig. 3.3 and Fig. 3.4, we used $N = 500$.

[36] D. Horsell, F. Tikhonenko, R. Gorbachev, and A. Savchenko, Weak localization in monolayer and bilayer graphene *Philosophical Transactions of the Royal Society A: Mathematical, Physical and Engineering Sciences*, vol. 366, no. 1863, pp. 245–250, 2008.

[37] Private communication with F. Koppens.

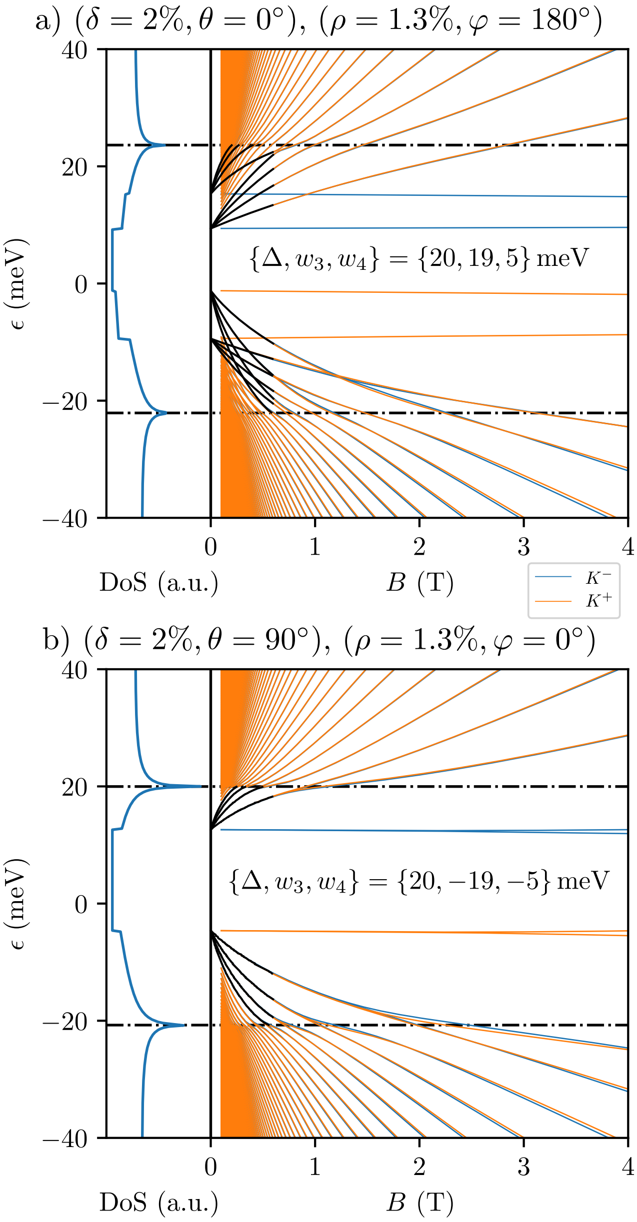

Figure 3.3: The zero magnetic field density of states (DoS) and numerically calculated Landau levels of bilayer graphene for $B > 0.1\,\mathrm{T}$ in the $\boldsymbol{K}^+$ (orange) and $\boldsymbol{K}^-$ (blue) valleys of bilayer graphene with an interlayer asymmetry $\Delta = 20\,\mathrm{meV}$ and a) 2% uniaxial zigzag strain and b) 2% uniaxial armchair strain (or related shear with parameters set by the relation in Eq. (3.2)). The van Hove singularities are highlighted as black dot-dashed lines. A semiclassical approximation [6] for Landau levels near the band edges in Fig. 3.2b) and c) (black lines) is used to extrapolate to $B = 0$. Note that the two-fold degeneracy of LLs at lower energies in b) is unique to the armchair direction of strain for which the spectrum in Fig. 3.2c) features two degenerate minivalleys. This is lifted in the vicinity of the van Hove singularities. For an arbitrary orientation of the strain axes, the minivalleys are not degenerate even at $B = 0$.

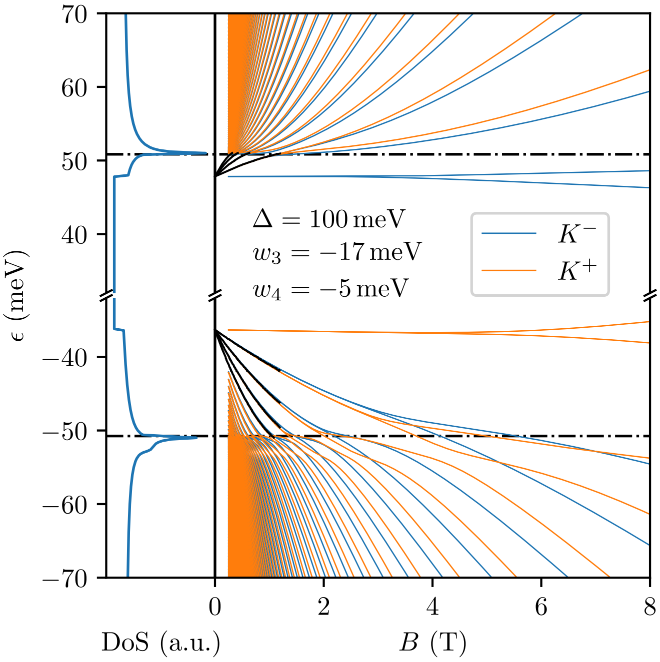

Figure 3.4: The density of states and numerically calculated Landau levels in both valleys for $B > 0.25\,\mathrm{T}$ of bilayer graphene with an interlayer asymmetry $\Delta = 100\,\mathrm{meV}$ and 2% uniaxial armchair strain, with equivalent shear given by Eq. (3.2). The line convention is shared with Fig. 3.3. Similarly to Fig. 3.3b), Landau levels with energies below the saddle point are 2-fold degenerate in each valley.

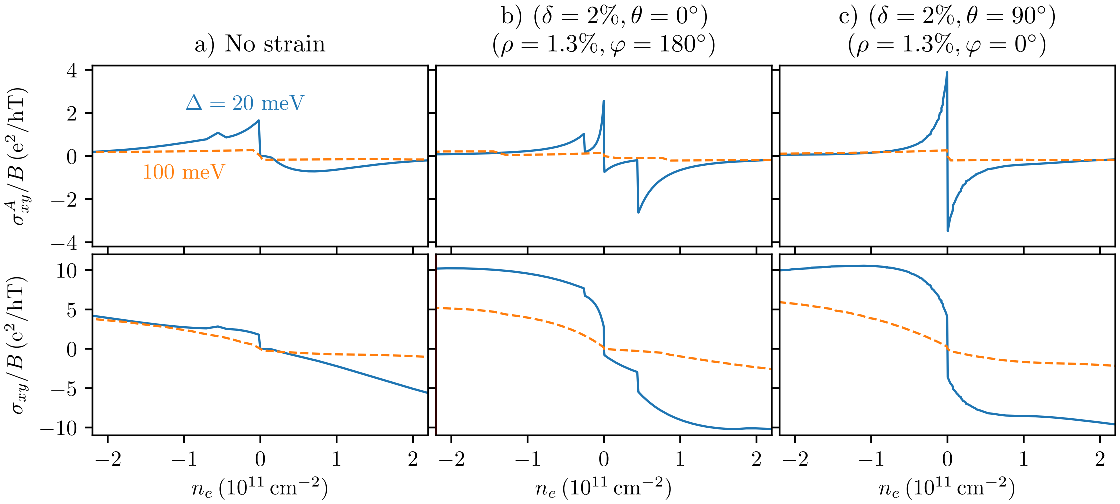

Figure 3.5: *Top to bottom.* The anomalous Hall conductivity σ^A_{xy} and total Hall conductivity σ_{xy} of bilayer graphene for a small interlayer asymmetry $\Delta = 20\,\mathrm{meV}$ (blue) and a large asymmetry 100 meV (orange) against carrier density n_e. *Left to right.* No strain, 2% uniaxial zigzag strain and 2% uniaxial armchair strain.

Chapter 4

Kagomé network of miniband-edge states in double-aligned graphene-hexagonal boron nitride structures

Preface

The contents of this chapter represent the main body of a manuscript previously published in Physical Review B [1]. The accompanying supplemental material is presented in the appendices. The manuscript was authored by Christian Moulsdale[1,2], Angelika Knothe[2] and Vladimir Fal'ko[1,2,3].

Christian Moulsdale performed all the analytical and numerical calculations and produced the figures for the manuscript, under the guidance and supervision of Angelika Knothe and Vladimir Fal'ko. The writing of the manuscript was primarily done by Christian Moulsdale, with assistance from Angelika Knothe and Vladimir Fal'ko.

---

[1] School of Physics and Astronomy, University of Manchester, Manchester M13 9PL, UK

[2] National Graphene Institute, University of Manchester, Manchester M13 9PL, UK

[3] Henry Royce Institute, Institute for Advanced Materials, Manchester M13 9PL, UK

Abstract

Twistronic heterostructures have recently emerged as a new class of quantum electronic materials with properties determined by the twist angle between the adjacent two-dimensional materials. Here we study moiré superlattice minibands in graphene (G) encapsulated in hexagonal boron nitride (hBN) with an almost perfect alignment with both the top and bottom hBN crystals. We show that, for such an orientation of the unit cells of the hBN layers that locally breaks inversion symmetry of the graphene lattice, the hBN/G/hBN structure features a Kagomé network of topologically protected chiral states with energies near the miniband edge, propagating along the lines separating the areas with different miniband Chern numbers.

Recently, graphene-based systems have been shown to host various "weak topological" effects [2] among their electronic properties [3, 4, 5, 6, 7, 8, 9, 10, 11, 12, 13, 14, 15, 16, 17, 18, 19, 20, 21, 22], which stem from the Berry phase/curvature in the electronic band structure of mononolayer graphene [23, 24] or its Bernal bilayers [25, 4, 26, 27, 12, 17, 19, 28, 22, 29]. The topological effects manifest themselves in chiral states forming at the edges of the system or around internal structural defects, and propagating in opposite directions in the two valleys of graphene. These chiral states have been studied in detail in gapped bilayer graphene with either AB/BA domain boundaries [30, 8, 9], or an electrostatically inverted interlayer asymmetry gap [31, 10].

Weak topological states have also emerged in the context of twistronic graphene systems [7, 32, 33, 34, 32, 35, 33, 14, 16] and in heterostructures of graphene (G) and hexagonal boron (hBN). The electronic properties of the latter system are qualitatively modified by the moiré superlattice [36, 37, 38, 39] (mSL) with a period $\lambda \approx a/\sqrt{\delta^2+\theta^2}$ (reaching 14 nm for small misalignment angles $\theta \to 0$, determined by the G-hBN lattice mismatch, $\delta \approx 0.018$). The system features a well-defined first miniband edge on the valence side of the graphene layer's dispersion [37, 38], as illustrated in Fig. 4.1.

The encapsulation of graphene between two hBN crystals with a high-precision alignment [40] leads to a further refinement of the superlattice effects, caused by the interference of Dirac electrons Bragg-scattered off the moiré superlattice (mSL) determined by the top and bottom G/hBN interfaces. Here, we study the influence of the

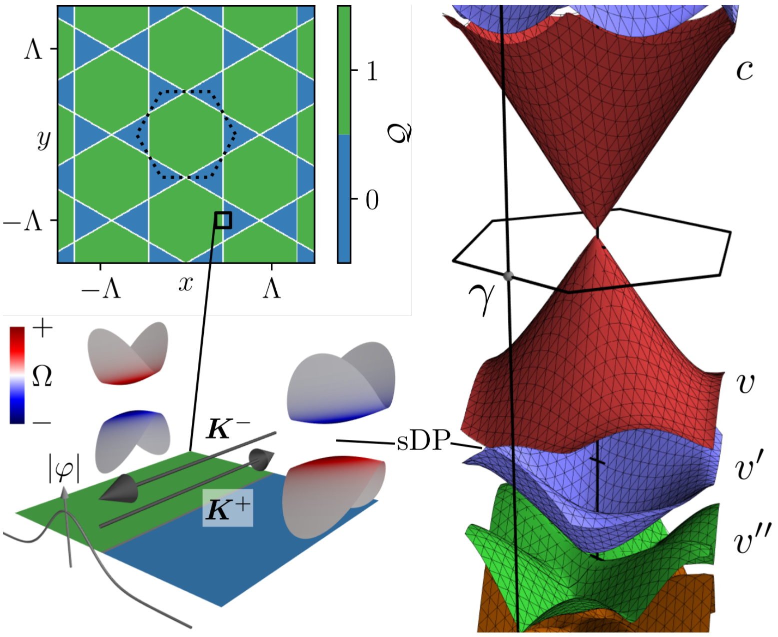

Figure 4.1: A typical miniband spectrum of graphene encapsulated into mutually aligned hBN crytals. *Top inset.* Map of locally-defined v-miniband Chern number, Q. *Bottom inset.* Dispersion and Berry curvature at the v/v' miniband edge in the gaped regions and chiral 1D modes counter-propagating in $K^{\pm}$ valleys along a Kagomé network of locally gapless v/v' miniband edges.

relative lateral offset $\boldsymbol{\tau}$ between the top and bottom hBN crystals on moiré minibands in double-aligned hBN/G/hBN structures, considering the orientation (parallel versus antiparallel) of the unit cells in the hBN lattices. For graphene's minibands, the unit cell orientation matters due to the lack of inversion symmetry in the hBN monolayer, which is maximally passed onto graphene encapsulated between two hBN layers with parallel unit cell orientations but mutually cancels in the antiparallel case.

The inversion asymmetry, induced by hBN in graphene, leads to minigaps at the moiré miniband edges [37] (in particular, at the bottom edge of the first miniband on the valence band side, v, corresponding to graphene doping of 4 holes per moiré supercell), of graphene's dispersion in Fig. 4.1, whose size, together with the Chern numbers of the minibands [41, 42], depends on the lateral offset between the top and bottom hBN crystals. For hBN/G/hBN structures with a small misalignment angle, $\tilde{\theta} \ll \delta$, between the top and bottom hBN layers, this offset varies across the coordinate space, as

$$\boldsymbol{\tau}(\boldsymbol{r}) = \tilde{\theta}\boldsymbol{e}_z \times \boldsymbol{r}, \tag{4.1}$$

which leads to a long-period, $\Lambda \approx a/|\tilde{\theta}|$, variation of the mSL properties (see Fig. 4.2). A peculiar feature of this modulation is the closing and reopening of a minigap at the v/v' miniband edge, which occurs along the lines forming a Kagomé structure in the real space, sketched in Fig. 4.1. Below, we study electron states at the v/v' miniband edge, confined to this Kagomé network and discuss how chiral one-dimensional states (propagating in opposite directions in the $\boldsymbol{K}^{\pm}$ valleys) provide this system with a finite conductivity even when its Fermi level would be set between the v and v' miniband edges in the gapped areas of the structure, with a characteristic pattern of Aharanov-Bohm oscillations.

The above statement is based on the analysis of local miniband characteristics of the trilayer structure depicted in Fig. 4.2. Here, the bottom/top hBN monolayers with parallel orientation of their non-symmetric unit cells are twisted with respect to graphene by $\theta \pm \frac{1}{2}\tilde{\theta}$, respectively, with small mutual misalignment $|\tilde{\theta}| \ll \delta$, which determines the spatial variation of their local offset in Eq. 4.1. For each fixed offset $\boldsymbol{\tau}$, the Hamiltonian [43, 37, 44, 45] of electrons in the $\boldsymbol{K}^{\xi}$ valley ($\xi = \pm$) of graphene is

$$\begin{aligned}
&\hat{H} = -i\hbar v\boldsymbol{\sigma}\cdot\nabla + 2\sum_{\mathcal{P}=\pm}\sum_{m=0}^{5}\mathfrak{C}_m e^{i\boldsymbol{G}_m\cdot\boldsymbol{r}}U_{\mathcal{P},m} + \frac{1}{2}\Delta_{cv}\sigma_z,\\
&U_{\mathcal{P},m} = u_0^{\mathcal{P}}\mathcal{P}^{m+\frac{1}{2}} + (-\mathcal{P})^{m+\frac{1}{2}}(u_3^{\mathcal{P}}\sigma_z - i\xi u_1^{\mathcal{P}}\boldsymbol{e}_m\cdot\boldsymbol{\sigma})\\
&\boldsymbol{\sigma} = (\xi\sigma_x, \sigma_y), \quad \Delta_{cv} \approx \frac{2}{3}\sum_{m=0}^{5}(\mathfrak{C}_m^2\Delta_u - \mathfrak{S}_m^2\Delta_h),\\
&\mathfrak{C}_m = \cos(\tfrac{1}{2}\boldsymbol{g}_m\cdot\boldsymbol{\tau}), \quad \mathfrak{S}_m = \sin(\tfrac{1}{2}\boldsymbol{g}_m\cdot\boldsymbol{\tau}).
\end{aligned} \tag{4.2}$$

The values of the parameters used are given in Table S1 in the Supplemental Material (SM), and the expression for graphene encapsulated between hBN monolayers with antiparallel orientation of their unit cells is given in SM S2.

The first term in Eq. (4.2) is the Dirac Hamiltonian for electrons in monolayer graphene [43]. The second term describes the mSL produced by the layers, with the reciprocal mSL vectors, $\boldsymbol{G}_m \approx \delta\boldsymbol{g}_m - \theta\boldsymbol{e}_z \times \boldsymbol{g}_m$, expressed in terms of the reciprocal

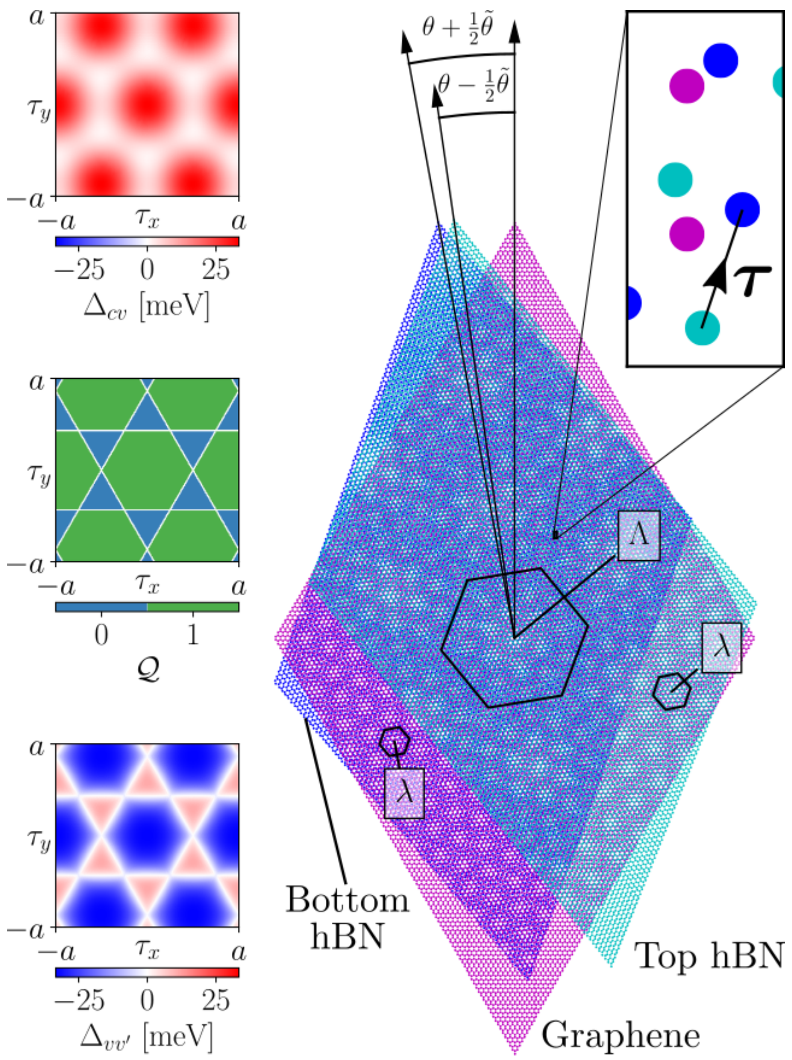

Figure 4.2: *Right.* Graphene encapsulated between bottom and top hBN layers with twists $\theta \pm \frac{1}{2}\tilde{\theta}$, respectively ($|\tilde{\theta}| \ll \delta$). The interference of the layers results in a mSL of period λ, featuring a long-period variation of period Λ, whose unit cells are shown. *Inset.* The offset vector $\boldsymbol{\tau}$ between the unit cells of the top and bottom hBN layers has components (τ_x, τ_y) along the zigzag and armchair axes, respectively. *Inset.* The valley Chern number $\mathcal{Q}$ of miniband v, the gap Δ_{cv} and the minigap $\Delta_{vv'}$ against offset for aligned hBN layers ($\tilde{\theta} = 0$).

lattice vectors of graphene, $\boldsymbol{g}_m = \frac{4\pi}{\sqrt{3}a}\boldsymbol{e}_z \times \boldsymbol{e}_m, \quad \boldsymbol{e}_m = (\cos\frac{m\pi}{3}, \sin\frac{m\pi}{3})$, $m = 0, 1, ..., 5$. This term includes mSL potentials, sublattice asymmetry gaps and gauge fields of parity $\mathcal{P} = \pm$ (under spatial inversion), quantified using the parameters $u_0^{\mathcal{P}}$, $u_3^{\mathcal{P}}$ and $u_1^{\mathcal{P}}$, respectively.

The orientation and offset $\boldsymbol{\tau}$ of the unit cells in each hBN layer determine the magnitude of the odd-parity terms in Eq. (4.2), which are responsible for the inversion symmetry breaking features in the dispersion, such as the opening of a minigap between minibands v and v'. This corresponds to graphene doping of 4 holes per moiré supercell, with electron density $-4n_0$ ($n_0 = 2/\sqrt{3}\lambda^2$). In the parametrisation of Hamiltonian (4.2), we take into account that the positions of the graphene atoms rearrange to minimise graphene's adhesion energy with the hBN layers while maintaining the mSL period [46, 47, 48, 45]. The in-plane and out-of-plane rearrangements combine with the second term to give the respective contributions, Δ_u and Δ_h, to the sublattice asymmetry gap Δ_{cv}. This gap appears in the odd parity, non-oscillatory third term, which breaks the sublattice symmetry of graphene. In antiparallel alignment, the contributions to the odd parity terms from each layer cancel, and inversion symmetry is preserved. Instead, we focus on parallel alignment where the inversion symmetry breaking is enhanced, depending strongly on the offset $\boldsymbol{\tau}$.

To study minibands of Dirac electrons in this system, we diagonalise Hamiltonian (4.2) using the basis of plane-wave Dirac states, folded onto the mSL Brillouin zone shown in Fig. 4.1. An example of a typical miniband dispersion is shown in Fig. 4.1, with other examples displayed in SM S3. Similarly to single-interface G/hBN heterostructures [37, 36, 49, 50, 51, 52, 38], this system features a well-defined first valence miniband, v for twists $|\theta| \leq 1^\circ$, whereas on the conduction band side the minibands strongly overlap on the energy axis. The inversion symmetry breaking produces a minigap, $\Delta_{vv'}$, at the edge between minibands v and v', whose magnitude, together with the v/v' edge position in the Brillouin minizone, depends on the offset $\boldsymbol{\tau}$. The dependence of the minigap $\Delta_{vv'}$ on the offset $\boldsymbol{\tau}$ is shown in the bottom inset of Fig. 4.2. This panel shows that $\Delta_{vv'}$ (which is formally defined below) takes zero value and also changes sign on the lines which approximately correspond to the condition $\mathfrak{C}_m = 0$. This variation should be contrasted with the $\boldsymbol{\tau}$-dependence of the gap Δ_{cv} across the main Dirac point at the c/v miniband edge shown on the top inset, where one can see that Δ_{cv} never changes sign.

Along the lines on the $\boldsymbol{\tau}$ maps, where the minigap at the v/v' miniband edge closes and reopens as a function of $\boldsymbol{\tau}$, the Chern number $\xi\mathcal{Q}$ [41, 42] of miniband v also changes (note that the miniband's Chern number has opposite sign in the $\boldsymbol{K}^{\xi}$ valleys,

$\xi = \pm$). Here, Q is found by computing the integral of the miniband's Berry curvature over the mSL Brillouin minizone (see SM S4 for details). The resulting map of $Q(\boldsymbol{\tau})$ dependence is displayed as the middle inset in Fig. 4.2. The correlation between the behavior of the inversion-asymmetry gap $\Delta_{\nu\nu'}$ at its edge with miniband ν' and of its Chern number suggests a simultaneous change of quantum topological properties of states in both ν and ν', captured by the effective Hamiltonian [53] applicable to the part of the Brillouin minizone in the vicinity of this edge,

$$\begin{aligned} H_{\boldsymbol{q}}^{\nu\nu'} =& \varepsilon_{\nu\nu'} + \tfrac{1}{2}\Delta_{\nu\nu'}\sigma_z \\ &+ \hbar(\xi v_s^x q_x \sigma_x + v_s^y q_y \sigma_y) + \xi\hbar \boldsymbol{v}_a \cdot \boldsymbol{q}, \end{aligned} \tag{4.3}$$

whose basis is minibands ν and ν'. Here, $\boldsymbol{q}$ is the wave vector relative to the position of the band edge, $\boldsymbol{v}_s$ and $\boldsymbol{v}_a$ are the symmetric and antisymmetric velocity, respectively, (the latter of which tilts the dispersion along the axis parallel to $\boldsymbol{v}_a$ [53]) and $\varepsilon_{\nu\nu'}$ is a constant energy shift. The parameters in Eq. (4.3) are fitted numerically to the minibands computed using Eq. (4.2) SM S5. The sign of $\Delta_{\nu\nu'}$ is determined by the sign of the Berry curvature at the miniband edge, which changes simultaneously with the change of the Chern number.

The variation of the offset $\boldsymbol{\tau}$ over the plane of a hBN/G/hBN structure, given by Eq. (4.1), enables us to map the the computed dependence of miniband characteristics displayed on the insets in Fig. 4.2 onto the real space: for this, we only need to rotate those plots by 90° and rescale then by a factor $1/\tilde{\theta}$. This produces a Kagomé network of lines where the secondary minigap, $\Delta_{\nu\nu'}$, closes and then inverts its sign, and where the Chern number of miniband ν changes (from 0 to 1). We show in SM S6 that the shape of this network is independent of the model parameters. Topologically protected chiral channels form along these lines, supporting spin-degenerate, one-dimensional states which propagate in opposite directions in the time-reversed valleys.

The form and dispersion of these states can be found (in SM S7) by analyzing Hamiltonian (4.3) with $\boldsymbol{q} \approx (q_\parallel, -i\partial_{x_\perp})$ and $\Delta_{\nu\nu'} \approx x_\perp \partial_{x_\perp}\Delta_{\nu\nu'}|_{x_\perp=0}$ ($\partial_{x_\perp}\Delta_{\nu\nu'}|_{x_\perp=0} \sim |u_3^-|/\Lambda > 0$) where $x_\parallel$ and $x_\perp$ are local coordinates along and perpendicular to the Kagomé network line. These states have a Jackiw-Rebbi [54] form $\varphi_{q_\parallel} \approx e^{iq_\parallel x_\parallel} e^{-x_\perp^2/2\aleph^2} \zeta_{q_\parallel}$ ($\zeta_{q_\parallel}$ is a two-component vector), with Gaussian confinement within a length $\aleph \sim \sqrt{2\hbar v_s^x \Lambda/|u_3^-|}$

perpendicular to the interface, and disperse linearly, $\varepsilon(q_\parallel) = \xi\hbar\mathcal{V}q_\parallel$, with a 1D velocity $\mathcal{V} \sim v_s^x$. To consider these states independently for each segment of the Kagomé network, we should require $\lambda < \aleph \ll \Lambda$, which is satisfied for mismatches $|\tilde{\theta}| < 0.1°$.

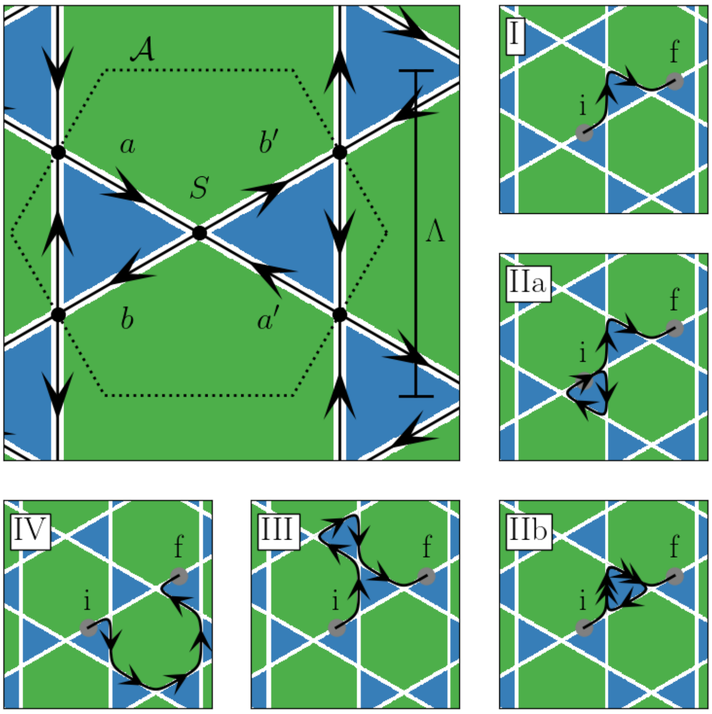

Figure 4.3: *Top left.* The hexagonal structural element of the Kagomé network of chiral channels of area $\mathcal{A} = \sqrt{3}\Lambda^2/2$ and containing one $\mathcal{Q} = 0$ bowtie and one $\mathcal{Q} = 1$ hexagon. The chiral propagation of electrons in the $\boldsymbol{K}_+$ valley is shown, scattering at the three nodes. *Clockwise from top right.* The five shortest paths for an electron wave packet to propagate from an injection position “i” to “f” (double arrows indicate a channel is traversed twice).

For a gapped moiré miniband spectrum, one could expect insulating behavior of a perfectly aligned hBN/G/hBN doped to the v/v' miniband edge. For slightly ($|\tilde{\theta}| \ll \delta$) misaligned hBN crystals, the long-range variation of the local hBN-hBN offset and a network of chiral states, which it generates inside the minigap $\Delta_{vv'}$, quenches the resistivity of the hBN/G/hBN structure. While the exact calculations of the limiting resistivity would require a more rigorous consideration, based on the previous experiences of two-dimensional models for the network of 1D states [32, 33, 55], we expect its value to correspond to a conductivity $\sigma_{xx} \sim e^2/h$ and to exhibit Aharonov-Bohm oscillations as a function of an out-of-plane magnetic field B. To describe the latter, we consider coherent electron waves (separately in the $\boldsymbol{K}_\pm$ valleys) on a network sketched in Fig. 4.3, where the structural element includes three nodes connected by chiral channels. At each node, an incoming wave packet scatters left or right according to the scattering matrix

$$\begin{pmatrix} b \\ b' \end{pmatrix} = S \begin{pmatrix} a \\ a' \end{pmatrix}, \quad S = e^{i\eta/3} \begin{pmatrix} \sqrt{P_R} & i\sqrt{P_L} \\ i\sqrt{P_L} & \sqrt{P_R} \end{pmatrix} \tag{4.4}$$

whose factor of i takes into account the Maslov's phase, and whose scattering probabilities, P_R and P_L ($P_R + P_L = 1$), can be considered as energy-independent within the narrow energy window of $\Delta_{\nu\nu'}$ (see SM S8 for details).

As a monochromatic wave of energy ε propagates across the network, its amplitude evolves according to the scattering matrix at the nodes and acquiring phase factors, $e^{i\varepsilon\Lambda/2\mathcal{V}}$, after passing each ballistic segment of the network. At longer distances, partial waves, e.g., split from an incoming wave at "i" (see the side panels in Fig. 4.3), rejoin and interfere in another ballistic segment "f". An important feature of a periodic and C_3 rotationally symmetric network, such as in Figs. 4.1 and 4.3, is that the effect of the interference, constructive or destructive, of chiral edge states that travel from "i" to "f" along paths containing the same number, N, of segments does not depend on the exact energy (or wavelength) of the electron. This is because their ballistic phases, $e^{iN\varepsilon\Lambda/2\mathcal{V}}$, are the same, producing the interference contribution determined only by their shapes through the energy-independent scattering amplitudes in Eq. (4.4). On the contrary, the interference of waves brought together by paths with a different number of segments, such as I and IV in Fig. 4.3), oscillates from constructive to destructive (and back) upon energy variation at the scale of $\hbar\mathcal{V}/\Lambda$.

Therefore, in the high-temperature regime, where $k_BT \gg \hbar\mathcal{V}/\Lambda$, the interference effects between waves arriving from "i" to "f" along paths of different lengths would be wiped out by the smearing of the Fermi step for electrons. The interference between waves brought from "i" to "f" by same-length paths (such as IIa, IIb, III and IV in Fig. 4.3) would survive thermal averaging, without suppression, though this contribution would be sensitive to the external magnetic field, due to the Aharonov-Bohm phases from magnetic field fluxes encircled by the pairs of same-length paths.

When discussing the interference effects in electronic transport at high temperatures, we are also conscious of the inelastic decoherence of electron waves, which efficiently destroys interference effects for the longer paths. For a system with decoherence length ℓ, this can be accounted by a suppression factor $e^{-\Lambda/4\ell}$ applied to each ballistic segment of the Kagomé network. Therefore, to discuss the high-temperature limit, we consider the shortest paths that can contribute to the interference effect in transport, shown in the side panels of Fig. 4.3. These paths are related to the 'forward' electron propagation from a segment in one network unit cell to the equivalent segment in the next one, counted in the direction of the propagation of the chiral edge state (for valley K). These shortest paths contain three (I) and six (IIa, IIb, III, IV) ballistic segments of length $\Lambda/2$, and the interfering amplitude at the point "f" for a wave starting at "i" with unit amplitude would be

$$\begin{aligned}\psi \approx & -e^{i\pi\phi/4\phi_0}\sqrt{P_L^2 P_R z^3} + z^6 e^{i\pi\phi/2\phi_0} \times \\ & (-2P_L P_R^2 + P_L^2 P_R + e^{-i2\pi\phi/\phi_0} P_L^2 P_R),\end{aligned}$$

where $z = e^{i\eta/3} e^{i\varepsilon\Lambda/2\hbar\mathcal{V}} e^{-\Lambda/4\ell}$. We also account for additional phases, induced by the out-of-plane magnetic field and described in terms of magnetic field flux, $\phi = B\mathcal{A}$ through the unit cell area, $\mathcal{A} = \sqrt{3}\lambda^2/2$, of the Kagomé network ($\phi_0 = h/e$ is the flux quantum).

Then, we express the probability $\langle \mathcal{W} \rangle_T$ for the electron to get from the segment "i" to "f", averaged over the $k_B T$ energy interval near the Fermi level, as

$$\begin{aligned}\langle \mathcal{W} \rangle_T \approx & P_L^2 P_R |z|^6 + [4P_L^2 P_R^4 + 2P_L^4 P_R^2]|z|^{12} \\ & + 2[P_L^4 P_R^2 - 2P_L^3 P_R^3]|z|^{12} \cos\left(\frac{2\pi\phi}{\phi_0}\right),\end{aligned} \tag{4.5}$$

whose second line originates from the encircled Aharonov-Bohm phases, which, for the pairs of shortest paths, are all determined by the magnetic field flux through the unit cell area of the Kagomé network. As the probability, described by Eq. (4.5), is a characteristic of the forward propagation of electrons, its oscillations also determine the Aharonov-Bohm oscillations in the network conductivity (see SM S9 for backwards propagation),

$$\sigma_{xx}(\phi) \approx \frac{e^2}{h}\left[\alpha + \beta e^{-5\Lambda/2\ell}\cos\left(\frac{2\pi\phi}{\phi_0}\right)\right], \tag{4.6}$$

where $\alpha, \beta \sim 1$.

Overall, we have demonstrated the existence of a Kagomé network of chiral states lying in the minigap at the edge of the first moiré miniband on the valence band side of graphene encapsulated between hBN with parallel unit cells. This edge state network gives rise to quenched resistivity, $\sim h/e^2$, of graphene even when its Fermi level doping reaches that minigap. This conductivity, in Eq. (4.6), exhibits Aharonov-Bohm oscillations, whose period is determined by the area of the unit cell of the Kagomé network and, consequently, the misalignment. For the networks with a longer decay length ℓ (or a shorter period), the magnitude of the Aharonov-Bohm oscillations should increase, accompanied by the emergence of a finer structure, composed of higher frequency harmonics corresponding to rational factor between the magnetic field flux through the Kagomé network cell and flux quantum, ϕ_0. Such edge state networks emphasize the role of twistronic heterostructures as hosts of topological phenomena and deserve further theoretical studies, e.g., taking into account electron-electron interactions in the chiral channels [56].

4.A Parameters used in hBN/G/hBN Hamiltonian in Eq. (2)

The table of parameters used in Eq. (2) of the main text is shown in Tab. 4.1. An alternative parameterisation of the superlattice interaction is found in [37]. The alternative superlattice potentials $u_{0,1,2,3}$ and $\tilde{u}_{0,1,2,3}$ are related to the potentials $u^{\pm}_{0,1,3}$ in this paper by

$$\begin{aligned}
u_0 &= u_0^+, \quad u_1 = \frac{\delta}{\sqrt{\delta^2+\theta^2}}u_1^+, \quad u_2 = \frac{-\theta}{\sqrt{\delta^2+\theta^2}}u_1^+, \quad u_3 = u_3^+, \\
\tilde{u}_0 &= u_0^-, \quad \tilde{u}_1 = \frac{\delta}{\sqrt{\delta^2+\theta^2}}u_1^-, \quad \tilde{u}_2 = \frac{-\theta}{\sqrt{\delta^2+\theta^2}}u_1^-, \quad \tilde{u}_3 = u_3^-.
\end{aligned} \tag{4.7}$$

Parameter	Value	Reference
a	$0.246\,\mathrm{nm}$	[57]
v	$10^6\,\mathrm{m/s}$	[57]
δ	0.018	[37]
$u_0^\pm$	$\pm V_\pm/2$	[37]
$u_1^\pm$	$-V_\pm$	[37]
$u_3^\pm$	$-\sqrt{3}V_\pm/2$	[37]
V_+	$17\,\mathrm{meV}$	[38]
V_-	$3\,\mathrm{meV}$	[38]
Δ_u	$8\,\mathrm{meV}$	[45]
Δ_h	$2\,\mathrm{meV}$	[45]

Table 4.1: Table of parameters used in Eq. (2) of the main text.

4.B Hamiltonian for antiparallel orientation of the hBN unit cells

The Hamiltonian of graphene encapsulated between two aligned layers of hBN depends on the alignment of the unit cells in the hBN layers. The Hamiltonian for parallel unit cells is given in Eq. (2) of the main text, featuring odd parity terms that break inversion symmetry. The Hamiltonian for antiparallel unit cells is,

$$
\begin{aligned}
&\hat{H} = -i\hbar v\boldsymbol{\sigma}\cdot\nabla + 2\textstyle\sum_{m=0}^{5} e^{i\boldsymbol{G}_m\cdot\boldsymbol{r}}\times\\
&\qquad\quad \{[\mathfrak{C}_m u_0^+ - (-1)^m\mathfrak{S}_m u_0^-] + i[(-1)^m\mathfrak{C}_m u_1^+ + \mathfrak{S}_m u_1^-]\sigma_z +\\
&\qquad\qquad \xi[(-1)^m\mathfrak{C}_m u_3^+ + \mathfrak{S}_m u_3^-]\boldsymbol{e}_m\cdot\boldsymbol{\sigma})\},\\
&\boldsymbol{\sigma} = (\xi\sigma_x,\sigma_y),\quad \mathfrak{C}_m = \cos(\boldsymbol{g}_m\cdot\boldsymbol{\tau}/2),\quad \mathfrak{S}_m = \sin(\boldsymbol{g}_m\cdot\boldsymbol{\tau}/2)\\
&\boldsymbol{G}_m \approx \delta\boldsymbol{g}_m - \theta\boldsymbol{e}_z\times\boldsymbol{g}_m,\quad \boldsymbol{g}_m = \tfrac{4\pi}{\sqrt{3}a}\boldsymbol{e}_z\times\boldsymbol{e}_m,\quad \boldsymbol{e}_m = (\cos\tfrac{m\pi}{3},\sin\tfrac{m\pi}{3}),\quad m = 0,1,...,5,
\end{aligned}
\tag{4.8}
$$

where $\boldsymbol{\tau}$ is the lateral offset between the unit cell centres in each hBN layer. Note that the odd parity superlattice potentials $u_{0,1,3}^-$ result in a contribution to the Hamiltonian which has even parity under inversion and inversion symmetry is preserved in this system.

4.C Examples of calculated miniband structures

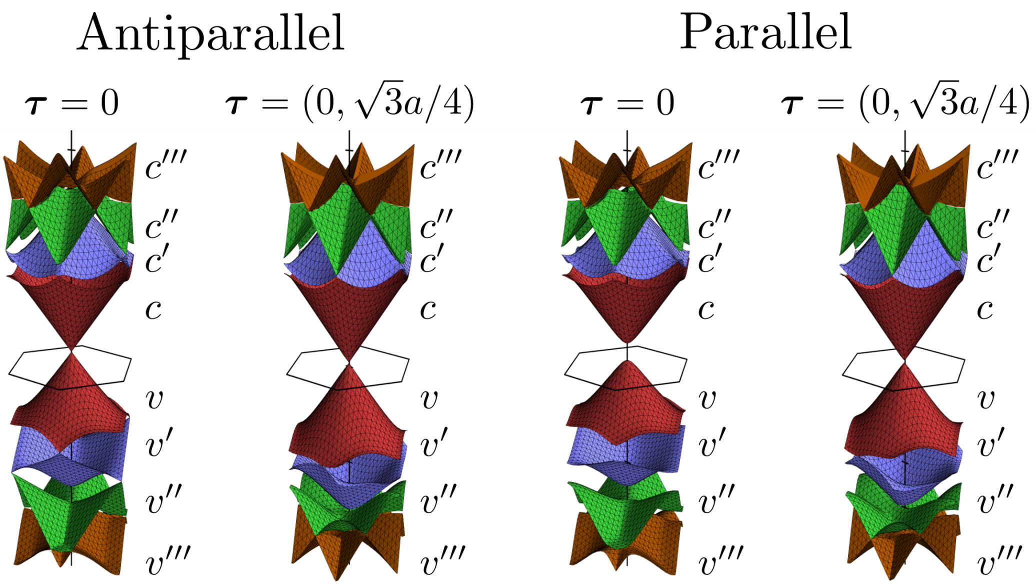

Figure 4.4: Miniband dispersions for parallel and antiparallel alignment of the unit cells in the hBN layers with various lateral offsets $\boldsymbol{\tau}$ between the hBN layers.

The first term of the Hamiltonians in Eq. (2) of the main text and (4.8) is the Dirac Hamiltonian of electrons in graphene. This has plane wave solutions $\psi_{\boldsymbol{k}}^{c_0/v_0}(\boldsymbol{r}) = \frac{1}{\sqrt{2}}(1, \pm e^{i\xi \arctan(k_y/k_x)})$, corresponding to the conduction (c_0) and valence (v_0) bands of energy $\pm\hbar v|\boldsymbol{k}|$, respectively. We diagonalise the full Hamiltonians using the zone-folded wavefunction $\Psi_{\boldsymbol{k}}(\boldsymbol{r}) = \sum_{\alpha=c_0,v_0}\sum_{\boldsymbol{G}} c^{\alpha}_{\boldsymbol{k}+\boldsymbol{G}}\psi^{\alpha}_{\boldsymbol{k}+\boldsymbol{G}}(\boldsymbol{r})$ of wave vector $\boldsymbol{k}$ in the moiré superlattice (mSL) Brillouin minizone (sBZ). In the space spanned by the coefficients $\{c^{\alpha}_{\boldsymbol{k}+\boldsymbol{G}}\}$, the Hamiltonian is represented by a $2M \times 2M$ matrix $\mathcal{H}_{\boldsymbol{k}}$. Terms in Eq. (2) of the main text and (4.8) containing $e^{i\boldsymbol{G}_m\cdot\boldsymbol{r}}$ give off-diagonal elements in $\mathcal{H}_{\boldsymbol{k}}$ between coefficients with momenta separated by $\boldsymbol{G}_m$. We sum over the shortest M reciprocal mSL vectors $\boldsymbol{G}$ required for the lowest four energy eigenvalues of $\mathcal{H}_{\boldsymbol{k}}$ to converge. In this case, convergence is reached with the $M = 19$ vectors which are the sum of at most two of the six shortest non-zero reciprocal mSL vectors $\boldsymbol{G}_m$ $(m = 0, 1, ..., 5)$.

The conduction and valence band reconstruct into $2M$ minibands of energy $\varepsilon_{n\boldsymbol{k}}$ and wavefunction $\chi_{n\boldsymbol{k}}$ in the coefficient basis. We show the dispersion of the first four valence (v, v', v'', v''') and conduction (c, c', c'', c''') minibands for zero offset $(\boldsymbol{\tau} = 0)$ in

Fig. 4.4. The minibands are similar for each alignment, except antiparallel alignment of the hBN unit cells, which preserves inversion symmetry, gives a gapless spectrum and parallel alignment, which breaks inversion symmetry, gives a gapful spectrum. We also show the dispersions for an offset $\boldsymbol{\tau} = (0, \sqrt{3}a/4)$ satisfying $\mathfrak{C}_0 = 0$. In this case, despite the inversion symmetry breaking, there are band closures in the dispersion for parallel alignment, including the secondary minigap on the valence side between minibands v and v' (as discussed in the main text).

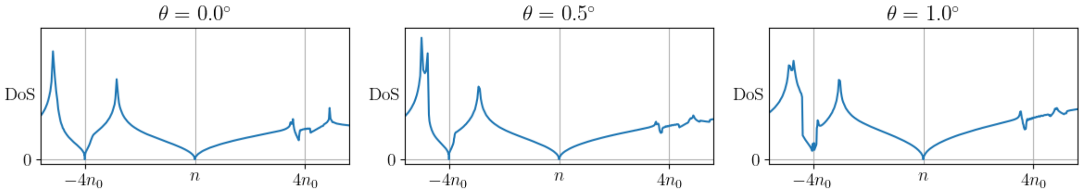

Figure 4.5: The density of states against electron density n for various twists with offset $\boldsymbol{\tau} = (0, \sqrt{3}a/4)$.

We show the density of states for parallel hBN unit cells against the electron density n (including the four-fold spin and valley degeneracy) for the offset $\boldsymbol{\tau} = (0, \sqrt{3}a/4)$ which closes the secondary minigap in Fig. 4.5. A filled miniband contributes a value $n_0 = 2/(\sqrt{3}\lambda^2)$ to the electron density, so the edge between the minibands v and v' corresponds to electron density $n = -4n_0$. For small twists, $|\theta| < 1°$, the density of states is zero at $n = -4n_0$, and there is no overlap between these bands on the energy axis. There is overlap on the conduction side between minibands c and c' since the density of states is non-zero at $n = 4n_0$. For larger twists, $|\theta| \geq 1°$, minibands v and v' overlap with non-zero density of states at $n = -4n_0$.

4.D Topological characteristics of the minibands

When inversion symmetry is broken, the topology of miniband n is represented by its valley Chern number ξQ_n [58, 59, 60, 41, 5, 61, 42], which is given by the integral of

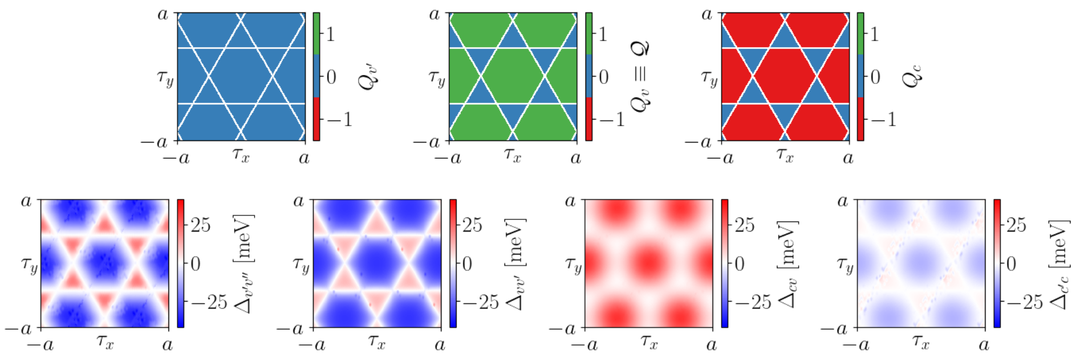

Figure 4.6: *Top row.* Valley Chern numbers of minibands v' to c against offset $\boldsymbol{\tau}$. *Bottom row.* The minigaps $\Delta_{v'v''}$, $\Delta_{vv'}$, Δ_{cv} and $\Delta_{c'c}$ of the miniband edges v'/v'', v/v', c/v and c'/c.

the miniband's Berry curvature $\Omega_{n\boldsymbol{k}}$ over the mSL Brillouin minizone,

$$\begin{aligned} Q_n &= \frac{1}{2\pi}\int_{\text{sBZ}} d^2k\, \Omega_{n\boldsymbol{k}}, \\ \Omega_{n\boldsymbol{k}} &= -2\,\text{Im}\sum_{m\neq n} \frac{[\chi^\dagger_{n\boldsymbol{k}}(\partial_{k_x}\mathcal{H}_{\boldsymbol{k}})\chi_{m\boldsymbol{k}}][\chi^\dagger_{m\boldsymbol{k}}(\partial_{k_y}\mathcal{H}_{\boldsymbol{k}})\chi_{n\boldsymbol{k}}]}{(\varepsilon_{n\boldsymbol{k}}-\varepsilon_{m\boldsymbol{k}})^2}. \end{aligned} \tag{4.9}$$

In the expression for the Berry curvature, we sum across the other minibands m. The valley Chern number has opposite signs in each valley since the Berry curvature has odd parity under inversion as a result of time reversal symmetry. In the main text, we define the valley Chern number of the first valence miniband as $Q \equiv Q_v$. We plot the valley Chern numbers of the second valence miniband v' to the first conduction miniband c against offset $\boldsymbol{\tau}$ in Fig. 4.6. The valley Chern numbers of minibands v and c change as the $\mathfrak{C}_m = 0$ lines are crossed in offset space and the secondary minigaps close.

4.E Effective Hamiltonian at the v/v' miniband edge

The secondary minigap on the valence side, $\Delta_{vv'}$, closes for offsets along the $\mathfrak{C}_m = 0$ lines. For offsets near these lines ($\mathfrak{C}_m \sim 0$), the minigap is non-zero at a miniband edge appearing at wavenumber $\boldsymbol{k}_e$. Expanding about the miniband edge, $\boldsymbol{q} = \boldsymbol{k} - \boldsymbol{k}_e$, the first and second valence minibands have dispersions [53],

$$\varepsilon_{v/v'} \approx \varepsilon_{vv'} + \xi\hbar\boldsymbol{v}_a\cdot\boldsymbol{q} \pm \sqrt{(\hbar v_s^x q_x)^2 + (\hbar v_s^y q_y)^2 + (\Delta_{vv'}/2)^2}. \tag{4.10}$$

This is parameterised by a constant energy shift $\varepsilon_{vv'}$, symmetric velocity $\boldsymbol{v}_s$, anti-symmetric velocity $\boldsymbol{v}_a$ and the secondary minigap $\Delta_{vv'}$, whose sign is determined by the Berry curvature,

$$\Omega_{v/v'} \approx \mp\frac{1}{4}\xi\Delta_{vv'}v_s^x v_s^y[(\Delta_{vv'}/2)^2 + (\boldsymbol{v}_s\cdot\boldsymbol{q})^2]^{-3/2}. \tag{4.11}$$

The miniband edge does not appear at a high symmetry point of the mSL Brillouin minizone since the offset is non-zero. Hence, the anti-symmetric velocity is non-zero ($\boldsymbol{v}_\text{a} \neq 0$), and the dispersion is tilted [53]. The dispersion and Berry curvature are described by the effective Hamiltonian in Eq. (3) of the main text and are plotted in Fig. 1 of the main text. We plot the secondary minigap $\Delta_{vv'}$ against offset $\boldsymbol{\tau}$ in Fig. 4.6. As described in the main text, the sign of the secondary minigap $\Delta_{vv'}$ changes sign as the $\mathfrak{C}_m = 0$ lines are crossed, inverting the Berry curvature of the minibands. This transfers a unit of valley Chern number between the minibands, giving the transition in $\mathcal{Q}$ in Fig. 4.6.

We can derive a similar effective Hamiltonian at the edge between the first conduction miniband c and the second conduction miniband c'. This allows us to define the secondary minigap on the conduction side, $\Delta_{c'c}$, which we plot in Fig. 4.6. The minibands undergo a similar inversion at this band edge as the $\mathfrak{C}_m = 0$ lines are crossed, transferring a unit of valley Chern number between them. Finally, we repeat this process for the edge between the second and third valence minibands, v' and v'' respectively, with the corresponding minigap $\Delta_{v'v''}$ also changing sign as the $\mathfrak{C}_m = 0$ lines are crossed. The inversion of the miniband structure at the edges of the second valence miniband with the first and third valence minibands cancels out pairwise and $\mathcal{Q}_{v'} \equiv 0$. The principal gap Δ_{cv} between the first valence miniband and the first conduction miniband never closes.

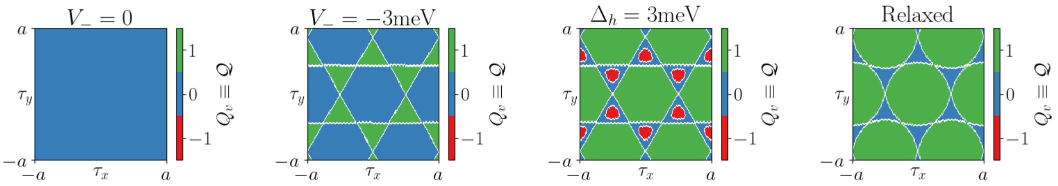

Figure 4.7: The valley Chern number Q_v of the first valence miniband v against offset (τ_x, τ_y) for various modifications to the parameters in Tab. 4.1.

4.F Robustness of the Kagomé network of chiral states

In Fig. 4.7., we demonstrate that our main finding of a Kagomé network of topologically protected one-dimensional chiral channels is robust against the choice of model parameters within a reasonable range. The phase transitions of the valley Chern number Q_v of the first valence miniband v are associated with the change in sign of the secondary minigap $\Delta_{vv'}$ at its edge with the second valence miniband v'. Hence, flipping the sign of the odd parity superlattice potential V_- swaps the phases and reverses the direction of the chiral channels while preserving the network. Turning off the inversion symmetry breaking in the interaction with the hBN layers by setting $V_- = 0$ prevents the transitions entirely as seen when comparing Fig. 2 of the main text to Fig. 4.7, and there is no network of channels.

If $\Delta_h/\Delta_u > \frac{1}{3}$, then the principal gap Δ_{cv} in Eq. (2) of the main text closes near the offset unit cell corners, giving the second phase transition to $Q_v = -1$ observed in Fig. 4.7 for $\Delta_h = 3\,$meV. This would produce a disconnected network of channels in the principal gap, which would not affect the network at the secondary minigap. A full treatment of the relaxation of the graphene layer onto the hBN layers results in terms other than Δ_{cv} [45]. The most significant of these mixes the superlattice potentials u_j^s, suppressing the odd potentials u_j^-. With an increased $V_- = 6\,$meV to compensate, we find the phase diagram in Fig. 4.7. This forms a Kagomé network which is qualitatively similar to Fig. 2 of the main text.

4.G Chiral states at the v/v' miniband edge

We consider interfaces along the y-axis in Fig. 1 of the main text, corresponding to the $\mathcal{C}_0 = 0$ lines in offset space. The other interfaces are related by the six-fold symmetry of the network. At the edge between the first and second valence minibands, the fitted parameters in Eq. (3) are $v_s^x \approx 0.2v$, $v_s^y \approx 0.9v$, $v_a^x \approx \pm 0.1v$ (for interfaces along the $\mathcal{Q} = 0$ triangles of shape $\triangleright$ and $\triangleleft$, respectively) and $v_a^y = 0$. We choose the basis with components perpendicular and parallel to the interface with unit vectors $\boldsymbol{e}_\perp = \pm\boldsymbol{e}_x$ and $\boldsymbol{e}_\parallel = \pm\boldsymbol{e}_y$, respectively, such that the gradient of the secondary minigap perpendicular to the interface is $\partial_{x_\perp}\Delta_{vv'} \approx 0.7|\tilde{\theta}|\,\mathrm{eV/nm} > 0$.

After performing the substitution $\boldsymbol{q} \to (q_\parallel, -i\partial_{x_\perp})$ discussed in the main text, we solve with the Jackiw-Rebbi ansatz $\varphi_{q_\parallel} = e^{iq_\parallel x_\parallel}\mathcal{J}_{q_\parallel}(x_\perp)$ for the wavefunction of the channel state which propagates with wavenumber $q_\parallel$ along the interface [54]. We use the finite difference method to find the two-component vector function $\mathcal{J}_{q_\parallel}(x_\perp)$ which confines the state perpendicular to the interface, subject to the boundary conditions $\lim_{x_\perp \to \pm\infty}\mathcal{J}_{q_\parallel}(x_\perp) = 0$. This takes the Gaussian form $\mathcal{J}_{q_\parallel}(x_\perp) \approx e^{-x_\perp/2\aleph^2}\zeta_{q_\parallel}$, where $\aleph \approx 2\tilde{\theta}^{-1/2}a$ and $\zeta_{q_\parallel}$ is a two-component vector which is independent of position. The state has linear dispersion $\xi\hbar\mathcal{V}q_\parallel$, with velocity $\mathcal{V} \approx 0.3v$. The direction of propagation is opposite for states along the triangles $\triangleright$ and $\triangleleft$ and for each valley. The channel states and their confinement are shown in Fig. 1 of the main text. We require that the lateral confinement of the channel state is longer than the mSL period ($\aleph > \lambda$) and much shorter than the period of the long-range variation ($\aleph \ll \Lambda$). These give the constraints $|\tilde{\theta}| < 4\delta^2$ and $|\tilde{\theta}| \ll 1/4$, respectively. We assume that the mismatch is small, $|\tilde{\theta}| \ll \delta$, when we construct the system, and the latter constraint is automatically met. Hence, the only constraint is that $|\tilde{\theta}| < 0.1°$.

4.H Kagomé network sites and scattering amplitudes for chiral states

We show scattering of channel states in the $\boldsymbol{K}^+$ valley at a node of the network in Fig. 4.8 (we neglect scattering with states in the $\boldsymbol{K}^-$ valley). The amplitudes of the incoming $(a_{\triangleright/\triangleleft})$ $(a/a'$ in the main text, respectively) and outgoing $(b_{\triangleright/\triangleleft})$ $(b/b'$ in the main text,

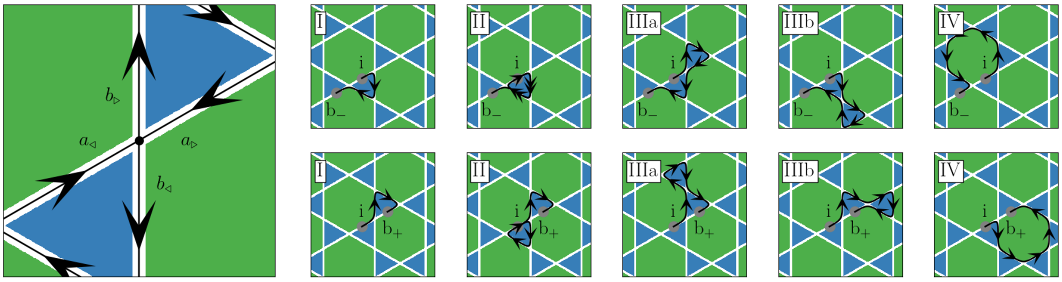

Figure 4.8: *Left.* Scattering of channel states in the $\boldsymbol{K}^+$ valley at a node of the network. The amplitudes of the incoming $(a_{\triangleright/\triangleleft})$ $(a/a'$ in the main text, respectively) and outgoing $(b_{\triangleright/\triangleleft})$ $(b/b'$ in the main text, respectively) modes along the $Q = 0$ triangles $\triangleright$ and $\triangleleft$, respectively, are highlighted. *Right.* The five shortest paths for an electron wave packet in the $\boldsymbol{K}^+$ valley to propagate from an injection position “in” to “$\mathrm{b}_\mp$” (*Top and bottom rows respectively.*). Double arrows indicate a channel is traversed twice.

respectively) states on channels along the $Q = 0$ triangles $\triangleright$ and $\triangleleft$, respectively, are related by the scattering matrix S of the node:

$$\begin{pmatrix} b_\triangleright \\ b_\triangleleft \end{pmatrix} = S \begin{pmatrix} a_\triangleright \\ a_\triangleleft \end{pmatrix}, \quad S = \begin{pmatrix} S_{\triangleright,\triangleright} & S_{\triangleright,\triangleleft} \\ S_{\triangleleft,\triangleright} & S_{\triangleleft,\triangleleft} \end{pmatrix}. \tag{4.12}$$

We constrain the scattering amplitudes using the symmetries of the system:

- Unitarity: $(S^{-1} = S^\dagger)$
- Time reversal symmetry: $(S^T = S)$
- Six-fold rotational symmetry:
  - 120° rotation: S is the same at each node
  - 180° rotation: $S_{\triangleright,\triangleright} = S_{\triangleleft,\triangleleft}$ and $S_{\triangleright,\triangleleft} = S_{\triangleleft,\triangleright}$

This gives the scattering amplitudes $S_{\triangleright,\triangleright} = S_{\triangleleft,\triangleleft} = e^{i\eta/3}\sqrt{P_R}$ and $S_{\triangleright,\triangleleft} = S_{\triangleleft,\triangleright} = ie^{i\eta/3}\sqrt{P_L}$ described in the main text, with real parameters η, P_L and $P_R = 1 - P_L$ (the latter of which are the left-and right-hand turn probabilities, respectively).

4.I Aharonov-Bohm oscillations of transport characteristics of the Kagomé network

In Fig. 3 of the main text, we show the five shortest paths contributing to an electron wave packet propagating from a position “i” to “f”. The wave packet starts and ends on channels propagating in the same direction, and advances along this direction by a period of the long-range variation during the propagation. These paths are the dominant paths contributing to the Aharonov-Bohm oscillations of the electronic transport against an external magnetic field $-B\boldsymbol{e}_z$ when the decoherence length ℓ is comparable to the period of the long-range variation ($\ell \sim \Lambda$).

We show in Fig. 4.8 two more sets of paths contributing to the Aharonov-Bohm oscillations where the propagation direction of the electron wave packet is flipped. The wave packet propagates forwards along the initial direction by half a long-range variation period to “b$_+$” or backwards by half a long-range variation period to “b$_-$”. Summing over the paths shown in Fig. 4.8, both of these sets of paths have the same total amplitude,

$$\psi \approx ie^{i\phi/4\phi_0}\sqrt{P_L P_R^2}z^3 + ie^{i\phi/2\phi_0}\sqrt{P_L P_R^5}z^6 - 2ie^{i\phi/2\phi_0}\sqrt{P_L^3 P_R^3}z^6 + ie^{-i3\phi/2\phi_0}\sqrt{P_L^5 P_R}z^6, \tag{4.13}$$

for $\ell \sim \Lambda$, where $z = e^{i\eta/3}e^{i\varepsilon\Lambda/2\hbar\mathcal{V}}e^{-\Lambda/4\ell}$ in terms of the energy ε. The magnetic flux through a unit cell of the long-range variation is $\phi = B\mathcal{A}$ (the area of the unit cell is $\mathcal{A} = \sqrt{3}\Lambda^2/2$) and the magnetic flux quantum is $\phi_0 = h/|e|$. The terms in the amplitude ψ correspond to the amplitudes of paths I, II, IIIa/b (with equal contributions) and IV, respectively. The amplitude ψ exhibits Shubnikov-de Haas style oscillations in the energy ε and Aharonov-Bohm oscillations in the flux ϕ. As for “i” to “f”, the thermal averaging at high temperatures ($k_B T \gg \hbar\mathcal{V}/\Lambda$ in the main text) suppresses the interference of paths of different length, and only the Aharonov-Bohm oscillations of period ϕ_0 commensurate with the long-range variation remain.

At high temperatures, the Aharonov-Bohm oscillations will only feature harmonics in the flux ϕ of period an integer multiple of ϕ_0 and commensurate with the long-range variation, which we now prove. At such temperatures, only paths of the same length will interfere in the amplitude between two points. The chirality of the channels ensures that the shortest path between the points is unique. We can lengthen the path at each node in one of two ways:

1. Add a clockwise loop around a $Q = 0$ triangle, increasing the length by $3\Lambda/2$ and the Peierls phase by $\pi\phi/4\phi_0$, converting path I to paths II or III.
2. Add a counter-clockwise loop around a $Q = 1$ hexagon, increasing the length by 3Λ and the Peierls phase by $-3\pi\phi/2\phi_0$.

If the intermediate paths remain connected, then we can add loops and then remove others to create new paths. For example, we convert path I to path IV in Fig. 4.8 by adding a hexagon and removing a triangle, increasing the length by $3\Lambda/2$ and the Peierls phase by $-7\pi\phi/4\phi_0$. Hence, each time the paths grow $3\Lambda/2$ longer, their Peierls phases increase by $\pi\phi/4\phi_0$ or $-7\pi\phi/4\phi_0$ and the Peierls phase difference is always an integer multiple of $2\pi\phi/\phi_0$.

The paths shown, from “i” to “f” and “$b_\pm$”, are the leading contributions to the Aharonov-Bohm oscillations at high temperatures. This is because they feature the shortest paths (I) where it is possible to add a hexagon then remove a triangle, increasing the Peierls phase by $-7\pi\phi/4\phi_0$. This gives the Peierls phase difference of $2\pi\phi/\phi_0$ with the paths where a triangle was added, which give the harmonic of period ϕ_0 which dominates the Aharonov-Bohm oscillations.

Bibliography

[1] C. Moulsdale, A. Knothe, and V. Fal’ko, Kagome network of miniband-edge states in double-aligned graphene–hexagonal boron nitride structures *Phys. Rev. B*, vol. 105, p. L201112, May 2022.

[2] L. Fu and C. L. Kane, Topological insulators with inversion symmetry *Phys. Rev. B*, vol. 76, p. 045302, Jul 2007.

[3] Y. Zhang, Y.-W. Tan, H. L. Stormer, and P. Kim, Experimental observation of the quantum Hall effect and Berry’s phase in graphene *Nature*, vol. 438, pp. 201–204, Nov 2005.

[4] K. S. Novoselov, E. McCann, S. V. Morozov, V. I. Fal’ko, M. I. Katsnelson, U. Zeitler, D. Jiang, F. Schedin, and A. K. Geim, Unconventional quantum Hall

effect and Berry's phase of 2π in bilayer graphene *Nature Physics*, vol. 2, pp. 177–180, Mar 2006.

[5] D. Xiao, W. Yao, and Q. Niu, Valley-Contrasting Physics in Graphene: Magnetic Moment and Topological Transport *Phys. Rev. Lett.*, vol. 99, p. 236809, Dec 2007.

[6] J. Li, I. Martin, M. Büttiker, and A. F. Morpurgo, Topological origin of subgap conductance in insulating bilayer graphene *Nature Physics*, vol. 7, pp. 38–42, Jan 2011.

[7] P. San-Jose and E. Prada, Helical networks in twisted bilayer graphene under interlayer bias *Phys. Rev. B*, vol. 88, p. 121408(R), Sep 2013.

[8] L. Ju, Z. Shi, N. Nair, Y. Lv, C. Jin, J. Velasco, C. Ojeda-Aristizabal, H. A. Bechtel, M. C. Martin, A. Zettl, J. Analytis, and F. Wang, Topological valley transport at bilayer graphene domain walls *Nature*, vol. 520, pp. 650–655, Apr 2015.

[9] L.-J. Yin, H. Jiang, J.-B. Qiao, and L. He, Direct imaging of topological edge states at a bilayer graphene domain wall *Nature Communications*, vol. 7, p. 11760, Jun 2016.

[10] J. Li, K. Wang, K. J. McFaul, Z. Zern, Y. Ren, K. Watanabe, T. Taniguchi, Z. Qiao, and J. Zhu, Gate-controlled topological conducting channels in bilayer graphene *Nature Nanotechnology*, vol. 11, pp. 1060–1065, Dec 2016.

[11] M. Eich, F. Herman, R. Pisoni, H. Overweg, A. Kurzmann, Y. Lee, P. Rickhaus, K. Watanabe, T. Taniguchi, M. Sigrist, T. Ihn, and K. Ensslin, Spin and Valley States in Gate-Defined Bilayer Graphene Quantum Dots *Phys. Rev. X*, vol. 8, p. 031023, Jul 2018.

[12] A. Knothe and V. Fal'ko, Influence of minivalleys and Berry curvature on electrostatically induced quantum wires in gapped bilayer graphene *Phys. Rev. B*, vol. 98, p. 155435, Oct 2018.

[13] R. Kraft, I. V. Krainov, V. Gall, A. P. Dmitriev, R. Krupke, I. V. Gornyi, and R. Danneau, Valley Subband Splitting in Bilayer Graphene Quantum Point Contacts *Phys. Rev. Lett.*, vol. 121, p. 257703, Dec 2018.

[14] S. Huang, K. Kim, D. K. Efimkin, T. Lovorn, T. Taniguchi, K. Watanabe, A. H. MacDonald, E. Tutuc, and B. J. LeRoy, Topologically Protected Helical States in Minimally Twisted Bilayer Graphene *Phys. Rev. Lett.*, vol. 121, p. 037702, Jul 2018.

[15] K. Komatsu, Y. Morita, E. Watanabe, D. Tsuya, K. Watanabe, T. Taniguchi, and S. Moriyama, Observation of the quantum valley Hall state in ballistic graphene superlattices *Science Advances*, vol. 4, no. 5, p. eaaq0194, 2018.

[16] D. K. Efimkin and A. H. MacDonald, Helical network model for twisted bilayer graphene *Phys. Rev. B*, vol. 98, p. 035404, Jul 2018.

[17] H. Overweg, A. Knothe, T. Fabian, L. Linhart, P. Rickhaus, L. Wernli, K. Watanabe, T. Taniguchi, D. Sánchez, J. Burgdörfer, F. Libisch, V. I. Fal'ko, K. Ensslin, and T. Ihn, Topologically Nontrivial Valley States in Bilayer Graphene Quantum Point Contacts *Phys. Rev. Lett.*, vol. 121, p. 257702, Dec 2018.

[18] C. Dutreix, H. González-Herrero, I. Brihuega, M. I. Katsnelson, C. Chapelier, and V. T. Renard, Measuring the Berry phase of graphene from wavefront dislocations in Friedel oscillations *Nature*, vol. 574, pp. 219–222, Oct 2019.

[19] Y. Lee, A. Knothe, H. Overweg, M. Eich, C. Gold, A. Kurzmann, V. Klasovika, T. Taniguchi, K. Wantanabe, V. Fal'ko, T. Ihn, K. Ensslin, and P. Rickhaus, Tunable Valley Splitting due to Topological Orbital Magnetic Moment in Bilayer Graphene Quantum Point Contacts *Phys. Rev. Lett.*, vol. 124, p. 126802, Mar 2020.

[20] Y. Shi, S. Xu, Y. Yang, S. Slizovskiy, S. V. Morozov, S.-K. Son, S. Ozdemir, C. Mullan, J. Barrier, J. Yin, A. I. Berdyugin, B. A. Piot, T. Taniguchi, K. Watanabe, V. I. Fal'ko, K. S. Novoselov, A. K. Geim, and A. Mishchenko, Electronic phase separation in multilayer rhombohedral graphite *Nature*, vol. 584, pp. 210–214, Aug 2020.

[21] Y. Li, M. Amado, T. Hyart, G. P. Mazur, and J. W. A. Robinson, Topological valley currents via ballistic edge modes in graphene superlattices near the primary Dirac point *Communications Physics*, vol. 3, p. 224, Dec 2020.

[22] C. Tong, R. Garreis, A. Knothe, M. Eich, A. Sacchi, K. Watanabe, T. Taniguchi, V. Fal'ko, T. Ihn, K. Ensslin, and A. Kurzmann, Tunable Valley Splitting and Bipolar Operation in Graphene Quantum Dots *Nano Letters*, vol. 21, no. 2, pp. 1068–1073, 2021. PMID: 33449702.

[23] D. P. DiVincenzo and E. J. Mele, Self-consistent effective-mass theory for intralayer screening in graphite intercalation compounds *Phys. Rev. B*, vol. 29, pp. 1685–1694, Feb 1984.

[24] T. Ando, T. Nakanishi, and R. Saito, Berry's Phase and Absence of Back Scattering in Carbon Nanotubes *Journal of the Physical Society of Japan*, vol. 67, no. 8, pp. 2857–2862, 1998.

[25] E. McCann and V. I. Fal'ko, Landau-Level Degeneracy and Quantum Hall Effect in a Graphite Bilayer *Phys. Rev. Lett.*, vol. 96, p. 086805, Mar 2006.

[26] M. Mucha-Kruczyński, I. L. Aleiner, and V. I. Fal'ko, Strained bilayer graphene: Band structure topology and Landau level spectrum *Phys. Rev. B*, vol. 84, p. 041404(R), Jul 2011.

[27] C. Moulsdale, A. Knothe, and V. Fal'ko, Engineering of the topological magnetic moment of electrons in bilayer graphene using strain and electrical bias *Phys. Rev. B*, vol. 101, p. 085118, Feb 2020.

[28] A. Knothe and V. Fal'ko, Quartet states in two-electron quantum dots in bilayer graphene *Phys. Rev. B*, vol. 101, p. 235423, Jun 2020.

[29] A. Knothe, L. I. Glazman, and V. I. Fal'ko. arXiv:2104.03399, 2021.

[30] F. Zhang, A. H. MacDonald, and E. J. Mele, Valley Chern numbers and boundary modes in gapped bilayer graphene *Proceedings of the National Academy of Sciences*, vol. 110, no. 26, pp. 10546–10551, 2013.

[31] I. Martin, Y. M. Blanter, and A. F. Morpurgo, Topological Confinement in Bilayer Graphene *Phys. Rev. Lett.*, vol. 100, p. 036804, Jan 2008.

[32] C. De Beule, F. Dominguez, and P. Recher, Aharonov-Bohm Oscillations in Minimally Twisted Bilayer Graphene *Phys. Rev. Lett.*, vol. 125, p. 096402, Aug 2020.

[33] C. De Beule, F. Dominguez, and P. Recher, Network model and four-terminal transport in minimally twisted bilayer graphene *Phys. Rev. B*, vol. 104, p. 195410, Nov 2021.

[34] N. R. Walet and F. Guinea, The emergence of one-dimensional channels in marginal-angle twisted bilayer graphene *2D Materials*, vol. 7, p. 015023, dec 2019.

[35] S. G. Xu, A. I. Berdyugin, P. Kumaravadivel, F. Guinea, R. Krishna Kumar, D. A. Bandurin, S. V. Morozov, W. Kuang, B. Tsim, S. Liu, J. H. Edgar, I. V. Grigorieva, V. I. Fal'ko, M. Kim, and A. K. Geim, Giant oscillations in a triangular network of one-dimensional states in marginally twisted graphene *Nature Communications*, vol. 10, p. 4008, Sep 2019.

[36] M. Yankowitz, J. Xue, D. Cormode, J. D. Sanchez-Yamagishi, K. Watanabe, T. Taniguchi, P. Jarillo-Herrero, P. Jacquod, and B. J. LeRoy, Emergence of superlattice Dirac points in graphene on hexagonal boron nitride *Nature Physics*, vol. 8, pp. 382–386, May 2012.

[37] J. R. Wallbank, A. A. Patel, M. Mucha-Kruczyński, A. K. Geim, and V. I. Fal'ko, Generic miniband structure of graphene on a hexagonal substrate *Phys. Rev. B*, vol. 87, p. 245408, Jun 2013.

[38] M. Lee, J. R. Wallbank, P. Gallagher, K. Watanabe, T. Taniguchi, V. I. Fal'ko, and D. Goldhaber-Gordon, Ballistic miniband conduction in a graphene superlattice *Science*, vol. 353, no. 6307, pp. 1526–1529, 2016.

[39] Y.-N. Ren, Y. Zhang, Y.-W. Liu, and L. He, Twistronics in graphene-based van der Waals structures *Chinese Physics B*, vol. 29, p. 117303, oct 2020.

[40] Y. Yang, J. Li, J. Yin, S. Xu, C. Mullan, T. Taniguchi, K. Watanabe, A. K. Geim, K. S. Novoselov, and A. Mishchenko, In situ manipulation of van der Waals heterostructures for twistronics *Science Advances*, vol. 6, no. 49, p. eabd3655, 2020.

[41] T. Fukui, Y. Hatsugai, and H. Suzuki, Chern Numbers in Discretized Brillouin Zone: Efficient Method of Computing (Spin) Hall Conductances *Journal of the Physical Society of Japan*, vol. 74, no. 6, pp. 1674–1677, 2005.

[42] Y. Ren, Z. Qiao, and Q. Niu, Topological phases in two-dimensional materials: a review vol. 79, p. 066501, may 2016.

[43] J. W. McClure, Diamagnetism of Graphite *Phys. Rev.*, vol. 104, pp. 666–671, Nov 1956.

[44] J. Wallbank, M. Mucha-Kruczynski, X. Chen, and V. Fal'ko, Moiré superlattice effects in graphene/boron-nitride van der Waals heterostructures *Annalen der Physik*, vol. 527, pp. 359 – 376, June 2015.

[45] M. Szyniszewski, E. Mostaani, A. Knothe, V. Enaldiev, A. C. Ferrari, V. I. Fal'ko & N. D. Drummond. Unpublished.

[46] P. San-Jose, A. Gutiérrez-Rubio, M. Sturla, and F. Guinea, Spontaneous strains and gap in graphene on boron nitride *Phys. Rev. B*, vol. 90, p. 075428, Aug 2014.

[47] P. San-Jose, A. Gutiérrez-Rubio, M. Sturla, and F. Guinea, Electronic structure of spontaneously strained graphene on hexagonal boron nitride *Phys. Rev. B*, vol. 90, p. 115152, Sep 2014.

[48] J. Jung, A. M. DaSilva, A. H. MacDonald, and S. Adam, Origin of band gaps in graphene on hexagonal boron nitride *Nature Communications*, vol. 6, p. 6308, Feb 2015.

[49] L. A. Ponomarenko, R. V. Gorbachev, G. L. Yu, D. C. Elias, R. Jalil, A. A. Patel, A. Mishchenko, A. S. Mayorov, C. R. Woods, J. R. Wallbank, M. Mucha-Kruczynski, B. A. Piot, M. Potemski, I. V. Grigorieva, K. S. Novoselov, F. Guinea, V. I. Fal'ko, and A. K. Geim, Cloning of Dirac fermions in graphene superlattices *Nature*, vol. 497, pp. 594–597, May 2013.

[50] M. S. Fuhrer, Critical Mass in Graphene *Science*, vol. 340, pp. 1413–1414, June 2013.

[51] W. Yang, G. Chen, Z. Shi, C.-C. Liu, L. Zhang, G. Xie, M. Cheng, D. Wang, R. Yang, D. Shi, K. Watanabe, T. Taniguchi, Y. Yao, Y. Zhang, and G. Zhang, Epitaxial growth of single-domain graphene on hexagonal boron nitride *Nature Materials*, vol. 12, pp. 792–797, Sep 2013.

[52] G. L. Yu, R. V. Gorbachev, J. S. Tu, A. V. Kretinin, Y. Cao, R. Jalil, F. Withers, L. A. Ponomarenko, B. A. Piot, M. Potemski, D. C. Elias, X. Chen, K. Watanabe, T. Taniguchi, I. V. Grigorieva, K. S. Novoselov, V. I. Fal'ko, A. K. Geim, and A. Mishchenko, Hierarchy of Hofstadter states and replica quantum Hall ferromagnetism in graphene superlattices *Nature Physics*, vol. 10, pp. 525–529, Jul 2014.

[53] M. O. Goerbig, J.-N. Fuchs, G. Montambaux, and F. Piéchon, Tilted anisotropic Dirac cones in quinoid-type graphene and $\alpha-(\text{BEDT-TTF})_2\text{I}_3$ *Phys. Rev. B*, vol. 78, p. 045415, Jul 2008.

[54] R. Jackiw and C. Rebbi, Solitons with fermion number ½ *Phys. Rev. D*, vol. 13, pp. 3398–3409, Jun 1976.

[55] J. M. Lee, M. Oshikawa, and G. Y. Cho, Non-Fermi Liquids in Conducting Two-Dimensional Networks *Phys. Rev. Lett.*, vol. 126, p. 186601, May 2021.

[56] M. Killi, T.-C. Wei, I. Affleck, and A. Paramekanti, Tunable Luttinger Liquid Physics in Biased Bilayer Graphene *Phys. Rev. Lett.*, vol. 104, p. 216406, May 2010.

[57] A. H. Castro Neto, F. Guinea, N. M. R. Peres, K. S. Novoselov, and A. K. Geim, The electronic properties of graphene *Rev. Mod. Phys.*, vol. 81, pp. 109–162, Jan 2009.

[58] D. J. Thouless, M. Kohmoto, M. P. Nightingale, and M. den Nijs, Quantized Hall Conductance in a Two-Dimensional Periodic Potential *Phys. Rev. Lett.*, vol. 49, pp. 405–408, Aug 1982.

[59] Quantal phase factors accompanying adiabatic changes *Proceedings of the Royal Society of London. A. Mathematical and Physical Sciences*, vol. 392, pp. 45–57, Mar. 1984.

[60] M. Kohmoto, Topological invariant and the quantization of the Hall conductance *Annals of Physics*, vol. 160, no. 2, pp. 343–354, 1985.

[61] D. Xiao, M.-C. Chang, and Q. Niu, Berry phase effects on electronic properties *Rev. Mod. Phys.*, vol. 82, pp. 1959–2007, Jul 2010.

Chapter 5

Band Gap Opening in Bilayer Graphene-$CrCl_3$/$CrBr_3$/CrI_3 van der Waals Interfaces

Preface

The contents of this chapter represent the main body of a manuscript previously published in ACS Nano Letters [1]. The accompanying supporting information is presented in the appendices. The manuscript was authored by Giulia Tenasini[1,2], David Soler-Delgado[1,2], Zhe Wang[1,3], Fengrui Yao[1,2], Dumitru Dumcenco[1], Enrico Giannini[1], Kenji Watanabe[4], Takashi Taniguchi[5], Christian Moulsdale[6,7], Aitor Garcia-Ruiz[6,7], Vladimir I. Fal'ko[6,7,8], Ignacio Gutiérrez-Lezama[1,2] and Alberto F. Morpurgo[1,2].

This publication is the result of a collaboration between experimentalists in the

---

[1] Department of Quantum Matter Physics, University of Geneva, 24 Quai Ernest Ansermet, CH-1211 Geneva, Switzerland

[2] Group of Applied Physics, University of Geneva, 24 Quai Ernest Ansermet, CH-1211 Geneva, Switzerland

[3] MOE Key Laboratory for Non-equilibrium Synthesis and Modulation of Condensed Matter, Shaanxi Province Key Laboratory of Advanced Materials and Mesoscopic Physics, School of Physics, Xi'an Jiaotong University, Xi'an 710049, China.

[4] Research Center for Functional Materials, NIMS, 1-1 Namiki, Tsukuba 305-0044, Japan

[5] International Center for Materials Nanoarchitectonics, NIMS, 1-1 Namiki, Tsukuba 305-0044, Japan

[6] National Graphene Institute, University of Manchester, Manchester M13 9PL, UK

[7] School of Physics & Astronomy, University of Manchester, Manchester M13 9PL, UK

[8] Henry Royce Institute for Advanced Materials, Manchester M13 9PL, UK

Quantum Electronics group at the Université de Genève and theorists in the Condensed Matter Physics group at the National Graphene Institute at the University of Manchester. The experimental work was primarily performed by Giulia Tenasini, under the guidance and supervision of Ignacio Gutiérrez-Lezama and Alberto F. Morpurgo. The theoretical work was primarily performed by Christian Moulsdale, under the guidance and supervision of Vladimir Fal'ko. The writing of the manuscript was primarily done by Alberto F. Morpurgo, with assistance from the listed authors. Christian Moulsdale's contribution includes performing all the analytical and numerical calculations for the dielectric screening of the displacement field by the Landau levels in bilayer graphene and fitting the observed energy gap of each substrate, and providing the data used in Figure 5.4 b and c.

Abstract

We report experimental investigations of transport through bilayer graphene (BLG)/chromium trihalide (CrX$_3$; X=Cl, Br, I) van der Waals interfaces. In all cases, a large charge transfer from BLG to CrX$_3$ takes place (reaching densities in excess of 10^{13} cm^{-2}), and generates an electric field perpendicular to the interface that opens a band gap in BLG. We determine the gap from the activation energy of the conductivity and find excellent agreement with the latest theory accounting for the contribution of the σ bands to the BLG dielectric susceptibility. We further show that for BLG/CrCl$_3$ and BLG/CrBr$_3$ the band gap can be extracted from the gate voltage dependence of the low-temperature conductivity, and use this finding to refine the gap dependence on the magnetic field. Our results allow a quantitative comparison of the electronic properties of BLG with theoretical predictions and indicate that electrons occupying the CrX$_3$ conduction band are correlated.

Van der Waals (vdW) interfaces provide a vast playground for creating new systems with engineered electronic properties, by stacking suitably chosen atomically thin crystals (or 2D materials) on top of each other. Examples include hexagonal Boron Nitride (hBN) encapsulation of graphene [2, 3, 4], proximity induced spin-orbit coupling in graphene on semiconducting transition metal dichalcogenide substrates

[5, 6, 7, 8, 9, 10, 11], or the creation of so-called $\Gamma-\Gamma$ interfaces [12, 13]. Recently, the discovery of 2D magnets and their use in vdW heterostructures has further broadened the scope of phenomena that can be explored [14, 15, 16, 17, 18, 19]. In these systems, the wave functions of electrons in the non-magnetic material extend into the magnetic one and experience some of the magnetic interaction, enabling magnetism to be proximity induced in graphene or other 2D materials [20, 21, 14, 22, 23, 24, 25, 26, 27, 28, 29]. However, deterministically controlling magnetism by proximity and predicting what aspect of magnetism can be induced into non-magnetic materials are challenges that remain to be solved because many different phenomena – such as strain, hybridization, charge transfer, and more – occur simultaneously at van der Waals interfaces [30, 16, 31, 32], influencing the interfacial electronic properties. In particular, electrostatic effects often dominate the behavior of heterostructures formed by low-charge-density systems, such as 2D semiconductors and semimetals. As a result, significant charge transfer can occur and lead to new phenomena mediated by changes in electron concentration or orbital occupation [33]. Indeed, recent work reported spin-dependent interlayer charge transfer in magnetic vdW heterostructures [34, 35, 36] and concluded that its detailed analysis is of key importance for improving the control of interfacial properties.

Here, we report the systematic behavior of vdW interfaces formed by bilayer graphene (BLG) [37, 38] and chromium trihalide crystals (CrX_3; X=Cl, Br, I) [39, 40, 41, 42, 43, 44, 45, 46]. All systems exhibit a large transfer of electrons from graphene to the magnetic material, reaching values in excess of 10^{13} cm^{-2}, producing a large electric field perpendicular to the interface and a gap in BLG. When gating the BLG at the charge neutrality point (CNP), the gap induces a low-temperature suppression of the conductance of four orders of magnitude or more, exhibiting a sharp onset as a function of gate voltage. We determine the size of the band gap by analyzing the temperature dependence of the transfer curves (i.e., conductance-vs-gate voltage), and find excellent agreement with the results of the latest ab initio calculations of the electrostatically induced gap in BLG, which include dielectric screening due to the polarizability of the σ bonds in the graphene lattice [47]. We also find that the gap in BLG can be determined by looking exclusively at the low-temperature gate voltage dependence of the conductance, a result that provides information about the nature of

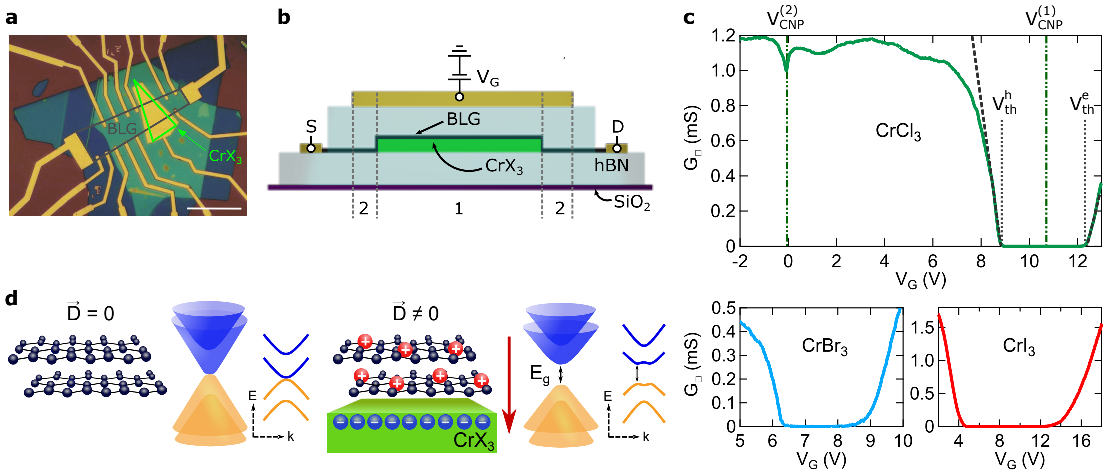

Figure 5.1: **Band gap opening in BLG/CrX$_3$ interfaces. (a)** Optical micrograph and **(b)** schematics of a representative device (the scale bar in (a) is 20 μm), based on a BLG/CrX$_3$ heterostructure encapsulated in hBN. A metallic gate electrode is deposited onto the top hBN layer, and is coupled to two distinct regions: a central part formed by the BLG/CrX$_3$ interface (region 1) and two adjacent parts where BLG is in contact only with hBN (region 2). Transport is measured using metallic source (S) and drain contacts (D) and probes the two regions connected in series. **(c)** Square conductance $G_\square$ as a function of gate voltage V_G measured in a heterostructure of BLG-on-CrCl$_3$ at 250 mK (green curve, top). Two characteristic features are visible in the transfer curve: a small conductance dip close to $V_\mathrm{G} = 0$ V corresponding to the CNP of graphene in region 2 ($V_{CNP}^{(2)}$) and a pronounced suppression at large V_G ($V_{CNP}^{(1)}$) that originates from gating BLG-on-CrCl$_3$ (i.e., region 1) to charge neutrality. The black dashed lines represent linear extrapolations to extract the threshold voltages for holes V_{th}^{h} and electrons V_{th}^{e}. Virtually identical behaviour is observed in heterostructures of BLG and CrBr$_3$ (light-blue, bottom) and BLG-on-CrI$_3$ (red, bottom). **(d)** Schematics of the BLG band structure in the absence (left) and presence (right) of a perpendicular displacement field $\vec{D}$, showing that at finite field a gap E_g is present at charge neutrality. As visible on the right side of the panel, the displacement field is generated by the large transfer of electrons from BLG to CrX$_3$ occurring at the vdW interface.

the electronic states in the CrX$_3$, and that enables the quantitative determination of the dependence of the BLG band gap on the applied magnetic field.

Figure 5.1a shows an optical microscope image of a representative device employed for our transport studies. A BLG with an elongated rectangular shape is placed on top of an exfoliated CrX$_3$ thin crystal, using a by-now conventional dry transfer method

[48]. The process is carried out in the controlled environment of a glove box and the interface is encapsulated in hBN to prevent degradation upon exposure to air. Metal contacts to BLG are patterned using standard micro-fabrication techniques, and a gate electrode is deposited onto the top hBN, enabling the charge density in the BLG layer to be tuned. The device schematics in Figure 5.1b highlights how the gate is coupled to two distinct regions: a central part formed by the BLG/CrX_3 interface (which we refer to as region 1) and two parts on the sides, where BLG is in contact only with hBN (which we refer to as region 2) that effectively act as contacts to the gapped part of the structure. This device feature is important to understand some aspects of the measurements that we present later.

The gate voltage dependence of the square conductance $G_\square$ of a device with BLG-on-$CrCl_3$, shown in Figure 5.1c (green curve), reveals two characteristic features that originate from regions 1 and 2. The small conductance dip close to $V_G = 0$ V is the manifestation of the charge neutrality point (CNP) of BLG-on-hBN (region 2), and the pronounced suppression (four orders of magnitude) at large V_G originates from having gated BLG-on-$CrCl_3$ (region 1) to charge neutrality. The shift of the BLG CNP toward high, positive gate voltages indicates that a large number of electrons are transferred from BLG to the $CrCl_3$ crystal (10^{13} cm^{-2}). Analogous behavior and a large hole doping in BLG (see Section S1 of the Supporting Information for transfer curves in a broader range of gate voltages) are also observed in heterostructures formed by BLG and $CrBr_3$ (light-blue curve) and in BLG-on-CrI_3 (red curve; in agreement with the earlier observations [33, 49]).

The observed charge transfer generates a strong electric field perpendicular to the interface that causes the opening of a band gap in BLG [50, 38, 51, 52, 53, 54, 55] (see the schematic band diagrams in Figure 5.1d). As a result, when the chemical potential in BLG is shifted to charge neutrality by applying a suitable gate voltage, this leads to a robust insulating state. The sharp onset of this insulating state as a function of V_G implies the absence of large electrostatic potential fluctuations at the BLG/CrX_3 interfaces, indicating that charge transfer from CrX_3 to BLG is rather homogeneous. To compare quantitatively the experimental observations made in heterostructures based

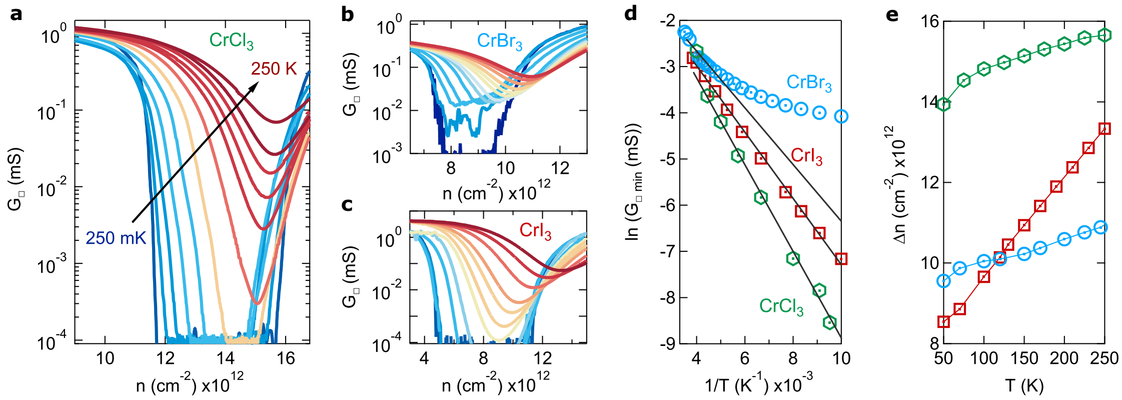

Figure 5.2: **Temperature evolution of the square conductance in BLG/CrX$_3$ heterostructures.** Square conductance $G_\square$ as function of charge density n measured at different temperatures between 250 mK (blue) and 250 K (red) for **(a)** BLG-on-CrCl$_3$,**(b)** CrBr$_3$ and **(c)** CrI$_3$. **(d)** Arrhenius plot of the minimum square conductance measured for the three different heterostructures (CrCl$_3$ green hexagons, CrI$_3$ red squares, CrBr$_3$ light-blue circles). Activation energies are obtained by fitting the linear part in the high-temperature range (grey lines). **(e)** Temperature dependence of the charge Δn transferred from BLG to CrX$_3$ for the investigated interfaces (the different colors and symbols represent data measured on different interfaces, as indicated in (d)).

on the different CrX$_3$, we convert the applied gate voltage to the corresponding accumulated charge density n, as $n = \frac{\varepsilon\varepsilon_0}{\mathrm{t}}\frac{V_{\mathrm{G}}-V_{\mathrm{CNP}}^{(2)}}{e}$ (ε and t are the relative dielectric constant and thickness of the hBN layer, and $V_{CNP}^{(2)}$ is the gate voltage corresponding to the CNP in region 2, see Figure 5.1c). The concentration of electrons transferred from BLG in CrX$_3$ is then given by $\Delta n = \frac{\varepsilon\varepsilon_0}{t}\frac{V_{CNP}^{(1)}-V_{CNP}^{(2)}}{e}$ (where $V_{CNP}^{(1)}$ is the gate voltage corresponding to the CNP of BLG-on-CrX$_3$, i.e. in region 1; see Figure 5.1c again), and is directly proportional to the displacement field present at the BLG/CrX$_3$ interfaces, $D = e\Delta n$ (we use this relation to calculate the values of the displacement field in Figure 5.3).

We determine the size of the band gap from the temperature (T) evolution of the transfer curves, plotted in Figure 5.2a-c for CrCl$_3$, CrBr$_3$, and CrI$_3$, respectively. Data are shown for selected values of T between 250 mK (blue curve) and 250 K (red). The activation energies for the three heterostructures are extracted by looking at the minimum square conductance $G_\square^{min}$ (corresponding to $G_\square$ at the CNP of BLG/CrX$_3$), by fitting the linear part of the Arrhenius plot in the high-temperature range, where the charge carriers are dominated by a thermally activated behavior (see Figure 5.2d). The larger activation energy E_a is observed in BLG-on-CrCl$_3$ (green hexagons) where the gap ($E_g = 2E_a$) is estimated to be 162 meV; band gaps of 124 meV and 108 meV are found for BLG-on-CrI$_3$ (red squares) and on CrBr$_3$ (light-blue circles), respectively.

The same measurements show that the position of the CNP, i.e., the density of charge transferred from BLG to CrX$_3$, is temperature-dependent (as summarized in Figure 5.2e), implying that the perpendicular electric field responsible for the opening of the band is not constant as T is varied. For BLG-on-CrCl$_3$ (green) and on CrBr$_3$ (light-blue) the position of CNP changes by less than 10% throughout the full range investigated, and by significantly less over the range used to determine the size of the band gap, so that the effect can be disregarded. For CrI$_3$ (red) the change is larger, corresponding to a more sizable indetermination for the electric field value responsible for the opening of the gap in BLG. The precise microscopic origin of the T dependence of CNP in BLG-on-CrI$_3$ is currently not understood, and is likely determined by the electronic properties of CrX$_3$, which are materials with very narrow bands, whose behavior deviates from that of conventional semiconductors (see also the below discussion on the determination of the gap from the gate voltage dependence of the transfer curves).

The band gap dependence on the electric field for the three different BLG/CrX$_3$ interfaces is compared to the calculated gap in Figure 5.3. The electric field dependence of the gap predicted for $\varepsilon_z = 2.6$ –corresponding to the theoretically expected dielectric susceptibility when accounting for the polarizability of the σ bands– is represented by the blue line. For comparison we also show calculations with $\varepsilon_z = 1$ (grey line) as in [38]. The empty symbols of different colors (CrCl$_3$, green hexagon; CrI$_3$, red square; CrBr$_3$, light-blue circle) represent our experimental data, and the error bar denotes the indetermination on the electric field due to the temperature dependence of the charge transferred from BLG to CrX$_3$, as just discussed above. These data agree perfectly with theory that considers $\varepsilon_z = 2.6$ using the method proposed in [47], and deviate very significantly from the $\varepsilon_z = 1$ curve. This result should be underscored, because experimental values for the band gap reported in the early days of research on graphene were larger, and it was argued that quantitative agreement was obtained for $\varepsilon_z = 1$ (the deviation likely originated from a insufficiently sharp dependence of the conductance

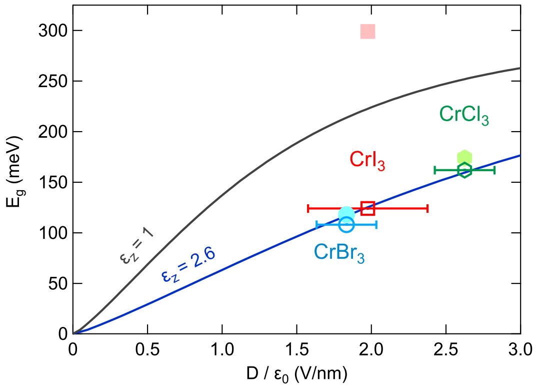

Figure 5.3: **Electric field dependence of the band gap in BLG/CrX$_3$ interfaces.** The continuous lines represent the band gap as a function of displacement field D predicted by ab initio calculations, considering or ignoring the contribution to the dielectric susceptibility ε_z due to the electrons that occupy the σ band of BLG [47]. The empty symbols represent the experimental data obtained from the temperature dependence of the conductance measured in our devices. It is apparent that the experimental data are in excellent agreement with theoretical prediction for $\varepsilon_z = 2.6$. The error bars for the displacement field ($D = e\Delta n$, see main text) correspond to the variation of charge transferred from BLG to CrX$_3$ (and consequently of D) as temperature is varied. Filled symbols indicate the experimental values of E_g extracted from the threshold voltages of low-temperature transfer curves using Equation (1). For CrCl$_3$ and CrBr$_3$ the agreement with the gap values obtained from the temperature-dependent measurements is excellent.

on V_{G} due to the lower quality of the BLG-on-$\mathrm{SiO_2}$ devices used in earlier experiments [55]).

Having determined the band gap from the analysis of the temperature dependence of the square conductance, we now present an alternative way that relies exclusively on the analysis of the low-temperature $\mathrm{G}_\square$-vs-V_{G} curves. From analyzing our data, we find that for BLG on both $\mathrm{CrCl_3}$ and $\mathrm{CrBr_3}$, the gap is quantitatively given by

$$E_g = \frac{C\left(V_{th}^{e} - V_{th}^{h}\right)}{e\,\rho_{\mathrm{BLG}}} \tag{5.1}$$

Here, V_{th}^{e} and V_{th}^{h} are the threshold voltages for electron and hole conductance (obtained by extrapolating to zero the conductance measured as a function of gate voltage, as illustrated by the dashed lines in Figure 5.1c) and $\rho_{\mathrm{BLG}} = 2m^*/\pi h^2$ is the density of states in gapless BLG contacts (i.e., region 2 in Figure 5.1b), next to the gapped region where BLG is on the $\mathrm{CrX_3}$ layer (region 1). Equation (1) gives the gap values represented with filled symbols in Figure 5.3, in perfect agreement with the values obtained from the T dependence of the minimum conductance for both BLG-on-$\mathrm{CrCl_3}$ and BLG-on-$\mathrm{CrBr_3}$; for BLG-on-$\mathrm{CrI_3}$, instead, Eq. (1) gives a value that deviates by nearly a factor of 2 from the correct one. We discuss below the origin of Eq. (1), the condition for its validity, and why it fails to give the correct value of the gap for $\mathrm{CrI_3}$.

The possibility to use Eq. (1) to extract the band gap of BLG enables the detailed dependence of the gap on the magnetic field, not yet addressed in previous studies, to be probed in an experimentally straightforward way. To this end, it suffices to measure the conductance as a function of gate voltage for different values of the magnetic field, as shown in Figure 5.4a for a BLG-on-$\mathrm{CrCl_3}$ device. The left and right panels zoom in on the onset of threshold for both electron and hole conduction, which shift upon increasing the applied magnetic field, resulting in a decrease in (V_{th}^{e}-V_{th}^{h}), and therefore a decrease in the BLG band gap. The full dependence of the gap on B for BLG-on-$\mathrm{CrCl_3}$ and for BLG-on-$\mathrm{CrBr_3}$ (represented by the green hexagons and light-blue circles, respectively) is compared to the theoretically calculated dependence (orange line) in Figure 5.4b. Theory predicts that the gap decreases as a result of the formation of Landau levels [2], which causes the top of the valence band to increase in energy and

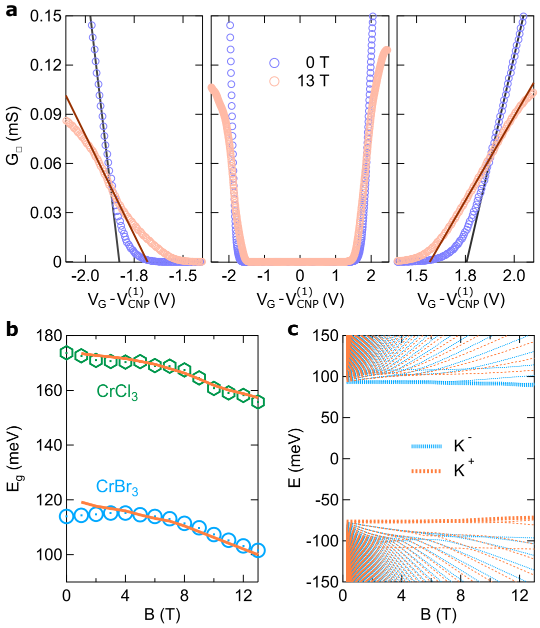

Figure 5.4: **Magnetic field dependence of the BLG band gap.** **(a)**, Square conductance $G_\square$ as a function of gate voltage V_G shifted with respect to the value of CNP $V_{CNP}^{(1)}$, measured in a BLG/CrCl$_3$ heterostructure at 0 T and with an applied magnetic field of 13 T. The left and the right panels zoom in on the onset of conduction for holes and electrons: the corresponding threshold voltages V_{th}^h and V_{th}^e shift upon increasing the magnetic field, resulting in a decrease in (V_{th}^e-V_{th}^h) and therefore in a decrease in the band gap extracted using Eq. (1). **(b)**, Magnetic field dependence of the energy gap for BLG-on-CrCl$_3$ (green empty hexagons) and for BLG-on-CrBr$_3$ (light-blue empty circles); the size of the symbols corresponds to the experimental uncertainty associated with the error in the determination of the threshold voltages. The continuous orange lines represent the calculated band gap considering appropriate screened interlayer asymmetry potentials and including a screening potential for non-zero magnetic fields, as predicted by theory to calculate the Landau level spectrum. The experimental data are in excellent agreement with the theoretical predictions. **(c)**, Landau levels calculated for a screened interlayer asymmetry potential of $|\Delta| = 215$ meV resulting in an experimentally observed gap of $E_g = 170$ meV at zero applied magnetic field. The dependence of the gap on the magnetic field is determined by the difference in the energies of the lowest Landau level in the conduction and valence bands.

the bottom of the conduction band to decrease (see Figure 5.4c). This is a counter-intuitive behavior that contrasts what would be expected for electrons in a conventional two-dimensional electron gas (i.e., electrons described by a scalar wave function, for which the formation of Landau levels would lead to an increase in the gap at finite B). At a quantitative level, a change in the gap between 10% and 15% is expected as B increases up to 13 T, which results in perfect agreement with experiments without the need to introduce any free fitting parameters. To confirm the soundness of this result and exclude significant contributions of other mechanisms to the observed magnetic field dependence of the band gap, we also considered whether the charge transferred from BLG to $\mathrm{CrX_3}$ depends on the magnetic field. This is important because a change in charge transfer would lead to a corresponding change in the perpendicular electric field and thus in the size of the band gap. Nevertheless, the analysis of the magnetic field dependence of the CNP (Section S2 of the Supporting Information) shows that, even if charge transfer slightly decreases at high magnetic fields, the quantitative effect on the gap is very small, close to the sensitivity of the experiment, and negligible in a first approximation.

Such excellent quantitative agreement shows the usefulness of Eq. (1) and confirms its validity. To understand heuristically the origin of Eq. (1) we look at how the electrostatic and electrochemical potentials vary in the different regions of our devices (see Figure 5.1b), i.e., in region 1 where BLG is in contact with the $\mathrm{CrX_3}$ layer and in region 2 where BLG is on hBN. A change ΔV_{G} in applied gate voltage causes a variation in the electrochemical and electrostatic potentials $\Delta\mu$ and $\Delta\phi$ in both regions, with the two quantities related by $\Delta\mu = e\Delta\phi + \Delta E_F$ (ΔE_F is the change in Fermi energy induced by the variation in the density of accumulated electrons in BLG, i.e., $\Delta E_F = C\Delta V_{\mathrm{G}}/e\rho_{\mathrm{BLG}}$). Since the entire structure is at equilibrium for all gate voltages, the change in electrochemical potential is uniform, such that $\Delta\mu^{(1)} = \Delta\mu^{(2)}$, or $e\Delta\phi^{(1)} + \Delta E_F^{(1)} = e\Delta\phi^{(2)} + \Delta E_F^{(2)}$. Whenever the electrochemical potential in region 1 is inside the gap of BLG –and at sufficiently low temperature- $\Delta E_{\mathrm{F}}{}^{(1)} = 0$, because no states are available to add charge. Under these conditions, therefore, a variation in gate voltage only changes the electrostatic potential in region 1, so that we have $e\Delta\phi^{(2)} + \Delta E_F^{(2)} = e\Delta\phi^{(1)}$. As $\Delta E_{\mathrm{F}}^{(2)} = C\Delta V_{\mathrm{G}}/e\rho_{\mathrm{BLG}}$, we obtain $e\Delta\phi^{(1)} - e\Delta\phi^{(2)} = C\Delta V_{\mathrm{G}}/e\rho_{\mathrm{BLG}}$, a relation that determines the relative band alignment between region 1 and 2. While we sweep the gate voltage from $V_\mathrm{G} = V_{th}^h$ to $V_\mathrm{G} = V_{th}^e$, this relation always holds, because throughout this V_G interval the electrochemical potential in region 1 is inside the gap. Since at $V_\mathrm{G} = V_{th}^h$ the electrochemical potential in region 2 is aligned with the valence band edge in region 1 and at $V_\mathrm{G} = V_{th}^e$ the electrochemical potential in region 2 is aligned with the conduction band edge in region 1, we obtain $E_g = e\Delta\phi^{(1)} - e\Delta\phi^{(2)}$, and Eq. (1) then follows directly using that $e\Delta\phi^{(1)} - e\Delta\phi^{(2)} = C\Delta V_\mathrm{G}/e\rho_\mathrm{BLG}$. We interpret this result by saying that a change in V_G lowers the bands of BLG in region 1 and in region 2 (which effectively forms the source and drain contacts to the transistor channel), but changes E_F only in region 2 (because only region 2 is gapless), and it is this change in Fermi energy that shifts the electrochemical potential from the valence to the conduction band edge.

The argument above relies on the assumption that charge transferred from BLG to the underlying CrX$_3$ layer is fixed: at low temperature, a change in V_G does not change the charge accumulated in the CrX$_3$ layer. This is not what would happen if electrons in CrX$_3$ behaved as independent, non-interacting particles, i.e., if CrX$_3$ could be described as a conventional semiconductor. We attribute this behavior to the very narrow bands of CrX$_3$ –electrons added to CrX$_3$ are virtually localized on the Cr orbitals– which make electrons hosted in these materials strongly correlated, because the strength of their Coulomb interaction is larger than the bandwidth. As a result, at low temperature, the electrons transferred from BLG to the surface of CrX$_3$ create an energetically stable correlated state (we imagine a spatially ordered distribution of electrons localized on Cr atoms that minimizes energy), which has an energy gap for adding or removing electrons. This assumption appears to be fully consistent with the behavior observed in BLG interfaces with CrCl$_3$ and CrBr$_3$, for which Eq. (1) works perfectly, but not for BLG-on-CrI$_3$, for which Eq. (1) gives a factor of 2 deviation as compared to the actual gap. The reason for this difference between the different CrX$_3$ compounds likely originates from the fact that the charge transferred from BLG to CrI$_3$ does vary as V_G is varied (possibly because the width of the conduction band of CrI$_3$ is somewhat larger than that of CrCl$_3$ and CrBr$_3$), an observation that seems consistent with the pronounced temperature dependence of charge transfer from BLG to CrI$_3$ (see Figure 5.2e). This conclusion underscores the unconventional nature of the semiconducting properties of chromium trihalides, which calls for more detailed future investigations, and the fact that the study of transport through BLG/CrX_3 interfaces allows differences in the electronic properties of the different members of this family to be evidenced.

In summary, we have performed a systematic analysis of different phenomena determining the transport properties of vdW interfaces based on BLG and chromium trihalide crystals ($CrCl_3$, $CrBr_3$ and CrI_3). In all cases, a very large charge transfer from graphene to CrX_3 is found to occur, which causes the opening of a band gap in BLG. A detailed comparison shows that the values of the gap determined experimentally are in excellent agreement with the latest ab initio calculations, which include the effect of the polarizability of the σ bands in the graphene honeycomb lattice. We furthermore show that it is possible to determine the band gap quantitatively by looking exclusively at the low-temperature gate voltage dependence of the conductivity, a finding that we exploit to determine how the band gap depends on the applied magnetic field. Besides providing indications as to the correlated nature of electrons transferred onto the very narrow conduction band of CrX_3, our work establishes a remarkable quantitative agreement between different electronic properties of BLG and corresponding theoretical predictions.

Supporting Information

The Supporting Information is available free of charge on the ACS publications website at https://pubs.acs.org/doi/10.1021/acs.nanolett.2c02369.

- Transfer curves for BLG-on-$CrBr_3$ and BLG-on-CrI_3 devices; Magnetic field dependence of charge neutrality point.

Acknowledgements

The authors gratefully acknowledge Alexandre Ferreira for technical support, and Nicolas Ubrig and Sergey Slizovskiy for fruitful discussions. We acknowledge support from the Swiss National Science Foundation, the EU Graphene Flagship project, EPSRC

CDT Graphene-NOWNANO, and EPSRC grants EP/S030719/1 and EP/V007033/1. Z. W. acknowledges the National Natural Science Foundation of China (Grants no. 11904276) and the Fundamental Research Funds for the Central Universities. K. W. and T. T. acknowledge support from the Elemental Strategy Initiative conducted by the MEXT, Japan (Grant Number JPMXP0112101001) and JSPS KAKENHI (Grant Numbers 19H05790, 20H00354, and 21H05233).

5.A Transfer curves for BLG-on-CrBr$_3$ and BLG-on-CrI$_3$ devices

In the main text we show that the gate dependence of the square conductance of BLG-on-CrCl$_3$ devices exhibits two characteristic features, which originate from the two different regions forming our samples. Specifically, we observe a pronounced suppression of the square conductance at large gate voltages, around the charge neutrality point (CNP) of BLG-on-CrX$_3$ ($V_{CNP}^{(1)}$), as well as a smaller conductance dip in correspondence of the CNP of BLG-on-hBN ($V_{CNP}^{(2)}$).

For BLG-on-CrBr$_3$ and BLG-on-CrI$_3$ the data in the main text only focus on the part at high gate voltages and do not show the suppression of the square conductance close to $V_G = 0$ V, in correspondence of the CNP of BLG-on-hBN. For completeness, in Figure 5.5 we show the transfer curves in the full data range also for the CrBr$_3$ and CrI$_3$ samples, to confirm that the behavior of these devices is analogous to that of BLG-on-CrCl$_3$ devices. Remarkably, the suppression of square conductance around $V_{CNP}^{(2)}$ is very pronounced for BLG-on-CrBr$_3$ as compared to the other samples, suggesting that for this device a gap is formed also close to the CNP of BLG-on-hBN, probably due to the close relative alignment of BLG and hBN. Albeit unrelated to the main subject of the present work, this observation is interesting in its own right, because the opening of a gap in aligned monolayer graphene on hBN is known to occur ([56, 57, 58]), but to the best of our knowledge the same phenomenon has not yet been reported for BLG on hBN.

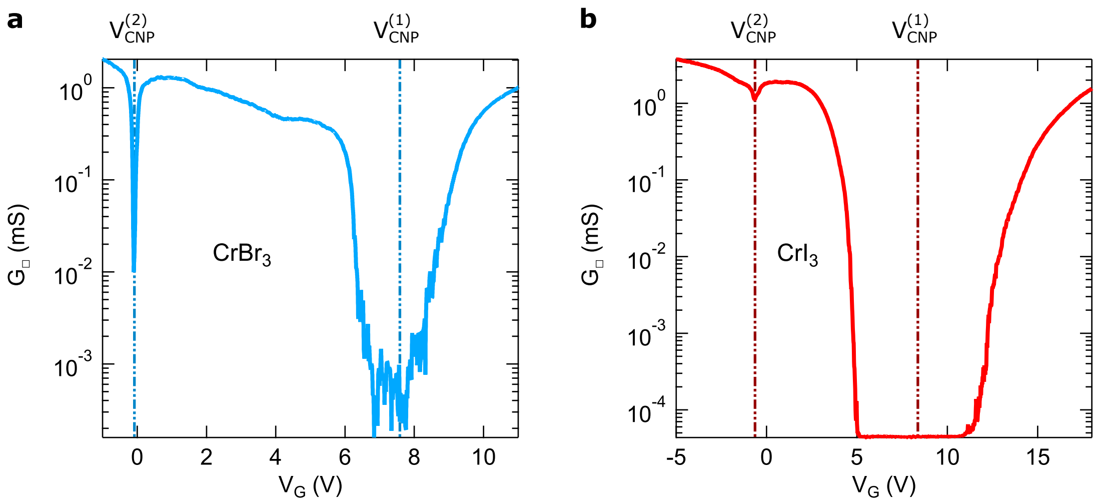

Figure 5.5: Transfer curves $G_\square$-vs-V_G measured at T = 250 mK in the full gate voltage range for BLG-on-$CrBr_3$ (**a**) and BLG-on-CrI_3 (**b**) devices. The dashed lines indicate the positions of CNP of BLG-on-CrX_3 ($V_{CNP}^{(1)}$) and of BLG-on-hBN ($V_{CNP}^{(2)}$).

5.B Magnetic field dependence of charge neutrality point

In the main text we discuss the dependence of the band gap in BLG-on-$CrCl_3$ and BLG-on-$CrBr_3$ devices on magnetic field and find (see Figure 4b) a sizable decrease as the field is increased from 0 T to 13 T (the gap decreases by more than 10% in BLG-on-$CrCl_3$ and by nearly 20% in BLG-on-$CrBr_3$). The effect is in quantitative agreement with predictions that take into account the formation of Landau levels in BLG, without the need to introduce any fitting parameters. For completeness, here we analyze the evolution of the position of charge neutrality point $V_{CNP}^{(1)}$ with magnetic field to investigate whether the charge transferred from BLG to the magnetic materials does depend on magnetic field. This is important, because a strong dependence of the transferred charge on field would imply that another mechanism needs to be considered when analysing how the band gap depends on magnetic field.

As visible in Figure 5.6, for both $CrBr_3$ and $CrCl_3$ we observe that $V_{CNP}^{(1)}$ shifts to lower gate voltages upon increasing magnetic field from 0 T to 13 T, indicating that the charge transferred from BLG to the magnetic materials slightly decreases at higher field. At a quantitative level, $V_{CNP}^{(1)}$ changes by approximately 1% for CrCl$_3$ and by nearly 2% for CrBr$_3$, which implies a correspondingly small decrease in perpendicular electric field and in the size of the band gap E_g. The change in gap due to this effect is approximately one order of magnitude smaller than the change in band gap observed in the experiments. This observation shows that the change in gap caused by the change in charge transfer is at most 10% of the variation in band gap actually observed in the experiments, and confirms the validity of the analysis reported in the main text. In summary, the change in gap due to the magnetic field dependence of the transferred charge is small, close to the sensitivity of the experiments, and negligible in a first approximation.

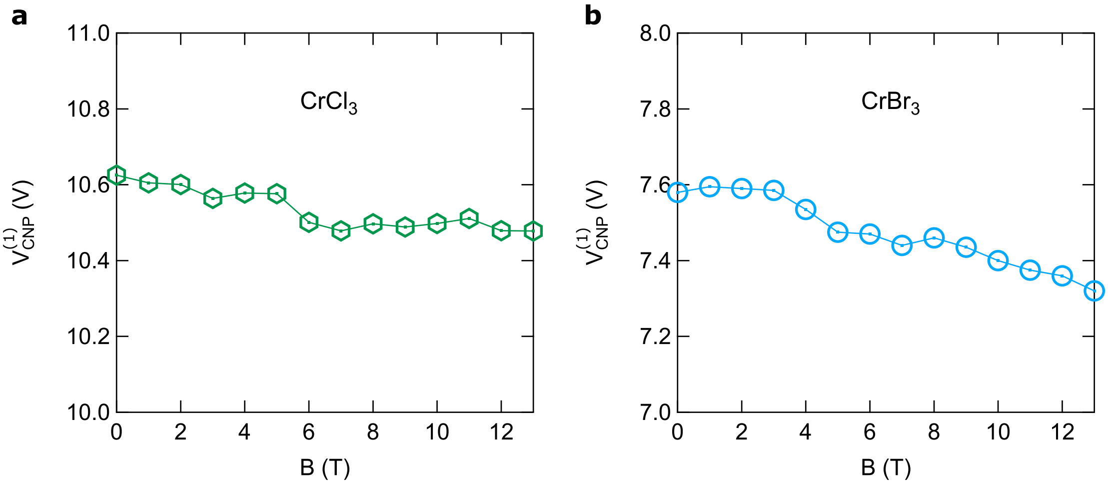

Figure 5.6: Magnetic field dependence of charge neutrality point $V_{CNP}^{(1)}$ for BLG-on-CrCl$_3$ (**a**) and BLG-on-CrBr$_3$ (**b**) devices.

Bibliography

[1] G. Tenasini, D. Soler-Delgado, Z. Wang, F. Yao, D. Dumcenco, E. Giannini, K. Watanabe, T. Taniguchi, C. Moulsdale, A. Garcia-Ruiz, V. I. Fal'ko, I. Gutiérrez-Lezama, and A. F. Morpurgo, Band Gap Opening in Bilayer Graphene-CrCl3/CrBr3/CrI3 van der Waals Interfaces *Nano Letters*, vol. 22, no. 16, pp. 6760–6766, 2022. PMID: 35930625.

[2] A. Varlet, D. Bischoff, P. Simonet, K. Watanabe, T. Taniguchi, T. Ihn, K. Ensslin, M. Mucha-Kruczyński, and V. I. Fal'ko, Anomalous Sequence of Quantum Hall Liquids Revealing a Tunable Lifshitz Transition in Bilayer Graphene *Physical Review Letter*, vol. 113, p. 116602, Sep 2014.

[3] R. Ribeiro-Palau, C. Zhang, K. Watanabe, T. Taniguchi, J. Hone, and C. R. Dean, Twistable electronics with dynamically rotatable heterostructures *Science*, vol. 361, no. 6403, pp. 690–693, 2018.

[4] N. R. Finney, M. Yankowitz, L. Muraleetharan, K. Watanabe, T. Taniguchi, C. R. Dean, and J. Hone, Tunable crystal symmetry in graphene–boron nitride heterostructures with coexisting moiré superlattices *Nature Nanotechnology*, vol. 14, pp. 1029–1034, Nov. 2019.

[5] A. Avsar, J. Y. Tan, T. Taychatanapat, J. Balakrishnan, G. K. Koon, Y. Yeo, J. Lahiri, A. Carvalho, A. S. Rodin, E. C. O'Farrell, G. Eda, A. H. C. Neto, and B. Özyilmaz, Spin–orbit proximity effect in graphene *Nature Communications*, vol. 5, p. 4875, 9 2014.

[6] Z. Wang, D. Ki, H. Chen, H. Berger, A. H. MacDonald, and A. F. Morpurgo, Strong interface-induced spin–orbit interaction in graphene on WS_2 *Nature Communications*, vol. 6, p. 8339, 9 2015.

[7] Z. Wang, D.-K. Ki, J. Y. Khoo, D. Mauro, H. Berger, L. S. Levitov, and A. F. Morpurgo, Origin and Magnitude of 'Designer' Spin-Orbit Interaction in Graphene on Semiconducting Transition Metal Dichalcogenides *Physical Review X*, vol. 6, p. 041020, Oct. 2016.

[8] M. Gmitra and J. Fabian, Proximity Effects in Bilayer Graphene on Monolayer WSe_2: Field-Effect Spin Valley Locking, Spin-Orbit Valve, and Spin Transistor *Physical Review Letter*, vol. 119, p. 146401, Oct 2017.

[9] T. S. Ghiasi, J. Ingla-Aynés, A. A. Kaverzin, and B. J. van Wees, Large Proximity-Induced Spin Lifetime Anisotropy in Transition-Metal Dichalcogenide/Graphene Heterostructures *Nano Letters*, vol. 17, pp. 7528–7532, Dec. 2017.

[10] J. Y. Khoo, A. F. Morpurgo, and L. Levitov, On-Demand Spin–Orbit Interaction from Which-Layer Tunability in Bilayer Graphene *Nano Letters*, vol. 17, no. 11, pp. 7003–7008, 2017. PMID: 29058917.

[11] L. A. Benítez, J. F. Sierra, W. Savero Torres, A. Arrighi, F. Bonell, M. V. Costache, and S. O. Valenzuela, Strongly anisotropic spin relaxation in graphene–transition metal dichalcogenide heterostructures at room temperature *Nature Physics*, vol. 14, pp. 303–308, Mar. 2018.

[12] D. J. Terry, V. Zólyomi, M. Hamer, A. V. Tyurnina, D. G. Hopkinson, A. M. Rakowski, S. J. Magorrian, N. Clark, Y. M. Andreev, O. Kazakova, K. Novoselov, S. J. Haigh, V. I. Fal'ko, and R. Gorbachev, Infrared-to-violet tunable optical activity in atomic films of GaSe, InSe, and their heterostructures *2D Materials*, vol. 5, p. 041009, sep 2018.

[13] N. Ubrig, E. Ponomarev, J. Zultak, D. Domaretskiy, V. Zólyomi, D. Terry, J. Howarth, I. Gutiérrez-Lezama, A. Zhukov, Z. R. Kudrynskyi, Z. D. Kovalyuk, A. Patané, T. Taniguchi, K. Watanabe, R. V. Gorbachev, V. I. Fal'ko, and A. F. Morpurgo, Design of van der Waals interfaces for broad-spectrum optoelectronics *Nature Materials*, vol. 19, pp. 299–304, 2 2020.

[14] D. Zhong, K. L. Seyler, X. Linpeng, R. Cheng, N. Sivadas, B. Huang, E. Schmidgall, T. Taniguchi, K. Watanabe, M. A. McGuire, W. Yao, D. Xiao, K.-M. C. Fu, and X. Xu, Van der Waals engineering of ferromagnetic semiconductor heterostructures for spin and valleytronics *Science Advances*, vol. 3, p. e1603113, May 2017.

[15] M. Gibertini, M. Koperski, A. F. Morpurgo, and K. S. Novoselov, Magnetic 2D materials and heterostructures *Nature Nanotechnology*, vol. 14, pp. 408–419, May 2019.

[16] C. Gong and X. Zhang, Two-dimensional magnetic crystals and emergent heterostructure devices *Science*, vol. 363, p. eaav4450, Feb. 2019.

[17] K. F. Mak, J. Shan, and D. C. Ralph, Probing and controlling magnetic states in 2D layered magnetic materials *Nature Reviews Physics*, vol. 1, pp. 646–661, Nov. 2019.

[18] B. Huang, M. A. McGuire, A. F. May, D. Xiao, P. Jarillo-Herrero, and X. Xu, Emergent phenomena and proximity effects in two-dimensional magnets and heterostructures *Nature Materials*, vol. 19, pp. 1276–1289, Dec. 2020.

[19] H. Kurebayashi, J. H. Garcia, S. Khan, J. Sinova, and S. Roche, Magnetism, symmetry and spin transport in van der Waals layered systems *Nature Reviews Physics*, vol. 4, pp. 150–166, jan 2022.

[20] Z. Qiao, W. Ren, H. Chen, L. Bellaiche, Z. Zhang, A. H. MacDonald, and Q. Niu, Quantum Anomalous Hall Effect in Graphene Proximity Coupled to an Antiferromagnetic Insulator *Physical Review Letter*, vol. 112, p. 116404, Mar 2014.

[21] J. C. Leutenantsmeyer, A. A. Kaverzin, M. Wojtaszek, and B. J. V. Wees, Proximity induced room temperature ferromagnetism in graphene probed with spin currents *2D Materials*, vol. 4, p. 014001, 11 2016.

[22] C. Tang, B. Cheng, M. Aldosary, Z. Wang, Z. Jiang, K. Watanabe, T. Taniguchi, M. Bockrath, and J. Shi, Approaching quantum anomalous Hall effect in proximity-coupled YIG/graphene/h-BN sandwich structure *APL Materials*, vol. 6, p. 026401, 11 2017.

[23] K. L. Seyler, D. Zhong, B. Huang, X. Linpeng, N. P. Wilson, T. Taniguchi, K. Watanabe, W. Yao, D. Xiao, M. A. McGuire, K. M. C. Fu, and X. Xu, Valley Manipulation by Optically Tuning the Magnetic Proximity Effect in WSe_2/CrI_3 Heterostructures *Nano Letters*, vol. 18, pp. 3823–3828, 6 2018.

[24] C. Cardoso, D. Soriano, N. A. García-Martínez, and J. Fernández-Rossier, Van der Waals Spin Valves *Physical Review Letter*, vol. 121, p. 067701, Aug 2018.

[25] M. U. Farooq and J. Hong, Switchable valley splitting by external electric field effect in graphene/CrI_3 heterostructures *npj 2D Materials and Applications*, vol. 3, pp. 1–7, 12 2019.

[26] C. Tang, Z. Zhang, S. Lai, Q. Tan, and W. Gao, Magnetic Proximity Effect in Graphene/$CrBr_3$ van der Waals Heterostructures *Advanced Materials*, vol. 32, p. 1908498, 4 2020.

[27] Y. Wu, Q. Cui, M. Zhu, X. Liu, Y. Wang, J. Zhang, X. Zheng, J. Shen, P. Cui, H. Yang, and S. Wang, Magnetic Exchange Field Modulation of Quantum Hall Ferromagnetism in 2D van der Waals $CrCl_3$/Graphene Heterostructures *ACS Applied Materials and Interfaces*, vol. 13, pp. 10656–10663, 3 2021.

[28] M. Vila, J. H. Garcia, and S. Roche, Valley-polarized quantum anomalous Hall phase in bilayer graphene with layer-dependent proximity effects *Physical Review B*, vol. 104, p. L161113, 10 2021.

[29] T. S. Ghiasi, A. A. Kaverzin, A. H. Dismukes, D. K. de Wal, X. Roy, and B. J. van Wees, Electrical and thermal generation of spin currents by magnetic bilayer graphene *Nature Nanotechnology*, vol. 16, pp. 788–794, 5 2021.

[30] M. M. Ugeda, A. J. Bradley, S. F. Shi, F. H. D. Jornada, Y. Zhang, D. Y. Qiu, W. Ruan, S. K. Mo, Z. Hussain, Z. X. Shen, F. Wang, S. G. Louie, and M. F. Crommie, Giant bandgap renormalization and excitonic effects in a monolayer transition metal dichalcogenide semiconductor *Nature Materials*, vol. 13, pp. 1091–1095, 8 2014.

[31] Q. Tong, M. Chen, and W. Yao, Magnetic Proximity Effect in a van der Waals Moiré Superlattice *Physical Review Applied*, vol. 12, p. 024031, Aug 2019.

[32] B. Zhou, J. Balgley, P. Lampen-Kelley, J. Q. Yan, D. G. Mandrus, and E. A. Henriksen, Evidence for charge transfer and proximate magnetism in graphene–$\alpha-RuCl_3$ heterostructures *Physical Review B*, vol. 100, p. 165426, 10 2019.

[33] S. Jiang, L. Li, Z. Wang, K. F. Mak, and J. Shan, Controlling magnetism in 2D CrI_3 by electrostatic doping *Nature Nanotechnology*, vol. 13, pp. 549–553, 7 2018.

[34] D. Zhong, K. L. Seyler, X. Linpeng, N. P. Wilson, T. Taniguchi, K. Watanabe, M. A. McGuire, K. M. C. Fu, D. Xiao, W. Yao, and X. Xu, Layer-resolved magnetic proximity effect in van der Waals heterostructures *Nature Nanotechnology*, vol. 15, pp. 187–191, 1 2020.

[35] T. P. Lyons, D. Gillard, A. Molina-Sánchez, A. Misra, F. Withers, P. S. Keatley, A. Kozikov, T. Taniguchi, K. Watanabe, K. S. Novoselov, J. Fernández-Rossier, and A. I. Tartakovskii, Interplay between spin proximity effect and

charge-dependent exciton dynamics in $MoSe_2/CrBr_3$ van der Waals heterostructures *Nature Communications*, vol. 11, pp. 1–9, 11 2020.

[36] S. Mashhadi, Y. Kim, J. Kim, D. Weber, T. Taniguchi, K. Watanabe, N. Park, B. Lotsch, J. H. Smet, M. Burghard, and K. Kern, Spin-Split Band Hybridization in Graphene Proximitized with alpha-$RuCl_3$ Nanosheets *Nano Letters*, vol. 19, pp. 4659–4665, July 2019.

[37] K. S. Novoselov, E. McCann, S. V. Morozov, V. I. Fal'ko, M. I. Katsnelson, U. Zeitler, D. Jiang, F. Schedin, and A. K. Geim, Unconventional quantum Hall effect and Berry's phase of 2π in bilayer graphene *Nature Physics*, vol. 2, pp. 177–180, 2 2006.

[38] E. McCann and V. I. Fal'ko, Landau-Level Degeneracy and Quantum Hall Effect in a Graphite Bilayer *Physical Review Letters*, vol. 96, p. 086805, 3 2006.

[39] H. Wang, V. Eyert, and U. Schwingenschlögl, Electronic structure and magnetic ordering of the semiconducting chromium trihalides $CrCl_3$, $CrBr_3$, and CrI_3 *Journal of Physics: Condensed Matter*, vol. 23, p. 116003, mar 2011.

[40] W.-B. Zhang, Q. Qu, P. Zhu, and C.-H. Lam, Robust intrinsic ferromagnetism and half semiconductivity in stable two-dimensional single-layer chromium trihalides *J. Mater. Chem. C*, vol. 3, pp. 12457–12468, 2015.

[41] M. A. McGuire, H. Dixit, V. R. Cooper, and B. C. Sales, Coupling of Crystal Structure and Magnetism in the Layered, Ferromagnetic Insulator CrI_3 *Chemistry of Materials*, vol. 27, no. 2, pp. 612–620, 2015.

[42] J. Liu, Q. Sun, Y. Kawazoe, and P. Jena, Exfoliating biocompatible ferromagnetic Cr-trihalide monolayers *Phys. Chem. Chem. Phys.*, vol. 18, pp. 8777–8784, 2016.

[43] B. Huang, G. Clark, E. Navarro-Moratalla, D. R. Klein, R. Cheng, K. L. Seyler, D. Zhong, E. Schmidgall, M. A. McGuire, D. H. Cobden, W. Yao, D. Xiao, P. Jarillo-Herrero, and X. Xu, Layer-dependent ferromagnetism in a van der Waals crystal down to the monolayer limit *Nature*, vol. 546, pp. 270–273, jun 2017.

[44] Z. Wang, I. Gutiérrez-Lezama, N. Ubrig, M. Kroner, M. Gibertini, T. Taniguchi, K. Watanabe, A. Imamoğlu, E. Giannini, and A. F. Morpurgo, Very large tunneling magnetoresistance in layered magnetic semiconductor CrI$_3$ *Nature Communications*, vol. 9, pp. 1–8, jun 2018.

[45] Z. Wang, M. Gibertini, D. Dumcenco, T. Taniguchi, K. Watanabe, E. Giannini, and A. F. Morpurgo, Determining the phase diagram of atomically thin layered antiferromagnet CrCl$_3$ *Nature Nanotechnology*, vol. 14, pp. 1116–1122, nov 2019.

[46] S. Acharya, D. Pashov, B. Cunningham, A. N. Rudenko, M. Rösner, M. Grüning, M. van Schilfgaarde, and M. I. Katsnelson, Electronic structure of chromium trihalides beyond density functional theory *Physical Review B*, vol. 104, p. 155109, Oct 2021.

[47] S. Slizovskiy, A. Garcia-Ruiz, A. I. Berdyugin, N. Xin, T. Taniguchi, K. Watanabe, A. K. Geim, N. D. Drummond, and V. I. Fal'ko, Out-of-Plane Dielectric Susceptibility of Graphene in Twistronic and Bernal Bilayers *Nano Letters*, vol. 21, no. 15, pp. 6678–6683, 2021.

[48] P. J. Zomer, S. P. Dash, N. Tombros, and B. J. van Wees, A transfer technique for high mobility graphene devices on commercially available hexagonal boron nitride *Applied Physics Letters*, vol. 99, p. 232104, Dec. 2011.

[49] S. Jiang, L. Li, Z. Wang, J. Shan, and K. F. Mak, Spin tunnel field-effect transistors based on two-dimensional van der Waals heterostructures *Nature Electronics*, vol. 2, pp. 159–163, 4 2019.

[50] E. McCann, Asymmetry gap in the electronic band structure of bilayer graphene *Physical Review B*, vol. 74, p. 161403, Oct 2006.

[51] T. Ohta, A. Bostwick, T. Seyller, K. Horn, and E. Rotenberg, Controlling the Electronic Structure of Bilayer Graphene *Science*, vol. 313, pp. 951–954, 8 2006.

[52] E. V. Castro, K. S. Novoselov, S. V. Morozov, N. M. R. Peres, J. M. B. L. dos Santos, J. Nilsson, F. Guinea, A. K. Geim, and A. H. C. Neto, Biased Bilayer Graphene: Semiconductor with a Gap Tunable by the Electric Field Effect *Physical Review Letter*, vol. 99, p. 216802, Nov 2007.

[53] J. B. Oostinga, H. B. Heersche, X. Liu, A. F. Morpurgo, and L. M. Vandersypen, Gate-induced insulating state in bilayer graphene devices *Nature Materials*, vol. 7, pp. 151–157, 12 2008.

[54] A. B. Kuzmenko, I. Crassee, D. van der Marel, P. Blake, and K. S. Novoselov, Determination of the gate-tunable band gap and tight-binding parameters in bilayer graphene using infrared spectroscopy *Physical Review B*, vol. 80, p. 165406, Oct 2009.

[55] Y. Zhang, T. T. Tang, C. Girit, Z. Hao, M. C. Martin, A. Zettl, M. F. Crommie, Y. R. Shen, and F. Wang, Direct observation of a widely tunable bandgap in bilayer graphene *Nature*, vol. 459, pp. 820–823, 6 2009.

[56] G. Giovannetti, P. A. Khomyakov, G. Brocks, P. J. Kelly, and J. van den Brink, Substrate-induced band gap in graphene on hexagonal boron nitride: Ab initio density functional calculations *Physical Review B*, vol. 76, p. 073103, Aug 2007.

[57] B. Hunt, J. D. Sanchez-Yamagishi, A. F. Young, M. Yankowitz, B. J. LeRoy, K. Watanabe, T. Taniguchi, P. Moon, M. Koshino, P. Jarillo-Herrero, and R. C. Ashoori, Massive Dirac Fermions and Hofstadter Butterfly in a van der Waals Heterostructure *Science*, vol. 340, pp. 1427–1430, June 2013.

[58] L. A. Ponomarenko, R. V. Gorbachev, G. L. Yu, D. C. Elias, R. Jalil, A. A. Patel, A. Mishchenko, A. S. Mayorov, C. R. Woods, J. R. Wallbank, M. Mucha-Kruczynski, B. A. Piot, M. Potemski, I. V. Grigorieva, K. S. Novoselov, F. Guinea, V. I. Fal'ko, and A. K. Geim, Cloning of Dirac fermions in graphene superlattices *Nature*, vol. 497, pp. 594–597, May 2013.

Chapter 6

Semimetallic and semiconducting graphene-hBN multilayers with parallel or reverse stacking

Preface

The contents of this chapter represent the main body of a manuscript submitted to Physical Review B. A preprint is available on arXiv [1]. The manuscript was authored by Xi Chen[1,2], Christian Moulsdale[1,2], Vladimir Fal'ko[1,2,3] and Angelika Knothe[1,4].

Parts of material included in the manuscript are based on exploratory analytical and numerical calculations of the electronic structure performed by Xi Chen in support of their application for the degree of Master of Science, under the guidance and supervision of Christian Moulsdale, Angelika Knothe and Vladimir Fal'ko. Further refined calculations of the electronic structure and the topological character shown in Fig. 6.2 and 6.3 were performed by Christian Moulsdale and Angelika Knothe under the guidance and supervision of Vladimir Fal'ko. The writing of the manuscript, including the production of the figures, was primarily done by Angelika Knothe, with assistance from Christian Moulsdale and Vladimir Fal'ko.

---

[1] National Graphene Institute, University of Manchester, Manchester M13 9PL, UK

[2] Department of Physics and Astronomy, University of Manchester, Manchester M13 9PL, UK

[3] Henry Royce Institute, Institute for Advanced Materials, Manchester M13 9PL, UK

[4] Institut für Theoretische Physik, Universität Regensburg, D-93040 Regensburg, Germany

Abstract

We theoretically investigate 3D layered crystals of alternating graphene and hBN layers with different symmetries. Depending on the hopping parameters between the graphene layers, we find that these synthetic 3D materials can feature semimetallic, gapped, or Weyl semimetal phases. Our results demonstrate that 3D crystals stacked from individual 2D materials represent a new materials class with emergent properties different from their constituents.

6.1 Introduction

Thanks to the recent progress in the layer-to-layer assembly of two-dimensional atomic lattices, it is now possible to combine individual atomic layers to create new, synthetic crystals that would be difficult to achieve with any other bottom-up technique. Such layered three-dimensional (3D) materials with engineered stacking series can exhibit emergent characteristics different from the properties of their individual constituent layers. Moreover, such assembly of layers allows for multiple stacking orders of consecutive layers with different symmetries. Therefore, 3D crystals obtained from stacking individual atomic layers one by one represent yet a new materials class compared to the individual 2D sheets and their few-layer counterparts.

One widespread choice is to combine graphene with hexagonal boron nitride (hBN). Heterostructures of various numbers and stacking arrangements of graphene and hBN layers feature, e.g., diverse super-lattice moiré effects [2, 3, 4, 5, 6, 7, 8, 9], topological states [10, 11], correlated states and superconductivity [12, 13], dielectric and ferroelectric properties [14, 15, 16], and exotic Hofstadter butterflies [17, 18].

Here, we describe the hybrid tight-binding and $k.p$-theory for the low-energy states of 3D synthetic crystals constructed from alternately stacked graphene and hBN monolayers. At a single interface between graphene and hBN monolayers, the two lattices have slightly different lattice constants, and straining one lattice to fit the lattice constant of the other is energetically very costly [19]. However, in a 3D bulk system with hBN layers alternating on either side of each monolayer graphene, the adhesion energy

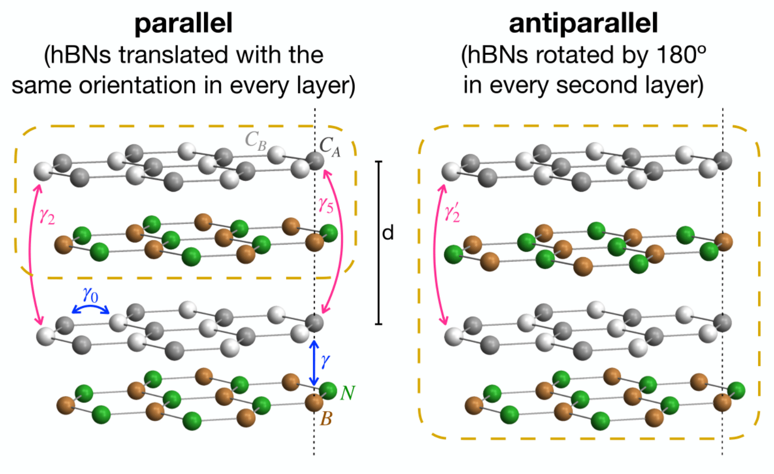

Figure 6.1: 3D crystals of graphene and hBN monolayers periodically stacked in the z-direction. Subsequent hBN layers are oriented either in parallel (left, all hBN layers translated copies with the same orientation) or antiparallel to each other (right, adjacent hBNs in every second layer rotated with respect to each other). Depending on the unknown hopping parameters γ_5, γ_2, and γ_2' between graphene sheets separated by the hBN layers, these artificial materials exhibit Weyl semimetal phases. The dashed orange boxes illustrate that the unit cell in the z-direction is twice as large for antiparallel stacking as for parallel arrangements.

would promote the favourable atomic stacking of carbon and boron/nitrogen atoms. Recent ab initio density functional theory [20] and diffusion Monte Carlo calculations [19] consistently revealed that the interplay of adhesion and strain favours carbon atoms to align with boron atoms to minimize the total potential energy[4].

We study the two extreme cases of periodic 3D stacking obtained by i) translating the hBN layers in the stacking process (hence all hBN layers are parallel to each other) or ii) alternatingly rotating the hBNs before placing them onto the graphene, resulting in adjacent hBN crystals in every second layer being antiparallel to each other (c.f. Fig. 6.1). For these two types of perfectly z-periodic sequencing, graphene/hBN stacks with parallel (translated) and antiparallel (alternatingly rotated) hBN layers, we study the resulting stacks' 3D band structures. We find that, depending on the interlayer graphene hopping parameters, such a 3D crystal can feature different types of semimetallic spectra, including overlapping electron and hole pockets and, in particular, type I and type II Weyl cones. Such Weyl semimetals are 3D phases of matter whose electronic properties and topology entail protected surface states and anomalous responses to external electric and magnetic fields [21, 22, 23, 24, 25, 26].

Hence, in this work, we propose a novel candidate for a Weyl material in which the 3D structure is obtained by successively stacking 2D atomic sheets [27]. Conversely, probing such widely different material characteristics may allow conclusions about the sign and the relative magnitude of the inter-layer hoppings in graphene/hBN stacks, which are notoriously difficult to determine theoretically and experimentally.

This manuscript is structured as follows: In section 6.2, we give the low-energy effective Hamiltonians for 3D graphene/hBN stacks with the two types of z-periodic stacking shown in Fig. 6.1, featuring parallel hBN layers or antiparallel hBN layers. Subsequently, in section 6.3, we discuss the possible 3D band structures which emerge for both cases as a function of different hopping parameters. We discuss our results in section 6.4 and give details of the derivations in the appendix.

6.2 Low-energy effective Hamiltonians

Starting from a hybrid $k.p$ theory-tight binding approach[28] for the differently stacked 3D graphene/hBN crystals in Fig. 6.1 we derive the low-energy effective Hamiltonians for the electrons on the graphene layers subject to perturbations from the adjacent hBNs [3, 29, 30]. Hybridization between graphene and hBN orbitals has been studied previously and used in earlier studies of, e.g., moiré superlattices of single graphene/hBN interfaces [8]. Here, we use second order perturbation theory in the interlayer hoppings to exclude the boron and nitrogen bands (see Appendix A for details of the calculation). For the 3D graphene/hBN stacks with translated (parallel, p) hBN layers the resulting low-energy Hamiltonian for the electrons in graphene read,

$$H_p = \begin{pmatrix} -\frac{2\gamma^2}{V_B}(1+\cos k_z d) + 2\gamma_5 \cos k_z d & v\pi^\dagger \\ v\pi & 2\gamma_2 \cos k_z d \end{pmatrix}, \tag{6.1}$$

operating in the space spanned the two-component wave function $\Psi = (\psi_{C_A}, \psi_{C_B})$ describing electronic amplitudes on the C_A and C_B sites of the graphene lattice. For the stacking sequence where the adjacent hBN layers are rotated by 180° with respect to each other (antiparallel, ap), the size of the unit cell doubles compared to the parallel stacking case and we find the low-energy Hamiltonian,

$$H_{ap} = \begin{pmatrix} -\frac{2\gamma^2}{V_B} & v\pi^\dagger & (1+e^{2idk_z})(\gamma_5 - \frac{\gamma^2}{V_B}) & 0 \\ v\pi & 0 & 0 & \gamma_2 + \gamma_2' e^{2idk_z} \\ (1+e^{-2idk_z})(\gamma_5 - \frac{\gamma^2}{V_B}) & 0 & -\frac{2\gamma^2}{V_B} & v\pi^\dagger \\ 0 & \gamma_2 + \gamma_2' e^{-2idk_z} & v\pi & -\frac{2\gamma^2}{V_B}(1+\cos k_z d) \end{pmatrix}, \tag{6.2}$$

written in the basis of C_A and C_B sites of two subsequent graphene layers. In the Hamiltonians above, $\pi = p_x + ip_y$ ($\mathbf{p} = -i\hbar\nabla$), $V_B \approx 3.34$ eV is the onsite potential of boron (measured with respect to the on-site potential of carbon), $v \approx 10^6$ m/s, and $d \approx 0.64$ nm is the distance between the graphene layers as indicated in Fig. 6.1. For a faithful description of low-energy features in the electronic structure it is crucial to retain all the relevant couplings between different atomic sites [29]. Here, we take into account γ (between carbon and boron atoms), as well as the inter-layer coupling parameters between graphene layers, γ_5, γ_2, and γ_2' between the in-equivalent carbon atoms C_A (separated by a boron atom) and C_B (separated by a void or a nitrogen atom). The precise values of these hoppings are a priori unknown. To explore the full parameter space, we we treat γ_5, γ_2, and γ_2' as free parameters in relation to $\gamma \approx 0.38$ eV in the following discussion. In the conclusion section of this manuscript, Sec. 6.4, we discuss how one may estimate the coupling parameters and how they may be manipulated in an experiment.

6.3 Semimetal band structures

The relative magnitude and sign of the hopping parameters between different atomic lattice sites determines the electronic properties of the 3D graphene/hBN crystals in Fig. 6.1. We separately discuss stacks with translated (parallel) and rotated (antiparallel) adjacent hBN layers.

6.3.1 Parallel stacking

We find that a 3D graphene/hBN crystal with parallely oriented hBN layers either features overlapping electron and hole pockets, or type I, or type II Weyl points depending

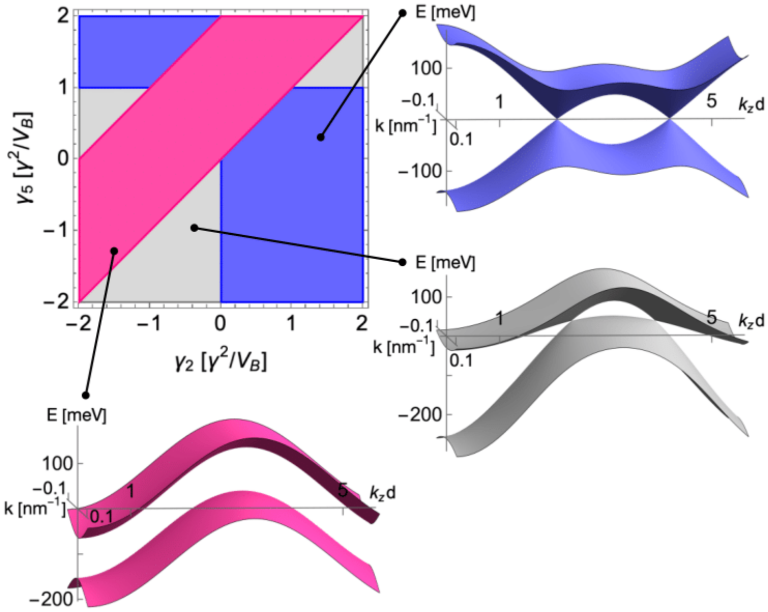

Figure 6.2: Phase diagram and possible dispersions of a 3D graphene/hBN stack with parallel hBN layers (left crystal stucture in Fig. 6.1). We find a gapped phase (magenta), and type I/II semimetal phases (blue/gray).Parameters for the dispersions: $\gamma_2 = -0.5\gamma^2/V_B$, $\gamma_5 = -\gamma^2/V_B$ (gray); $\gamma_2 = \gamma^2/V_B$, $\gamma_5 = 0$ (blue); $\gamma_2 = -\gamma^2/V_B$, $\gamma_5 = 0$ (magenta). At charge neutrality, the Fermi energy corresponds to zero energy, $E_F = 0$.

on the hopping parameters γ_2 and γ_5. Figure 6.2 demonstrates this parametric dependence of the electronic properties, showing the phase diagram in the plane spanned by the inter-layer hoppings and examples for the distinct possible 3D band structure types that we obtain from diagonalising H_p in Eq. 6.1. In the gapless phases, linear Weyl nodes[31, 23, 32, 27, 21, 33] form at momentum points $\mathbf{k}_0 = (0,0,k_{z0})$ with

$$k_{z0} = \pm\frac{1}{d}\arccos\left[-\frac{\gamma^2}{\gamma^2 + V_B(\gamma_2 - \gamma_5)}\right]. \tag{6.3}$$

These touchings can be type I Weyl nodes (closed or point-like Fermi surfaces, blue phase in Fig. 6.2) or type II Weyl nodes (overlap between electron and hole bands leading to open Fermi surfaces, gray phase in Fig. 6.2) [21, 26, 33], and we find them to be Chern-nontrivial with Chern numbers $C = \pm1$.

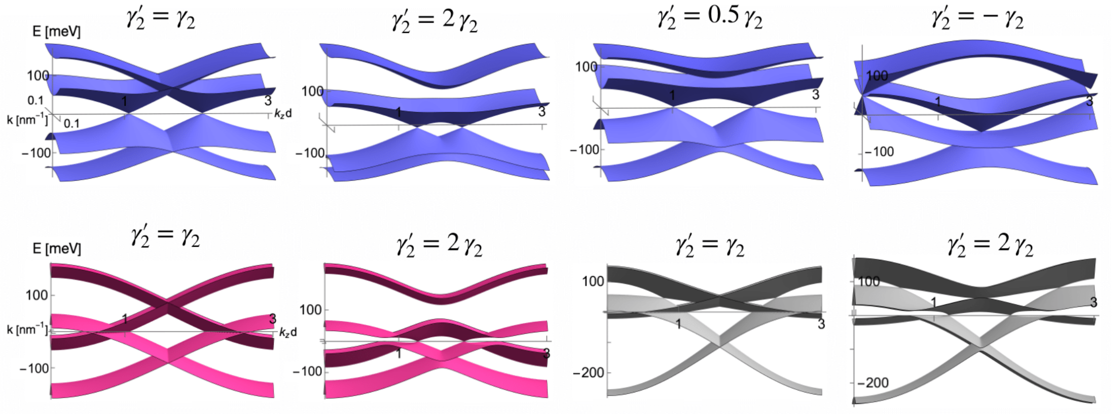

Figure 6.3: For a graphene/hBN stack where adjecent hBN layers are antiparallel to each other (right crystal stucture in Fig. 6.1), we identify the regimes with clearly distinguishable type I Weyl cones near the Fermi energy $E_F = 0$. Top row: $\gamma_2 = \gamma^2/V_B$, $\gamma_5 = 0$ (similar to the blue phase in Fig. 6.2). For most values of γ_2' the cones are well-isolated on the energy axes. Only in the case of a sign change, $\gamma_2 = -\gamma_2'$, the cones are obscured by overlapping bands. Bottom row: $\gamma_2 = -\gamma^2/V_B$, $\gamma_5 = 0$ (magenta) or $\gamma_2 = -0.5\gamma^2/V_B$, $\gamma_5 = -\gamma^2/V_B$ (gray). Most of the features are obscured by overlapping bands near the Fermi energy. Other choices of γ_2' yield similar pictures.

6.3.2 Antiparallel stacking

We diagonalize H_{ap} in Eq. 6.2 to obtain the 3D band structures of graphene/hBN stacks with antiparallel arrangement of adjacent hBN layers. We demonstrate in Fig. 6.3 that similarly to the stacks with parallel hBN layers, we find parametric regimes in which the bands feature well-separated Weyl nodes (blue dispersions, top row). For other choices of parameters the features of the bands (type II Weyl cones in the gray dispersion, band gaps in the magenta dispersions, bottom row) are occluded by overlapping or near-overlapping of the bands near the Fermi energy. Especially if the hoppings between C_B carbon atoms via a void and via a nitrogen atom are unequal, $\gamma_2' \neq \gamma_2$, we find substantial asymmetry between electron and hole bands. Note that the periodicity of the unit cell in the case of antiparallely stacked hBN layers is twice as large compared to the case of parallel stacking, c.f. Fig. 6.1, doubling the lattice constant along the z-axis.

6.4 Conclusion

We presented the possible electronic structure of 3D stacks of alternating graphene and hBN layers with different symmetries. The atomic arrangements we consider represent the most stable configurations for carbon and boron/nitrogen atoms in single adjacent layers[20, 19]. However, the hopping parameters between graphene atoms in different layers are currently unknown. We identify regimes with different electronic properties (semimetallic, gapped, Weyl semimetals) upon varying these hopping parameters. These regimes with different electronic band structures would make for distinctively different experimental signatures. Therefore, identifying signatures of the band structure in both transport and spectroscopy experiments may help to identify the relative sign and magnitude of these unknown material parameters and set boundaries for their values which are hard to determine microscopically otherwise. Moreover, we anticipate that these out-of-plane hopping parameters could be manipulated, e.g., by applying perpendicular pressure to the 3D stacks [34, 35, 36]. Depending on the relative scaling of the hopping between adjacent layers (γ) or graphene-graphene hopping over the next layer ($\gamma_2, \gamma_2', \gamma_5$), pressure may increase the chance of reaching the Weyl-semimetal phase in the phase diagramm, Fig. 6.2.

Individual layers of graphene and hBN are very commonly combined in heterostructures with increasing precision and control, making the proposed crystals of alternating monolayers achievable in experiment. Using these 3D stacks of graphene and hBN as examples, we have demonstrated that artificial 3D crystals of individual atomic layers represent a new 3D materials class with intriguing, potentially topologically non-trivial electronic properties only now achievable in experiments. Besides the cases of alternating sequencing studied in this work, one may consider other stacking sequences with longer periods[37, 38], stacking faults, interlayer twisting, and the combination of multiple different 2D materials. Such considerations are left for further studies.

6.A Derivation of the low-energy Hamiltonians

For the parallel stacking we start from the 4×4 Hamiltonian,

$$H = \begin{pmatrix} H_G & T^\dagger \\ T & H_{hBN} \end{pmatrix}, \tag{6.4}$$

in the basis of the graphene and hBN atomic sites (C_A, C_B, N, B), where,

$$\begin{aligned} H_G =& \begin{pmatrix} 2\gamma_5 \cos k_z d & v\pi^\dagger \\ v\pi & 2\gamma_2 \cos k_z d \end{pmatrix}, \quad H_{hBN} = \begin{pmatrix} V_N & 0 \\ 0 & V_B \end{pmatrix}, \\ T^\dagger =& \frac{1}{3}(1+e^{ik_z d}) \sum_j \begin{pmatrix} \gamma_{1N} & \gamma_{1B} e^{i\frac{2\pi j}{3}} \\ \gamma_{1N} e^{-i\frac{2\pi j}{3}} & \gamma_{1B} \end{pmatrix} e^{i(\mathbf{K}_j - \mathbf{K}_0)\cdot \mathbf{r}_0}, \\ \mathbf{K}_j =& \pm \frac{4\pi}{3a}(\cos\frac{2\pi j}{3}, -\sin\frac{2\pi j}{3}), \end{aligned} \tag{6.5}$$

and for the relaxed equilibrium stacking considered in the main text the interlayer offset is $\mathbf{r}_0 = (0, \frac{a}{\sqrt{3}})$. Eliminating the hBN sites,

$$H_p = H_G + T^\dagger (-H_{hBN})^{-1} T, \tag{6.6}$$

we arrive at the expression in Eq. 6.1 in the main text.

Similarly, for alternate stacking, we start from the Hamiltonian,

$$\tilde{H} = \begin{pmatrix} H_{GG} & \tilde{T}^\dagger \\ \tilde{T} & H_{hBNhBN} \end{pmatrix}, \tag{6.7}$$

in the basis $(C_A, C_B, \tilde{C}_A, \tilde{C}_B, N, B, \tilde{N}, \tilde{B})$, and,

$$H_{GG} = \begin{pmatrix} 0 & v\pi^\dagger & \gamma_5(1+e^{2ik_zd}) & 0 \\ v\pi & 0 & 0 & \gamma_2+\gamma_2' e^{2ik_zd} \\ \gamma_5(1+e^{-2ik_zd}) & 0 & 0 & v\pi^\dagger \\ 0 & \gamma_2+\gamma_2' e^{-2ik_zd} & v\pi & 0 \end{pmatrix}, \tag{6.8}$$

$$H_{hBNhBN} = \begin{pmatrix} V_N & 0 & 0 & 0 \\ 0 & V_B & 0 & 0 \\ 0 & 0 & V_N & 0 \\ 0 & 0 & 0 & V_B \end{pmatrix}, \quad \tilde{T}^\dagger = \begin{pmatrix} 0 & \gamma_1 & 0 & \gamma_1 e^{i2k_zd} \\ 0 & 0 & 0 & 0 \\ 0 & \gamma_1 & 0 & \gamma_1 \\ 0 & 0 & 0 & 0 \end{pmatrix}, \tag{6.9}$$

and we obtain H_{ap} in Eq. 6.2 via,

$$H_{ap} = H_{GG} + \tilde{T}^\dagger(-H_{hBNhBN})^{-1}\tilde{T}. \tag{6.10}$$

Bibliography

[1] X. Chen, C. Moulsdale, V. I. Fal'ko, and A. Knothe, Semimetallic and semiconducting graphene-hBN multilayers with parallel or reverse stacking arXiv:2210.16393, 2022.

[2] Z. Wang, Y. B. Wang, J. Yin, E. Tóvári, Y. Yang, L. Lin, M. Holwill, J. Birkbeck, D. J. Perello, S. Xu, J. Zultak, R. V. Gorbachev, A. V. Kretinin, T. Taniguchi, K. Watanabe, S. V. Morozov, M. Anđelković, S. P. Milovanović, L. Covaci, F. M. Peeters, A. Mishchenko, A. K. Geim, K. S. Novoselov, V. I. Fal'ko, A. Knothe, and C. R. Woods, Composite Super-Moiré Lattices in Double-Aligned Graphene Heterostructures *Science Advances*, vol. 5, p. eaay8897, Dec. 2019.

[3] P. Moon and M. Koshino, Electronic Properties of Graphene/Hexagonal-Boron-Nitride Moiré Superlattice *Physical Review B*, vol. 90, p. 155406, Oct. 2014.

[4] Y. Sakai, T. Koretsune, and S. Saito, Electronic Structure and Stability of Layered Superlattice Composed of Graphene and Boron Nitride Monolayer *Physical Review B*, vol. 83, p. 205434, May 2011.

[5] Y. Yang, J. Li, J. Yin, S. Xu, C. Mullan, T. Taniguchi, K. Watanabe, A. K. Geim, K. S. Novoselov, and A. Mishchenko, In Situ Manipulation of van Der Waals Heterostructures for Twistronics *Science Advances*, vol. 6, no. 49, p. eabd3655.

[6] L. Wang, S. Zihlmann, M.-H. Liu, P. Makk, K. Watanabe, T. Taniguchi, A. Baumgartner, and C. Schönenberger, New Generation of Moiré Superlattices in Doubly Aligned hBN/Graphene/hBN Heterostructures *Nano Letters*, vol. 19, pp. 2371–2376, Apr. 2019.

[7] N. R. Finney, M. Yankowitz, L. Muraleetharan, K. Watanabe, T. Taniguchi, C. R. Dean, and J. Hone, Tunable Crystal Symmetry in Graphene–Boron Nitride Heterostructures with Coexisting Moiré Superlattices *Nature Nanotechnology*, vol. 14, pp. 1029–1034, Nov. 2019.

[8] J. R. Wallbank, M. Mucha-Kruczyński, X. Chen, and V. I. Fal'ko, Moiré Superlattice Effects in Graphene/Boron-Nitride van Der Waals Heterostructures *Annalen der Physik*, vol. 527, no. 5-6, pp. 359–376, 2015.

[9] K. Zollner, M. Gmitra, and J. Fabian, Heterostructures of Graphene and hBN: Electronic, Spin-Orbit, and Spin Relaxation Properties from First Principles *Physical Review B*, vol. 99, p. 125151, Mar. 2019.

[10] C. Hu, V. Michaud-Rioux, W. Yao, and H. Guo, Moiré Valleytronics: Realizing Dense Arrays of Topological Helical Channels *Physical Review Letters*, vol. 121, p. 186403, Nov. 2018.

[11] C. Moulsdale, A. Knothe, and V. Fal'ko, Kagom\'e Network of Chiral Miniband-Edge States in Double-Aligned Graphene-Hexagonal Boron Nitride Structures *arXiv:2202.06667 [cond-mat]*, Feb. 2022.

[12] G. Chen, A. L. Sharpe, P. Gallagher, I. T. Rosen, E. J. Fox, L. Jiang, B. Lyu, H. Li, K. Watanabe, T. Taniguchi, J. Jung, Z. Shi, D. Goldhaber-Gordon, Y. Zhang, and F. Wang, Signatures of Tunable Superconductivity in a Trilayer Graphene Moiré Superlattice *Nature*, vol. 572, pp. 215–219, Aug. 2019.

[13] X. Sun, S. Zhang, Z. Liu, H. Zhu, J. Huang, K. Yuan, Z. Wang, K. Watanabe, T. Taniguchi, X. Li, M. Zhu, J. Mao, T. Yang, J. Kang, J. Liu, Y. Ye, Z. V. Han, and

Z. Zhang, Correlated States in Doubly-Aligned hBN/Graphene/hBN Heterostructures *Nature Communications*, vol. 12, p. 7196, Dec. 2021.

[14] Q. Li, M. Liu, Y. Zhang, and Z. Liu, Hexagonal Boron Nitride-Graphene Heterostructures: Synthesis and Interfacial Properties *Small*, vol. 12, no. 1, pp. 32–50, 2016.

[15] Y. Wang, S. Jiang, J. Xiao, X. Cai, D. Zhang, P. Wang, G. Ma, Y. Han, J. Huang, K. Watanabe, T. Taniguchi, A. S. Mayorov, and G. Yu, Tunable ferroelectricity in hBN intercalated twisted double-layer graphene *arXiv:2102.12398 [cond-mat]*, 2021.

[16] Z. Zhu, S. Carr, Q. Ma, and E. Kaxiras, Electric field-tunable layer polarization in graphene/boron nitride twisted quadrilayer superlattices *arXiv:2209.10636 [cond-mat]*, 2022.

[17] X. Chen, J. R. Wallbank, M. Mucha-Kruczyński, E. McCann, and V. I. Fal'ko, Zero-Energy Modes and Valley Asymmetry in the Hofstadter Spectrum of Bilayer Graphene van Der Waals Heterostructures with hBN *Physical Review B*, vol. 94, p. 045442, July 2016.

[18] T. Fabian, M. Kausel, L. Linhart, J. Burgdörfer, and F. Libisch, Wannier Diagram and Brown-Zak Fermions of Graphene on Hexagonal Boron-Nitride *arXiv:2111.01755 [cond-mat]*, Nov. 2021.

[19] M. Szyniszewski, E. Mostaani, V. Enaldiev, A. C. Ferrari, and N. D. Drummond *private communication*.

[20] G. Giovannetti, P. A. Khomyakov, G. Brocks, P. J. Kelly, and J. van den Brink, Substrate-Induced Band Gap in Graphene on Hexagonal Boron Nitride: Ab Initio Density Functional Calculations *Physical Review B*, vol. 76, p. 073103, Aug. 2007.

[21] N. P. Armitage, E. J. Mele, and A. Vishwanath, Weyl and Dirac Semimetals in Three-Dimensional Solids *Reviews of Modern Physics*, vol. 90, p. 015001, Jan. 2018.

[22] M. N. Chen, W. C. Chen, and Y. Zhou, Topological Hybrid Semimetal Phases and Anomalous Hall Effects in a Three Dimensional Magnetic Topological Insulator *Journal of Physics: Condensed Matter*, vol. 34, p. 025502, Oct. 2021.

[23] A. A. Burkov, Weyl Metals *Annual Review of Condensed Matter Physics*, vol. 9, pp. 359–378, Mar. 2018.

[24] C. Zeng, S. Nandy, and S. Tewari, Chiral anomaly induced nonlinear Nernst and thermal Hall effects in Weyl semimetals *Phys. Rev. B*, vol. 105, p. 125131, Mar 2022.

[25] S. Das, K. Das, and A. Agarwal, Nonlinear magnetoconductivity in Weyl and multi-Weyl semimetals in quantizing magnetic field *Phys. Rev. B*, vol. 105, p. 235408, Jun 2022.

[26] T. M. Ballestad, A. Cortijo, M. A. H. Vozmediano, and A. Qaiumzadeh, Unconventional thermo-electric transport in tilted Weyl semimetals *arXiv:2209.14331[cond-mat.mes-hall]*, 2022.

[27] A. A. Burkov and L. Balents, Weyl Semimetal in a Topological Insulator Multilayer *Physical Review Letters*, vol. 107, p. 127205, Sept. 2011.

[28] A. Garcia-Ruiz, H. Deng, V. V. Enaldiev, and V. I. Fal'ko, Full Slonczewski-Weiss-McClure Parametrization of Few-Layer Twistronic Graphene *Physical Review B*, vol. 104, p. 085402, Aug. 2021.

[29] E. McCann and V. I. Fal'ko, Landau-Level Degeneracy and Quantum Hall Effect in a Graphite Bilayer *Physical Review Letters*, vol. 96, p. 086805, Mar. 2006.

[30] P. Giraud, Study of the Electronic Structure of Hexagonal Boron Nitride on Metals Substrates Master's thesis, Université des Sciences et Technologies Lille 1 Universidad del Pais Vasco - Euskal Herriko Unibertsitatea, San Sebastian, Spain, Sept. 2012.

[31] J. Cayssol, Introduction to Dirac Materials and Topological Insulators *Comptes Rendus Physique*, vol. 14, pp. 760–778, Nov. 2013.

[32] C.-K. Chiu, J. C. Y. Teo, A. P. Schnyder, and S. Ryu, Classification of Topological Quantum Matter with Symmetries *Reviews of Modern Physics*, vol. 88, p. 035005, Aug. 2016.

[33] M. O. Goerbig, J.-N. Fuchs, G. Montambaux, and F. Piéchon, Tilted anisotropic Dirac cones in quinoid-type graphene and $\alpha-(\mathrm{BEDT\text{-}TTF})_2\mathrm{I}_3$ *Physical Review B*, vol. 78, p. 045415, July 2008.

[34] B. Szentpéteri, P. Rickhaus, F. K. de Vries, A. Márffy, B. Fülöp, E. Tóvári, K. Watanabe, T. Taniguchi, A. Kormányos, S. Csonka, and P. Makk, Tailoring the Band Structure of Twisted Double Bilayer Graphene with Pressure *Nano Letters*, vol. 21, pp. 8777–8784, Oct. 2021.

[35] X. Lin, H. Zhu, and J. Ni, Pressure-induced gap modulation and topological transitions in twisted bilayer and twisted double bilayer graphene *Physical Review B*, vol. 101, 04 2020.

[36] M. Yankowitz, S. Chen, H. Polshyn, Y. Zhang, K. Watanabe, T. Taniguchi, D. Graf, A. F. Young, and C. R. Dean, Tuning superconductivity in twisted bilayer graphene *Science*, vol. 363, no. 6431, pp. 1059–1064, 2019.

[37] A. García-Ruiz, S. Slizovskiy, M. Mucha-Kruczyński, and V. I. Fal'ko, Spectroscopic Signatures of Electronic Excitations in Raman Scattering in Thin Films of Rhombohedral Graphite *Nano Letters*, vol. 19, pp. 6152–6156, Sept. 2019.

[38] A. García-Ruiz, J. J. P. Thompson, M. Mucha-Kruczyński, and V. I. Fal'ko, Electronic Raman Scattering in Twistronic Few-Layer Graphene *Physical Review Letters*, vol. 125, p. 197401, Nov. 2020.

Chapter 7

Umklapp electron-electron scattering in bilayer graphene moiré superlattice

Preface

The contents of this chapter represent the main body of a manuscript submitted to Physical Review Letters. The accompanying supplemental material is presented in the appendices. A preprint is available on arXiv [1]. The manuscript was authored by Christian Moulsdale[1,2] and Vladimir Fal'ko[1,2,3].

Christian Moulsdale performed all the analytical and numerical calculations and produced the figures for the manuscript, under the guidance and supervision of Vladimir Fal'ko. The writing of the manuscript was primarily done by Christian Moulsdale, with assistance from Vladimir Fal'ko.

Abstract

Recent experimental advances have been marked by the observations of ballistic electron transport in moiré superlattices in highly aligned heterostructures of graphene and hexagonal boron nitride (hBN). Here, we predict that

---

[1] Department of Physics and Astronomy, University of Manchester, Manchester M13 9PL, UK

[2] National Graphene Institute, University of Manchester, Manchester M13 9PL, UK

[3] Henry Royce Institute, Institute for Advanced Materials, Manchester M13 9PL, UK

a high-quality graphene bilayer aligned with an hBN substrate features T^2-dependent resistivity caused by umklapp electron-electron (Uee) scattering from the moiré superlattice, that is, a momentum kick by Bragg scattering experienced by a pair of electrons. Substantial Uee scattering appears upon p-doping of the bilayer above a threshold density, which depends on the twist angle between graphene and hBN, and its contribution towards the resistivity grows rapidly with hole density until it reaches a peak value, whose amplitude changes non-monotonically with the superlattice period. We also analyse the influence of an electrostatically induced bandgap in the bilayer and trigonal warping it enhances in the electron dispersion on the electron-electron umklapp scattering.

Umklapp electron-electron (Uee) scattering is a fundamental process contributing towards the electrical resistivity of ultraclean metals. In this process, a pair of electrons interact via Coulomb repulsion and simultaneously transfer momentum, $\hbar\boldsymbol{g}$, to the crystalline lattice, where $\boldsymbol{g}$ is a reciprocal lattice vector (Bragg vector) of this lattice. Taking into account this momentum kick, the wavevectors of the incoming ($\boldsymbol{k}_{1/2}$) and outgoing ($\boldsymbol{k}_{3/4}$) electron states satisfy the following condition:

$$\boldsymbol{k}_3+\boldsymbol{k}_4=\boldsymbol{k}_1+\boldsymbol{k}_2+\boldsymbol{g}. \tag{7.1}$$

When such a process relocates a pair of electrons across the Fermi surfaces, as illustrated in Fig. 7.1 (left-hand-side panel), the resulting two-electron back-scattering generates resistivity, in contrast to “normal” Coulomb scattering, which conserves the total momentum of the pair. The Uee contribution towards the resistivity typically has a T^2 temperature dependence [2], but it is difficult to otherwise vary its strength in metals, where the electron density and a size of the Fermi surface are set by the material’s chemistry, and the latter may not contain states that satisfy the condition in Eq. (7.1).

With the availability of long-period superlattices, such as moiré superlattices (mSL) in incommensurate heterostructures of graphene [3, 4, 5, 6, 7, 8, 9, 10, 11] or twisted graphene bilayers [12, 13, 14, 15], it becomes feasible to vary the electron density across the range where Uee processes can be switched on/off and, then, its strength substantially varied. In a monolayer graphene/hexagonal boron nitride (hBN) heterostructure, it has been observed that, above a well-defined threshold density (which depends on the mSL period and, therefore, on the twist angle between graphene and hBN crystals), the rate of mSL-Uee gradually increases, becoming a dominant factor in the resistivity at room temperature [11, 16].

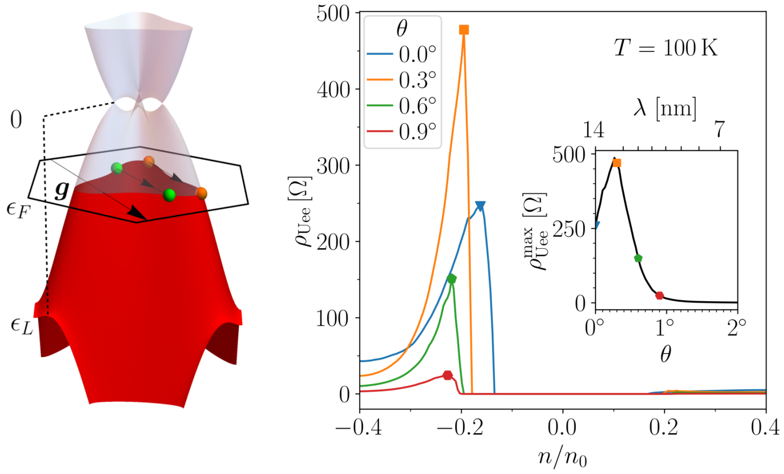

Figure 7.1: Left: Umklapp electron-electron (Uee) scattering by a moiré superlattice in BLG. ε_F and ε_L are the Fermi energy and saddle point energy in the first mSL miniband on the valence side, respectively, counted from the conduction-valence band edge. Right: The non-monotonic evolution of the contribution, $\rho_{\mathrm{Uee}} = T^2 f(n)$, of Uee scattering to the electrical resistivity against electron density, n, for various twists angles, θ, between graphene and hBN, at $T = 100\,\mathrm{K}$ (Uee processes dominate when $T \ll |\varepsilon_F|/k_B, |\varepsilon_F - \varepsilon_L|/k_B$). Inset: Peak value of the Uee resistivity, whose magnitude, $\rho_{\mathrm{Uee}}^{\max}$, is shown as a function of the mSL period, λ (and θ).

Here, we claim that mSL-Uee processes are important for understanding electronic transport in highly aligned bilayer graphene (BLG)/hBN heterostructures, where they make a substantial contribution,

$$\rho_{\mathrm{Uee}} \propto T^2 |n - n_*|^{1/2}, \tag{7.2}$$

towards the resistivity, Fig. 7.1. As for the mSL in monolayer graphene, this contribution appears only above a threshold density, n_*, growing rapidly just above the threshold. However, at higher densities and specifically for bilayer graphene, the resistivity falls off with the density of states, which results in a prominent peak, $\rho_{\mathrm{Uee}}^{\max}$, in the density-dependent resistivity. The size of this peak increases non-monotonically with the mSL period, λ, (maximum value for $\lambda \approx 13\,\mathrm{nm}$) as a result of the interplay between the trigonal warping of the dispersion of electrons in BLG [17, 18] and the mSL periodicity. This contrasts with the mSL in monolayer graphene, where the Uee resistivity increases monotonically with both density and mSL period [11, 16], $\rho_{\mathrm{Uee}} \propto T^2|n-n_*|^{3/2}$, due to the suppressed backscattering of Dirac electrons.

The above predictions are derived by considering Uee scattering in the BLG/hBN heterostructure sketched in Fig. 7.2, enabled by the mSL at the graphene/hBN interface, which period is determined by a $\delta = 1.8\%$ lattice mismatch between graphene and hBN and a misalignment angle, θ. Projecting onto the low-energy bands of bilayer graphene in its $\boldsymbol{K}^\xi$ valley ($\xi = \pm$), the electronic properties of this system can be described by a 2×2 effective Hamiltonian, [19, 20, 21, 3, 5]

$$\hat{H} = \frac{-1}{2m_*}\begin{pmatrix} 0 & \hat{\pi}^{\dagger 2} \\ \hat{\pi}^2 & 0 \end{pmatrix} + v_3\begin{pmatrix} 0 & \hat{\pi} \\ \hat{\pi}^\dagger & 0 \end{pmatrix} + \frac{\alpha\hat{\boldsymbol{p}}^2}{2m_*}\left(\begin{smallmatrix} 1 & 0 \\ 0 & 1 \end{smallmatrix}\right) - \frac{\Delta}{2}\left(1 - \frac{\hat{\boldsymbol{p}}^2}{m_*\gamma_1}\right)\left(\begin{smallmatrix} 1 & 0 \\ 0 & -1 \end{smallmatrix}\right) + \sum_{m=0}^{5}\hat{M}_{\boldsymbol{g}_m},$$

$$\hat{M}_{\boldsymbol{g}_m} = \begin{pmatrix} [u_0 + i(-1)^m u_3]e^{i\boldsymbol{g}_m\cdot\boldsymbol{r}} & \frac{1}{\sqrt{2m_*\gamma_1}}u_1(-1)^{m+1}e^{-i\xi m\pi/3}e^{i\boldsymbol{g}_m\cdot\boldsymbol{r}}\hat{\pi}^\dagger \\ \frac{1}{\sqrt{2m_*\gamma_1}}u_1(-1)^{m+1}e^{i\xi m\pi/3}\hat{\pi}e^{i\boldsymbol{g}_m\cdot\boldsymbol{r}} & \frac{1}{2m_*\gamma_1}[u_0 - i(-1)^m u_3]\hat{\pi}e^{i\boldsymbol{g}_m\cdot\boldsymbol{r}}\hat{\pi}^\dagger \end{pmatrix}, \tag{7.3}$$

where $\hat{\pi} = \hbar(-i\xi\partial_x + \partial_y)$ and $\hat{\boldsymbol{p}}^2 = -\hbar^2(\partial_x^2 + \partial_y^2)$. The first three terms are intrinsic to BLG, representing the effective electron mass, $m_* = \gamma_1/(2v^2) \approx 0.032m_e$, from the intralayer ($v$) and vertical interlayer (γ_1) couplings, trigonal warping from the skew interlayer (v_3) couplings [23] and a parabolic shift which lifts the particle-hole (eh) symmetry (α) [24], respectively. The fourth term represents an electrostatically controlled interlayer potential asymmetry, Δ.

The final term in Eq. (7.3) represents the effects of the mSL sketched in Fig. 7.2, with harmonics corresponding to the first star of mSL Bragg vectors, $\boldsymbol{g}_m \approx \delta\cdot\boldsymbol{G}_m - \theta(\boldsymbol{e}_z\times\boldsymbol{G}_m)$ ($m = 0, 1, \cdots, 5$), where $\boldsymbol{G}_m = \frac{4\pi}{\sqrt{3}a}(-\sin\frac{m\pi}{3}, \cos\frac{m\pi}{3})$ is a graphene Bragg vector. This is parameterised by $u_{0/1/3}$, corresponding to an energy shift, gauge field and mass term in the graphene layer closest to the hBN layer, respectively [25]. Each harmonic, $\hat{M}_{\boldsymbol{g}_m}$, couples plane wave states separated by $\boldsymbol{g}_m$, which reconstructs the conduction and valence bands of isolated BLG into minibands (see Fig. 7.1).

For electrons on a superlattice, Coulomb interaction leads to mSL-Uee processes (see Fig. 7.1): two electrons from one side of the Fermi line backscatter together to the other side, receiving a momentum kick ($\boldsymbol{g} = \boldsymbol{g}_m$) from the mSL. Such processes

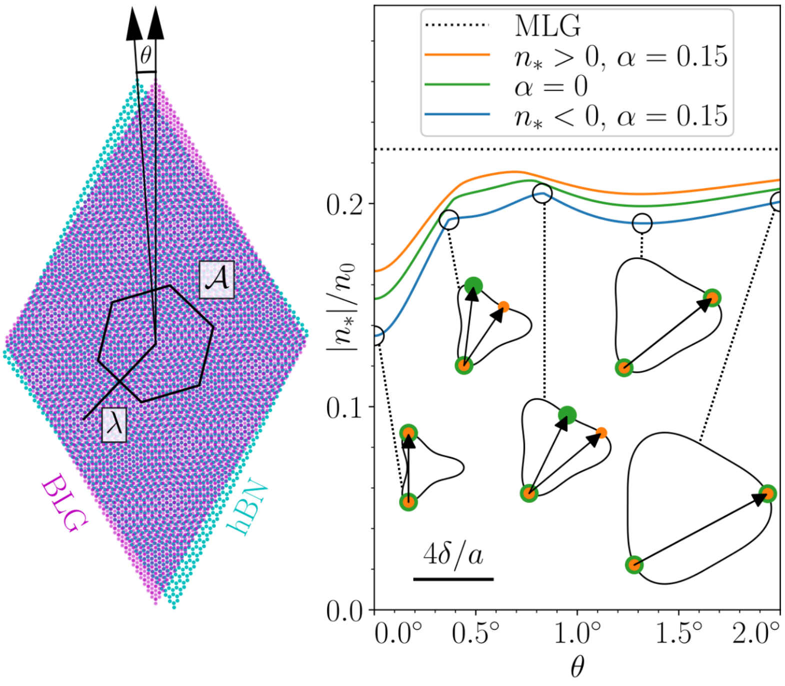

Figure 7.2: Left: The lattice mismatch ($\delta \approx 1.8\%$) and twist, θ, between BLG and hBN gives rise to a moiré superlattice with period, $\lambda \approx a/\sqrt{\delta^2+\theta^2}$, and unit cell of area, $\mathcal{A} = \sqrt{3}\lambda^2/2$. Right: The mSL-normalised magnitude, $|n_*|/n_0$ ($n_0 = 4/\mathcal{A}$) of the threshold density of holes, $n_* < 0$, or electrons, $n_* > 0$, at which Uee scattering becomes possible due to a sufficiently large Fermi line. The threshold density, n_*, was calculated as a function of twist angle θ taking into account the particle-hole asymmetry in the BLG Hamiltonian ($\alpha = 0.15$), and compared to the symmetric cases of $\alpha = 0$ and the monolayer graphene superlattice ($|n_*| \approx 0.23 n_0$).

only occur when the size of the Fermi contour is sufficiently large compared to $|\boldsymbol{g}|$, giving a threshold electron density, n_*, which decreases with the size of the mSL unit cell as seen in Fig. 7.2 for the gapless spectrum with $\Delta = 0$. The mSL-normalised threshold, n_*/n_0, (due to spin-valley degeneracy, $n_0 = 4/\mathcal{A}$ corresponds to one filled miniband) increases non-monotonically with θ as the isoenergy lines become decreasingly concave with density, a consequence of the trigonal warping and most significant when $|n| < 2m^2v_3^2/\pi$. This distinguishes the threshold behaviour in bilayer graphene, pulling down from the value $|n_*|/n_0 = \pi/(8\sqrt{3}) \approx 0.23$ established for the the isotropic Dirac spectrum of monolayer graphene. Also, it is important to consider the effects of a conduction-valence band asymmetry in the bilayer dispersion, accounted for by the third term in Eq. (7.3) with $\alpha = 0.15$ [23]. The latter affects the concavity of the isoenergy lines, especially in the first valence miniband, making the threshold density, $|n_*|$, slightly different for n- and p-doping of BLG mSL - see Fig. 7.2.

In the following, we derive the amplitudes for mSL-Uee processes, treating the mSL and electron-electron interactions in the lowest-order perturbation scheme. This is implemented for densities just above the threshold, n_*, where the resonant mixing of plane wave states is negligible, and we neglect the reconstruction of the electron dispersion into minibands. We account for the four leading Feynman diagrams involving Coulomb and mSL scattering of electrons off and back on to the Fermi level via an intermediate virtual state,

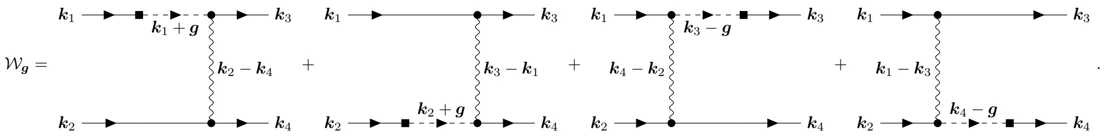

(7.4)

In each diagram, the initial and final momenta are related by Eq. (7.1); $\wr^{\boldsymbol{q}} \equiv \tilde{V}(\boldsymbol{q}) \approx W$ is the screened Coulomb interaction; $\blacksquare \equiv \hat{M}_{\boldsymbol{g}}$ is an mSL interaction harmonic which imparts momentum kick $\hbar \boldsymbol{g}$; and $\overset{\boldsymbol{p}}{\dashrightarrow}$ is a propagator of an electron in the virtual state [26, 27, 28, 29, 30]. To mention, the mSL scattering amplitudes feature a particle-hole asymmetry, generic for graphene/hBN heterostructures, with values typically an order of magnitude larger in the valence miniband as compared to the conduction miniband [3, 4, 5, 6].

Equipped with the amplitudes in Eq. (7.4), we use linear transport theory [31, 32, 11] (see SM) to calculate the contribution of Uee processes to the resistivity,

$$\rho_{\mathrm{Uee}} = \frac{h}{6e^2}(k_B T)^2 \sum_{m=0}^{5} \int \frac{d\theta_1 d\theta_2}{|\boldsymbol{k}_3 \times \boldsymbol{k}_4|} \frac{k_1 k_2 k_3 k_4}{|v_{k1} v_{k2} v_{k3} v_{k4}|} |\mathcal{W}_{\boldsymbol{g}_m}|^2 \frac{v_{x1}(v_{x1}+v_{x2}-v_{x3}-v_{x4})}{(\int d\theta k v_x^2/|v_k|)^2}. \tag{7.5}$$

In this expression, $\boldsymbol{k}_i = k_i(\cos\theta_i, \sin\theta_i)$ is the wavevector of each electron ($i = 1, 2, 3, 4$) on the Fermi line, and $\boldsymbol{v}_i$ its group velocity. In Fig. 7.1, the results of this analysis are summarised for the vertically unbiased heterostructure, $\Delta = 0$. The Uee contribution is isotropic ($\rho^{\mathrm{Uee}}_{\alpha\beta} \equiv \rho_{\mathrm{Uee}}\delta_{\alpha\beta}$) due to the C_3 symmetry of the mSL. Also, note that the "normal" (momentum-conserving) electron-electron scattering suppresses higher order harmonics in the non-equilibrium distribution of electrons, so that accounting for Uee becomes the same as accounting for an additional momentum transfer from the accelerated electrons (by the electric field) in the scattering time approximation (see SM). Here, we limit the analysis of Uee to the density range of $0.1n_0 < |n| < 0.4n_0$, excluding from the analysis electron-hole scattering at the principal miniband edge and staying away from the mSL-induced van Hove singularity, where the perturbative treatment of the mSL interaction becomes inaccurate [33, 34].

Typically, the Uee contribution in Eq. (7.5), $\rho_{\text{Uee}} \approx T^2 f(n)$, rises rapidly above the threshold, $f(n) \propto |n - n_*|^{1/2}$. This singular behaviour originates from the rapid expansion of the phase space around the incoming/outgoing points in Fig. 7.2, with $\boldsymbol{k}_3 \times \boldsymbol{k}_4 = 0$ at the threshold. The exception is an initial interval of linear scaling, $f(n) \propto |n - n_*|$, found for the mSL with a twist angle in the range of $0.3^\circ < \theta < 0.8^\circ$.

We also find that the interlayer potential asymmetry, Δ, which opens a homogeneous bandgap in BLG [35, 36, 37, 38], has a pronounced effect on the Uee processes. The gap promotes formation of three well-separated minivalleys at the BLG band edges, which persist up to the density $|n| \sim 2m|\Delta|^2/(\pi\gamma_1)$. The separation of the minivalleys increases with $|\Delta|$, thus, decreasing the threshold doping density, $|n_*|$, at which the Uee channel opens. For example, in the aligned BLG/hBN heterostructure ($\theta = 0$) with $|\Delta| = \Delta_r \approx 75\,\text{meV}$, the minivalleys are separated by the $\frac{1}{2}\boldsymbol{g}_m$, so that Uee scattering transfers pairs of electrons between these minivalleys even at small doping (corresponding to $n_* = 0$, as shown in Fig. 3.b)).

The results of numerical computations of the Uee resistivity contribution, ρ_{Uee}, across a broad range of parameters are summarised in Fig. 7.3 c). We highlight the regions where the resistivity is dominated by Uee processes, excluding a butterfly-shaped region where thermally-activated electron-hole scattering processes may dominate. The wings of this butterfly, shown in the bottom panel, differ for n- and p-doping, which reflects the particle-hole asymmetry of the BLG dispersion (here, we use $\alpha = 0.15$ [24]), conversely being mirrored by charge neutrality ($n = 0$) for $\alpha = 0$ in the top panel. Regardless of α, the wings are mirrored by $\Delta = 0$, where the wavefunctions feature zero layer polarisation. In contrast, the Uee contribution differs for positive and negative Δ. This is because the interlayer asymmetry gap (vertical bias) shifts the weight of the low-energy electron states towards/away from the bottom graphene layer, hence, increasing/reducing the mSL scattering strength determined by the hBN crystal aligned

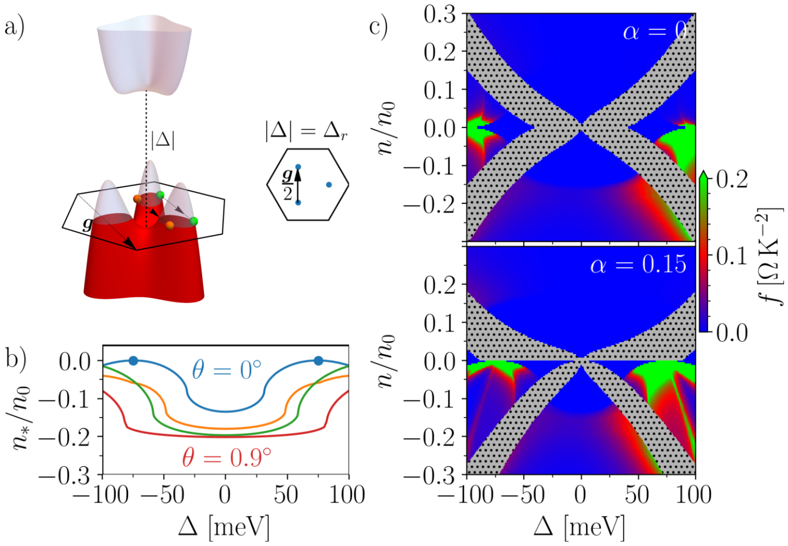

Figure 7.3: a) Umklapp electron-election (Uee) scattering with momentum kick, $\hbar\boldsymbol{g}$, between the three minivalleys in the valence miniband for non-zero interlayer potential asymmetry, Δ, opening a gap between the minibands. The minivalley edges are connected by $\boldsymbol{g}/2$ when this system is aligned (zero twist, $\theta = 0$) and $|\Delta| = \Delta_r$ (inset). b) The non-monotonic evolution of the valence miniband threshold density, n_*, with Δ for various twists, $\theta = 0°$ to $0.9°$ from top to bottom, and $\alpha = 0.15$ ($n_* = 0$ when $\theta = 0$ and $|\Delta| = \Delta_r \approx 75\,\mathrm{meV}$). c) The temperature-independent component, f, of the dominant contribution, $\rho_{\mathrm{Uee}} \approx T^2 f$, of Uee processes to the electrical resistivity against electron density, n, and Δ, with ($\alpha = 0$) and without ($\alpha = 0.15$) particle-hole symmetry, respectively. We exclude a (grey, dotted) butterfly-shaped region in each panel where the contribution of other processes are significant, whose wings are mirrored by zero layer polarisation ($\Delta = 0$), and charge neutrality ($n = 0$) when $\alpha = 0$.

with the BLG flake. Also, as in monolayer graphene mSL, Uee processes are much stronger for p-doping (first miniband of holes) than for n-doping, due to the particle-hole symmetry breaking by the mSL potential [3, 11]

Overall, we predict a strong contribution of umklapp electron-electron scattering of moiré superlattice towards the resistivity of highly-aligned BLG/hBN heterostrucutres, with a non-monotonic density dependence near the Uee threshold. While the Uee role would increase at higher temperatures, at low densities (near the threshold) it will compete with electron-hole scattering processes, promoted by electron-hole activation across the conduction-valence band edge [39]. Hence, for a more accurate description of the Coulomb scattering effect in the resistivity of mSL in bilayer graphene, one would need to account for both Uee and electron-hole scattering on equal footing. Also, one may want to extend the Uee analysis onto a broader range of miniband fillings, by calculating Uee rates using the full details of the mSL minibads spectra and Wannier functions, as attempted for a model graphene superlattice [40]. Such a calculation may offer additional features in $\rho_{\mathrm{Uee}}(n)$ when approaching the opposite (high-density) miniband edge or for deeper minibands, though, for quantititative validity, that has to be performed using a mSL model with the experimentally verified parameters [41].

We thank A. Knothe, S. Slizovskiy, K. Novoselov and R. K. Kumar for useful discussions. We acknowledge support from EU Graphene Flagship Project, EPSRC Grants No. EPSRC CDT Graphene-NOWNANO EP/L01548X/1, EP/S019367/1, EP/P026850/1 and EP/N010345/1. All the research data supporting this publication is directly available within this publication and supplemental material accompanying this publication.

7.A Non-orthogonality of monolayer graphene Hamiltonian

The generic 2×2 Hamiltonian for the two sublattices of monolayer graphene, A and B, in the (A,B) basis is

$$\hat{H} = \begin{pmatrix} \varepsilon_A & -\gamma_0 g(\boldsymbol{k}) \\ -\gamma_0 f^*(\boldsymbol{k}) & \varepsilon_B \end{pmatrix}, \tag{7.6}$$

where $\varepsilon_{A/B}$ are the on-site energy of the $2p^z$ graphene orbitals in each sublattice, A/B, γ_0 is the nearest-neighbour hopping parameter, and

$$g(\boldsymbol{k}) = e^{ik_y a/\sqrt{3}} + 2e^{-ik_y a/(2\sqrt{3})}\cos\left(\frac{k_x a}{2}\right), \tag{7.7}$$

for plane wave states of momentum $\hbar\boldsymbol{k}$ [42]. The $2p^z$ orbitals on each sublattice are non-orthogonal, so that we derive the energy eigenvalues, ε, and corresponding wavefunction, ψ, by solving the generalised eigenvalue equation,

$$\hat{H}\left|\psi(\boldsymbol{k})\right\rangle = \varepsilon S\left|\psi(\boldsymbol{k})\right\rangle, \tag{7.8}$$

where the overlap matrix is

$$S = \begin{pmatrix} 1 & sg(\boldsymbol{k}) \\ sg^*(\boldsymbol{k}) & 1 \end{pmatrix}, \tag{7.9}$$

with $s \approx 0.13$ quantifying this overlap. We can orthogonalize this Hamiltonian using the transformation

$$\hat{H} \to S^{-1/2}\hat{H}S^{-1/2} \approx \hat{H} - \frac{1}{2}\{\hat{H}, S - I\}, \tag{7.10}$$

to first order in S, where I is the 2×2 identity matrix, and $\{A,B\} \equiv AB + BA$ is an anticommutator. This results in an extra term in the Hamiltonian, $s\gamma_0|g(\boldsymbol{k})|^2 I$, which breaks particle-hole symmetry.

7.B Effective two-band model of bilayer graphene

The full 4×4 Hamiltonian of bilayer graphene accounts for each of the two sublattices, A and B, in each layer [19, 20, 22]. However, in Bernal stacking, the A atoms of the top layer are directly above the B atoms of the bottom layer (see Fig. 2 of the main text) and have a large interlayer coupling, γ_1. This results in two high-energy bands ($|\varepsilon| > \gamma_1$) primarily located on these dimer atoms, alongside the low-energy bands primarily located on the non-dimer atoms which dominate the contribution of Umklapp electron-electron (Uee) processes to the resistivity.

We use a Schrieffer-Wolff transformation to project the high-energy bands onto the low-energy bands, giving an effective 2×2 Hamiltonian at the $\boldsymbol{K}^{\pm}$ points:

$$\begin{aligned}\hat{H}_0 =& \frac{-1}{2m_*}\begin{pmatrix}0 & \hat{\pi}^{\dagger 2}\\ \hat{\pi}^2 & 0\end{pmatrix} + v_3\begin{pmatrix}0 & \hat{\pi}\\ \hat{\pi}^{\dagger} & 0\end{pmatrix} + \frac{\alpha_1}{2m_*}\begin{pmatrix}\hat{\pi}^{\dagger}\hat{\pi} & 0\\ 0 & \hat{\pi}\hat{\pi}^{\dagger}\end{pmatrix}\\ & -\frac{\Delta}{2}\left[\begin{pmatrix}1 & 0\\ 0 & -1\end{pmatrix} - \frac{1}{m_*\gamma_1}\begin{pmatrix}\hat{\pi}^{\dagger}\hat{\pi} & 0\\ 0 & -\hat{\pi}\hat{\pi}^{\dagger}\end{pmatrix}\right].\end{aligned} \tag{7.11}$$

Note that we neglect a constant energy term corresponding to the mean on-site potential. Particle-hole symmetry breaking is achieved by the third term ($\alpha_1 \approx 0.15$), alongside a small, additional parabolic shift, $\frac{\alpha_2 \hat{p}^2}{2m_*}I$ ($\alpha_2 \sim 0.01$), which accounts for the the next-nearest-neighbour intralayer couplings and non-orthogonality of graphene orbitals in Sec. 7.A, expanded at the $\boldsymbol{K}^{\pm}$ points. The momentum operators commute in the absence of an external magnetic field, and Eq. (7.11) simplifies to give the first four terms in Eq. (3) of the main text, with $\alpha = \alpha_1 + \alpha_2 \approx 0.15$ [23, 24]. Considering plane wave states of wavevector, $(\boldsymbol{K}^{\pm}+)\boldsymbol{k}$, in the Brillouin zone, this Hamiltonian features a conduction and valence band of energies, $\varepsilon_{\pm}(\boldsymbol{k})$ ($\varepsilon_+ > \varepsilon_-$), and wavefunctions, $|\psi_{\pm}(\boldsymbol{k})\rangle = e^{i\boldsymbol{k}\cdot\boldsymbol{r}}u_{\pm}(\boldsymbol{k})$, respectively, satisfying the eigenvalue equation, $\hat{H}_0\,|\psi_{\pm}(\boldsymbol{k})\rangle = \varepsilon_{\pm}(\boldsymbol{k})\,|\psi_{\pm}(\boldsymbol{k})\rangle$.

The final term in the Hamiltonian in Eq. (3) of the main text represents the moiré superlattice (mSL) interaction with the hBN layer, featuring harmonics, $\hat{M}_{\boldsymbol{g}_m}$, for each of the first star of mSL Bragg vectors, $\boldsymbol{g}_m$ ($m = 0, 1, \cdots 5$) [3, 4, 5, 6, 41]. The harmonic $\hat{M}_{\boldsymbol{g}_m}$ couples plane wave states of wavevector $\boldsymbol{k}$ and $\boldsymbol{k}+\boldsymbol{g}_m$: $\langle\psi_{s'}(\boldsymbol{k}+\boldsymbol{g}_m)|\hat{M}_{\boldsymbol{g}_m}|\psi_s(\boldsymbol{k})\rangle \neq 0$ ($s, s' = \pm$). Hence, we derive the reconstructed dispersion from the eigenvalue equation with the zone-folded wavefunction,

$$|\Psi(\boldsymbol{k})\rangle = \sum_{\boldsymbol{g}}\sum_{s=\pm} c^{s}_{\boldsymbol{k}+\boldsymbol{g}}\,|\psi_s(\boldsymbol{k}+\boldsymbol{g})\rangle\,, \tag{7.12}$$

where $c^{s}_{\boldsymbol{k}+\boldsymbol{g}}$ are complex coefficients and we sum over the mSL Bragg vectors, $\boldsymbol{g}$ [3, 5]. This gives a collection of minibands (see Fig. 1) in the moiré Brillouin zone (mBZ), and the conduction and valence minibands are converged when we sum over mSL Bragg vectors, $\boldsymbol{g}$, which are the sum of at most two of the first star vectors, $\boldsymbol{g}_m$. As discussed in the main text, we can neglect the mSL-induced reconstruction of the bands in the relevant density ranges, $n/n_* \ll 4$.

Depending upon the interlayer potentially asymmetry, Δ, and density, n, the Fermi line will have one of three forms:

1. A single contour centred on the origin.
2. Two non-touching contours, each centred on the origin. We neglect this regime, since it is narrow on the energy axis, and the resistivity will be dominated by impurity scattering at the van Hove singularities [33, 34].
3. Three non-touching contours (minivalleys), $p = 0, 1, 2$, centred on the three band edges, $\boldsymbol{k}_c^{(p)} = k_c(\cos\frac{p2\pi}{3}, \sin\frac{p2\pi}{3})$ ($k_c > 0$), respectively [18]. The contours do not enclose the origin, and are related by the three-fold rotational symmetry. We expand about the centre of the minivalley, $\boldsymbol{k} \to \boldsymbol{k}_c^{(p)} + \boldsymbol{k}$:

$$\boldsymbol{k} = k\left(\cos\left(\theta + \frac{p2\pi}{3}\right), \sin\left(\theta + \frac{p2\pi}{3}\right)\right), \tag{7.13}$$

such that $k(\theta)$ is the same for each minivalley. We suppress the contour index for simplicity in the following sections, implicitly summing over the valid contours.

7.C Screened Coulomb interaction

The unscreened Coulomb potential in real space is

$$V_0(\boldsymbol{r}) \equiv V_0(r) = \frac{e^2}{4\pi\kappa\varepsilon_0 r}, \tag{7.14}$$

where $\kappa \approx 2.6$ is the dielectric constant of bilayer graphene in hBN [28]. Performing the in-plane Fourier transformation on this potential gives

$$\tilde{V}_0(\boldsymbol{Q}) \equiv \tilde{V}_0(Q) = \frac{e^2}{2\kappa\varepsilon_0 Q}, \tag{7.15}$$

for the momentum transfer, $\hbar\boldsymbol{Q}$. Electron states screen this potential and, in the random phase approximation [26, 27, 28, 29], the screened potential is given by

$$\tilde{V}(\boldsymbol{Q}) = \frac{\tilde{V}_0(Q)}{1 + \tilde{V}_0(Q)\Pi_0(\boldsymbol{Q})}, \tag{7.16}$$

where the static polarisation, including the two-fold spin degeneracy, is given by

$$\Pi_0(\boldsymbol{Q}) = -2 \sum_{s,s'=\pm} \sum_{\xi=\pm} \int \frac{d^2k}{(2\pi)^2} \frac{f_0(\varepsilon_s(\boldsymbol{k})) - f_0(\varepsilon_{s'}(\boldsymbol{k}+\boldsymbol{Q}))}{\varepsilon_s(\boldsymbol{k}) - \varepsilon_{s'}(\boldsymbol{k}+\boldsymbol{Q})} |\langle \psi_s(\boldsymbol{k}) | \psi_{s'}(\boldsymbol{k}+\boldsymbol{Q}) \rangle|^2, \tag{7.17}$$

in terms of the equilibrium distribution function for Fermi energy, ε_F,

$$f_0(\varepsilon) = \frac{1}{e^{(\varepsilon-\varepsilon_F)/(k_B T)} + 1}. \tag{7.18}$$

In the low-temperature regime discussed in the main text, we approximate the distribution function as a step, $\partial f_0 / \partial \varepsilon \approx -\delta(\varepsilon - \varepsilon_F)$, and the polarisation is dominated by intra-band overlaps and small momentum transfers, $\boldsymbol{Q} \approx 0$:

$$\Pi_0(\boldsymbol{Q}) \approx \Pi_0(0) = \frac{1}{\pi^2} \int d\theta \frac{k}{|v_k|}, \tag{7.19}$$

where we integrate over the Fermi surface, and the electron group velocity is $\boldsymbol{v}(\boldsymbol{k}) = \hbar^{-1} \nabla_{\boldsymbol{k}} \varepsilon(\boldsymbol{k})$. Since the screening is strong ($\tilde{V}_0(Q)\Pi_0(\boldsymbol{Q}) \gg 1$) in the region of interest, we approximate the screened potential as a contact potential, $V(\boldsymbol{r}) \approx W\delta(\boldsymbol{r})$, where

$$W = \Pi_0(0)^{-1}. \tag{7.20}$$

7.D Matrix elements

The matrix element, $\mathcal{W}_{\boldsymbol{g}}$, for Uee scattering by the mSL Bragg vector, $\boldsymbol{g} = \boldsymbol{g}_m$, is the sum of four diagrams where electrons 1, 2, 3 and 4 scatter off the mSL, respectively, shown as Feynman diagrams in Eq. (4) of the main text. These give the respective terms in the explicit expression,

$$\mathcal{W}_{\boldsymbol{g}} = X_{\boldsymbol{g}}(1,2,3,4) + X_{\boldsymbol{g}}(2,1,4,3) + X^*_{-\boldsymbol{g}}(3,4,1,2) + X^*_{-\boldsymbol{g}}(4,3,2,1), \tag{7.21}$$

where

$$X_{\boldsymbol{g}}(a,b,c,d) = \sum_{s'=\pm} \frac{\langle \psi_{s'}(\boldsymbol{k}_a+\boldsymbol{g})|\hat{M}_{\boldsymbol{g}}|\psi_s(\boldsymbol{k}_a)\rangle}{\varepsilon_s(\boldsymbol{k}_a)-\varepsilon_{s'}(\boldsymbol{k}_a+\boldsymbol{g})}\tilde{V}(\boldsymbol{k}_b-\boldsymbol{k}_d)$$
$$\times \langle \psi_s(\boldsymbol{k}_c)|\psi_{s'}(\boldsymbol{k}_a+\boldsymbol{g})\rangle \langle \psi_s(\boldsymbol{k}_d)|\psi_s(\boldsymbol{k}_b)\rangle\,, \qquad (7.22)$$

summing over both bands for the intermediate virtual electron [11, 16]. Spatial inversion is equivalent to taking the complex conjugate of the matrix elements, which leaves the magnitude of Eq. (7.22) unchanged. In the main text, we restrict the integral to the Fermi surface, $\varepsilon_{1/2/3/4} = \varepsilon_F$.

7.E Linear response theory

The Boltzmann equation for the electron distribution function, $f(\boldsymbol{k})$, of an electron with wavevector, $\boldsymbol{k}$, in the presence of an external electric field, $\boldsymbol{E}$, is given by

$$e\boldsymbol{E}\cdot\nabla_{\boldsymbol{k}} f(\boldsymbol{k}) = I\{f(\boldsymbol{k})\}, \qquad (7.23)$$

where the collision integral, $I\{f(\boldsymbol{k})\}$, is determined by electron scattering [31, 32, 11]. Note that the electron charge is negative, $e<0$. The equilibrium distribution (7.18), appropriate for $\boldsymbol{E}=0$, satisfies the detailed balance condition, $I\{f_0(\varepsilon)\}=0$. We expand about this equilibrium distribution to first order in the chemical potential shift, $\phi(\boldsymbol{k})$:

$$f(\boldsymbol{k}) = f_0(\varepsilon(\boldsymbol{k})) - \left.\frac{\partial f_0}{\partial \varepsilon}\right|_{\varepsilon=\varepsilon(\boldsymbol{k})} \phi(\boldsymbol{k}). \qquad (7.24)$$

Expanding Eq. (7.23) to first order in $\phi(\boldsymbol{k})$ gives the linearised Boltzmann equation,

$$eEv_E(\boldsymbol{k})\left.\frac{\partial f_0}{\partial \varepsilon}\right|_{\varepsilon=\varepsilon(\boldsymbol{k})} = I\{\phi(\boldsymbol{k})\}, \qquad (7.25)$$

which relates the kinetic function, $v_E(\boldsymbol{k}) = \boldsymbol{v}(\boldsymbol{k})\cdot\boldsymbol{E}/E$, to $\phi(\boldsymbol{k})$. This equation is inverted to give the corresponding shift, $\phi(\boldsymbol{k})$, for the known kinetic function, $v_E(\boldsymbol{k})$, from which we calculate the scattering-limited longitudinal electrical conductivity as

$$\sigma = \frac{4e}{E}\int \frac{d^2\boldsymbol{k}}{(2\pi)^2} v_E \frac{\partial f_0}{\partial \varepsilon}\phi, \tag{7.26}$$

with corresponding resistivity, $\rho \equiv \sigma^{-1}$. As a result of the C_3 symmetry, the resistivity is isotropic and independent of the field direction, so we set $\boldsymbol{E} = (E, 0, 0)$ for simplicity.

The collision integral for Uee scattering is given by [31, 32, 11, 16]

$$\begin{aligned} I_{\mathrm{Uee}}\{\phi(\boldsymbol{k}_1)\} = \frac{4}{k_B T}\sum_{m=0}^{5}\int \frac{d^2\boldsymbol{k}_2 d^2\boldsymbol{k}_3 d^2\boldsymbol{k}_4}{(2\pi)^6} 2\pi\delta(\Delta\varepsilon)(2\pi)^2\delta^{(2)}(\Delta\boldsymbol{k} - \boldsymbol{g}_m)|\mathcal{W}_{\boldsymbol{g}_m}|^2\Delta\phi \\ \times \frac{1}{16}\prod_{i=1}^{4}\mathrm{sech}\left(\frac{\varepsilon_i - \varepsilon_F}{2k_B T}\right), \end{aligned} \tag{7.27}$$

in terms of the change,

$$\Delta f = f(\boldsymbol{k}_3) + f(\boldsymbol{k}_4) - f(\boldsymbol{k}_1) - f(\boldsymbol{k}_2), \tag{7.28}$$

of the total $f = \phi, \varepsilon, \boldsymbol{k}$ during the process. The Dirac delta functions ensure energy and momentum (including kick $\hbar\boldsymbol{g}$) conservation of the incoming and outgoing electrons. At low temperatures, we restrict this to an integral over the Fermi surface since

$$\delta(\varepsilon_3 + \varepsilon_4 - \varepsilon_1 - \varepsilon_2)\prod_{i=1}^{4}\mathrm{sech}\left(\frac{\varepsilon_i - \varepsilon_F}{2k_B T}\right) \approx \frac{32\pi^2 (k_B T)^3}{3}\prod_{i=1}^{4}\delta(\varepsilon_i - \varepsilon_F). \tag{7.29}$$

We simplify using the constant relaxation time approximation, where the collision integral, $I\{f(\boldsymbol{k})\}$, of a scattering process is approximated by

$$I\{f(\boldsymbol{k})\} = -\hbar\frac{f(\boldsymbol{k}) - f_0(\varepsilon(\boldsymbol{k}))}{\tau}, \tag{7.30}$$

in terms of a constant scattering time, τ [11, 16]. Expanding to first order in the chemical potential shift, $\phi(\boldsymbol{k})$, the collision integral simplifies to

$$I\{\phi(\boldsymbol{k})\} = \frac{\hbar}{\tau}\frac{\partial f_0}{\partial \varepsilon}\bigg|_{\varepsilon=\varepsilon(\boldsymbol{k})}\phi(\boldsymbol{k}). \tag{7.31}$$

Inserting this into the linearised Boltzmann equation in Eq. (7.25), we easily find the solution,

$$\phi(\boldsymbol{k}) = -eE\tau v_x(\boldsymbol{k})/\hbar, \tag{7.32}$$

with scattering time,

$$\frac{\hbar}{\tau} = \int d^2k I\{v_x\}v_x \bigg/ \left(\int d^2k \frac{\partial f_0}{\partial \varepsilon} v_x^2 \right), \tag{7.33}$$

found self-consistently for a collision integral linear in ϕ. Then, the Uee contribution to the resistivity, ρ_{Uee}, in the low-temperature regime is given by Eq. (5) of the main text.

7.F Low-density resistivity

At density, n, just above the threshold, n_*, Uee scattering will be restricted to the immediate vicinity of the points shown in Fig. 2 of the main text. The wavevector, $\boldsymbol{k}$, velocity, $\boldsymbol{v}$, and scattering amplitudes, $\mathcal{W}_{\boldsymbol{g}}$, are approximately constant in this range, so the resistivity has the approximate form,

$$\rho_{\text{Uee}} \propto T^2 \sum_{m=0}^{5} \int \frac{d\theta_1 d\theta_2}{|\sin(\theta_3 - \theta_4)|}. \tag{7.34}$$

The size of the phase space in the integral scales according to $|n - n_*|$, so we have $\rho_{\text{Uee}} \propto T^2 |n - n_*|^{1/2}$, except for $\rho_{\text{Uee}} \propto T^2 |n - n_*|$ in the region discussed in the main text corresponding to split Uee scattering, where $\sin(\theta_3 - \theta_4)$ is also approximately constant.

Bibliography

[1] C. Moulsdale and V. Fal'ko, Umklapp electron-electron scattering in bilayer graphene moiré superlattice arXiv:2211.01005, 2022.

[2] A. H. MacDonald, R. Taylor, and D. J. W. Geldart, Umklapp electron-electron scattering and the low-temperature electrical resistivity of the alkali metals *Phys. Rev. B*, vol. 23, pp. 2718–2730, Mar 1981.

[3] J. R. Wallbank, A. A. Patel, M. Mucha-Kruczyński, A. K. Geim, and V. I. Fal'ko, Generic miniband structure of graphene on a hexagonal substrate *Phys. Rev. B*, vol. 87, p. 245408, Jun 2013.

[4] B. Hunt, J. D. Sanchez-Yamagishi, A. F. Young, M. Yankowitz, B. J. LeRoy, K. Watanabe, T. Taniguchi, P. Moon, M. Koshino, P. Jarillo-Herrero, and R. C. Ashoori, Massive Dirac Fermions and Hofstadter Butterfly in a van der Waals Heterostructure *Science*, vol. 340, no. 6139, pp. 1427–1430, 2013.

[5] X. Chen, J. R. Wallbank, M. Mucha-Kruczyński, E. McCann, and V. I. Fal'ko, Zero-energy modes and valley asymmetry in the Hofstadter spectrum of bilayer graphene van der Waals heterostructures with hBN *Phys. Rev. B*, vol. 94, p. 045442, Jul 2016.

[6] M. Yankowitz, Q. Ma, P. Jarillo-Herrero, and B. J. LeRoy, van der Waals heterostructures combining graphene and hexagonal boron nitride *Nature Reviews Physics*, vol. 1, pp. 112–125, Feb 2019.

[7] M. Yankowitz, J. Xue, D. Cormode, J. D. Sanchez-Yamagishi, K. Watanabe, T. Taniguchi, P. Jarillo-Herrero, P. Jacquod, and B. J. LeRoy, Emergence of superlattice Dirac points in graphene on hexagonal boron nitride *Nature Physics*, vol. 8, pp. 382–386, May 2012.

[8] C. R. Dean, L. Wang, P. Maher, C. Forsythe, F. Ghahari, Y. Gao, J. Katoch, M. Ishigami, P. Moon, M. Koshino, T. Taniguchi, K. Watanabe, K. L. Shepard, J. Hone, and P. Kim, Hofstadter's butterfly and the fractal quantum Hall effect in moiré superlattices *Nature*, vol. 497, pp. 598–602, May 2013.

[9] L. A. Ponomarenko, R. V. Gorbachev, G. L. Yu, D. C. Elias, R. Jalil, A. A. Patel, A. Mishchenko, A. S. Mayorov, C. R. Woods, J. R. Wallbank, M. Mucha-Kruczynski, B. A. Piot, M. Potemski, I. V. Grigorieva, K. S. Novoselov, F. Guinea, V. I. Fal'ko, and A. K. Geim, Cloning of Dirac fermions in graphene superlattices *Nature*, vol. 497, pp. 594–597, May 2013.

[10] R. K. Kumar, X. Chen, G. H. Auton, A. Mishchenko, D. A. Bandurin, S. V. Morozov, Y. Cao, E. Khestanova, M. B. Shalom, A. V. Kretinin, K. S. Novoselov,

L. Eaves, I. V. Grigorieva, L. A. Ponomarenko, V. I. Fal'ko, and A. K. Geim, High-temperature quantum oscillations caused by recurring Bloch states in graphene superlattices *Science*, vol. 357, no. 6347, pp. 181–184, 2017.

[11] J. R. Wallbank, R. Krishna Kumar, M. Holwill, Z. Wang, G. H. Auton, J. Birkbeck, A. Mishchenko, L. A. Ponomarenko, K. Watanabe, T. Taniguchi, K. S. Novoselov, I. L. Aleiner, A. K. Geim, and V. I. Fal'ko, Excess resistivity in graphene superlattices caused by umklapp electron–electron scattering *Nature Physics*, vol. 15, pp. 32–36, Jan 2019.

[12] J. M. B. Lopes dos Santos, N. M. R. Peres, and A. H. Castro Neto, Graphene Bilayer with a Twist: Electronic Structure *Phys. Rev. Lett.*, vol. 99, p. 256802, Dec 2007.

[13] G. Li, A. Luican, J. M. B. Lopes dos Santos, A. H. Castro Neto, A. Reina, J. Kong, and E. Y. Andrei, Observation of Van Hove singularities in twisted graphene layers *Nature Physics*, vol. 6, pp. 109–113, Feb 2010.

[14] Y. Cao, V. Fatemi, A. Demir, S. Fang, S. L. Tomarken, J. Y. Luo, J. D. Sanchez-Yamagishi, K. Watanabe, T. Taniguchi, E. Kaxiras, R. C. Ashoori, and P. Jarillo-Herrero, Correlated insulator behaviour at half-filling in magic-angle graphene superlattices *Nature*, vol. 556, pp. 80–84, Apr 2018.

[15] Y. Cao, V. Fatemi, S. Fang, K. Watanabe, T. Taniguchi, E. Kaxiras, and P. Jarillo-Herrero, Unconventional superconductivity in magic-angle graphene superlattices *Nature*, vol. 556, pp. 43–50, Apr 2018.

[16] M. Kim, S. G. Xu, A. I. Berdyugin, A. Principi, S. Slizovskiy, N. Xin, P. Kumaravadivel, W. Kuang, M. Hamer, R. Krishna Kumar, R. V. Gorbachev, K. Watanabe, T. Taniguchi, I. V. Grigorieva, V. I. Fal'ko, M. Polini, and A. K. Geim, Control of electron-electron interaction in graphene by proximity screening *Nature Communications*, vol. 11, p. 2339, May 2020.

[17] C. Gold, A. Knothe, A. Kurzmann, A. Garcia-Ruiz, K. Watanabe, T. Taniguchi, V. Fal'ko, K. Ensslin, and T. Ihn, Coherent Jetting from a Gate-Defined Channel in Bilayer Graphene *Phys. Rev. Lett.*, vol. 127, p. 046801, Jul 2021.

[18] A. Knothe and V. Fal'ko, Influence of minivalleys and Berry curvature on electrostatically induced quantum wires in gapped bilayer graphene *Phys. Rev. B*, vol. 98, p. 155435, Oct 2018.

[19] E. McCann and V. I. Fal'ko, Landau-Level Degeneracy and Quantum Hall Effect in a Graphite Bilayer *Phys. Rev. Lett.*, vol. 96, p. 086805, Mar 2006.

[20] E. McCann and M. Koshino, The electronic properties of bilayer graphene *Reports on Progress in Physics*, vol. 76, p. 056503, apr 2013.

[21] The full 4×4 Hamiltonian features two more bands at energies $\sim \pm\gamma_1$ which are projected onto the lower-energy bands using a Schrieffer-Wolff transformation [19, 20].

[22] A. B. Kuzmenko, I. Crassee, D. van der Marel, P. Blake, and K. S. Novoselov, Determination of the gate-tunable band gap and tight-binding parameters in bilayer graphene using infrared spectroscopy *Phys. Rev. B*, vol. 80, p. 165406, Oct 2009.

[23] $v = 1.0 \times 10^6\,\mathrm{m\,s^{-1}}$, $\gamma_1 = 0.381\,\mathrm{eV}$ and $v_3 = 1.2 \times 10^5\,\mathrm{m\,s^{-1}}$ [22, 19, 20].

[24] $\alpha = 0.15$ due to the potential asymmetry between dimer and non-dimer atoms, skew interlayer couplings, next-nearest-neighbour intralayer couplings and non-orthogonality of atomic orbitals [22, 19, 20].

[25] $u_0 = 9\,\mathrm{meV}$, $u_1 = -17\,\mathrm{meV}$ and $u_3 = -15\,\mathrm{meV}$ [41].

[26] G. Borghi, M. Polini, R. Asgari, and A. H. MacDonald, Dynamical response functions and collective modes of bilayer graphene *Phys. Rev. B*, vol. 80, p. 241402(R), Dec 2009.

[27] O. V. Gamayun, Dynamical screening in bilayer graphene *Phys. Rev. B*, vol. 84, p. 085112, Aug 2011.

[28] S. Slizovskiy, A. Garcia-Ruiz, A. I. Berdyugin, N. Xin, T. Taniguchi, K. Watanabe, A. K. Geim, N. D. Drummond, and V. I. Fal'ko, Out-of-Plane Dielectric Susceptibility of Graphene in Twistronic and Bernal Bilayers *Nano Letters*, vol. 21, no. 15, pp. 6678–6683, 2021. PMID: 34296602.

[29] X. Liu, Z. Wang, K. Watanabe, T. Taniguchi, O. Vafek, and J. I. A. Li, Tuning electron correlation in magic-angle twisted bilayer graphene using Coulomb screening *Science*, vol. 371, no. 6535, pp. 1261–1265, 2021.

[30] We include the overlaps of the wavefunctions of the incoming and outgoing electrons with the operator at each vertex.

[31] J. M. Ziman, ch. 9.14. Oxford Univ. Press, 1960.

[32] L. D. Landau and E. M. Lifshitz, vol. 10, ch. 79. Pergamon Press Ltd., 1981.

[33] R. Hlubina, Effect of impurities on the transport properties in the Van Hove scenario *Phys. Rev. B*, vol. 53, pp. 11344–11347, May 1996.

[34] Y. Xu, F. Herman, V. Granata, D. Destraz, L. Das, J. Vonka, S. Gerber, J. Spring, M. Gibert, A. Schilling, X. Zhang, S. Li, R. Fittipaldi, M. H. Fischer, A. Vecchione, and J. Chang, Magnetotransport of dirty-limit van Hove singularity quasiparticles *Communications Physics*, vol. 4, p. 1, Jan 2021.

[35] K. F. Mak, C. H. Lui, J. Shan, and T. F. Heinz, Observation of an Electric-Field-Induced Band Gap in Bilayer Graphene by Infrared Spectroscopy *Phys. Rev. Lett.*, vol. 102, p. 256405, Jun 2009.

[36] Y. Zhang, T.-T. Tang, C. Girit, Z. Hao, M. C. Martin, A. Zettl, M. F. Crommie, Y. R. Shen, and F. Wang, Direct observation of a widely tunable bandgap in bilayer graphene *Nature*, vol. 459, pp. 820–823, Jun 2009.

[37] A. Ramasubramaniam, D. Naveh, and E. Towe, Tunable Band Gaps in Bilayer Graphene-BN Heterostructures *Nano Letters*, vol. 11, no. 3, pp. 1070–1075, 2011. PMID: 21275424.

[38] W. Zhang, C.-T. Lin, K.-K. Liu, T. Tite, C.-Y. Su, C.-H. Chang, Y.-H. Lee, C.-W. Chu, K.-H. Wei, J.-L. Kuo, and L.-J. Li, Opening an Electrical Band Gap of Bilayer Graphene with Molecular Doping *ACS Nano*, vol. 5, no. 9, pp. 7517–7524, 2011. PMID: 21819152.

[39] C. Tan, D. Y. H. Ho, L. Wang, J. I. A. Li, I. Yudhistira, D. A. Rhodes, T. Taniguchi, K. Watanabe, K. Shepard, P. L. McEuen, C. R. Dean, S. Adam, and J. Hone,

Dissipation-enabled hydrodynamic conductivity in a tunable bandgap semiconductor *Science Advances*, vol. 8, no. 15, p. eabi8481, 2022.

[40] H. Ishizuka and L. Levitov, Wide-range T2 resistivity and umklapp scattering in moiré graphene *New Journal of Physics*, vol. 24, p. 052001, may 2022.

[41] M. Lee, J. R. Wallbank, P. Gallagher, K. Watanabe, T. Taniguchi, V. I. Fal'ko, and D. Goldhaber-Gordon, Ballistic miniband conduction in a graphene superlattice *Science*, vol. 353, no. 6307, pp. 1526–1529, 2016.

[42] R. Saito, M. S. Dresselhaus, and G. Dresselhaus, *Physical Properties of Carbon Nanotubes*. Imperial College Press, 1998.

Chapter 8

Conclusion

Chapter 3: Engineering of the topological magnetic moment of electrons in bilayer graphene using strain and electrical bias. We predicted that the topological properties of electrons in bilayer graphene can be enhanced using strain and vertical bias. This was realised by a two orders of magnitude enhancement in the topological magnetic moment of electrons at the band edge, giving a large valley splitting in an external magnetic field, which is of great utility in valleytronics. In the original manuscript, we proposed that this valley splitting could be observed experimentally by pumping strained bilayer graphene with circularly polarised light and measuring the induced photocurrent [1, 2]. This has been corroborated by a recent theoretical study into the stacking-dependence of these photocurrents in van der Waals homostructures, including bilayer graphene, predicting that they can be directed with modest strain [3]. In light of recent surveys into bilayer graphene quantum dots, we also propose that the strain-enhanced valley splitting can be measured experimentally by comparing a strained quantum dot to its unstrained counterpart, either by direct measurement [4] or by the tunnelling amplitudes [5].

Chapter 4: Kagomé network of miniband-edge states in double-aligned graphene-hexagonal boron nitride structures. We predicted that a Kagomé network of chiral channels forms between regions of different topology in a highly-aligned hBN/graphene/hBN heterostructure. States in each valley propagate in opposite directions along these channels, providing another avenue for valleytronics, like Chapter 3. Considering the propagation of coherent electron wave packets through this network, we derived the form of the Aharonov-Bohm (AB) oscillations in the quenched electrical conductivity with respect to the external magnetic field. This provides the possibility of sub-Tesla electron AB periods without the need for complicated fabrication [6, 7], since the period is inversely proportional to the area of the network unit cell, and hence can be made arbitrarily small by reducing the misalignment. Further, the AB oscillations are an experimentally observable signature of inversion symmetry breaking with parallel hBN layers, as compared to the inversion symmetric heterostructure where one of the hBN layers is inverted. Our work has been expanded on by a study into the dispersion and topological properties of the network bands in an analogous Kagomé network in periodically strained graphene [8], while a study in twisted trilayer graphene has revealed a similar local dependence of the effective model parameters [9].

Chapter 5: Band Gap Opening in Bilayer Graphene-$CrCl_3$/$CrBr_3$/CrI_3 van der Waals Interfaces. We investigated the bandgap opening in bilayer graphene due to the charge transfer from its bottom layer to a magnetic chromium trihalide (CrX_3, X=Cl,Br,I) substrate. This presents another means to generate the vertical bias utilised in Chapters 3 and 7, in addition to electrostatic gating. The bandgap was determined to be large, up to 170 meV for $CrCl_3$, through a combination of the activation energy and gating dependence of the electrical connectivity. Performing a self-consistent calculation of the screening of the bandgap at finite magnetic fields, we demonstrated excellent agreement between the effective continuum and ab initio models of bilayer graphene, and experiment. This demonstrates the applicability of the modified Hartree screening method used, which accounts for the out-of-plane polarisation of the orbitals in each layer [10], to the substrate-induced bandgap. We demonstrated that the electrons in the CrX_3 layer feature strong correlation consistent with a narrow conduction band, as the transferred electrons are localised to the Cr atoms. Future improvements could be made for CrI_3, where the charge transfer depends on temperature, accounting for the less narrow bands and reduced correlation. The correlation has been observed in a recent study into the giant gate-tunable renormalization of the spin-correlated narrow-band states and bandgap of CrB_3 grown on graphene [11].

Chapter 6: Semimetallic and semiconducting graphene-hBN multilayers with parallel or reverse stacking. We considered commensurate 3D heterostructures composed of stacks of alternating graphene and hBN layers with matching periods. We considered two distinct configurations with parallel and antiparallel orientation of neighbouring hBN layers, as in Chapter 4, breaking and preserving inversion symmetry, respectively. The electronic properties depends on the hopping amplitudes between graphene layers, being either a trivial or Weyl semimetal, or a semiconductor when a gap is opened for the parallel configuration. This survey was limited by a lack of knowledge of these hopping amplitudes, which are being explored via ab initio calculations [12], whose results will be included in the revised manuscript. We were motivated by another ab initio study, suggesting that the adhesion energy between the layers is sufficiently strong for mutual relaxation and lattice period matching to occur [13]. We hope that our findings will in turn motivate experimentalists to explore the practicality of such a stacking method.

Chapter 7: Umklapp electron-electron scattering in bilayer graphene moiré superlattice. We predicted that umklapp electron-electron (Uee) scattering off the moiré superlattice in a p-doped bilayer graphene/hBN heterostructure provides a strong contribution to its electrical resistivity. Like the equivalent monolayer graphene/hBN heterostructure [14, 15], this features a T^2 depends on the temperature and a threshold hole density, below which Uee scattering is suppressed. However, the different chirality of bilayer graphene allows backscattering, and the resistivity rapidly grows above this threshold, before reaching a peak value which depends, alongside the threshold density, on the twist. We demonstrated that the Uee contribution can be substantially enhanced with a vertical bias, and the particle-hole symmetry breaking is strong enough that the contribution to the e-doped resistivity is negligible. The calculations in this publication were limited by practicality far more than any other included in this thesis. The incoming/outgoing electrons states were restricted to the Fermi line with a low-temperature approximation, avoiding a complex six-dimensional integral for a broadened Fermi surface, which was demonstrated to be valid in monolayer graphene [14, 15]. Further, the density range was restricted to avoid contributions from impurity scattering at the van Hove singularity [16, 17], which were beyond the scope of the perturbative approach used. We are not aware of a satisfactory resolution to both problems, although the first could be resolved using Monte Carlo integration, while the second by an effective model at the saddle point [16, 17].

All these results have been obtained in a low-energy scheme, using a Bloch state decomposition in the tight-binding model or an effective continuum model. The modified Hartree screening method [10] used in Chapters 5 and 7 has demonstrated that the effects of the higher-energy bands, including the structural σ bands, can have significant effects at low energies. In particular, the treatment of the mSL interaction in the graphene/hBN heterostructures in Chapters 4 and 7 relies upon an effective model [18, 19], although its validity has been demonstrated experimentally [20]. An alternative approach [21] uses the Slater-Kostner parameterisation of the tight-binding model, which accounts for both the π and σ bands [22, 23, 24, 25]. The limitations of this method include its reliance on a "commensurate" mSL, whose supercell features a finite number of graphene and hBN unit cells, and the rapidly increasing computational complexity with the size of the supercell. By comparison, the effective method allows for an incommensurate mSL and features a much smaller fixed complexity. A new method has been claimed to combine the advantages of both methods by considering the full tight-binding Hamiltonian projected onto a truncated basis of select Bloch states [26], which we will evaluate in future.

Except for the Uee scattering in Chapter 7 and the modified Hartree screening in Chapters 5 and 7, all calculations have been performed in a single-particle picture. We believe this is justified, since all the bands/minibands calculated are sufficiently dispersive to avoid many-body effects and the resulting electron correlation [27, 28, 29]. However, recent surveys suggest that strongly gapped bilayer graphene [30, 31] and hBN/graphene/hBN heterostructures with a gating-induced structural phase transition [32] feature sufficiently flat bands for these effects to become relevant. Further study into these effects is warranted, potentially accounting for the compact Wannier orbitals which have recently been proposed as a factor in Uee scattering in twisted bilayer graphene [33].

In this thesis, we have presented a collection of works describing the quantum properties of few-layer graphene and its van der Waals heterostructures. We have proposed many ways these can be modified, such as the strain-enhanced topological magnetic moment in bilayer graphene Chapter 3, alongside the vertical bias considered in this chapter and 7, whose potential substrate-induced origins are discussed in Chapter 5. We have demonstrated the importance of moiré superlattice effects in van der Waals heterostructures combining graphene and hexagonal boron nitride, such as the chiral Kagomé network in Chapter 4 and umklapp electron-electron scattering in Chapter 7. Finally, we have demonstrated the distinct electronic properties of three-dimensional commensurate stacks of alternating graphene and hexagonal boron nitride in Chapter 6. All these results are of theoretical and experimental significance, and we believe that they will inspire further study, especially by this author.

Bibliography

[1] S. Slizovskiy, E. McCann, M. Koshino, and V. I. Fal'ko. arXiv:1905.13094, 2019.

[2] Private communication with F. Koppens.

[3] Y. Xiong, L. kun Shi, and J. C. W. Song, Atomic configuration controlled photocurrent in van der Waals homostructures *2D Materials*, vol. 8, p. 035008, mar 2021.

[4] Y. Lee, A. Knothe, H. Overweg, M. Eich, C. Gold, A. Kurzmann, V. Klasovika, T. Taniguchi, K. Wantanabe, V. Fal'ko, T. Ihn, K. Ensslin, and P. Rickhaus, Tunable Valley Splitting due to Topological Orbital Magnetic Moment in Bilayer Graphene Quantum Point Contacts *Phys. Rev. Lett.*, vol. 124, p. 126802, Mar 2020.

[5] A. Knothe, L. I. Glazman, and V. I. Fal'ko, Tunneling theory for a bilayer graphene quantum dot's single- and two-electron states *New Journal of Physics*, vol. 24, p. 043003, apr 2022.

[6] S. Russo, J. B. Oostinga, D. Wehenkel, H. B. Heersche, S. S. Sobhani, L. M. K. Vandersypen, and A. F. Morpurgo, Observation of Aharonov-Bohm conductance oscillations in a graphene ring *Phys. Rev. B*, vol. 77, p. 085413, Feb 2008.

[7] J. Dauber, M. Oellers, F. Venn, A. Epping, K. Watanabe, T. Taniguchi, F. Hassler, and C. Stampfer, Aharonov-Bohm oscillations and magnetic focusing in ballistic graphene rings *Phys. Rev. B*, vol. 96, p. 205407, Nov 2017.

[8] C. D. Beule, V. T. Phong, and E. J. Mele, Network model for periodically strained graphene arXiv:2209.02554, 2022.

[9] Y. Mao, D. Guerci, and C. Mora, Moiré-of-moiré low-energy effective theory of twisted trilayer graphene arXiv:2210.11507, 2022.

[10] S. Slizovskiy, A. Garcia-Ruiz, A. I. Berdyugin, N. Xin, T. Taniguchi, K. Watanabe, A. K. Geim, N. D. Drummond, and V. I. Fal'ko, Out-of-Plane Dielectric Susceptibility of Graphene in Twistronic and Bernal Bilayers *Nano Letters*, vol. 21, no. 15, pp. 6678–6683, 2021. PMID: 34296602.

[11] P. Lyu, J. Sødequist, X. Sheng, Z. Qiu, A. Tadich, Q. Li, M. T. Edmonds, J. Redondo, M. Švec, T. Olsen, and J. Lu, Giant gate-tunable renormalization of spin-correlated flat-band states and bandgap in a 2D magnetic insulator arXiv:2212.02772, 2022.

[12] Private communication with K. Zollner.

[13] Private communication with M. Szyniszewski, E. Mostaani, A. Knothe, A. C. Ferrari, V. I. Fal'ko and N. D. Drummond.

[14] J. R. Wallbank, R. Krishna Kumar, M. Holwill, Z. Wang, G. H. Auton, J. Birkbeck, A. Mishchenko, L. A. Ponomarenko, K. Watanabe, T. Taniguchi, K. S. Novoselov, I. L. Aleiner, A. K. Geim, and V. I. Fal'ko, Excess resistivity in graphene superlattices caused by umklapp electron–electron scattering *Nature Physics*, vol. 15, pp. 32–36, Jan 2019.

[15] M. Kim, S. G. Xu, A. I. Berdyugin, A. Principi, S. Slizovskiy, N. Xin, P. Kumaravadivel, W. Kuang, M. Hamer, R. Krishna Kumar, R. V. Gorbachev, K. Watanabe, T. Taniguchi, I. V. Grigorieva, V. I. Fal'ko, M. Polini, and A. K. Geim, Control of electron-electron interaction in graphene by proximity screening *Nature Communications*, vol. 11, p. 2339, May 2020.

[16] R. Hlubina, Effect of impurities on the transport properties in the Van Hove scenario *Phys. Rev. B*, vol. 53, pp. 11344–11347, May 1996.

[17] Y. Xu, F. Herman, V. Granata, D. Destraz, L. Das, J. Vonka, S. Gerber, J. Spring, M. Gibert, A. Schilling, X. Zhang, S. Li, R. Fittipaldi, M. H. Fischer, A. Vecchione, and J. Chang, Magnetotransport of dirty-limit van Hove singularity quasiparticles *Communications Physics*, vol. 4, p. 1, Jan 2021.

[18] J. R. Wallbank, A. A. Patel, M. Mucha-Kruczyński, A. K. Geim, and V. I. Fal'ko, Generic miniband structure of graphene on a hexagonal substrate *Phys. Rev. B*, vol. 87, p. 245408, Jun 2013.

[19] X. Chen, J. R. Wallbank, M. Mucha-Kruczyński, E. McCann, and V. I. Fal'ko, Zero-energy modes and valley asymmetry in the Hofstadter spectrum of bilayer graphene van der Waals heterostructures with hBN *Phys. Rev. B*, vol. 94, p. 045442, Jul 2016.

[20] M. Lee, J. R. Wallbank, P. Gallagher, K. Watanabe, T. Taniguchi, V. I. Fal'ko, and D. Goldhaber-Gordon, Ballistic miniband conduction in a graphene superlattice *Science*, vol. 353, no. 6307, pp. 1526–1529, 2016.

[21] P. Moon and M. Koshino, Electronic properties of graphene/hexagonal-boron-nitride moiré superlattice *Phys. Rev. B*, vol. 90, p. 155406, Oct 2014.

[22] J. C. Slater and G. F. Koster, Simplified LCAO Method for the Periodic Potential Problem *Phys. Rev.*, vol. 94, pp. 1498–1524, Jun 1954.

[23] T. Nakanishi and T. Ando, Conductance of Crossed Carbon Nanotubes *Journal of the Physical Society of Japan*, vol. 70, no. 6, pp. 1647–1658, 2001.

[24] S. Uryu, Electronic states and quantum transport in double-wall carbon nanotubes *Phys. Rev. B*, vol. 69, p. 075402, Feb 2004.

[25] G. Trambly de Laissardière, D. Mayou, and L. Magaud, Localization of Dirac Electrons in Rotated Graphene Bilayers *Nano Letters*, vol. 10, no. 3, pp. 804–808, 2010. PMID: 20121163.

[26] W. Miao, C. Li, X. Han, D. Pan, and X. Dai, Truncated Atomic Plane Wave Method for the Subband Structure Calculations of Moiré Systems arXiv:2210.02026, 2022.

[27] R. Bistritzer and A. H. MacDonald, Moiré bands in twisted double-layer graphene *Proceedings of the National Academy of Sciences*, vol. 108, no. 30, pp. 12233–12237, 2011.

[28] Y. Cao, V. Fatemi, A. Demir, S. Fang, S. L. Tomarken, J. Y. Luo, J. D. Sanchez-Yamagishi, K. Watanabe, T. Taniguchi, E. Kaxiras, R. C. Ashoori, and P. Jarillo-Herrero, Correlated insulator behaviour at half-filling in magic-angle graphene superlattices *Nature*, vol. 556, pp. 80–84, Apr 2018.

[29] Y. Cao, V. Fatemi, S. Fang, K. Watanabe, T. Taniguchi, E. Kaxiras, and P. Jarillo-Herrero, Unconventional superconductivity in magic-angle graphene superlattices *Nature*, vol. 556, pp. 43–50, Apr 2018.

[30] D. Marchenko, D. V. Evtushinsky, E. Golias, A. Varykhalov, T. Seyller, and O. Rader, Extremely flat band in bilayer graphene *Science Advances*, vol. 4, no. 11, p. eaau0059, 2018.

[31] Private communication with A. Garcia-Ruiz.

[32] Private communication with K. S. Novoselov.

[33] H. Ishizuka and L. Levitov, Wide-range T2 resistivity and umklapp scattering in moiré graphene *New Journal of Physics*, vol. 24, p. 052001, may 2022.